THE UNIVERSITY OF OKLAHOMA

GRADUATE COLLEGE

THE RETRIEVAL OF INITIAL FORECAST FIELDS FROM SINGLE DOPPLER OBSERVATIONS OF A SUPERCELL THUNDERSTORM

A Dissertation

SUBMITTED TO THE GRADUATE FACULTY

in partial fulfillment of the requirements for the

degree of

DOCTOR OF PHILOSOPHY

By

STEPHEN SCOTT WEYGANDT

Norman, OK

1998

UMI Number: 9839808

THE RETRIEVAL OF INITIAL FORECAST FIELDS FROM SINGLE DOPPLER OBSERVATIONS OF A SUPERCELL THUNDERSTORM

A Dissertation

APPROVED FOR THE SCHOOL OF METEOROLOGY

BY

ACKNOWLEDGMENTS

I would like to express the vast debt of gratitude that I have for my co-advisors, Drs. Kelvin Droegemeier and Alan Shapiro. They have both been outstanding mentors; guiding my course of study, sharing their wisdom with me, and standing behind me whenever I needed it most. I have been greatly enriched by their influence and will forever value their friendship.

I am also very grateful to my other committee members, Drs. Douglas Lilly, Jerry Straka, Fred Carr and Leonid Dickey, for their guidance in this project and in my professional development as a scientist. My appreciation also extends to Dr. John Lewis, who served on my committee for much of this study, and invested a significant amount of time teaching me adjoint techniques.

Special thanks go to David Dowell for making me aware of the Arcadia, OK, supercell dataset, providing me with his dual-Doppler analyses, and teaching me the art of radar data editing. Thanks also go to Dr. Howard Bluestein for facilitating my use of the Arcadia data.

During the course of this study, I have benefited greatly from scientific discussions with and assistance from a number of individuals including Steve Lazarus, Keith Brewster, Ming Xue, Rich Carpenter, Gene Bassett, Adwait Sathye, DeWayne Mitchell, Phillip Spencer, Seon Ki Park, Scott and Yvette Richardson, Jeff Trapp and Sonia Lasher-Trapp, Kathy Kanak, Limin Zhao, Scott Ellis, Mark Askelson, Jian Zhang and Yuhe Liu. Their help and friendship is greatly appreciated. In addition to the people listed above, the friendship and support of a great number of colleagues in the local meteorological community has helped make Norman a place to call home.

Throughout the course of my studies I have received a great deal of support from my family. In particular, my mother, Mary Weygandt, has patiently encouraged me to see this endeavor through to its completion and my father, Phil Weygandt, has listened to my scientific explanations and helped to clarify my thinking. I will always be indebted to both of them.

Above all, however, my deepest thanks and gratitude go to my wife, Sue. Through all my studies, she has stood by me with love, support, patience and understanding (not to mention lots of graphics and proofreading). I truly could not have finished this without her. Lastly, thanks to my son Scott, who helped me to finish this by showing me what is most important in life.

This research was supported by the National Science Foundation through Grant ATM91-20009 to the Center for Analysis and Prediction of Storms and by a supplemental grant from the FAA. Computer support was provided by the Environmental Computing Applications System (ECAS) at the University of Oklahoma. ECAS is supported by the University of Oklahoma and the National Science Foundation under Grant EAR95-12145.

TABLE OF CONTENTS

LIST OF TABLES

LIST OF FIGURES

ABSTRACT

In this study, I test the hypothesis that sufficient information can be extracted from a time-series of single-Doppler observations to obtain a dynamically consistent analysis of a deep-convective storm. This is accomplished by developing a single-Doppler analysis/retrieval procedure and applying it to a real-data case of an Oklahoma supercell thunderstorm. Recognizing that the most sophisticated retrieval/analysis techniques (such as 4DVAR) are not practicable at this time, I have sought to incorporate key attributes of these techniques (such as the use of dynamic constraints and time-tendency information) into a simpler, more efficient method.

The new method features the sequential application of a single-Doppler velocity retrieval (SDVR) and a Gal-Chen type thermodynamic retrieval. By utilizing simpler subsets of the full dynamic equations in this manner, some of the difficulties associated with full-model adjoints (solution non-uniqueness and extreme computational expense) can be circumvented. The two main sequential retrieval components are augmented by a wind blending procedure, a variational wind adjustment, and a simple method for specifying moisture fields.

For the SDVR, Shapiro's two-scalar technique is adapted for use on deep convective storms by applying it in a moving reference frame. Two possible moving reference frames (both calculated from the radar data) are tested: one that follows the *storm motion* and one that follows the *mean wind*. Verification of the retrieved wind field against a corresponding dual-Doppler analysis indicates significantly improved results for both moving reference frames compared with the fixed frame.

The SDVR skill scores are especially good at low-levels; however, most of the retrieved azimuthal velocity is associated with polar vorticity. Missing from the retrieved fields (compared to the dual-Doppler analysis) is the low-level azimuthal convergence. Consistent with this, the SDVR only retrieves about half of the 55 m s^{-1} updraft present in the dual-Doppler analysis.

Following the velocity blending and adjustment steps, the thermodynamic retrieval is applied to both the single- and dual-Doppler-derived wind fields, yielding realistic looking and qualitatively similar perturbation potential temperature fields. An analysis of the terms in the vertical momentum equation is performed to document their contribution to the retrieved potential temperature. Comparisons with predictions from simple linear theory indicate a good agreement. The perturbation pressure and vorticity fields are also found to be in reasonable agreement with linear theory predictions for deep-convection in sheared flow.

Following the moisture specification step, short-range numerical predictions are initiated from both the single- and dual-Doppler-derived fields. In both cases, the general storm evolution and deviant storm motion are reasonably well predicted for a period of about 35 minutes. Sensitivity experiments indicate that the predicted storm evolution is strongly dependent on the initial moisture fields, with rainwater exerting the greatest influence.

Based on the results from this study, I conclude that for this particular case the time-series of single-Doppler observations contain sufficient information to obtain a dynamically consistent analysis suitable for initializing a storm-scale numerical prediction model. Furthermore, the Arcadia storm appears to exhibit at least some degree of predictability. Based on these encouraging findings, continued development of this and other single-Doppler retrieval techniques is recommended.

CHAPTER 1

INTRODUCTION

1.1 Statement of the problem

The recent installation of the WSR-88D Doppler radar network (Klazura and Imy 1993), combined with continuing increases in computer power, has heightened prospects for the operational implementation of numerical models designed to explicitly predict individual thunderstorms and their larger aggregates (Lilly 1990a; Droegemeier 1990, 1997). Toward that end, this decade has witnessed a significant research effort geared toward the development of numerical analysis and prediction techniques suitable for convective-scale phenomena and observing systems.

Based on the premise that a dynamically consistent analysis that resolves internal thunderstorm structures is necessary to successfully initialize an explicit storm-scale prediction model, and recognizing the fact that Doppler radars currently represent the only data source for such an analysis, much of the research effort to date has focused on obtaining initial forecast fields from Doppler radar observations. Because the large distance between WSR-88D radars generally precludes multiple-Doppler wind syntheses, any operational procedure for initializing numerical models from Doppler radar data will need to rely on data from a network of radars that together only provide *single-Doppler* coverage over the total area.

There are many unanswered questions pertaining to the problem of storm-scale numerical weather prediction using single-Doppler observations, including:

1) What is the predictability limit for individual convective storms?
2) What degree of detail is needed in the initial forecast fields in order to successfully predict the evolution of individual convective elements?
3) Can single-Doppler observations provide sufficient information to produce dynamically consistent analyses that resolve internal thunderstorm structures?
4) Which analysis and retrieval techniques are best suited to the task of obtaining thunderstorm-scale initial analyses from single-Doppler observations?
5) How will the choice of analysis and retrieval procedures be affected by the practical constraints imposed by a real-time operational setting?

In this thesis, I focus on the third question and test the general hypothesis that *sufficient information can be extracted from a time-series of single-Doppler observations to obtain a dynamically consistent analysis of a thunderstorm.* This hypothesis is tested by developing a single-Doppler analysis/retrieval procedure and applying it to single-Doppler observations of a supercell thunderstorm to generate a set of initial forecast fields. These fields and a numerical prediction initialized from them are verified using dual-Doppler observations. The retrieval procedure is suitable for very high resolution (Δx = 1 km) analyses and very short range predictions (0-2 hours) over a region approximately covering the domain of a single WSR-88D Doppler radar (200 x 200 km^2).

Any successful radar analysis/retrieval scheme will likely be built upon the foundation provided by over 40 years of meteorological data analysis research. Therefore, it is important to gain a clear understanding of the strengths and weaknesses of existing analysis procedures, as well as their relationship to the storm-scale numerical weather prediction problem (defined as the prediction of the explicit updraft and downdraft structures of the most energetic mesoscale systems). With that goal in mind, I now present a critical review of the significant developments in meteorological data analysis research.

1.2 Review of meteorological data analysis

Meteorologists have long grappled with the task of organizing the multitude of different atmospheric observations into a coherent picture that describes complicated atmospheric processes. As described by Daley (1991), the first attempts at solving this problem focused on hand-drawn subjective analyses of pressure which emphasized spatial and temporal smoothness. These proved to be quite illuminating and led to significant advances in our understanding of mid-latitude cyclones (Bjerknes and Solberg, 1922). Bjerknes' father had already realized that weather prediction was fundamentally an initial value problem in fluid dynamics, and that Newton's laws of motion could be used to predict the future state of the atmosphere given an accurate initial state (Bjerknes 1904).

L.F. Richardson was the first person to test the elder Bjerknes' theory in his landmark attempt to numerically integrate a weather prediction model (Richardson, 1922). In order to obtain an analysis of the initial atmospheric state, he subjectively contoured the pressure and wind observations and then read off the appropriate value for each model gridpoint. Nearly 30 years later, the same analysis procedure was still in use when Charney et al. (1950) performed the first successful numerical integration of a weather prediction model.

By that time, however, the need for a more systematic (and quicker) method for obtaining model initial fields had been recognized, and research on so-called "objective analysis" procedures had begun.

Most of the present meteorological data analysis algorithms (and much of the theory) were developed for synoptic-scale phenomena, observing networks, and models. For this scale, over 40 years of testing and refinement have led to the acceptance of certain analysis principles, including 1) the use of a background field, 2) the use of error statistics, and 3) the use of physical constraints. A variety of different techniques that utilize these principles have been thoroughly investigated and form the basis for the meteorological data analysis procedures presently used in operational prediction centers around the world.

Separately, a host of single-Doppler radar analysis techniques have been developed. Used primarily for diagnostic studies with research radar datasets and for nowcasting guidance, these algorithms were generally not developed for the task of generating initial forecast fields and have not always made use of the above principles. They do, however, accommodate some of the unique aspects of Doppler radar data, including 1) observations of two non-traditional fields (reflectivity and radial velocity), 2) observations in a non-traditional coordinate system (spherical) and 3) observations with very high spatial and temporal resolution (compared to synoptic-scale space and time scales). Because Doppler radars provide only radial velocity and reflectivity information, and only within precipitation or boundary-layer regions, radar data analysis techniques have tended to emphasize the "retrieval" of unobserved fields, as opposed to the analysis of well sampled fields.

For any scale of motion, the available set of meteorological observations provides an incomplete description of the atmospheric state and contains both random and systematic errors. Because of this, additional information is usually used to aid the meteorological analysis procedure. Over the years, this information has taken many forms, including spatial and temporal smoothness, use of a background estimate, knowledge of the statistical error structures of the observations and the background fields, and the use of physical and mathematical constraints.

As mentioned previously, synoptic-scale data analysis has been aided greatly by three sources of additional information. First, a *background estimate* of the field to be analyzed can usually be obtained from a previous analysis or model prediction. The analyzed value of the field is then calculated as a small modification to the background estimate. Second, information about the *statistical structure of the observational and background errors* is known from long term records. This information can be used to help determine weight factors in the analysis. Finally, the different *atmospheric fields are related by simple approximations* to the governing equations. Using these relations, observations of one variable (e.g., pressure) can be used to infer information about other variables (e.g. wind components).

For convective-scale analysis of single-Doppler radar data, the utility of the three information sources described above has yet to be ascertained, though obvious problems exist. First, the nature of thunderstorms (small-scale, large amplitude, intermittent perturbations to the more slowly varying large-scale flow) has, up to now, precluded the determination of good estimates of background fields *within thunderstorms*. Second, the knowledge of error structures, which is so important to the success of synoptic-scale statistical analysis schemes, is much less complete on the convective-scale. This is especially true along the edges of storms, where there exists a sharp gradient in the density of observations, as well as a transition between flows of different scales. Finally, the balanced flow approximations that have significantly aided synoptic-scale analysis are generally not valid on the convective-scale. This precludes the use of simple geostrophic or hydrostatic relations in storm-scale analysis procedures.

Fortunately, Doppler radar observations feature certain qualities that help offset the above limitations. First, WSR-88D radars provide a time-series of three-dimensional volume-scans with a temporal resolution of about five minutes. This facilitates the use of time-tendency information in parameter retrieval algorithms. Second, the radar data are available at very high spatial resolution (typically a kilometer or less in all directions). By using Lagrangian techniques or appropriately chosen moving reference frames, one can exploit this high spatial resolution to effectively improve the temporal resolution of the radar observations (Gal-Chen 1982).

With the above differences in mind, I divide meteorological data analysis techniques into two classes: 1) methods developed primarily for synoptic-scale analysis of data from traditional observing platforms (radiosondes, wind profilers, satellites) and 2) methods developed for storm-scale analysis of Doppler radar data. It is important to note that some overlap exists between these two classes.

1.2.1 Synoptic-scale techniques

The earliest meteorological research on objective data analysis procedures dates back to the late 1940's and focused on the synoptic-scale observation network. Panofsky (1949) and Gilchrist and Cressman (1954) described objective analysis procedures that obtained a least squares fit of a polynomial expansion to the observed data values. In 1955, Bergthorsson and Doos introduced a new procedure in which the analysis was performed on an "observation increment", defined as a deviation of the observation from a "background" field. An "analysis increment" was calculated from an appropriately weighted linear combination of the observational increments.

Much subsequent research has focused on methods for specifying the weights in the above procedures. Cressman (1959) and Barnes (1964) used isotropic, distance-dependent formulations for the weight functions, while Bergthorsson and Doos (1955) used weights that were empirically calculated from the long term statistics of errors associated with the observed, forecast, and mean fields. In the widely used successive correction method, a series of incremental corrections is computed with the output analysis serving as the background for the next iteration.

The use of statistical information about the observation and background errors in the formulation of the analysis weights was first suggested by Eliassen (1954) and studied extensively by Gandin (1963). It has since become known as "statistical" or "optimal" interpolation. The multivariate form of this powerful technique allows for the inclusion of linear dynamical constraint relations among variables while providing a least squares, minimum-variance estimate (Lorenc 1981). For synoptic-scale flows, the multivariate approach with geostrophic constraints has been very successful and many operational centers have used some form of it with output from previous forecasts serving as the background field (Dey and Morone 1985).

Kalman filtering (Kalman 1960; Ghil et al. 1981) is a more elaborate extension of statistical interpolation that includes a prediction of the time evolution of the statistical error structure so that analyses can be performed at successive times. Unfortunately, two factors have limited its application to rather simple models (Daley 1991). First, the procedure requires a specification of the "system" (model) error covariance, which is difficult to determine in practice. Second, calculation of the predicted error covariances is extremely computer intensive.

As the "filtered" atmospheric models used during the 1950's and early 1960's gave way to more realistic "primitive equation" models, a further complexity was added to the data analysis problem. For synoptic-scale systems, the pressure and velocity fields are in a state of near geostrophic and non-divergent balance. If the model's initial fields do not reflect a similar quasi-balanced state, spurious large-amplitude inertia-gravity waves can be excited.

Filtered models are not affected by this problem because they do not admit these waveforms as solutions. For the primitive equation models, however, the imbalances lead to a "noisy" adjustment period at the beginning of the model integration that can adversely affect the subsequent model solution. This issue, which was not understood in Richardson's time, was one of the factors leading to the failure of his prediction. A number of so-called "initialization" procedures have been developed to remedy this problem, including the use of damping numerical schemes (Matsuno 1966), geostrophic or balance equations to obtain the wind field (Hinkelmann 1951; Charney 1955; Phillips 1960), and normal-mode techniques to remove inertia-gravity waves (Dickinson and Williamson 1972; Williamson and Dickenson 1976; Machenhauer 1977; Baer 1977). An alternative method, known as dynamic initialization, was introduced by Miyakoda and Moyer (1968) and Nitta and Hovermale (1969). It uses the numerical model itself to damp spurious inertia-gravity waves through repeated forward and backward integrations around the initial time.

Beginning in the late 1960's, a series of new remote sensing platforms was implemented and offered the potential for supplying a nearly continuous stream of observations. It ultimately led to a new method for ingesting asynchronous data and obtaining balanced initial conditions. In 1969, Charney et al. showed that the repeated insertion of data into a forward-integrating model could induce a response in the data void regions, eventually leading to model state that was both faithful to the observations and in balance with the model equations. Thompson (1961) had previously shown that a model could be used to propagate information from data-rich regions to data-sparse regions. The general principle of using the model itself to assimilate a stream of asynchronous observations has since come to be known as *continuous data assimilation*. Two weaknesses of the procedure are that the inserted data sometimes "shock" the model (i.e., produce geostrophic imbalances that lead to the excitation of spurious inertia-gravity waves) and that the model sometimes "rejects" the inserted data (i.e., the inserted data have no lasting impact on the numerical solution).

A related procedure, known as dynamic relaxation or nudging (Hoke and Anthes 1976; Davies and Turner 1977), minimizes the "shock" problem by utilizing extra terms in the prognostic equations to gradually force the model state toward the observations. A weakness common to both direct insertion and dynamic relaxation methods is the lack of an explicit method for dealing with errors in the observations. Despite these shortcomings, continuous data assimilation combines the analysis and initialization tasks into one procedure and has been widely used (Daley 1991).

Simultaneous to the development of continuous data assimilation techniques, an alternative class of analysis/initialization procedures was being developed based on the principles of variational calculus. Introduced to the meteorological community in the 1950's by Sasaki (1955, 1958), the variational formalism provides an elegant method for minimizing analysis departures from observations while simultaneously enforcing specified physical constraints. These constraints can either be *strong* , in which they must be exactly satisfied at each point in the analysis grid, or *weak* , in which departures from the constraint are minimized over the entire analysis grid (Sasaki 1970).

Early work focused on the application of diagnostic constraints to the spatial analysis problem. Sasaki (1969) and Thompson (1969) independently pioneered the extension of these methods to include time-dependent equations as strong constraints. Variational principles were utilized to transform the constrained minimization problem into an unconstrained problem involving the associated Euler-Lagrange equations. The difficulties associated with solving the Euler-Lagrange equations were eventually circumvented by use of the adjoint equations to determine the gradient of the cost function (with respect to the control variables), combined with descent algorithms for finding the cost function's minimum from the gradient information.

Meteorological application of adjoint techniques was first discussed by Marchuk (1974). LeDimet (1982) arrived at the same result by expressing the problem in terms of the optimal control theory work of Lions (1971). Active research in four-dimensional variational (4DVAR) techniques continued through the 1980's, with both theoretical advancements and practical implementations for simplified models (Lewis and Derber 1985; LeDimet and Talagrand 1986; Talagrand and Courtier 1987; Thacker and Long 1988).

The 1990's have seen the application of 4DVAR techniques to increasingly sophisticated models (Navon et al. 1992; Thepaut et al. 1993; Zou et al. 1993), as well as emphasis on the problem of non-differentiable "switches" (Bao and Warner 1993; Bao and Kuo 1995; Xu 1996a,b; Zou 1995) and the more computationally efficient "quasi-inverse" method (Wang et al. 1997; Pu et al. 1997). Despite these advances and rapid increases in computer power, real-time application of 4DVAR techniques to operational prediction models is still not practical due to the excessive amount of computer time needed to find the minimum of the cost function for large operational numerical models.

1.2.2 Radar data techniques

Over the past 40 years a variety of single-Doppler radar data analysis and retrieval procedures have been developed. They typically have utilized simple dynamic or kinematic constraints in a variational formulation to "retrieve" wind, thermodynamic and microphysical information not directly observed by the radar. The earliest retrieval techniques focused on finding area- or volume-average wind quantities. In the method known as Velocity Azimuth Display (VAD), a linear wind model is fit to the radial velocity data from a scan circle (or portion thereof) to obtain mean estimates of certain kinematic quantities (horizontal wind, divergence and deformation) (Lhermitte and Atlas 1961; Browning and Wexler 1968; Easterbrook 1975). Volume Velocity Processing (VVP) is a similar technique in which the linear wind field assumption is applied over a specified volume, yielding local estimates of kinematic quantities (Waltdteufel and Corbin 1979; Koscielny et al. 1982). These methods are not well suited for thunderstorms, where the actual wind field is not a linear function of the space coordinates.

Another class of wind retrievals estimates the wind field from the motion of radar echo patterns. These echo tracking algorithms, which can be applied to conventional or Doppler radar data, have been explored by Rhinehart (1979), Smythe and Zrnic (1983) and Tuttle and Foote (1990). The best results have been obtained for clear-air boundary layers, however, where reflectivity conservation is least violated. There is usually a reduction in the spatial resolution of the retrieved wind structures relative to the structures in the radar data.

Within the past few years, more sophisticated single-Doppler velocity retrieval (SDVR) techniques have been developed. They utilize a variety of assumptions (conservation of reflectivity, radial velocity, mass; spatial smoothness; velocity stationarity, the frozen turbulence hypothesis), enforced as either weak constraints in a least squares formulation or as strong constraints in a 4DVAR formulation. These schemes have been applied mostly to clear-air boundary layers, yielding reasonably good results.

Shapiro et al. (1995a) developed a three-dimensional SDVR scheme by assuming that the time history of two conserved scalars plus the radial velocity is known. In addition to reflectivity, a second scalar was obtained by imposing a temporal constraint on the velocity field (either velocity stationarity or frozen turbulence). A least squares formulation leads to a Poisson equation for a pseudo-streamfunction, from which the unknown velocity components can be obtained.

Zhang and Gal-Chen (1996) assumed Lagrangian conservation of reflectivity and steadiness in eddy structures to develop a procedure for retrieving constant Cartesian wind components. A least squares formulation leads to a linear system of equations involving integral quantities which, when solved over the whole domain, yield mean flow components. Perturbation velocities were then found by solving the system within smaller grid "boxes".

Laroche and Zawadzki (1994) and Xu et al. (1994a,b; 1995) applied "simple" adjoint techniques to simplified prognostic equations for reflectivity or radial velocity. In addition to retrieving the unknown velocity components, these techniques obtain estimates for other unknowns in the constraint equations. The addition to the cost function of penalty terms involving spatial and temporal smoothness was found to improve the retrieval performance.

Another broad class of radar data retrieval procedures has dealt with the problem of diagnosing thermodynamic fields from a time-history of wind data. Theoretically applicable at any scale, these techniques have most frequently been used in conjunction with dual-Doppler-derived wind-fields. Gal-Chen (1978) and Hane and Scott (1978) described a variational technique to diagnose pressure perturbations from a horizontal average using the horizontal momentum equations as weak constraints. Buoyancy perturbations could then be obtained by applying the vertical momentum equation to the retrieved pressure field. Although the technique has proven useful in diagnostic studies (Hane et al 1981; Gal-Chen and Kropfli 1984; Parsons et al. 1987), it has two principal shortcomings (Daley 1991). First, unless the perturbation pressure is known along the lateral boundaries, the solution is not unique. Second, the temperature field cannot be obtained from the buoyancy field unless the moisture fields are known. Roux (1985) overcame the first difficulty by using a thermodynamic equation as an additional constraint. Unfortunately, this requires an estimate of the temperature tendency, which is not readily available. Sun and Crook (1996) demonstrated that adjoint techniques could also be used to retrieve thermodynamic fields from a time series of three-dimensional wind fields.

In addition to wind and thermodynamic retrievals, a number of procedures have been developed to deduce microphysical quantities from Doppler radar data. Typically they have assumed that a satisfactory three-dimensional wind field was available from a multiple-Doppler wind analysis. Rutledge and Hobbs (1983,1984) and Ziegler (1985,1988) independently developed techniques in which conservation equations for heat and moisture were integrated forward toward a steady-state using a prescribed time-invariant wind-field. Hauser and Ameyenc (1986) inverted steady-state forms of the conservation equations to obtain microphysical fields. Verlinde and Cotton (1990) documented some of the limitations of the steady-state assumption and later avoided it by fitting a fully time-dependent kinematic model to idealized observations using the adjoint technique (Verlinde and Cotton 1993).

A number of researchers have attempted to simultaneously retrieve all unknown fields at all gridpoints using 4DVAR techniques applied to the full prognostic equations. Sun et al. (1991) applied adjoint techniques to a dry Boussinesq model to retrieve wind and thermodynamic fields from model simulated observations of a single Cartesian wind component. They obtained promising results, but indicated that the temperature field was more difficult to retrieve than the unobserved wind components. Similar experiments by Kapitza (1991) with a dry anelastic model confirmed these difficulties and showed that additional information about the temperature field greatly aided its retrieval.

Real data tests by Sun and Crook (1994) produced good results for a dry gust front case. More recently, they tested the adjoint of a moist version of their model [Kessler

(1969) microphysical parameterization] using both simulated and real radar data (Sun and Crook 1997, 1998). Comparison of the results obtained using observations from one versus two Doppler radars indicated that all retrieved fields are less accurate when data from only one radar is available, and that accurate physical parameterizations of moist processes are necessary.

An alternative procedure for retrieving wind and thermodynamic information was proposed by Liou (1989). It utilized cycles of radial velocity insertion, thermodynamic retrieval and forward model integration. This "forward" procedure is a modified form of continuous data assimilation in which retrieved as well as observed data are inserted into the model. Because convective-scale models can more faithfully reproduce inertia-gravity waves (they may in fact play an important role for certain flow evolutions), the problem of inserted data shocking the model (i. e. exciting spurious inertia-gravity waves) is not as great for convective-scale models as it is for meso- and synoptic-scale models. While Liou's idealized test results showed some promise, Lilly (1990b) showed that the retrieval convergence rate for the cross-beam vorticity was related to the diffusive time-scale and therefore could be quite slow. A possible remedy for this is to incorporate one of the previously described wind retrievals into Liou's procedure. A theoretical drawback to this method is that it does not simultaneously use all the observations within the data assimilation window to retrieve the unobserved fields.

Although the focus of this study is single-Doppler retrievals, the dual-Doppler model initialization study of Lin et al. (1993) is worthy of note. They obtained initial forecast fields by applying a thermodynamic retrieval to dual-Doppler-derived 3-D wind fields and making some simple assumptions about the microphysical variables. A drawback of their study was the neglect of the velocity time-tendencies in the thermodynamic retrieval. A short-range numerical prediction initialized from their retrieved fields for the 20 May 1977

Del City, OK tornado case (Ray et al. 1981) was found to evolve faster than the observed storm.

Finally, Crook and Tuttle (1994) describe a single-Doppler initialization procedure that combines the TREC wind retrieval (Rhinehart 1979) with a thermodynamic retrieval. Use of their procedure to initialize three short-range model predictions of dry high plains gust fronts resulted in a modest improvement over a persistence forecast. Utilizing Zhang and Gal-Chen's (1996) wind retrieval, Lazarus (1996) tested a similar combined retrieval technique on a Florida multicell case. The wind retrieval performed quite well; however, the model predictions showed only a limited amount of skill.

1.3 The present study

As described previously, a number of factors have precluded direct application of many of the synoptic-scale analysis techniques to the radar data retrieval problem. Of the available procedures, full-model 4DVAR would appear to be ideally suited to the problem because it can retrieve unobserved fields, it uses the full-model equations as constraints, and in principle should not depend critically on accurate specification of a background field (except for solution convergence rate). A number of troublesome issues remain, however, which may significantly limit the viability of full-model 4DVAR techniques to the single-Doppler analysis problem.

First, the severe underdeterminancy of the problem may make it difficult to obtain a unique, converged solution without a good first guess. One possible remedy would be the use of some other technique to provide first-guess fields that places the solution within the basin of the cost function's true global minimum. Second, the strong non-linearity of deep-convective storms may also lead to solution non-uniqueness (Li 1991). Third, the many non-differentiable "on/off" switches found in moist physical parameterizations may lead to difficulties in locating the global minimum of the cost function (due to incorrect gradient information or topological complexity in the cost function). As shown by Park and Droegemeier (1997), this problem may be significant even when a very accurate first guess is given. Fourth, full-model 4DVAR with strong constraints strictly enforces a forecast model that is known to be an imperfect representation of the true atmosphere. Model errors are likely to be even greater for thunderstorm-scale flows than for synoptic-scale flows. [An alternative 4DVAR formulation that accounts for some model error has been studied by Derber (1989).] Finally, the computational expense of descent algorithms for finding the minimum of the cost function is still prohibitive for real-time applications. Typically, 50 to 100 iterations are needed to obtain a converged solution and each iteration requires three model integrations over the assimilation period.

A promising alternative to 4DVAR is the sequential application of simpler variational retrieval techniques that use direct specification of time-tendency information. In particular, a series of three single-Doppler wind retrievals, followed by a thermodynamic retrieval, represents a practicable method to obtain wind and thermodynamic information. *By utilizing simpler subsets of the full dynamic equations in this manner, it may be possible to circumvent some of the difficulties associated with the full-model adjoint techniques and still retain many of their attributes, including the use of dynamic constraints and time-tendency information.* Proceeding from that assumption and the general hypothesis stated in Section 1.1, I test herein the specific hypothesis that *a sequential application of wind and thermodynamic retrievals is sufficient to obtain a dynamically consistent analysis of a thunderstorm from a time-series of single-Doppler observations.*

The hypothesis is tested by application of such a procedure to a real-data case of an Oklahoma supercell that was sampled by two Doppler radars. Three criterion are used to evaluate the success of the procedure and by inference the validity of the hypothesis *for* *this case*. First, the accuracy of the retrieved fields compared to the available verification data is measured. Second, where verification data are unavailable, the degree to which the analyzed/retrieved fields satisfy the imposed constraints and conform to analytic predictions is evaluated. Third, a numerical forecast initialized from the analyzed/retrieved data is compared to the available verification data. A reasonably accurate model prediction would indicate that the retrieved fields are reasonably optimal for this model and set of observations.

For the wind retrieval, I use a modified form of Shapiro's (1995a) two-scalar technique (Weygandt et al. 1995). It was developed originally for clear-air boundary layers, but is one of the few retrievals that obtains complete 3-D wind-fields throughout the entire storm volume. Applying Shapiro's scheme to a deep-convective storm represents a significant extension from previous results obtained with it. The principal modification to the scheme is the application of it in a moving reference frame. A detailed evaluation of the results using the moving reference frame is an important sub-topic of this study.

For the thermodynamic retrieval, I use a slightly modified version of Gal-Chen's (1978) procedure (Shapiro and Lazarus 1993). Results are verified by measuring the fit of the retrieved fields to the constraint equations and comparing the retrieved fields for single- versus dual-Doppler wind analyses. In addition, an analysis of the terms in the vertical momentum equation is performed to assess their relative importance in the temperature retrieval.

For the numerical prediction experiments, I use the Advanced Regional Prediction System (ARPS) model (Xue et al. 1995). In order to supply complete initial conditions to the model, three additional analysis steps are added to the retrieval. First, the retrieved thunderstorm wind fields are blended with the environmental wind field (assumed available from a proximity sounding). Based on a quantitative analysis of several blending techniques (Ellis 1997), a fairly simple procedure is adopted for use in this study (described in Chapter 2). Second, using a procedure described by Shapiro et al. (1995b), the blended wind fields are adjusted to satisfy mass-conservation before the application of the thermodynamic retrieval. [a new mass-conservation adjustment procedure is derived in Appendix A.] Third, a very simple method for specifying moisture fields is used (described in Chapter 2). As noted in Section 1.3, focused research on microphysical retrieval techniques is being pursued by other investigators and is beyond the scope of this study.

A number of specific questions are addressed in this study:

1) Are reflectivity conservation and velocity stationarity suitable closure assumptions for a single-Doppler wind retrieval applied to a deep-convective storm?
2) How does the use of a moving reference frame affect the wind retrieval?
3) Does the wind retrieval provide sufficient cross-beam information to obtain useful thermodynamic information from the horizontal momentum equations?
4) Which vertical momentum equation terms are most important in the temperature retrieval?
5) How well do the retrieved fields match analytic predictions from simple linear theory?
6) What is the predictability limit for this storm using this analysis procedure?
7) How sensitive is this storm prediction to the various input fields?

In addition to answering the questions listed above, a practical goal of this study is the development of a new radar data analysis/retrieval procedure. Areas for possible application include nowcasting guidance, generation of background fields for more sophisticated analysis procedures (full model adjoint or analysis/prediction cycles), and initialization of numerical models. The modularity and computational efficiency of the algorithm should enhance its potential for operational implementation.

The organization of the thesis is as follows. In chapter 2, the components of the analysis procedure are described in detail. In chapter 3, a summary of the radar dataset and its processing is provided. The wind retrieval results are presented in Chapter 4 and the thermodynamic retrieval results are presented in Chapter 5. In chapter 6, results from the numerical predictions for both single-Doppler and dual-Doppler cases are discussed. Finally, conclusions from the study and recommendations for future work are presented in Chapter 7.

CHAPTER 2

METHODOLOGY

The proposed sequential single-Doppler retrieval procedure includes two primary components. The first is a single-Doppler velocity retrieval (SDVR) designed to deduce the unobserved cross-beam wind (azimuthal and polar) components from a time-series of single-Doppler observations (reflectivity and radial velocity information). The second is a thermodynamic retrieval which obtains the temperature and pressure fields from a time-series of three-dimensional wind fields. If the retrieval procedure is used to initialize a numerical prediction model (utilizing a proximity sounding for background fields), three other steps are included. These are a simple algorithm for blending the radar-retrieved winds with mean horizontal winds from the sounding, a variational adjustment of the blended wind field to satisfy mass-conservation and the observed radial velocity on the model grid, and a moisture specification step.

The procedure has some similarities to the dual-Doppler technique described by Lin et al. (1993); however, there are two major differences. First, this procedure utilizes a wind retrieval to obtain the three-dimensional velocities within the storm from a time-series of single-Doppler observations. Application of Lin's technique, which relies on a dual-Doppler analysis to supply the 3-D wind fields, is limited to situations where the storm is simultaneously scanned by two Doppler radars. Second, in contrast to Lin's study which neglected the velocity time-tendencies in the thermodynamic retrieval, in this study they are calculated from a time series of retrieved winds and are used in the thermodynamic retrieval.

A flow chart illustrating the entire procedure is shown in Figure 2.1. Note that the SDVR chosen for this study requires three successive single-Doppler volume scans so that centered time differences can be evaluated at the middle time level. Three successive applications of the wind retrieval (utilizing a total of five successive volume scans) yields the three successive 3-D wind estimates required to calculate centered time-derivatives for the thermodynamic retrieval. In this chapter, I describe each component of the analysis system in detail. With regard to the single-Doppler wind retrieval, I also describe the modifications needed to apply it in a moving reference frame.

2.1 Single-Doppler velocity retrieval

2.1.1 Basic formulation

The two-scalar wind retrieval described by Shapiro et al. (1995a) is selected for this study for a number of reasons. First, it is one of the few SDVR algorithms that directly obtains both unobserved wind components (azimuthal and polar) and is applicable throughout the depth of the storm. Many SDVR algorithms are limited to application at low elevation angles and require a separate vertical integration of the horizontal divergence to obtain vertical velocity (Zhang and Gal-Chen 1996, Xu et al. 1994a,b). Inclusion of both of these features directly in the retrieval makes the two-scalar technique ideally suited for application to a deep-convective storm with an intense updraft.

Second, the algorithm is easily modified to account for hydrometeor fallout and for application in a moving reference frame. Both of these factors are likely to be important for deep-convective retrievals. Third, the scheme is very computationally efficient, requiring only a few minutes of CPU time on a workstation for a typical 3-D grid.

The two-scalar velocity retrieval is applied in the "radar coordinate system" shown in Fig. 2.2, a spherical polar coordinate system (r, ϕ, θ) originating at the Doppler radar.

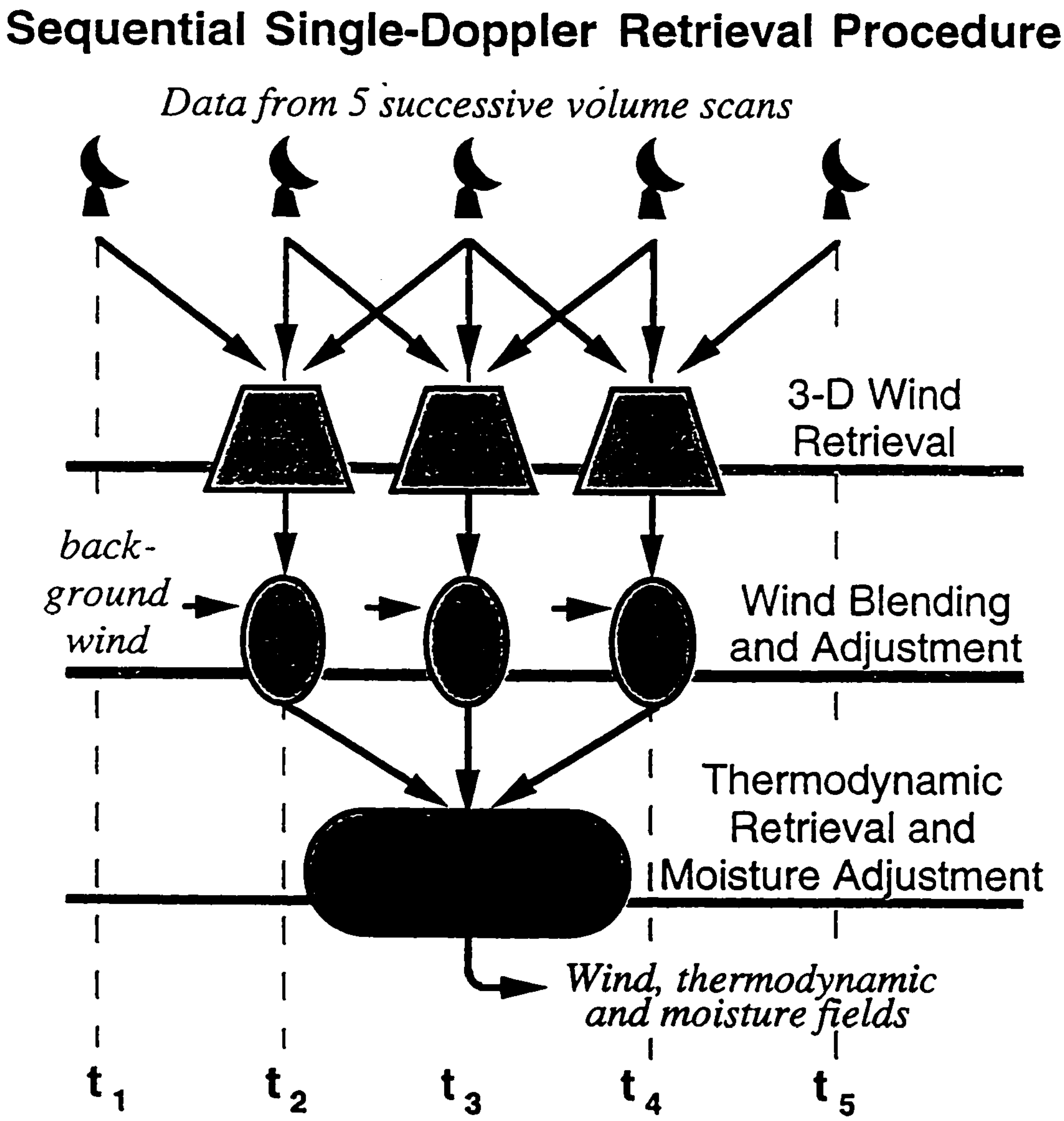

Figure 2.1 Flowchart illustrating the sequential single-Doppler retrieval procedure. Five successive single-Doppler volume scans are used to create 3-D windfields at three successive times. The retrieved wind fields are then blended with a background field and variationally adjusted. Finally, thermodynamic fields for the middle time-level are retrieved from the three sets of adjusted winds and the moisture fields are specified.

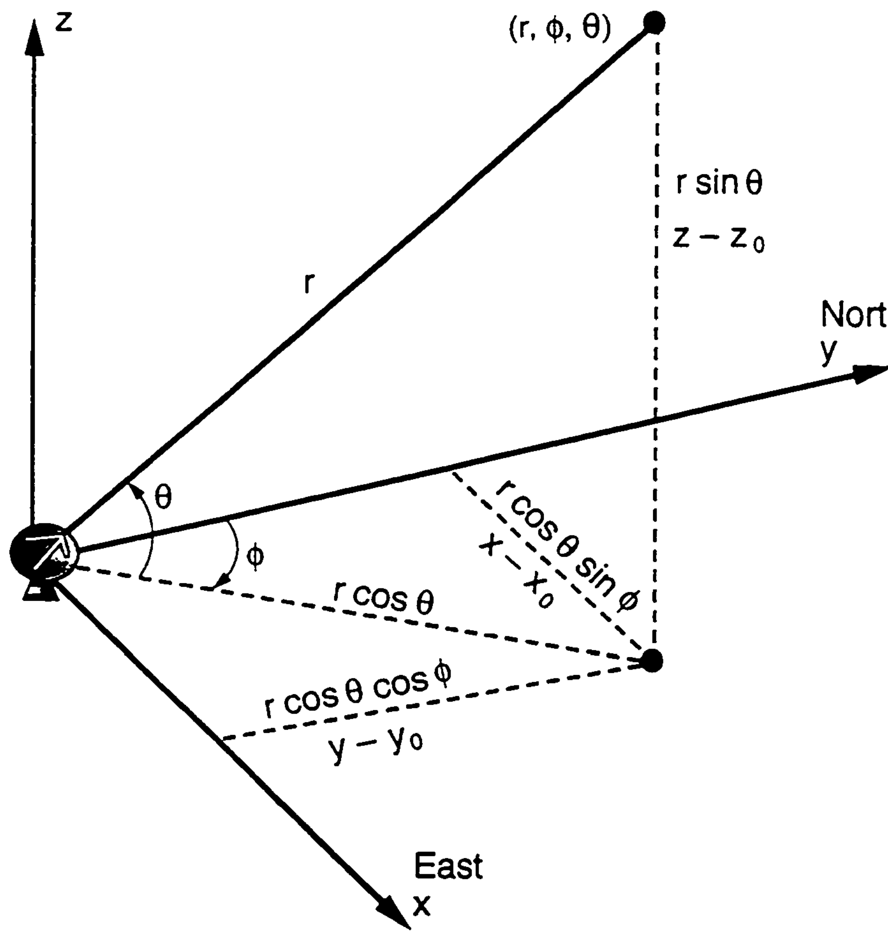

Figure 2.2 Spherical polar radar coordinate system (r, ϕ, θ) used in the single-Doppler retrieval procedure. The origin of the coordinate system is the input radar. The northerly azimuth angle is given by $\phi = 0$ (with ϕ increasing in a clockwise direction) and the local vertical through the origin is specified as $\theta = \pi/2$.

The local vertical through the radar is specified as $\theta = \pi/2$ and the northerly azimuth angle is specified as $\phi = 0$ (with ϕ increasing in a clockwise direction). The radial, azimuthal, and polar velocities are denoted v_r, v_ϕ, and v_θ, respectively.

The retrieval (described in detail by Shapiro et al. 1995a) assumes that the four-dimensional distribution of two conserved scalars and the radial velocity is known. Conservation equations for the two scalars (denoted A and B) are:

$$\frac{\partial A}{\partial t} + v_r \frac{\partial A}{\partial r} + \frac{v_\phi}{r \cos\theta} \frac{\partial A}{\partial \phi} + \frac{v_\theta}{r} \frac{\partial A}{\partial \theta} = S_A \quad , \tag{2.1}$$

$$\frac{\partial B}{\partial t} + v_r \frac{\partial B}{\partial r} + \frac{v_\phi}{r \cos\theta} \frac{\partial B}{\partial \phi} + \frac{v_\theta}{r} \frac{\partial B}{\partial \theta} = S_B \quad , \tag{2.2}$$

where S_A and S_B are known forcing terms (that might include subgrid-scale mixing or hydrometeor terminal velocity parameterizations). As will be described shortly, A is defined to be the log of the radar reflectivity and a temporal constraint is applied to the velocity field, enabling a second scalar (B) to be derived from the time tendency of A.

The equation of mass conservation, also expressed in radar coordinates is:

$$\frac{1}{r^2}\frac{\partial\left(r^2 v_r\right)}{\partial r} + \frac{1}{r\cos\theta}\frac{\partial v_\phi}{\partial \phi} + \frac{1}{r\cos\theta}\frac{\partial\left(\cos\theta\, v_\theta\right)}{\partial \theta} = 0 \quad . \tag{2.3}$$

Equation (2.3) can be exactly satisfied by expressing the unobserved spherical velocity components (v_ϕ and v_θ) in terms of a pseudo-streamfunction Q. The expressions for the azimuthal and polar velocities are:

$$v_\phi = -\frac{\partial Q}{\partial \theta} , \tag{2.4}$$

$$v_\theta = -\frac{1}{\cos\theta}\frac{\partial Q}{\partial \phi} - \frac{1}{r\cos\theta}\frac{\partial}{\partial r}\left(r^2\int_{\theta_0}^{\theta}\cos\Theta\, v_r\, d\Theta\right) , \tag{2.5}$$

where Θ is a dummy integration variable and θ_0 is an arbitrary function of r and ϕ. For this study θ_0 is taken as the lowest radar data level and a hole-filling procedure is used to fill in any gaps along the integration arc. The hole-filling procedure consists of solving a series of 2-D Laplace equations on ϕ-θ surfaces with zero-gradient lateral boundary conditions. It is similar to a 2-D Cartesian procedure described in section 2.3. Substitution of (2.4) and (2.5) into (2.1) and into (2.2) leads to a coupled pair of inhomogeneous linear partial differential equations for Q:

$$\frac{\partial Q}{\partial \theta}\frac{\partial A}{\partial \phi} - \frac{\partial Q}{\partial \phi}\frac{\partial A}{\partial \theta} + K_A = 0 , \tag{2.6}$$

$$\frac{\partial Q}{\partial \theta}\frac{\partial B}{\partial \phi} - \frac{\partial Q}{\partial \phi}\frac{\partial B}{\partial \theta} + K_B = 0 , \tag{2.7}$$

where

$$K_A = r\cos\theta\left(\frac{\partial A}{\partial t} + v_r\frac{\partial A}{\partial r} - S_A\right) - \frac{1}{r}\frac{\partial A}{\partial \theta}\frac{\partial}{\partial r}\left(r^2\int_{\theta_0}^{\theta}\cos\Theta\, v_r\, d\Theta\right) ,$$

$$K_B = r\cos\theta\left(\frac{\partial B}{\partial t} + v_r\frac{\partial B}{\partial r} - S_B\right) - \frac{1}{r}\frac{\partial B}{\partial \theta}\frac{\partial}{\partial r}\left(r^2\int_{\theta_0}^{\theta}\cos\Theta\, v_r\, d\Theta\right) .$$

Equations (2.6) and (2.7) can be solved for $\partial Q/\partial\phi$ and $\partial Q/\partial\theta$, yielding:

$$\frac{\partial Q}{\partial \phi} = \alpha \ , \quad \frac{\partial Q}{\partial \theta} = \beta \ . \tag{2.8}$$

where:

$$\alpha = \frac{K_B \frac{\partial A}{\partial \phi} - K_A \frac{\partial B}{\partial \phi}}{\frac{\partial A}{\partial \phi}\frac{\partial B}{\partial \theta} - \frac{\partial B}{\partial \phi}\frac{\partial A}{\partial \theta}} \ , \tag{2.9}$$

$$\beta = \frac{K_B \frac{\partial A}{\partial \theta} - K_A \frac{\partial B}{\partial \theta}}{\frac{\partial A}{\partial \phi}\frac{\partial B}{\partial \theta} - \frac{\partial B}{\partial \phi}\frac{\partial A}{\partial \theta}} \ . \tag{2.10}$$

An exact solution to (2.8) is not practical, because the presence of errors in the data would likely lead to a violation of the compatibility condition $\partial\alpha/\partial\theta = \partial\beta/\partial\phi$. As an alternative, a variational formulation of the problem can be used to obtain a solution that minimizes (in a least squares sense) departures from the exact satisfaction of (2.8). This is accomplished by defining a "cost function" which represents the errors associated with (2.8):

$$J = \iint \left[\left(\frac{\partial Q}{\partial \phi} - \alpha \right)^2 + \left(\frac{\partial Q}{\partial \theta} - \beta \right)^2 \right] d\phi \, d\theta \ , \tag{2.11}$$

where the integral is evaluated over a series of surfaces perpendicular to the radar beam. A least squares solution is obtained by setting the variation of J to zero. Integrating the resultant equation by parts yields:

$$\int \left(\frac{\partial Q}{\partial \phi} - \alpha\right)\Bigg|_{\phi_{beg}}^{\phi_{end}} \delta Q \, d\theta + \int \left(\frac{\partial Q}{\partial \theta} - \beta\right)\Bigg|_{\theta_{bot}}^{\theta_{top}} \delta Q \, d\phi$$

$$- \iint \left[\frac{\partial^2 Q}{\partial \phi^2} + \frac{\partial^2 Q}{\partial \theta^2} - \frac{\partial \alpha}{\partial \phi} - \frac{\partial \beta}{\partial \theta}\right] \delta Q \, d\phi \, d\theta = 0 \quad . \tag{2.12}$$

Since δQ is arbitrary, the integrand in the last term must vanish, yielding an elliptic equation for Q:

$$\frac{\partial^2 Q}{\partial \phi^2} + \frac{\partial^2 Q}{\partial \theta^2} = \frac{\partial \alpha}{\partial \phi} + \frac{\partial \beta}{\partial \theta} \quad . \tag{2.13}$$

If the denominator in the expressions for α and β vanishes, the solution will have a singularity. This problem is avoided by rejecting the computed α and β in regions where they are too large. The resultant data gaps are filled by solving a series of 2-D Laplace equations on ϕ-θ surfaces with zero-gradient lateral boundary conditions (similar to the procedure for hole-filling the radial velocity). Details of this procedure are discussed in Section 4.2.2.

The first two terms in (2.12) provide boundary conditions on the ϕ and θ faces. Because Q is not generally known on any of the boundaries, Neumann boundary conditions involving known quantities α and β are used:

$$\frac{\partial Q}{\partial \phi} = \alpha \quad \text{on } \phi \text{ faces} \; , \qquad \frac{\partial Q}{\partial \theta} = \beta \quad \text{on } \theta \text{ faces} \quad . \tag{2.14}$$

The two scalar fields are specified in the following manner. The reflectivity field supplied by the radar is used for the first scalar field:

$$A = 10 \log_{10} Z \quad (\mathrm{dBZ}) \ , \tag{2.15}$$

where Z is the reflectivity factor with units of (mm^6/m^3). The forcing term S_A accounts for the deviation of the hydrometeor motion from the air motion and is given as:

$$S_A = w_t(A) \frac{\partial A}{\partial z} \ , \tag{2.16}$$

where:

$$w_t = 3.088 \, Z^{0.0957} \ . \tag{2.17}$$

Eq. (2.17) is an approximate average of the empirical power law formulas of Rogers (1964) and Joss and Waldvogel (1970).

Application of a temporal constraint to the velocity field enables a second independent conservation equation to be derived. Shapiro et al. (1995a) discuss two possible velocity constraints: velocity stationarity and Taylor's frozen turbulence (velocity stationarity in a moving reference frame; Taylor 1938). Because of the large mean wind component for the supercell case studied herein, it is anticipated that Taylor's frozen turbulence hypothesis is the more appropriate assumption. It states that the local time tendency of the velocity field is assumed to be caused exclusively by some pattern translation velocity advecting a time-invariant pattern of turbulent eddies. This can be stated mathematically as:

$$\frac{\partial \vec{v}}{\partial t} + U \frac{\partial \vec{v}}{\partial x} + V \frac{\partial \vec{v}}{\partial y} = 0 \ , \tag{2.18}$$

where U and V are constant *translational components of the velocity pattern* and $\vec{v}$ is the *local velocity of the air parcels*. Taylor's hypothesis is valid for flows where the turbulent velocity fluctuations represent small perturbations superimposed upon a large translational velocity, and breaks down in regions of large mean shear. The velocity stationarity assumption is a special case of (2.18) in which the velocity pattern translation components (U and V) are zero.

To use Taylor's frozen turbulence hypothesis, a linear operator is defined:

$$L = \frac{\partial}{\partial t} + U\frac{\partial}{\partial x} + V\frac{\partial}{\partial y} \quad . \tag{2.19}$$

Application of (2.19) to (2.1) making use of (2.18) leads to the following equation:

$$\frac{\partial}{\partial t}\left[L(A)\right] + \vec{V}\cdot\nabla\left[L(A)\right] = L(S_A) \quad , \tag{2.20}$$

which is a conservation relation for a second scalar defined as:

$$B = L(A) = \frac{\partial A}{\partial t} + U\frac{\partial A}{\partial x} + V\frac{\partial A}{\partial y} \quad . \tag{2.21}$$

The forcing term for the second scalar equation is obtained by applying (2.19) to S_A :

$$S_B = L(S_A) = \frac{\partial S_A}{\partial t} + U\frac{\partial S_A}{\partial x} + V\frac{\partial S_A}{\partial y} \quad . \tag{2.22}$$

Using (2.16) for S_A, we get:

$$S_B = w_t \frac{\partial B}{\partial z} + \left(\frac{\partial w_t}{\partial t} + U \frac{\partial w_t}{\partial x} + V \frac{\partial w_t}{\partial y} \right) \frac{\partial A}{\partial z} \quad . \tag{2.23}$$

In order to utilize the frozen turbulence approximation, suitable system translation components (U, V) must be specified. This is accomplished using the method of Shapiro et al. (1995a). They obtained a variational solution for U and V from the radial velocity constraint equation described by Gal-Chen (1982). First, we take the time derivative following the parcel of $r^2 = x^2 + y^2 + z^2$ to obtain:

$$r\, v_r = x\, u + y\, v + w\, z \quad . \tag{2.24}$$

Application of (2.19) to (2.24) making use of (2.18) leads to:

$$L(r\, v_r) = U\, u + V\, v \quad . \tag{2.25}$$

Application of (2.19) to (2.25), again making use of (2.18), yields:

$$L^2(r\, v_r) = 0 \quad . \tag{2.26}$$

Using (2.24), (2.26) can be expanded to get:

$$A + 2UB + 2VC + U^2 D + V^2 E + 2UVF = 0 \quad , \tag{2.27}$$

where:

$$A = \frac{\partial^2}{\partial t^2}(r v_r) \qquad B = \frac{\partial^2}{\partial x \partial t}(r v_r) \qquad C = \frac{\partial^2}{\partial y \partial t}(r v_r)$$

$$D = \frac{\partial^2}{\partial x^2}(rv_r) \qquad E = \frac{\partial^2}{\partial y^2}(rv_r) \qquad F = \frac{\partial^2}{\partial x \partial y}(rv_r) \quad .$$

Because (2.18) is not satisfied exactly by the flow everywhere in the domain (due partly to discretization errors), direct evaluation of (2.27) would lead to spatially varying values of U and V. Constant values of U, V that minimize departures from (2.27) over the entire domain can be obtained from a least squares formulation of the problem.

We define a cost function with U and V as control parameters:

$$J = \iiint \left(A + 2UB + 2VC + U^2D + V^2E + 2UVF\right)^2 r^2\cos\theta \, dr\, d\phi\, d\theta\, dt \quad . \qquad (2.28)$$

Setting $\delta J = 0$ yields a pair of coupled cubic equations for U and V that can be solved using standard numerical techniques. The algebraic equations, along with a discussion of the solution technique, can be found in Shapiro et al. (1995a). Once a solution for U and V is found, B and S_B may be calculated from (2.21) and (2.23).

2.1.2 Use of moving reference frames

Previous studies with Shapiro's algorithm have focused primarily on clear-air and low reflectivity cases (Shapiro et al. 1995a, 1995c). For the present case, which is characterized by a deep-convective storm in an environment with a strong mean wind, the retrieval is applied in a moving reference frame. As described by Gal-Chen (1982), an appropriately chosen reference frame should maximize the accuracy of the evaluation of the local time tendencies. Furthermore, by shifting the radar observations into a reference frame moving with the storm, the amount of data "overlap" between the successive scans can also be maximized, as indicated by Figure 2.3. This is important, because centered time-differences valid at the middle time can only be calculated where radar data from the first and third volume scans overlap. For a rapidly moving storm and a large time interval between radar scans, the region of data overlap can be much smaller than the precipitation volume. Fig. 2.3a shows an extreme case in which there is no data overlap between the first and third volume scans. Shifting the data into a reference frame moving with the storm, as shown in Fig. 2.3b, will overcome this problem, and maximize the region over which the time tendencies can be calculated.

It is easy to show that the scalar conservation equations are equally valid in either a fixed or moving reference frame. For a fixed reference frame we have:

$$\left.\frac{\partial A}{\partial t}\right|_{fix} + \vec{v}_{fix} \cdot \nabla A = S_A \quad . \qquad (2.29)$$

The relationship between the velocities in a fixed reference frame ($\vec{v}_{fix}$) and the velocities in a reference frame moving with a constant horizontal speed ($\vec{v}_{mov}$) is:

$$\vec{v}_{mov} = \vec{v}_{fix} - U\hat{i} - V\hat{j} \quad , \qquad (2.30)$$

where U and V are the constant reference frame translation components in the x and y directions, respectively. Similarly, the relationship between the local scalar time tendencies in the two reference frames is:

$$\left.\frac{\partial A}{\partial t}\right|_{mov} = \left.\frac{\partial A}{\partial t}\right|_{fix} + U\frac{\partial A}{\partial x} + V\frac{\partial A}{\partial y} \quad . \qquad (2.31)$$

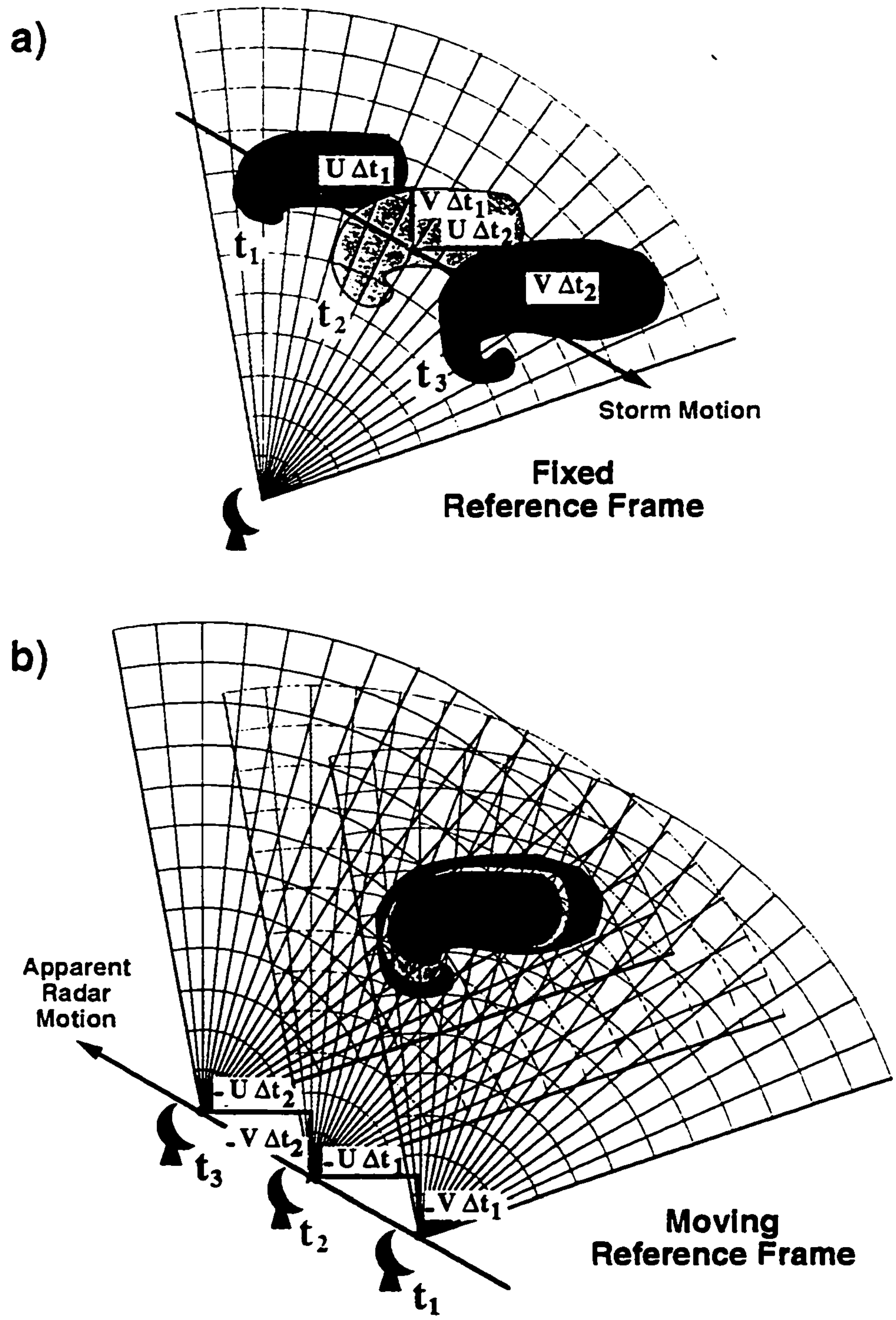

Figure 2.3 Schematic diagram illustrating the three time levels of radar data in a) a fixed reference frame and b) a moving reference frame. The transformation is accomplished by first shifting the time t_1 and t_3 fields by the appropriate x and y distances then interpolating the shifted fields to the time t_2 grid.

Substituting (2.29) and (2.30) into (2.31) yields:

$$\left.\frac{\partial A}{\partial t}\right|_{mov} + \vec{v}_{mov} \cdot \nabla A = S_A \quad , \tag{2.32}$$

The spherical velocity components in a moving reference frame are:

$$v_{r_{mov}} = v_{r_{fix}} - \cos\theta \sin\phi\, U - \cos\theta \cos\phi\, V \quad , \tag{2.33}$$

$$v_{\phi_{mov}} = v_{\phi_{fix}} - \cos\phi\, U + \sin\phi\, V \quad , \tag{2.34}$$

$$v_{\theta_{mov}} = v_{\theta_{fix}} + \sin\theta \sin\phi\, U + \sin\theta \cos\phi\, V \quad . \tag{2.35}$$

By substituting (2.33)-(2.35) into (2.3), one can verify that the mass conservation relation is also equally valid in a fixed or moving reference frame (as must be the case physically under Galilean invariance). The retrieval can therefore be applied in a moving reference frame.

Two least squares methods are available for computing the moving reference frame translation components (U and V) from the single-Doppler radar data. [Note that these components are different than the velocity pattern translation components discussed in Section 2.1.1]. The first technique utilizes a procedure describe by Gal-Chen (1982) for finding a reference frame that minimizes the time-tendencies of a given field. Application of his technique to the reflectivity field produces a reference frame that *moves with the storm*. This "storm propagation" reference frame should maximize the overlap of the radar fields among the different volume scans and provide for the most accurate evaluations of the reflectivity time derivatives. Difficulties would arise in cases where different echoes are moving in significantly different directions within the same domain.

Following Gal-Chen (1982), a cost function is defined as follows:

$$J = \iiint_\sigma \left(\frac{\partial A}{\partial t} + U \frac{\partial A}{\partial x} + V \frac{\partial A}{\partial y} \right)^2 W \, d\sigma \quad . \tag{2.36}$$

where W is a weighting function and σ represents the 3-D spatial domain. Setting $\delta J = 0$ yields a pair of equations for U and V:

$$\begin{aligned} a\,U + b\,V &= c \\ b\,U + d\,V &= e \quad . \end{aligned} \tag{2.37}$$

where:

$$a = \iiint_\sigma \left(\frac{\partial A}{\partial x} \right)^2 d\sigma \quad b = \iiint_\sigma \frac{\partial A}{\partial x} \frac{\partial A}{\partial y} d\sigma \quad c = \iiint_\sigma \frac{\partial A}{\partial t} \frac{\partial A}{\partial x} d\sigma$$

$$d = \iiint_\sigma \left(\frac{\partial A}{\partial y} \right)^2 d\sigma \qquad e = \iiint_\sigma \frac{\partial A}{\partial t} \frac{\partial A}{\partial y} d\sigma \; .$$

The second procedure yields a reference frame that moves with the *mean wind.* The advantage of this reference frame is that it effectively reduces the retrieval problem to one of obtaining the unobserved *perturbation velocity*. This would likely be very beneficial in situations where the mean wind represents a substantial portion of the total velocity field. However, difficulties could arise in cases where two regions with opposing flow yield a near zero mean flow (such as across a front).

To use this procedure, we define a cost function as follows:

$$J = \iiint_\sigma \left(v_r - U\frac{x}{r} - V\frac{y}{r} \right)^2 W\, d\sigma \quad . \tag{2.38}$$

where W is a weighting function and σ represents the 3-D spatial domain. Setting $\delta J = 0$ yields a pair of equations for U and V:

$$\begin{aligned} a\,U + b\,V &= c \\ b\,U + d\,V &= e \quad . \end{aligned} \tag{2.39}$$

where:

$$a = \iiint_\sigma \left(\frac{x}{r}\right)^2 d\sigma \qquad b = \iiint_\sigma \frac{xy}{r^2}\, d\sigma \qquad c = \iiint_\sigma \frac{x}{r} v_r\, d\sigma$$

$$d = \iiint_\sigma \left(\frac{y}{r}\right)^2 d\sigma \qquad e = \iiint_\sigma \frac{y}{r} v_r\, d\sigma \quad .$$

Once translation components U and V have been calculated for a given moving reference frame, the transformation is completed as indicated in Figure 2.3. First, the radial velocity for each of the three time levels is converted to its corresponding moving reference frame value using (2.33). Then, data from the first and third time levels are shifted to the middle time level using the following relations:

$$x_{mov} = x_{fix} \pm U\,\Delta\tau_{1,2}$$

$$y_{mov} = y_{fix} \pm V\,\Delta\tau_{1,2} \quad , \tag{2.40}$$

where $\Delta\tau_1$ is the time interval between the first and second volume scans (use the "+") and $\Delta\tau_2$ is the interval between the second and third volume scans (use the " - "). Finally, the shifted data from the first and third time-levels are tri-linearly interpolated to the spherical gridpoints from the middle time-level.

2.2 Velocity blending and adjustment

The SDVR yields the three spherical wind components on a spherical grid. Conversion of these components to Cartesian components and interpolation to the ARPS model (Cartesian) grid are the next steps. Unfortunately, the resultant gridded dataset still suffers from a couple of limitations. First, because the radar data coverage is incomplete, the retrieved wind typically will not completely cover the entire model domain volume (and may contain internal data "holes"). Second, despite the use of mass conservation as a wind retrieval constraint, the retrieved wind generally will not satisfy mass conservation on the model grid (due to discretization errors associated with the interpolation). If the retrieved wind fields are to be used to initialize a numerical model, it is desirable to "blend" them with a suitable background wind field and adjust them to satisfy mass conservation *on the model grid.* To accomplish these tasks, a simple blending and wind adjustment procedure has been incorporated into the retrieval system.

For operational applications, the retrieved winds would likely be blended with a background field consisting of a full 3-D analysis using data from all available sources (including a previous model forecast). For this study, however, the background field is limited to a vertical profile of mean horizontal wind components from a single proximity sounding. Therefore, a simpler blending procedure is adopted with the goal of providing a smooth transition from the radar-retrieved velocities to the mean horizontal winds and across any internal data holes. This can be accomplished by solving a Laplace equation to "fill" the data void regions following Lin et al. (1993). Dirichlet boundary conditions are typically supplied by the radar wind along the storm edge and from the proximity sounding along the model's lateral boundary. It is important to note that these techniques do not enforce mass conservation or any other *physical* constraints.

Based on Ellis' (1997) quantitative comparison of several elliptic hole-filling procedures, I choose to solve a series of 2-D Laplace equations for u and v and set the vertical velocity to zero outside the storm volume. For levels above or below the storm volume, the horizontal winds are set to the base-state sounding values. The hole-filling procedure can be posed as a variational problem in which horizontal gradients of the scalar field are minimized within the hole-filling region.

To do so, we define a cost function:

$$J = \iint \left(\nabla_h \xi\right) \cdot \left(\nabla_h \xi\right) dx\, dy \quad . \tag{2.41}$$

where ξ is any scalar field and $\nabla_h \xi = \hat{i} \frac{\partial \xi}{\partial x} + \hat{j} \frac{\partial \xi}{\partial y}$. Setting $\delta J = 0$ and noting that $\nabla_h \cdot \left(\delta\xi \, \nabla_h \xi\right) = \delta\xi \, \nabla_h^2 \xi + \nabla_h(\delta\xi) \cdot \nabla_h \xi$ leads to:

$$\delta J = \iint \left[\nabla_h \cdot \left(\delta\xi \, \nabla_h \xi\right) - \delta\xi \, \nabla_h^2 \xi\right] dx\, dy = 0 \quad . \tag{2.42}$$

Application of Green's theorem to the first term in the (2.42) yields:

$$\delta J = \int_c \left(\vec{n} \cdot \nabla_h \xi\right) \delta\xi \, ds - \iint \left(\nabla_h^2 \xi\right) \delta\xi \, dx\, dy = 0 \quad . \tag{2.43}$$

Since $\delta\xi$ is arbitrary, the second integrand must be exactly zero, yielding a 2-D Laplace equation for a scalar variable ξ.

$$\nabla_h^2 \xi = 0 \ . \tag{2.44}$$

The first term in (2.43) provides boundary conditions, with the Dirichlet condition ($\delta\xi$ = 0, i.e. ξ is specified) being the desired choice for this problem. Thus, the scalar velocity components (u and v) are specified on the interior boundaries from the retrieved data and on the exterior boundaries from the sounding data.

As noted before, the blended (hole-filled) wind field does not generally satisfy mass conservation. To enforce mass conservation over the entire model domain, a variational wind adjustment procedure described by Shapiro et al. (1995b) is applied. Patterned after Liou's (1989) adjustment, this procedure produces a wind field that minimizes departures from the input wind field while simultaneously satisfying anelastic mass conservation,

$$\frac{\partial \bar{\rho} u^a}{\partial x} + \frac{\partial \bar{\rho} v^a}{\partial y} + \frac{\partial \bar{\rho} w^a}{\partial z} = 0 \ , \tag{2.45}$$

and matching the observed radial wind component,

$$u^a x + v^a y + w^a z - v_r^o r = 0 \ , \tag{2.46}$$

where the superscripts 'a' and 'o' indicate the adjusted and observed velocities, respectively. A cost function composed of deviations of the adjusted velocities from the background and the two strong constraint terms is defined as follows:

$$J = \iiint_\sigma \left(\bar{\rho} u^a - \bar{\rho} u^m\right)^2 + \left(\bar{\rho} v^a - \bar{\rho} v^m\right)^2 + \left(\bar{\rho} w^a - \bar{\rho} w^m\right)^2 \ .$$

$$+ \lambda_1 \bar{\rho} \left(x\, u^a + y\, v^a + z\, w^a - r\, v_r^o\right) + \lambda_2 \left(\frac{\partial \bar{\rho} u^a}{\partial x} + \frac{\partial \bar{\rho} v^a}{\partial y} + \frac{\partial \bar{\rho} w^a}{\partial z}\right) d\sigma \ . \tag{2.47}$$

Taking the variation of (2.47) with respect to u^a and setting it equal to zero yields:

$$\iiint_\sigma \left[2\left(U^a - U^m\right)\delta U^a + \lambda_1 x \delta U^a + \lambda_2 \frac{\partial \delta U^a}{\partial x} \right] d\sigma = 0 \ , \tag{2.48}$$

where $U = \bar{\rho}\, u$. Integrating the last term by parts, (2.48) can be expressed as:

$$\iiint \left[2\left(U^a - U^m\right) + \lambda_1 x - \frac{\partial \lambda_2}{\partial x} \right] \delta U^a \, d\sigma + \iint \left(\lambda_2\, \delta U^a\right) dy\, dz \Big|_{x_W}^{x_E} = 0 \ , \tag{2.49}$$

where x_W and x_E indicate the west and east faces of the model domain. Since δU^a is arbitrary, the integrand in the first term must vanish everywhere, yielding the Euler-Lagrange equation:

$$2\left(U^a - U^m\right) + \lambda_1 x - \frac{\partial \lambda_2}{\partial x} = 0 \ . \tag{2.50}$$

The second term in (2.49) determines the boundary condition on the east and west faces. The two possible choices that make that term vanish are $\delta U^a = 0$ or $\lambda_2 = 0$. I choose the Dirichlet condition $\lambda_2 = 0$.

Taking the variation of (2.47) with respect to V^a and W^a, similar Euler-Lagrange equations for V^a and W^a can be derived:

$$2\left(V^a - V^m\right) + \lambda_1 y - \frac{\partial \lambda_2}{\partial y} = 0 \ , \tag{2.51}$$

$$2\left(W^a - W^m\right) + \lambda_1 z - \frac{\partial \lambda_2}{\partial z} = 0 \ . \tag{2.52}$$

For the V^a equation (2.51), the Dirichlet condition $\lambda_2 = 0$ is applied on the north and south faces of the model domain. For the W^a equation (2.52), however, the Neumann condition $\delta W^a = 0$ is chosen so that the model's impermeability condition at the bottom and top of the domain will not be violated. A more specific form of this boundary condition will be derived shortly.

Note that taking the variation of (2.47) with respect to λ_1 and λ_2 yields the original constraint equations (2.45) and (2.46). These, combined with (2.50)-(2.52), compose a coupled system of five equations for five unknowns (U^a, V^a, W^a, λ_1, and λ_2). U^a, V^a, and W^a can be eliminated by taking $x \cdot (2.50) + y \cdot (2.51) + z \cdot (2.52)$ and using (2.46) to yield:

$$\lambda_1 = \frac{2}{r^2}\left[\bar{\rho}\, r\, v_r^m - \bar{\rho}\, r\, v_r^o + \frac{1}{2}\vec{r} \cdot \nabla\lambda_2\right] \quad . \tag{2.53}$$

Similarly, taking $\partial/\partial x\,(2.50) + \partial/\partial y\,(2.51) + \partial/\partial z\,(2.52)$ and using (2.45) gives:

$$\nabla^2\lambda_2 = -\,2\,\nabla \cdot \bar{\rho}\vec{v}^m + \nabla \cdot \vec{r}\lambda_1 \quad . \tag{2.54}$$

Eliminating λ_1 between (2.53) and (2.54) yields an 2-D elliptic equation for λ_2 on spherical surfaces in terms of known quantities:

$$\nabla^2_{\phi,\theta}\lambda_2 = -\,2\,\nabla \cdot \bar{\rho}\vec{v}^m - \frac{2}{r^2}\frac{\partial}{\partial r}\left[r^2\bar{\rho}\left(v_r^o - v_r^m\right)\right] \quad . \tag{2.55}$$

Shapiro et al. (1995b) re-expressed (2.55) in Cartesian coordinates so that it could be solved on the ARPS grid. Because of the slow convergence associated with this formulation, I have instead elected to simultaneously solve (2.53) and (2.54) for λ_1 and λ_2 using an iterative procedure.

The top and bottom impermeability boundary condition ($\delta W^a = 0$) can now be expressed more explicitly using (2.53) and (2.54). Setting $W^a = W^m$, where the superscript 'm' indicates the model or background value, yields:

$$\frac{\partial \lambda_2}{\partial z} = \lambda_1 z = \frac{z}{x^2 + y^2}\left[2r\bar{\rho}\left(v_r^m - v_r^o\right) + \left(x\frac{\partial \lambda_2}{\partial x} + y\frac{\partial \lambda_2}{\partial y}\right)\right] . \qquad (2.56)$$

One deficiency of this procedure is that the adjusted radial velocity must exactly match the input radial velocity everywhere in the ARPS model domain. In areas where there are no radial velocity observations, v_r computed from the background or blended data is used as a strong constraint. An alternative variational wind adjustment procedure that uses the observed radial velocity as a weak constraint is derived in Appendix A. This alternative formulation allows the weight factor to be set to zero outside the radar-observed radial velocity region.

2.3 Thermodynamic retrieval and moisture specification

Once the retrieved wind field has been blended with the background and variationally adjusted, the resultant fields are used as input for the thermodynamic retrieval. The formulation follows Gal-Chen's (1978) procedure in which the horizontal momentum equations are used as weak constraints to compute the 2-D horizontal pressure field from the known velocity forcing terms. The complete 3-D pressure field is obtained by solving a series of 2-D Poisson equations on horizontal surfaces. The constraining horizontal momentum equations are:

$$\frac{\partial p'}{\partial x} = A = -\frac{\partial \bar{\rho} u}{\partial t} - \bar{\rho}\vec{v} \cdot \nabla u + \bar{\rho} f v + F_x \quad , \tag{2.57}$$

$$\frac{\partial p'}{\partial y} = B = -\frac{\partial \bar{\rho} v}{\partial t} - \bar{\rho}\vec{v} \cdot \nabla v - \bar{\rho} f u + F_y \quad . \tag{2.58}$$

An exact solution for the perturbation pressure is not practical, because the presence of errors in the data would likely lead to a violation of the compatibility condition $\partial A/\partial y = \partial A/\partial y$. As an alternative, a variational formulation of the problem can be used to obtain a solution that minimizes departures from the constraints in a least squares sense. Thus, a cost function is defined as:

$$J = \iint \left[\left(\frac{\partial p'}{\partial x} - A \right)^2 + \left(\frac{\partial p'}{\partial y} - B \right)^2 \right] dx\, dy \quad . \tag{2.59}$$

Setting $\delta J = 0$ and integrating by parts leads to:

$$\delta J = \int \left(\frac{\partial p'}{\partial x} - A \right) \Bigg|_{x_w}^{x_e} \delta p'\, dy + \int \left(\frac{\partial p'}{\partial y} - B \right) \Bigg|_{y_s}^{y_n} \delta p'\, dx$$

$$- \iint \left(\frac{\partial^2 p'}{\partial x^2} + \frac{\partial^2 p'}{\partial x^2} - \frac{\partial A}{\partial x} - \frac{\partial B}{\partial x} \right) \delta p'\, dx\, dy = 0 \quad . \tag{2.60}$$

Since $\delta p'$ is arbitrary, the integrand in the last term of (2.60) must vanish, yielding a 2-D Poisson equation for p':

$$\frac{\partial^2 p'}{\partial x^2} + \frac{\partial^2 p'}{\partial x^2} = \frac{\partial A}{\partial x} + \frac{\partial B}{\partial y} \quad . \tag{2.61}$$

Within the radar reflectivity region, the forcing function on the right hand side of (2.61) is calculated from the retrieved 3-D wind fields. Outside the reflectivity region, the forcing function is set to zero and (2.61) reduces to a 2-D Laplace equation for p'[as in the hole-filling equation, (2.44)]. This follows the recommendation of Ellis (1997), who compared the retrievals for various treatments of A and B using an observing system simulation experiment (OSSE) strategy.

The first two terms of (2.60) provide boundary conditions. We can either set $\delta p' = 0$, which leads to Dirichlet conditions (p' is specified on the boundary), or require the integrands to vanish, which lead to Neumann conditions ($\partial p'/\partial x = A$ on x – faces, $\partial p'/\partial y = B$ on y – faces). If Neumann boundary conditions are used, the retrieved perturbation pressure is only determined to within an arbitrary constant at each level (equivalent to an arbitrary function of height for the 3-D domain). Using the vertical momentum equation

$$\frac{\partial p'}{\partial z} = -\frac{\partial \bar{\rho} w}{\partial t} - \bar{\rho}\vec{v} \cdot \nabla w + \bar{\rho} g \left[\frac{\theta'}{\bar{\theta}} - \frac{p'}{\gamma \bar{p}} + .608 q_v' - q_c - q_r \right] + F_z \quad , \tag{2.62}$$

a first order linear differential equation can be derived for the unknown function of height (Shapiro and Lazarus 1993). Unfortunately, knowledge of the perturbation potential temperature and moisture terms is needed to solve this equation for the unknown function. I therefore utilize the background fields to provide values for p' on the model's lateral boundaries. If a full 3-D analysis is available, p' can be calculated from the complete pressure field. If only sounding data are available, $p' = 0$ can be used. In both cases it is desirable that the lateral boundaries be well displaced from the storm region. If the storm extends across any portion of the model's lateral boundary, Neumann conditions should be used for that portion of the boundary.

Once a unique solution for p' is obtained, (2.62) can be solved for θ', provided that the distribution of the moisture variables (q_v, q_c, q_r) is known. In practice, the rainwater mixing ratio (q_r) is computed from the observed radar reflectivity using a semi-empirical relationship (Kessler, 1969):

$$q_r = \frac{.001}{\bar{\rho}}\left[\frac{1}{17300}\exp\left(\frac{\ln 10}{10} Z_r\right)\right]^{4/7} , \tag{2.63}$$

where Z_r is the reflectivity in dBZ and q_r is the rainwater mixing ratio in kg kg^{-1}. Because ice microphysics are not used in the numerical prediction experiments of this study, the radar-observed reflectivity is truncated at 50 dBZ prior to the calculation of rainwater. Water vapor and cloud water effects are neglected in the temperature calculation. Following the recommendation of Ellis (1997), retrieved pressure and temperature are only retained within the radar reflectivity volume.

As a last step in the retrieval procedure, the water vapor is adjusted in the radar observed reflectivity region. Specifically, regions where the rainwater exceeds 0.1 g/kg and the retrieved vertical velocity exceeds 3 m/s are saturated using the retrieved potential temperature. This choice of rainwater and vertical velocity thresholds is designed to avoid saturating weak, possibly spurious updrafts along the periphery of the storm volume.

Calculation of the adjusted water vapor value is accomplished using Teten's formula:

$$q_{v\,sat} = \frac{380}{p}\exp\left[a_w\frac{(T-273.16)}{(T-b_w)}\right] , \tag{2.64}$$

where $a_w = 17.27$, $b_w = 35.86$, p is the pressure in Pa and T is the temperature in K. Because no reliable method for approximating the cloudwater field (q_c) is currently available, no attempt is made to specify it in the initial fields.

CHAPTER 3

THE ARCADIA SUPERCELL STORM

3.1 Meteorological overview

On 17 May 1981, a severe weather outbreak occurred in Oklahoma as described by Brewster (1984) and Dowell and Bluestein (1997, hereafter DB97). At 1200 UTC, the 500 mb map (Fig. 3.1) indicated a large closed circulation centered over Colorado. Associated with this feature, a band of 500 mb winds in excess of 50 knots extended from Nevada southeastward into the Texas Panhandle, then northeastward across central Oklahoma into southwest Missouri. The 1500 UTC surface map (Fig. 3.2a) indicated a low-pressure center (1000 mb) just north of Elkhart, KS. A dry line arced south-southeastward from the surface low through the eastern Texas panhandle, while a warm front extended eastward across northern Oklahoma. East of the dryline and south of the warm front, very humid air was in place with surface dewpoints in excess of 20 C. By 2100 UTC, the dryline had moved east and stretched from near Enid, OK, to just east of Wichita Falls, TX (see Fig. 3.2b). As indicated by the 2116 UTC special sounding obtained at Tuttle, OK (Fig. 3.3a), the warm, moist surface air, combined with 500 mb temperatures of -10 C, resulted in a lifted index of about -8 C. Other features of note on the sounding included a pronounced dry layer between 500 and 700 mb and strong southwesterly winds at mid- and upper-levels. The accompanying environmental hodograph (Fig. 3.3b) shows the existence of strong vertical wind shear in the lowest 5 km of the atmosphere ($\left|\Delta\vec{V}\right|_{0-6\,km} \approx 20\ m/s$).

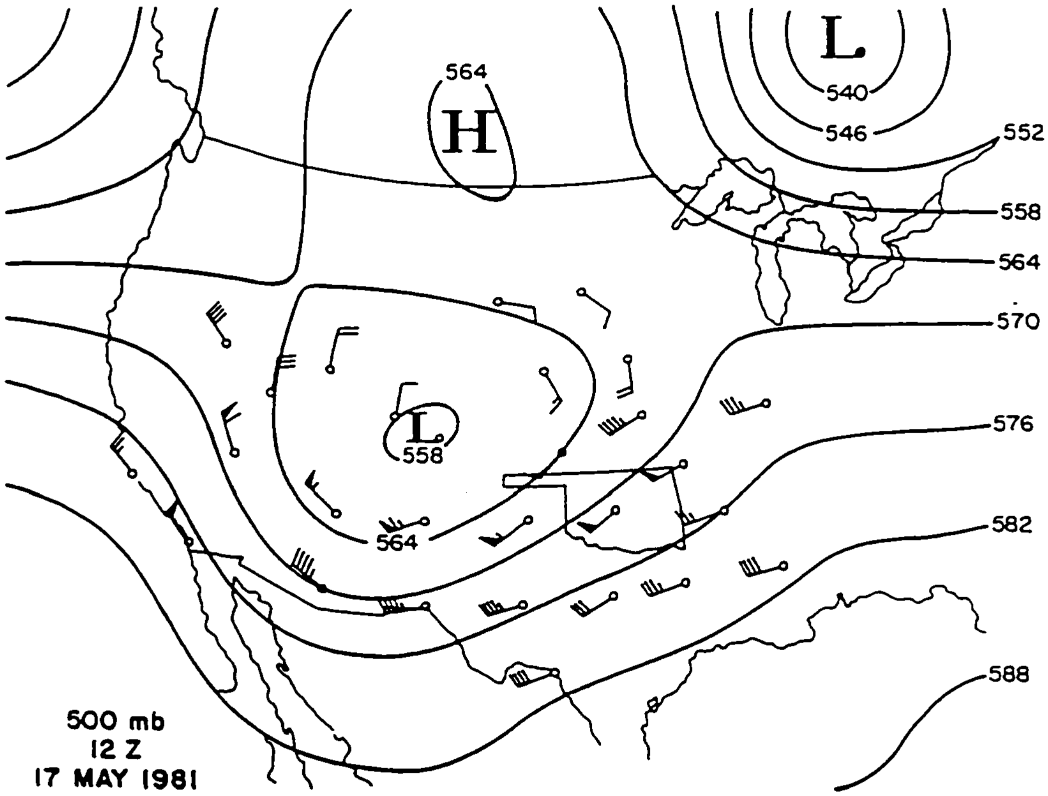

Figure 3.1 500 mb analysis for 1200 UCT, 17 May 1981 (from Brewster 1984). Heights are contoured every 6 dm and each wind barb represents 10 kts.

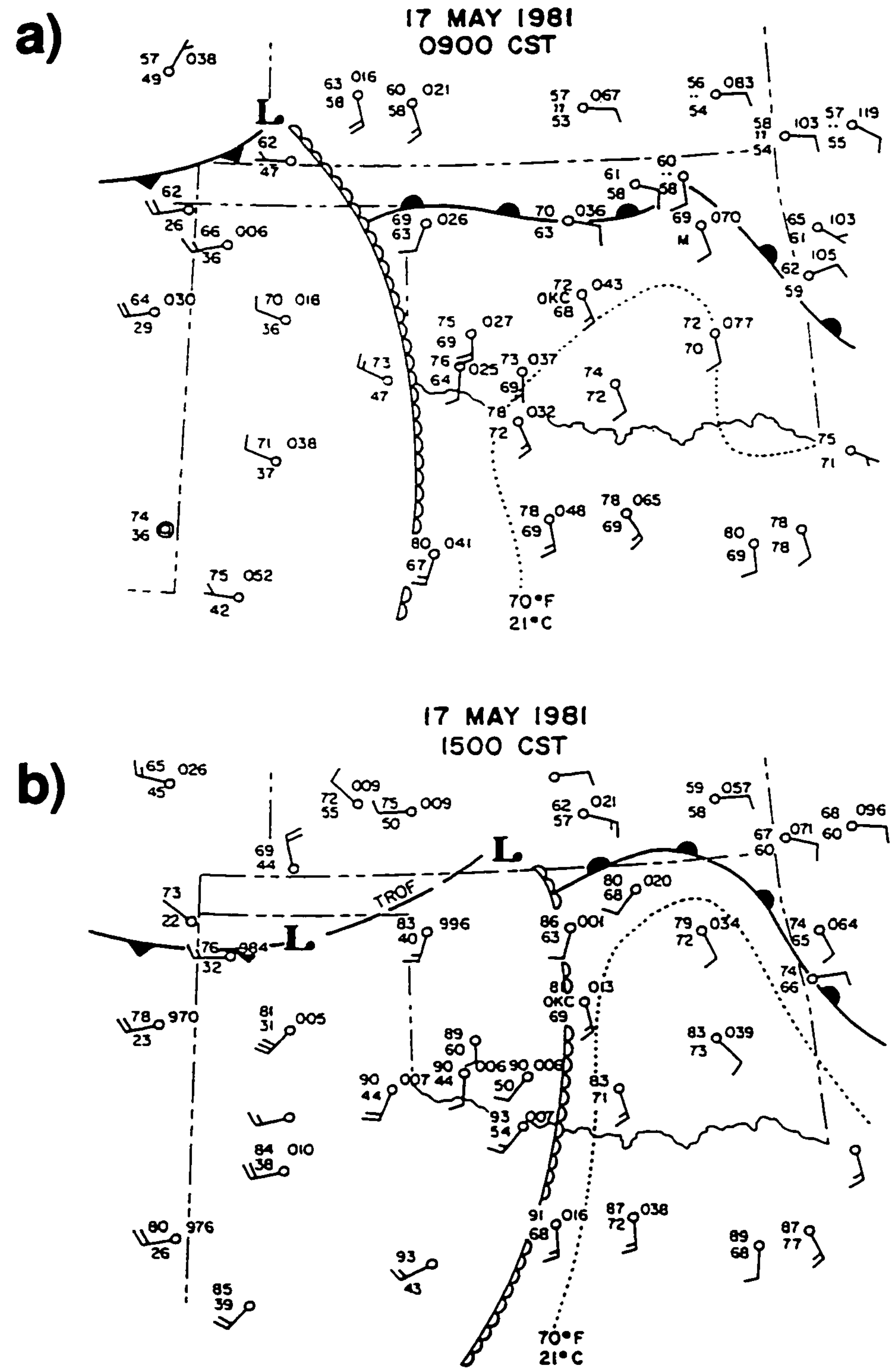

Figure 3.2 Surface analysis for a) 1500 UCT and b) 2100 UTC, 17 May 1981 (from Brewster 1984). Temperatures and dewpoints are in °F. Pressure is in tenths of mb and each wind barb represents 10 kts.

a)

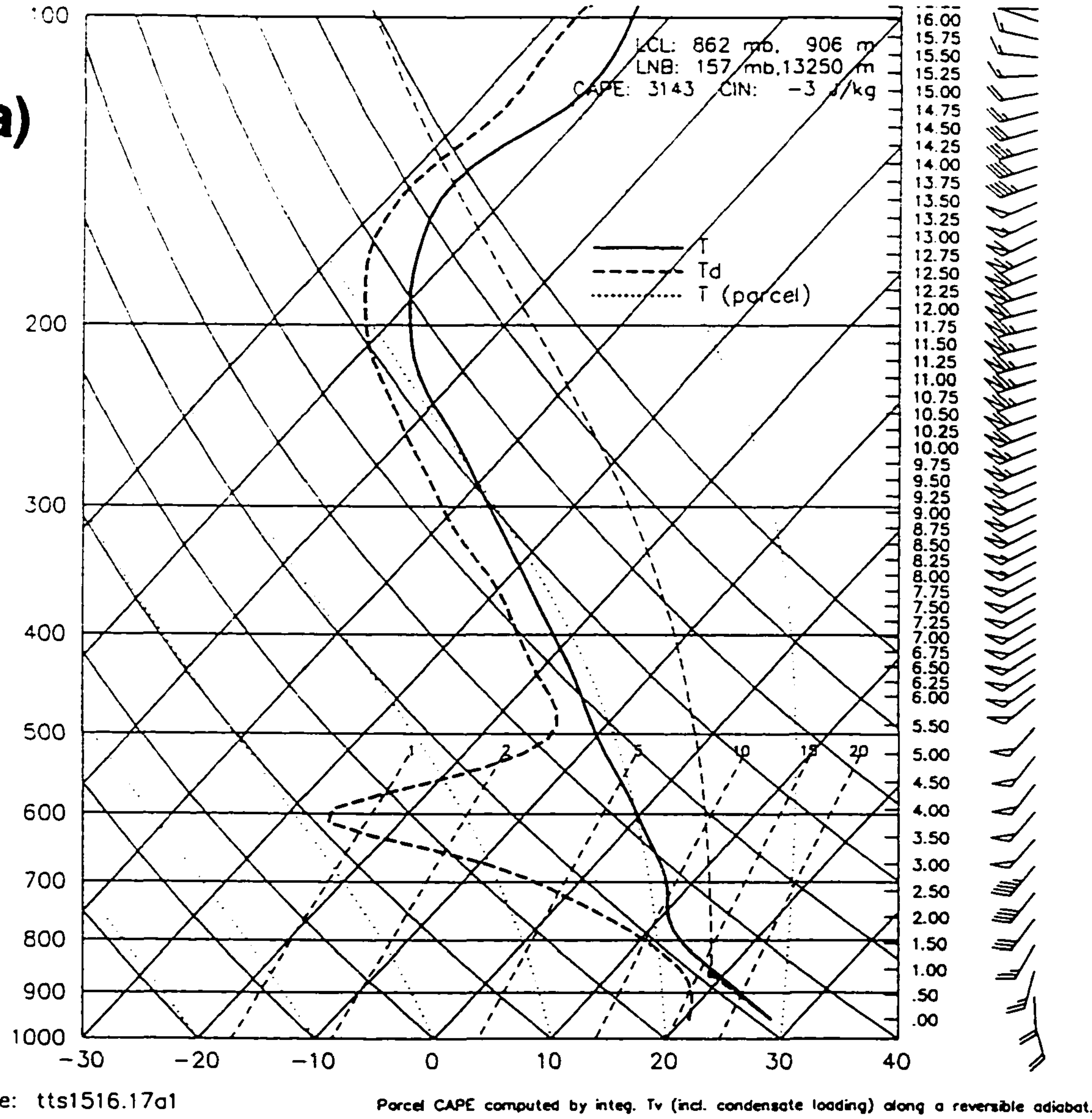

Figure 3.3 2115 UTC, 17 May 1981 sounding from Tuttle, OK. a) Skew-T diagram with temperature and dewpoint (°C) profiles indicated by solid and dashed lines, respectively. Full (half) wind barbs represent 5 m s^{-1} (2.5 m s^{-1}); flags represent 25 m s^{-1}. b) Wind hodograph with each circle denoting 5 m s^{-1} of wind speed. The "X" indicates the 0-6 km. mean wind. Heights are in km AGL.

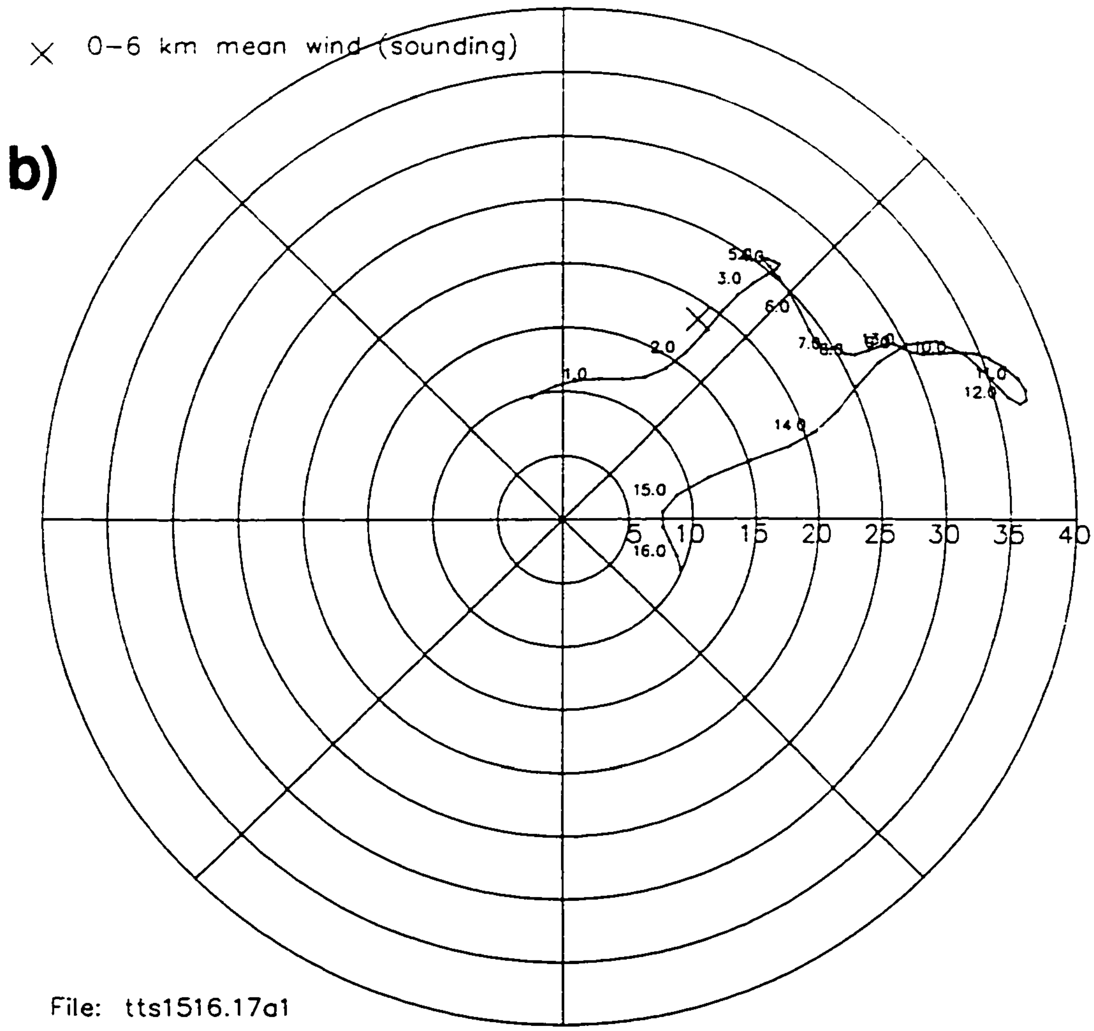

Figure 3.3 (Continued)

Thunderstorms initially developed around 2000 UTC, near the dryline-warm front intersection. Two isolated supercells subsequently developed in Central Oklahoma just before 2100 UTC. The first supercell formed near Pocasset, OK and moved northeast, producing an F2 tornado south of Arcadia, OK, from 2300-2310 UTC. Hereafter it is referred to as the Arcadia supercell and is the storm selected for this study. The second supercell formed near Rush Springs, OK, and also moved northeast, producing an F3 tornado near Tecumseh, OK, and an F4 tornado near Okema, OK (Brewster 1984).

3.2 The Doppler radar dataset

3.2.1 Radar data collection

As the Arcadia supercell moved across the northeast lobe of the National Severe Storms Laboratory dual-Doppler network, twelve coordinated dual-Doppler scans were obtained with the Norman and Cimarron 10-cm Doppler radars over a 1 hour period. Table 3.1 provides a summary of the first eleven dual-Doppler scans that were used in this study (the last set of coordinated scans was not used because of the small between-beam look angle). Fig. 3.4 illustrates the 2239 UTC position of the Arcadia storm relative to the two radars, and the northeast dual-Doppler lobe (delineated by between-beam angles of 45° and 135°). The Cimarron radar collected data with a range increment of 150 m, an azimuthal increment of ~0.6°, and an elevation angle increment that varied from ~0.5° near the ground to ~3.0° at mid and upper levels of the storm. The Norman radar had similar range and elevation angle increments, but an azimuthal increment of ~1.0°. Both radars had a beamwidth of 0.8°.

For this study, single-Doppler data from the Cimarron radar are used as input to the retrieval algorithms and dual-Doppler analyses from DB97 are used to verify the retrieved wind fields. Before use by either the single- or dual-Doppler routines, the radar

Table 3.1 Summary of the dual-Doppler dataset for the 17 May, 1981 Arcadia, OK, supercell thunderstorm. The beam angle and distances to the storm are shown for selected scans. All times are UTC.

Reference Time	Actual Time	Beam Angle	Distance to Radar	Number of Sweeps
2230	2228 - 2232	---	---	NOR - 12 CIM - 14
2234	2232 - 2236	75°	N - 40 km C - 25 km	NOR - 14 CIM - 13
2239	2236 - 2241	---	---	NOR - 15 CIM - 13
2243	2241 - 2244	---	---	NOR - 13 CIM - 12
2247	2245 - 2248	60°	N - 45 km C - 40 km	NOR - 14 CIM - 12
2251	2249 - 2252	---	---	NOR - 11 CIM - 11
2305	2302 - 2307	45°	N - 55 km C - 55 km	NOR - 18 CIM - 21
2310	2308 - 2311	---	---	NOR - 18 CIM - 16
2313	2311 - 2314	---	---	NOR - 14 CIM - 15
2318	2315 - 2320	---	---	NOR - 15 CIM - 13
2322	2320 - 2323	40°	N - 65 km C - 65 km	NOR - 15 CIM - 12

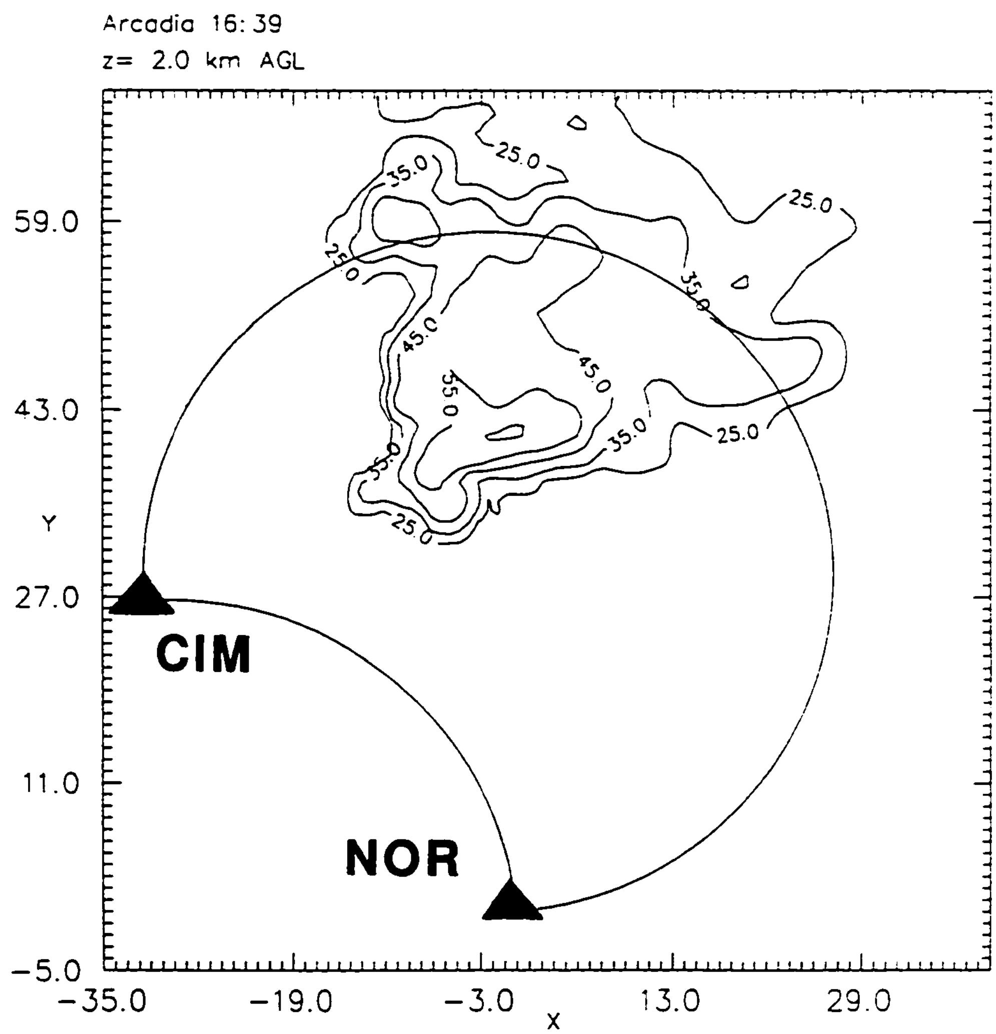

Figure 3.4 Locations of the radar sites (NORman and CIMarron) and the crescent shaped dual-Doppler lobe relative to the Arcadia storm at 2239 UTC. The grid origin is co-located with the Norman radar and x and y distances are in km.

data were manually "edited" to remove areas of contamination due to ground clutter, side-lobes and range-folding. In addition, the radial velocities were manually de-aliased.

3.2.2 Single-Doppler processing

Following the data editing steps, the reflectivity and radial velocity fields from the Cimarron data were prepared for the single-Doppler retrieval algorithm. This was accomplished by interpolating the data from the original spherical grid, in which the azimuthal increment varied slightly, to a new spherical grid with a constant azimuthal increment of $\Delta\phi = 2°$, a constant range increment of $\Delta r = 1$ km, and the original elevation angle increments. A 2-D Cressman (1959) algorithm with a circular influence region in the r-ϕ plane was used for the interpolation. For a given radar data point ('o') and analysis point ('a') pair, the weight function is:

$$W = \begin{cases} \dfrac{1-\delta}{1+\delta} & \text{for } \delta \le 1 \\ 0 & \text{for } \delta > 1 \end{cases} , \tag{3.1}$$

where:

$$\delta = \frac{(r_o - r_a)^2}{L_r^2} + \frac{(r\phi_o - r\phi_a)^2}{L_\phi^2} . \tag{3.2}$$

In (3.2), L_r and L_ϕ are the radii of influence in the range and azimuthal directions, respectively, r is the radar range and ϕ is the radar azimuth.

A special procedure for calculating range-dependent radii of influence was used for the interpolation. The principle underlying this procedure is to enforce local isotropy in the influence region while allowing the size of the influence region to increase with increasing range (in accordance with the variable grid resolution inherent in spherical grids). First, a constant aspect ratio between the radii of influence in the range and azimuthal directions is defined:

$$\alpha = L_r / L_\phi, \tag{3.3}$$

Local isotropy is enforced by setting $\alpha = 1$, yielding a circular influence region. The physical distances L_r and L_ϕ are related to the corresponding gridpoint distances by:

$$L_r = N_r \Delta r \quad , \tag{3.4}$$

$$L_\phi = N_\phi \, r \, \Delta\phi, \tag{3.5}$$

where N_r and N_ϕ are the fractional number of analysis gridpoints in the range and azimuthal radii of influence, respectively. Next, the product $N_r N_\phi$ is held constant for all r, resulting in an influence area that increases with increasing radar range. An expression for L_r as a function of range can be derived starting from a general formula for the area of the influence ellipse:

$$A = \pi L_r L_\phi = \pi \, r \, N_r \, N_\phi \, \Delta r \, \Delta\phi \quad . \tag{3.6}$$

Utilizing (3.3) in (3.6) and solving for L_r leads to:

$$L_r = K \sqrt{r} . \tag{3.7}$$

where

$$K = \sqrt{\alpha \, N_r \, N_\phi \, \Delta r \, \Delta\phi} \tag{3.8}$$

is constant for all values of radar range.

To utilize this formulation, a physical distance for the range radius of influence is specified for some reference range (L_r^* and r^*, respectively), as well as an aspect ratio (α, typically taken as 1). N_r^* and N_ϕ^* can then be calculated for the reference range from (3.4) and (3.5). Next, the constant K is determined and L_r is calculated for all values of range using (3.7). As a last step, N_r and N_ϕ can then be computed for all values of range, using (3.4) and (3.5). For this study, values of 20 km, 1.8 km, and 1 were chosen for N_r^*, N_ϕ^* and α. Note that N_r and N_ϕ apply to the analysis grid, and the physical distances L_r and L_ϕ must be used to determine which radar data points lie within the influence region of a given analysis gridpoint. Table 3.2 is a list of the computed radii of influence as a function of radar range, while Fig. 3.5 shows a sample of the resultant analysis for both reflectivity and radial velocity fields.

Because additional 3-D smoothing is applied to the radar fields as part of the wind retrieval algorithm, the objective analysis step described above serves mainly as a device to interpolate the data to a grid with a constant azimuthal spacing and to thin the data in the range direction. No smoothing was done in the elevation angle direction because of the coarser resolution and the expectation of greater stratification of the fields in that direction. Consistent with this, the wind retrieval algorithm is designed to utilize input data with a non-constant elevation angle increment.

Table 3.2 Range and azimuth radii of influence as a function of radar range for the Cressman interpolation procedure. La and Na in the table refer to L_ϕ and N_ϕ in the text.

REF RANGE	Lr	ALPHA	delr	delphi
20.0	1.800	1.0	1.0	2.0

pt	range	Lr	La	Nr	Na	NrNa
1	10.0	1.273	1.273	1.27	3.65	4.64
6	15.0	1.559	1.559	1.56	2.98	4.64
11	20.0	1.800	1.800	1.80	2.58	4.64
16	25.0	2.012	2.012	2.01	2.31	4.64
21	30.0	2.205	2.205	2.20	2.11	4.64
26	35.0	2.381	2.381	2.38	1.95	4.64
31	40.0	2.546	2.546	2.55	1.82	4.64
36	45.0	2.700	2.700	2.70	1.72	4.64
41	50.0	2.846	2.846	2.85	1.63	4.64
46	55.0	2.985	2.985	2.98	1.55	4.64
51	60.0	3.118	3.118	3.12	1.49	4.64
56	65.0	3.245	3.245	3.24	1.43	4.64
61	70.0	3.367	3.367	3.37	1.38	4.64
66	75.0	3.486	3.486	3.49	1.33	4.64
71	80.0	3.600	3.600	3.60	1.29	4.64
76	85.0	3.711	3.711	3.71	1.25	4.64
81	90.0	3.818	3.818	3.82	1.22	4.64
86	95.0	3.923	3.923	3.92	1.18	4.64
91	100.0	4.025	4.025	4.02	1.15	4.64

a)

b)

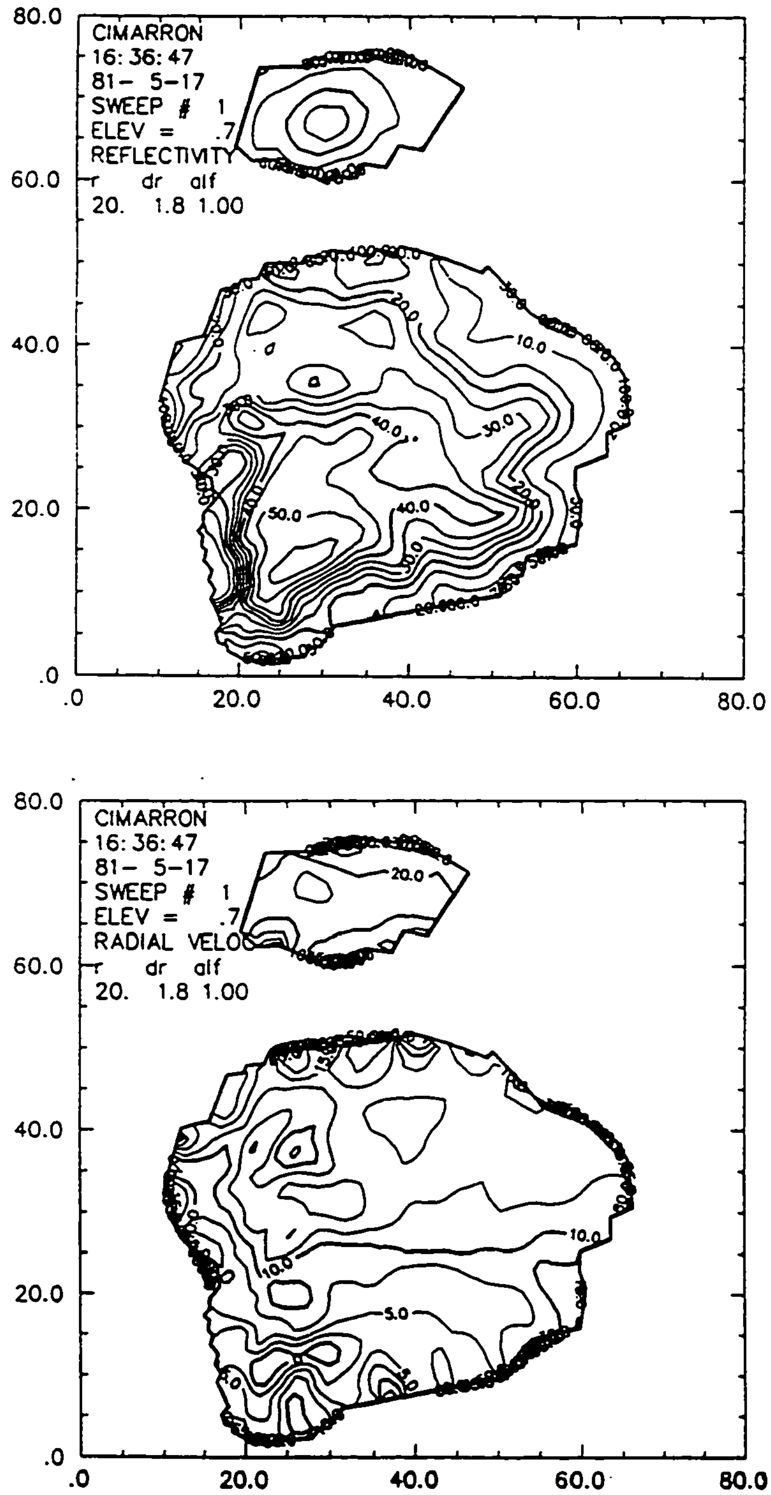

Figure 3.5 Objectively analyzed a) reflectivity and b) radial velocity fields from the 2239 UTC 0.7° scan of the Cimarron radar. Reflectivity and radial velocity are contoured every 5 dBZ and every 2.5 m s^{-1}, respectively. Grid distances are in km.

3.2.3 Dual-Doppler synthesis

The dual-Doppler analyses were obtained from David Dowell, who produced them for an observational study of tornadogenesis within the Arcadia storm (DB97). The reader is referred to DB97 for a detailed description of the dual-Doppler analysis procedure, and only a brief summary is provided here.

First, the radar data were interpolated to a common uniform Cartesian grid ($\Delta x = \Delta y =$ 0.8 km, $\Delta z = 0.5$ km) using a Cressman (1959) scheme with a spherical influence region of 1.2 km. Using this procedure, data from the lowest elevation angle were extrapolated to the ground. Next, a dual-equation system was iteratively solved in conjunction with a downward integration of the anelastic mass conservation equation to obtain vertical velocities. A boundary condition of $w = 0$ at the top of each data column was used for the downward integration, and an O'Brien (1970) correction was applied to insure vertical velocities of zero at the ground and data column top. It is important to note that inaccuracies associated with the assumed upper boundary condition, as well as the extrapolation of data from the lowest elevation angle to the ground, may lead to errors in the computed vertical velocity and to a lesser degree in the horizontal wind fields. Nevertheless, the horizontal velocities from the dual-Doppler analysis will be used for verifying the single-Doppler retrieved winds and comparisons of the retrieved and dual-Doppler vertical velocity will be presented.

3.3 Description of the storm evolution

At 2139 UTC, the time of the earliest dual-Doppler scan, the Arcadia storm was a mature supercell producing golfball-sized hail (Taylor 1982). As shown in Fig. 3.6, the storm appears to have just split at this time, with the left-moving cell located at about x =

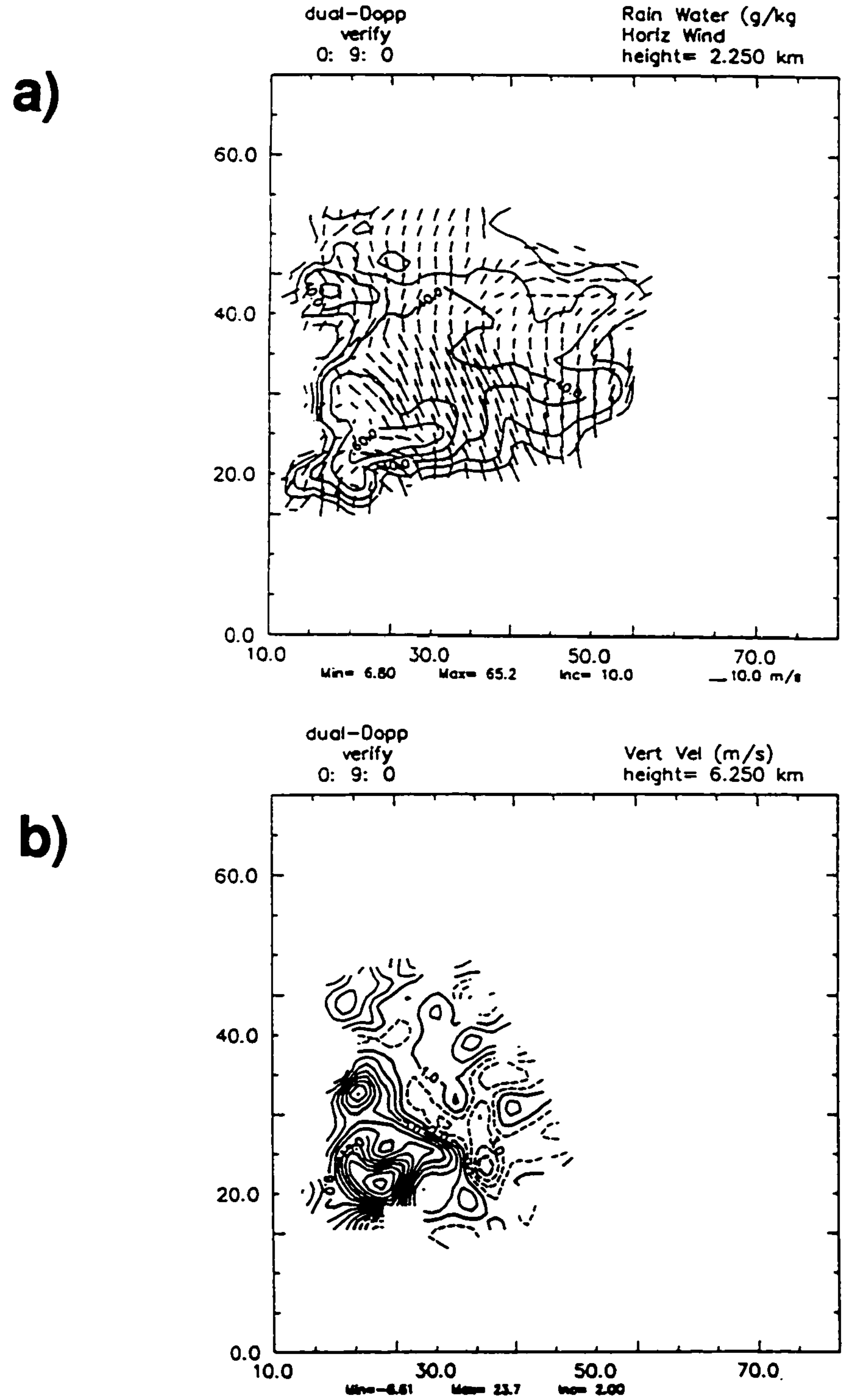

Figure 3.6 Low-level (z = 2.25 km) dual-Doppler analyzed a) reflectivity and storm-relative horizontal wind vectors, and b) vertical velocity for 2239 UTC. Reflectivity and vertical velocity are contoured every 10 dBZ and every 2 m s^{-1}, respectively. The Cimarron and Norman radars are located at x = -5, y = 10 and x = 27, y = -17, respectively. Grid distances are in km.

17 km, y = 43 km. The stronger, primary cell (located at about x = 24, y = 22) had an intense vertical velocity maximum (56 m/s at 12 km, not shown), a mid-level mesocyclone, and a reflectivity hook echo. By 2251 UTC (Fig. 3.7) the weaker cell had moved rapidly northward relative to the main cell, which was evolving into its tornadic phase. Fig. 3.8 shows the storm at 2305 UTC, midway through the life cycle of the tornado, which lasted from 2300-2310 UTC. Between 2251 UTC (Fig. 3.7) and 2305 UTC (Fig. 3.8), the maximum vertical velocity decreased significantly, especially at mid- and upper levels of the storm (not shown).

The 2313 UTC vertical velocity analysis (Fig. 3.9b) shows that the updraft from the post-tornadic cell was located to the northwest of a new updraft (located at x = 46, y = 31), the latter of which had developed to the southeast of the main precipitation core. Fig. 3.9a shows that the low-level westerly winds in the southwestern region of the storm had surged eastward, away from the decaying mesocyclone. By the final analysis time of 2322 UTC (Fig. 3.10), the newly developed southeastern updraft had become dominant. The overall storm, however, was becoming increasingly multicellular and a separate storm to the south was beginning to merge with it.

Because this dual-Doppler dataset spans the evolution of the storm from a mature supercell through its tornadic phase and into its decay phase, it provides an excellent retrieval and prediction test case. Single-Doppler retrieved wind fields will be directly verified against the dual-Doppler analyses, and numerical predictions initialized from the retrieved fields will be compared with the later dual-Doppler analyses.

a)

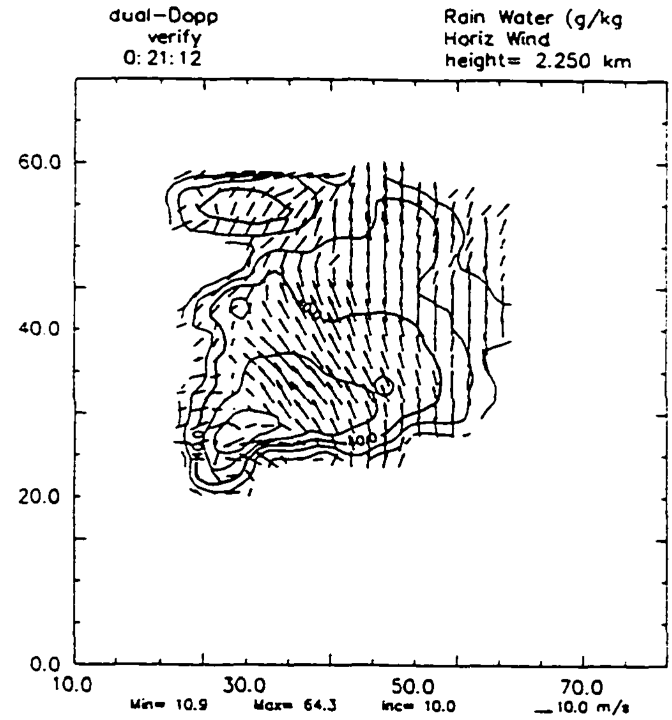

b)

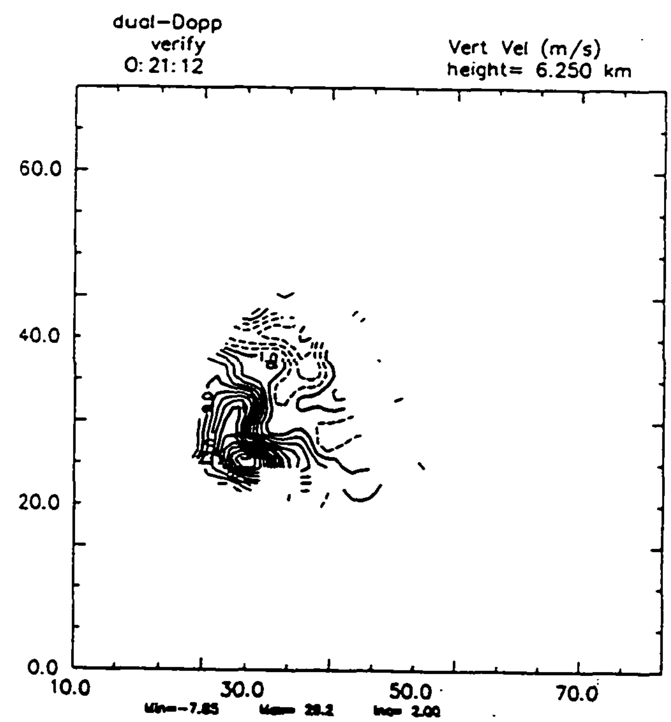

Figure 3.7 Low-level (z = 2.25 km) dual-Doppler analyzed a) reflectivity and storm-relative horizontal wind vectors, and b) vertical velocity for 2251 UTC. Contours, radar locations, and grid distances are as in Fig. 3.6.

a)

b)

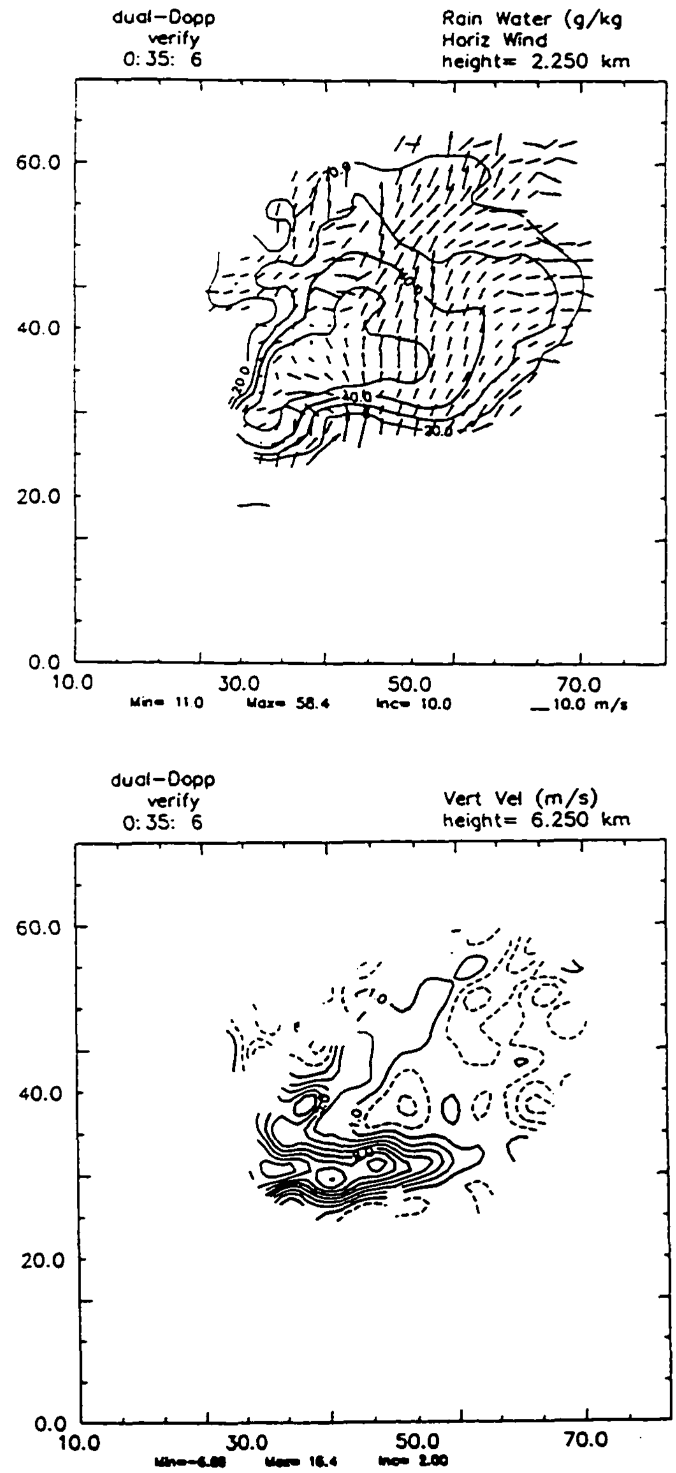

Figure 3.8 Low-level (z = 2.25 km) dual-Doppler analyzed a) reflectivity and storm-relative horizontal wind vectors, and b) vertical velocity for 2305 UTC. Contours, radar locations, and grid distances are as in Fig. 3.6.

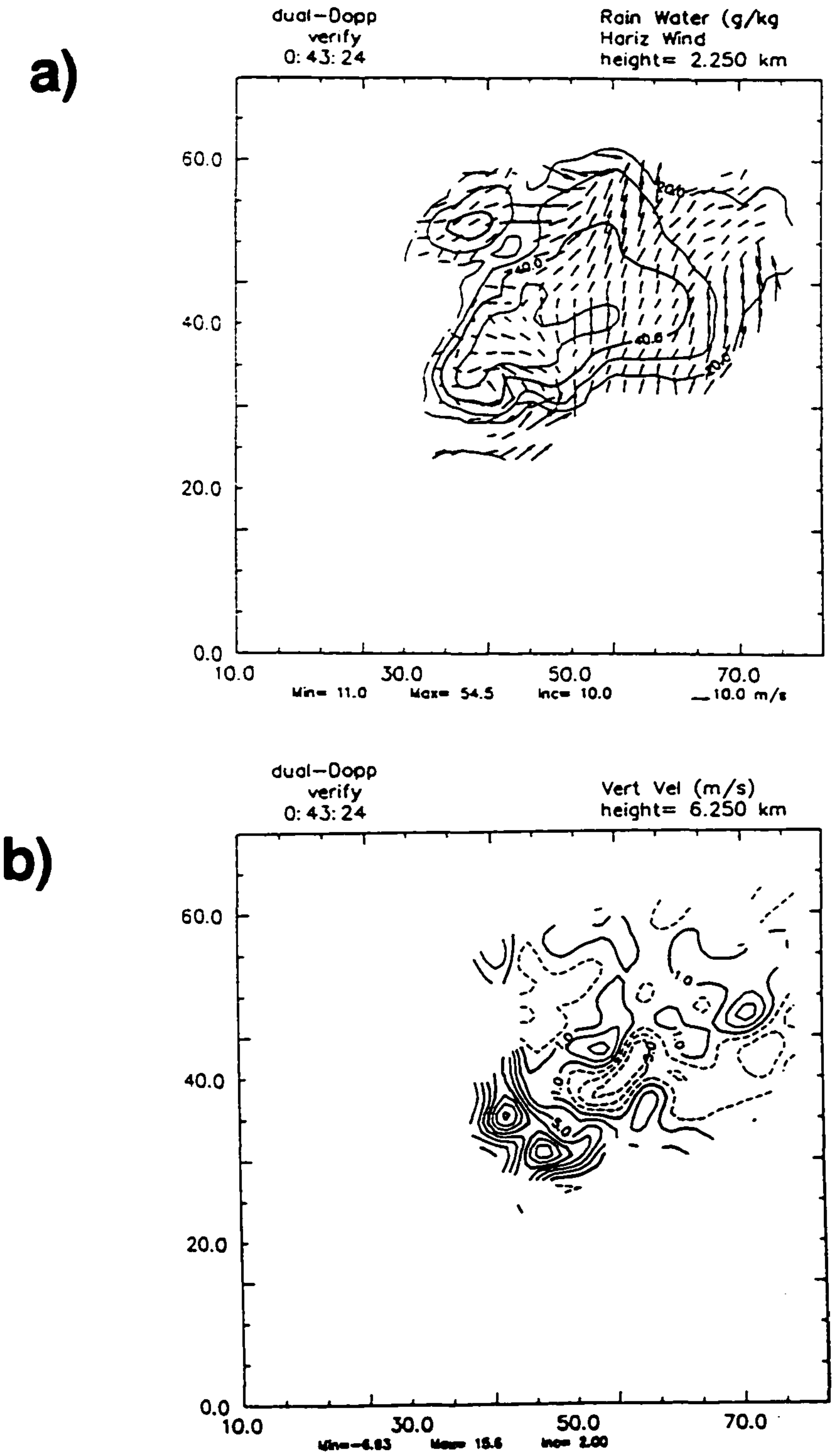

Figure 3.9 Low-level (z = 2.25 km) dual-Doppler analyzed a) reflectivity and storm-relative horizontal wind vectors, and b) vertical velocity for 2313 UTC. Contours, radar locations, and grid distances are as in Fig. 3.6.

a)

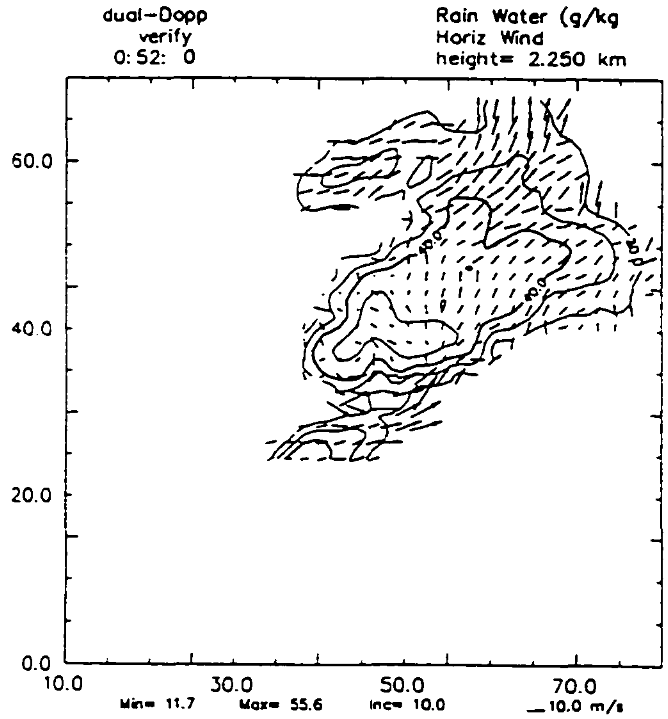

b)

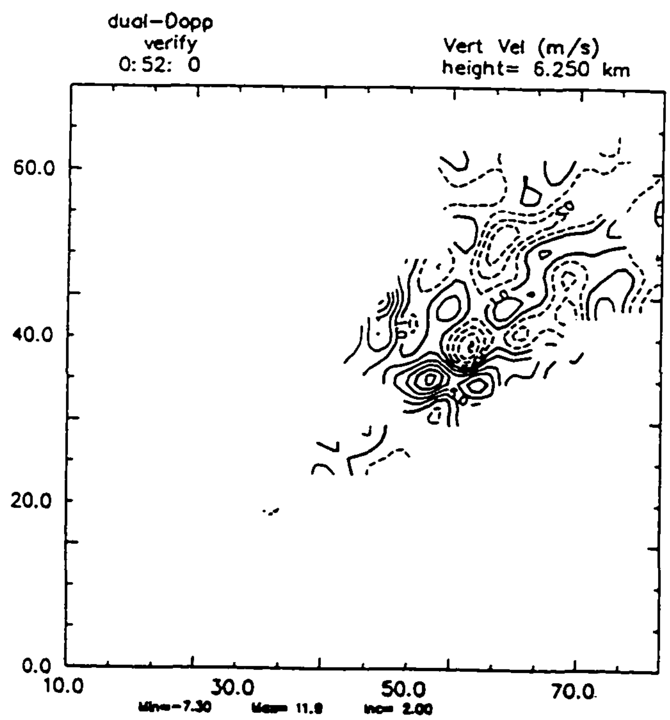

Figure 3.10 Low-level (z = 2.25 km) dual-Doppler analyzed a) reflectivity and storm-relative horizontal wind vectors, and b) vertical velocity for 2322 UTC. Contours, radar locations, and grid distances are as in Fig. 3.6.

CHAPTER 4

WIND RETRIEVAL RESULTS

As a first step in the sequential retrieval procedure, Shapiro's (1995a) two-scalar SDVR is applied to the Cimarron single-Doppler radar data. Because accurate retrieval of the two unobserved components is a cornerstone to the success of the entire sequential retrieval procedure, an extensive evaluation of the performance of the SDVR is presented. This is facilitated by the existence of high-resolution dual-Doppler data which are used to verify the SDVR results. Emphasis is placed on assessing the impact on retrieval performance of applying the retrieval in fixed versus moving reference frames.

Prior to discussing the wind retrieval results, some additional information concerning the details of the SDVR application and verification are presented in Section 4.1. These include a discussion of the spatial and temporal discretization; the data smoothing, rejection and hole-filling; and the validation procedure. Following this, the results for the fixed and moving reference frame experiments is presented in Section 4.2.

A further analysis of the retrieval results is presented in Section 4.3. Included is an examination of retrieved vorticity and divergence fields, presentation of results from an original wind decomposition and an illustration of the fields obtained by a simpler formulation of the SDVR. The wind decomposition illustrates the contribution from the various terms in the full-SDVR to the total Cartesian vertical velocity and also illustrates the differences between the full and simplified wind retrievals. Finally, the wind retrieval results are briefly summarized in Section 4.4.

4.1 Application details of the wind retrieval

4.1.1 Spatial and temporal discretization

The wind retrieval is performed on a spherical polar grid with uniform spacing in the radial and azimuthal directions. In the polar direction, the elevation angles from the input radar volume scans are used, resulting in non-uniform polar spacing. Three successive volume scans of input data are utilized (assumed valid at times t_1, t_2, t_3) with allowances for non-uniform intervals between the times. A Lagrange three-point interpolating polynomial (Carnahan et al. 1969) is used to calculate polar and temporal derivatives from the non-uniformly spaced data. The second scalar ($B = \partial A/\partial t + U\,\partial A/\partial x + V\,\partial A/\partial y$) is evaluated at three intermediate time levels, $t_{1.5}$, t_2, $t_{2.5}$. All necessary Cartesian derivatives [terms in the coefficients A-F in (2.28), the storm moving reference frame, the spatial derivatives in the definition of B, the A and B terminal velocity forcing] are calculated on the spherical grid using the following relations:

$$\frac{\partial}{\partial x} = \sin\phi\,\cos\theta\,\frac{\partial}{\partial r} + \frac{\cos\phi}{r\cos\theta}\frac{\partial}{\partial\phi} - \frac{\sin\phi\,\sin\theta}{r}\frac{\partial}{\partial\theta}\,, \tag{4.1}$$

$$\frac{\partial}{\partial y} = \cos\phi\,\cos\theta\,\frac{\partial}{\partial r} - \frac{\sin\phi}{r\cos\theta}\frac{\partial}{\partial\phi} - \frac{\cos\phi\,\sin\theta}{r}\frac{\partial}{\partial\theta}\,, \tag{4.2}$$

$$\frac{\partial}{\partial z} = \sin\theta\,\frac{\partial}{\partial r} + \frac{\cos\theta}{r}\frac{\partial}{\partial\theta}\,. \tag{4.3}$$

Radial and azimuthal derivatives are evaluated using centered differences. On the radar data coverage boundaries, radial and azimuthal derivatives are not calculated. Polar derivatives are computed using one-sided differences except as noted below.

The Poisson equation for the pseudo-streamfunction Q [Eq. (2.11)] is solved using a successive overrelaxation (SOR) technique on an irregular, staggered grid. Prior to the calculation of the forcing terms in (2.11), α and β are shifted by a half gridpoint in the ϕ and θ directions, respectively. $\partial\beta/\partial\theta$ in (2.11) is not evaluated at the top or bottom level of each data arc, resulting in the loss of one level at the top and bottom.

4.1.2 Data smoothing, rejection, and hole-filling

As discussed by Shapiro et al. (1995a), wind retrieval performance is sensitive to the data smoothing, rejection, and hole-filling. For this study, these tasks are accomplished via the following procedure. First, the raw input data (three time levels of reflectivity and radial velocity) are smoothed using the Cressman scheme described below. Following the calculation of α and β from the smoothed input fields, a data rejection step is performed to remove possible singularities. This procedure is also described below. Next , the resultant α and β fields are smoothed using the Cressman procedure. Finally, missing data points in the smoothed α and β fields are filled by solving a series of Laplace equations. On interior boundaries, known values of α and β are used, while on exterior boundaries, a zero-gradient condition is used.

The smoothing of the input fields and α and β is accomplished using a three-dimensional spherical Cressman procedure described by Zhao (1995). In her novel approach, each analysis point serves as the origin of a new rotated Cartesian coordinate system (x^*, y^*, z^*), and a corresponding new spherical coordinate system (r^*, ϕ^*, θ^*). As indicated in Fig. 4.1, the x^*- axis of the new Cartesian coordinate system is along the tangent of the azimuth through the analysis point. The y^*- axis is along the corresponding radial through the analysis point and the z^*- axis is along the tangent of the polar arc through the analysis point.

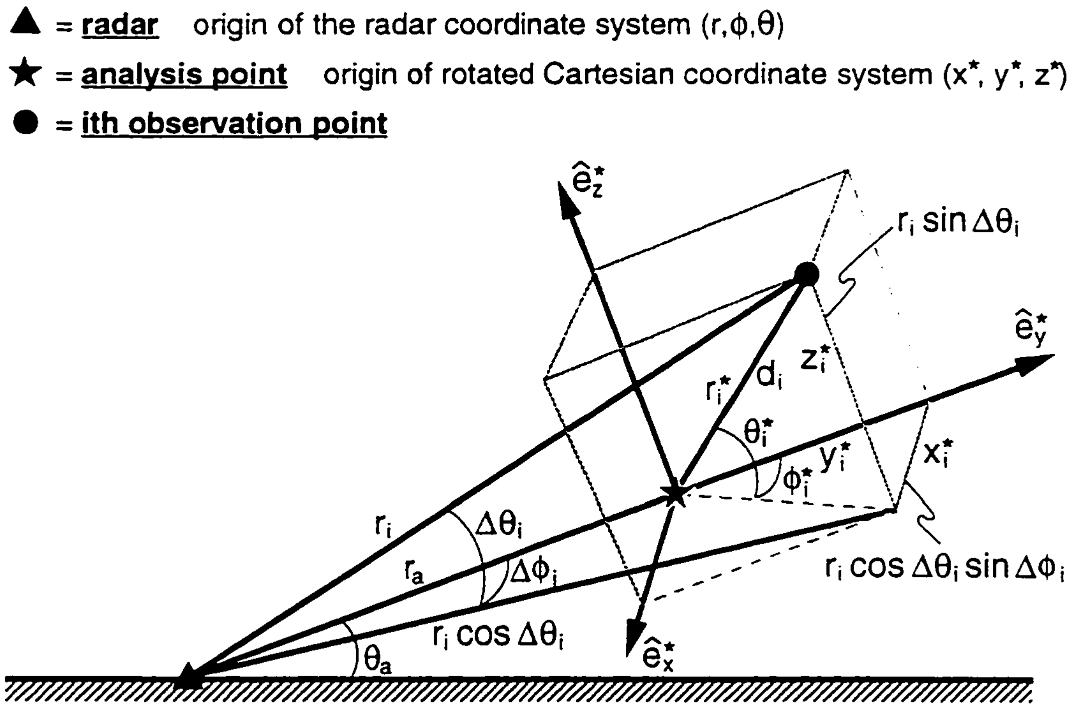

Figure 4.1 Diagram illustrating the two coordinate systems used in Zhao's (1995) 3-D spherical Cressman analysis procedure. The radar coordinate system (r, ϕ, θ) is as in Fig. 2.2 with the ath analysis point located at r_a, ϕ_a, θ_a. Each analysis point serves as the origin of a rotated Cartesian coordinate system (x^*, y^*, z^*). Within the Cartesian coordinate system, the ith observation point is located at x_i^*, y_i^*, z_i^*.

In this new coordinate system, with its origin ($x^*= 0$, $y^*= 0$, $z^*= 0$) defined at the analysis point, the Cressman weight function for the ith observation is:

$$W_i = \frac{1 - \delta_i}{1 + \delta_i} \quad , \tag{4.4}$$

where :

$$\delta_i = \frac{x_i^{*2}}{L_{x^*}^2} + \frac{y_i^{*2}}{L_{y^*}^2} + \frac{z_i^{*2}}{L_{z^*}^2} \quad . \tag{4.5}$$

x_i^* , y_i^* , z_i^* are the distances from the analysis point (origin) to the observation point, and L_{x^*} , L_{y^*} , L_{z^*} are user specified radii of influence.

In the new coordinate system the Cartesian and spherical location of a given observation point, i, can be related by:

$$x_i^{*2} = r_i^{*2} \cos^2 \theta_i^* \sin^2 \phi_i^* \quad , \tag{4.6}$$

$$y_i^{*2} = r_i^{*2} \cos^2 \theta_i^* \cos^2 \phi_i^* \quad , \tag{4.7}$$

$$z_i^{*2} = r_i^{*2} \sin^2 \theta_i^* \quad , \tag{4.8}$$

where:

$$r_i^{*2} = x_i^{*2} + y_i^{*2} + z_i^{*2} \quad . \tag{4.9}$$

Similarly, in the original radar coordinates we have:

$$x_i = r_i \cos \theta_i \sin \phi_i \quad , \tag{4.10}$$

$$y_i = r_i \cos \theta_i \cos \phi_i \quad , \tag{4.11}$$

$$z_i = r_i \sin \phi_i \quad . \tag{4.12}$$

where x_i, y_i, z_i, r_i, ϕ_i, and θ_i are measured from the radar origin. If, in the original radar coordinate system, a given analysis point (the origin of the new coordinate system for that point) has a defined location (x_a, y_a, z_a), then the distance between the ith observation point and the analysis point is given by:

$$d_i^2 = \left(x_i - x_a\right)^2 + \left(y_i - y_a\right)^2 + \left(z_i - z_a\right)^2 \quad . \tag{4.13}$$

The following relationships then exist between the two coordinate systems (see Fig. 4.1):

$$r_i^* = d_i \quad , \tag{4.14}$$

$$z_i^* = r_i \sin \Delta\theta_i \, , \tag{4.15}$$

$$x_i^* = r_i \cos \Delta\theta_i \sin \Delta\phi_i \quad , \tag{4.16}$$

where in the original coordinate system, $\Delta\theta_i = (\theta_i - \theta_a)$ and $\Delta\phi_i = (\phi_i - \phi_a)$. From these relations, the following expressions can be derived:

$$\sin^2\theta_i^* = \frac{r_i^2 \sin^2 \Delta\theta_i}{d_i^2} \quad , \tag{4.17}$$

$$\cos^2\theta_i^* = 1 - \sin^2\theta_i^* \quad , \tag{4.18}$$

$$\sin^2\phi_i^* = \frac{r_i^2 \cos^2\Delta\theta_i \sin^2 \Delta\phi_i}{d_i^2 \cos^2\theta_i^*} \quad , \tag{4.19}$$

$$\cos^2\phi_i^* = 1 - \sin^2\phi_i^* \quad . \tag{4.20}$$

A final expression for δ can be obtained by substituting (4.10) - (4.12) into (4.9) :

$$\delta_i = d_i^2 \left[\frac{\cos^2\theta_i^* \sin^2\phi_i^*}{L_{x^*}^2} + \frac{\cos^2\theta_i^* \cos^2\phi_i^*}{L_{y^*}^2} + \frac{\sin^2\theta_i^*}{L_{z^*}^2} \right] \quad . \tag{4.21}$$

The numerators of the terms inside the bracket can be computed using (4.17) - (4.20).

Values for the Cressman radii of influence (L_{x^*} , L_{y^*} , L_{z^*}) are specified using the following semi-empirical procedure. First, L_{x^*} and L_{y^*} are determined from:

$$L_{x^*} = L_{y^*} = N_h \max(\Delta r,\ r_i\,\Delta\phi) \ , \tag{4.22}$$

where N_h is a user-specified gridpoint distance for the "quasi-horizontal" direction in the new coordinate system. L_{z^*} is then specified as a fraction of L_{x^*} :

$$L_{z^*} = C\,L_{x^*} \quad , \tag{4.23}$$

where C is a user specified constant ratio.

The principle behind the "max" function in (4.22) is to smooth the fields in a locally isotropic manner, based on the largest of the local "quasi-horizontal" gridlengths. Then, based on the notion that gradients in the polar direction typically exceed those in the horizontal, the retained vertical structure is related to the horizontal by specifying a value of C that is less than unity in (4.23). For this study, the best results were obtained with N_h = 2.2 gridpoints and C = .75 for the radar input data and N_h = 6.1 gridpoints and C = .55 for α and β . This roughly corresponds to filtering 2 Δx features from the raw data and 6 Δx features from the α and β fields. Increased smoothing of the input fields was found to produce larger amplitudes in the retrieved velocities (due to smaller denominators in the expressions for α and β), but reduced skill scores. Increased smoothing of α and β led to smoother retrieved velocity fields. The selected values apparently represent an optimal setting for signal extraction and noise suppression, and seem to be rather robust, having yielded good results in applications of this SDVR to a number of different datasets (Shapiro et al. 1995a, 1997; Weygandt et al. 1995).

Following Shapiro et al. (1995a), the rejection of α and β points to remove possible singularities is accomplished using three criteria. First, α and β points are rejected if the denominators in (2.9) or (2.10) are smaller than a tolerable value (estimated from the typical errors in A and B). Second, in a crude attempt to limit errors in the numerators of (2.9) and (2.10), α and β are rejected when the local value of $\left|\partial A/\partial t + v_r\, \partial A/\partial r\right|$ is less than the estimated error in these terms. As a final check, α and β (which represent estimates of v_θ and v_ϕ) are rejected if their absolute value exceeds a specified threshold, here of 45 m s^{-1}.

4.1.3 Wind retrieval verification

The retrieved wind fields are verified against a set of independent dual-Doppler analyses provided by David Dowell. The dual-Doppler analysis procedure employed by Dowell has been briefly summarized in Section 3.2 and described in more detail by DB97. Because of possible errors associated with the dual-Doppler-derived vertical velocities, rigorous quantitative verification is carried out only for the purely horizontal azimuthal velocity. This is accomplished by first tri-linearly interpolating both the SDVR and dual-Doppler wind fields to a common Cartesian grid. To facilitate the thermodynamic retrieval and model predictions, this common Cartesian grid is chosen to be the ARPS model grid, and has constant horizontal and vertical grid spacings of 1.0 km and 0.5 km, respectively.

All fields are defined on scalar points and conversions between spherical and Cartesian wind components are accomplished using the following matrix transformations:

$$A \begin{bmatrix} v_r \\ v_\phi \\ v_\theta \end{bmatrix} = \begin{bmatrix} u \\ v \\ w \end{bmatrix}, \qquad A^T \begin{bmatrix} u \\ v \\ w \end{bmatrix} = \begin{bmatrix} v_r \\ v_\phi \\ v_\theta \end{bmatrix} \quad , \tag{4.24}$$

where:

$$A = \begin{bmatrix} \cos\theta \ \sin\phi & \cos\phi & -\sin\theta \ \sin\phi \\ \cos\theta \ \cos\phi & -\sin\phi & -\sin\theta \ \cos\phi \\ \sin\theta & 0 & \cos\theta \end{bmatrix} \quad . \tag{4.25}$$

Using the dual-Doppler derived fields as verification, two quantitative skill scores are calculated for the retrieved azimuthal velocity on the common verification grid. The first is the root mean square error, which gives a quantitative measure of the overall error in units matching those of the variable:

$$\mathrm{RMSE}\,(\chi) = \left[\frac{1}{N} \sum_{n=1}^{N} \left(\chi_n^R - \chi_n^D \right)^2 \right]^{1/2} \quad , \tag{4.26}$$

where χ_n^R and χ_n^R are the retrieved and dual-Doppler value of χ at the nth gridpoint, respectively. The second skill score is the Pearson linear correlation coefficient, which provides a measure of the pattern similarity between two fields and is given by:

$$\operatorname{corr}(\chi^R,\chi^D) = \frac{\left[\frac{1}{N}\sum_{n=1}^{N}\left(\chi_n^R - \bar{\chi}_n^R\right)\left(\chi_n^D - \bar{\chi}_n^D\right)\right]}{\left\{\left[\frac{1}{N}\sum_{n=1}^{N}\left(\chi_n^R - \bar{\chi}_n^R\right)^2\right]\left[\frac{1}{N}\sum_{n=1}^{N}\left(\chi_n^D - \bar{\chi}_n^D\right)^2\right]\right\}^{1/2}} \quad . \tag{4.27}$$

where:

$$\bar{\chi} = \frac{1}{N}\sum_{n=1}^{N}\chi_n \quad . \tag{4.28}$$

The correlation coefficient is bounded by the values of - 1 (indicating a perfect negative linear fit) and + 1 (indicating a perfect positive linear fit).

4.2 Fixed and moving reference frame results

As described in Chapter 2, Shapiro's two-scalar scheme has been modified by applying it in a moving reference frame. In this section, retrieval results from two different moving reference frame experiments (one moving with the storm and one moving with the mean wind) are compared with results from a fixed reference frame experiment. Before examining the retrieval performance for the different experiments, it is important to evaluate the accuracy with which the moving reference frames are computed from the single-Doppler data. As discussed in Section 2.2, simple least squares formulations are used to calculate both the storm propagation and mean wind translation components from a single sector scan of Doppler radar data. The results of the storm propagation calculation [obtained using Eq. (2.37)] are verified against subjectively computed storm motion components, whereas the results from the mean wind calculation [obtained using Eq. (2.39)] are verified against mean winds calculated from the dual-

Doppler analysis. The calculated and verification translation components for each of the three successive wind retrievals are compared in Table 4.1. Both the storm propagation and mean wind techniques perform reasonably well. Results are especially good for the mean wind components, with average errors under 1 m s^{-1}.

Table 4.2 shows the impact of the different moving reference frames on the overall retrieval results. Comparison of root mean square errors, correlation coefficients and domain maximum vertical velocity all indicate that both moving reference frame experiments perform substantially better than the fixed reference frame experiment. On average, the mean wind reference frame slightly outperforms the storm propagation reference frame. The retrieved maximum vertical velocities, while significant, are generally less than half of the magnitude obtained by the dual-Doppler analyses. The reasons for this deficiency will be examined in Sect. 4.3.

Fig. 4.2 shows, for the 2039 UTC wind retrieval, the vertical profiles of the RMS errors for the three moving reference frame experiments. The retrieved fields from this time have been selected for display because they are the ones used to initialize the prediction model, and their skill scores best match the three-retrieval average. The two moving reference frames show a 1-2 m s^{-1} superiority over the fixed frame for most levels. The only exception is near the storm top, where the mean wind experiment performed significantly better than either of the other experiments. The reasons for this particular feature, as well as the significant performance variations with height at low-levels, have not been identified.

The vertical profiles of domain maximum vertical velocity for the 2039 UTC experiments are shown in Fig. 4.3. All three experiments produce similar profiles, with overall maxima less than half that obtained from the dual-Doppler analysis. The mean wind moving reference frame produced the largest maximum and exhibits the most realistic profile shape. It is important to note that, because of the ad-hoc vertical velocity

Table 4.1 Comparison of the moving reference frame components calculated from the single-Doppler data with verification values for the three successive volumes scans.

Reference Frame Component		2234 UTC	2239 UTC	2243 UTC	AVG
STORM PROPAGATION (m/s)					
Single-Doppler	$\bar{U}$	7.4	6.9	8.0	**7.4**
Verification	$\bar{U}$	7.8	8.5	11.4	**9.2**
Single-Doppler	$\bar{V}$	5.3	5.6	5.7	**5.5**
Verification	$\bar{V}$	4.9	4.7	5.7	**5.1**
MEAN WIND (m/s)					
Single-Doppler	$\bar{U}$	22.1	22.4	21.9	**22.1**
Verification	$\bar{U}$	21.6	21.1	21.7	**21.5**
Single-Doppler	$\bar{V}$	12.9	13.0	13.4	**13.1**
Verification	$\bar{V}$	14.3	13.4	13.7	**13.8**

Table 4.2 Comparison of skill scores for different reference frame experiments for the three successive retrievals.

Skill Score	2234 UTC	2239 UTC	2243 UTC	AVG
RMS ERROR (m/s)				
FIXED	7.9	8.1	8.3	**8.1**
STORM PROP.	6.1	7.0	6.2	**6.4**
MEAN WIND	5.5	6.4	6.9	**6.3**
CORRELATION				
FIXED	.47	.43	.36	**.42**
STORM PROP.	.77	.68	.71	**.72**
MEAN WIND	.81	.73	.65	**.73**
MAXIMUM W (m/s)				
FIXED	27.8	19.2	23.9	**23.6**
STORM PROP.	27.8	20.9	26.3	**25.0**
MEAN WIND	25.9	24.9	28.1	**26.3**
DUAL-DOPP	63.2	55.8	54.4	**57.8**

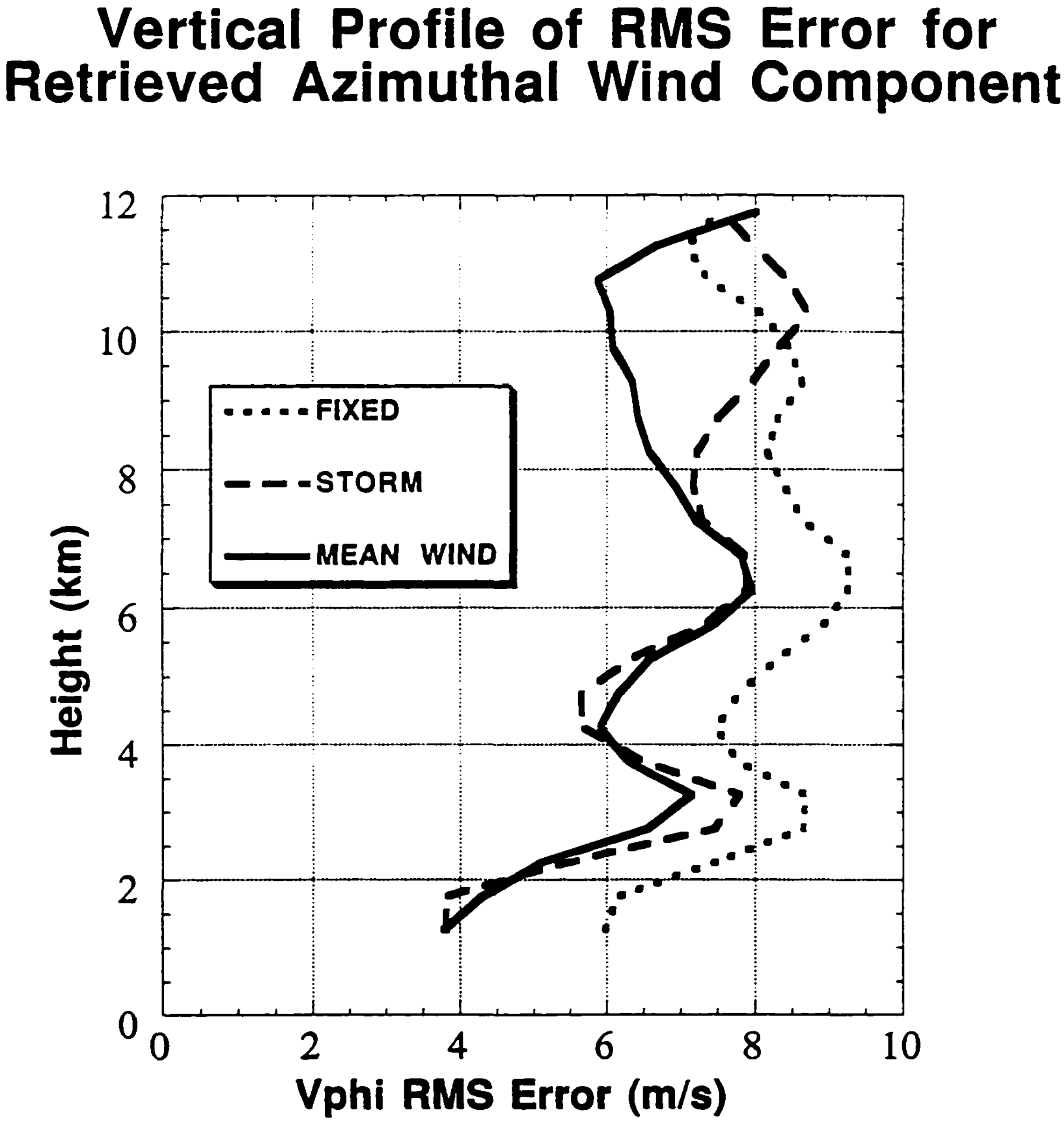

Figure 4.2 Vertical profile of azimuthal velocity RMS errors (m s^{-1}) for the 2239 UTC single-Doppler retrieval experiments.

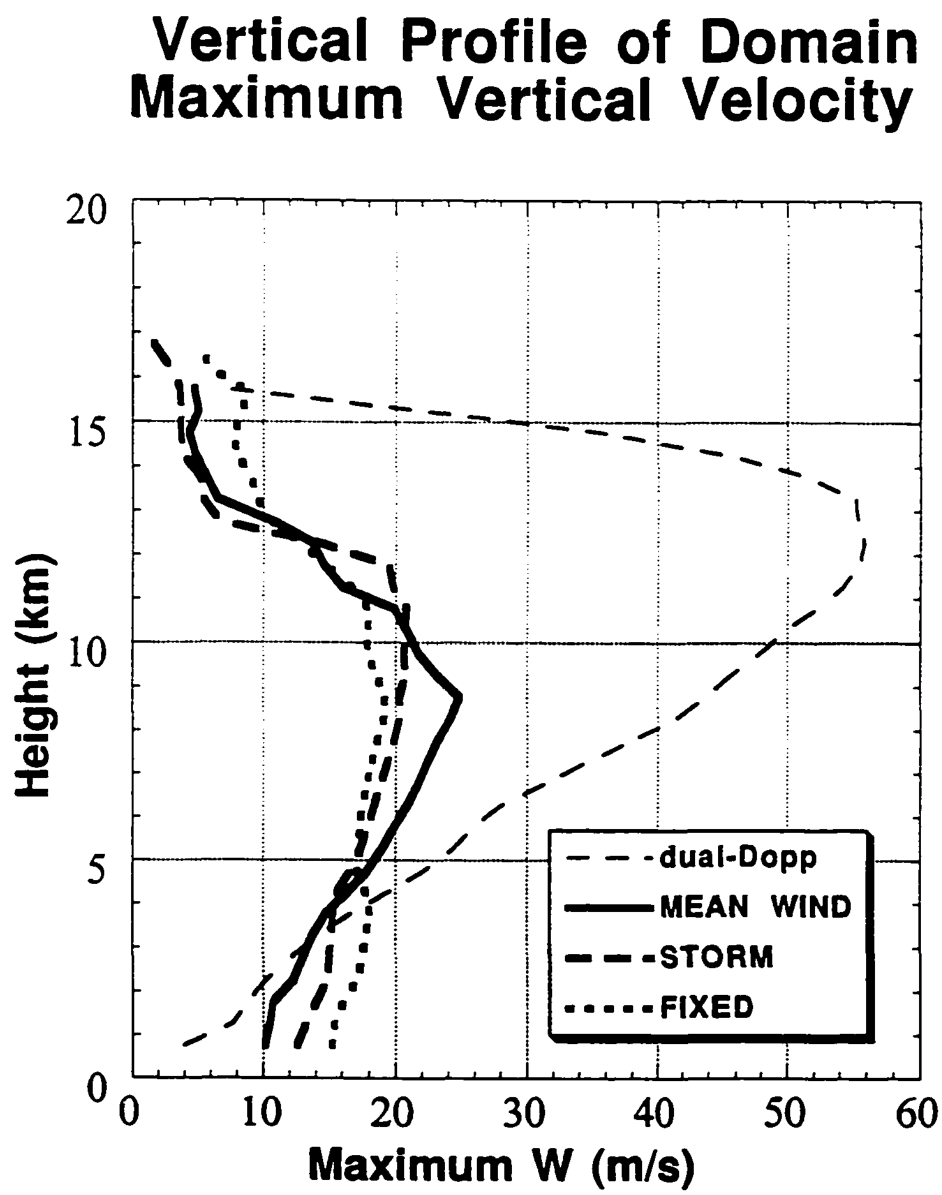

Figure 4.3 Vertical profile of the maximum vertical velocity (m s^{-1}) for the 2239 UTC dual-Doppler verification and the single-Doppler retrieval experiments.

assumptions made in the O'Brien correction that is used in the dual-Doppler analysis, care should be exercised in directly comparing the retrieved and dual-Doppler vertical velocity fields.

Individual plots from the 2039 UTC experiments are now examined to illustrate the SDVR performance in a more detailed manner. Fig. 4.4 shows the low-level ($z = 2.25$) storm-relative vector wind field from the dual-Doppler analysis, and the corresponding single-Doppler retrievals. Qualitative comparison of the different experiments illustrates the superiority of the mean wind reference frame. In particular, it best captures the zone of strong storm-relative southeasterly winds northeast of the mesocyclone. This is further illustrated in Fig. 4.5, a comparison of the retrieved versus dual-Doppler derived azimuthal velocity. The mean wind experiment clearly best captures the overall azimuthal velocity pattern, as reflected in the superior RMSE and correlation scores for this level. Also apparent is the loss of high-resolution detail in all three of the retrieval experiments.

The portion of the azimuthal velocity provided to the retrieval by the mean wind moving reference frame is given by:

$$\overline{V}_\phi = \hat{e}_\phi \cdot \left[U\,\hat{i} + V\,\hat{j} \right] = +\cos\phi\, U - \sin\phi\, V \quad . \tag{4.29}$$

Subtracting this "mean wind" portion of the field from the total retrieved azimuthal velocity yields the retrieved perturbation azimuthal velocity, v_ϕ' . This field represents the portion of the azimuthal velocity obtained solely from the pseudo-streamfunction, Q [Eq. (2.4)]. Fig. 4.6 shows a comparison of the perturbation azimuthal velocity from the dual-Doppler analysis and the mean wind reference frame retrieval. The large region of negative values is successfully retrieved; however, much of the small-scale detail is lost. Further examination of the retrieved field (Fig. 4.6b) reveals that most of the retrieved azimuthal velocity gradient is in the radial direction. This is indicative of polar vorticity,

a)

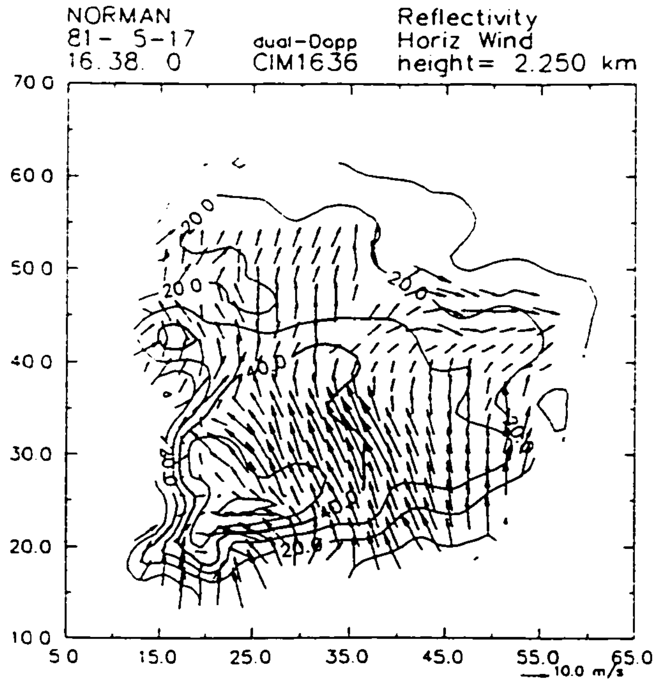

b)

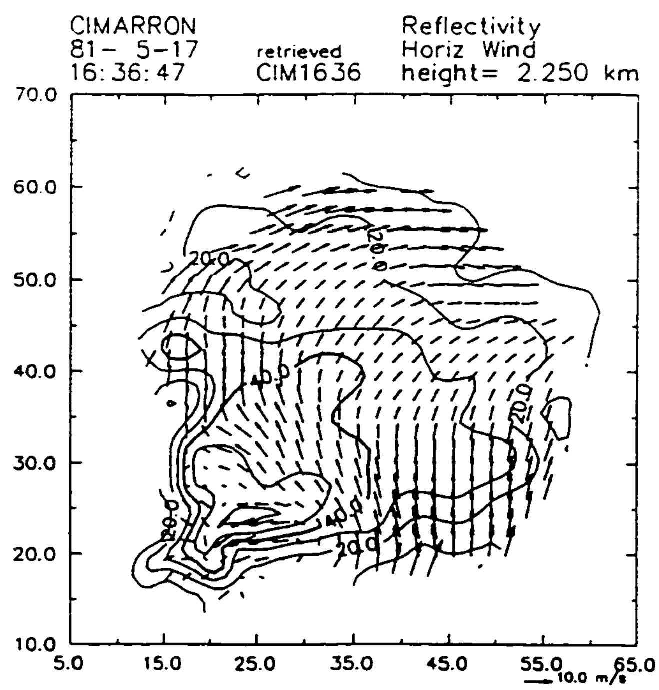

Figure 4.4 2239 UTC low-level (z = 2.25 km) reflectivity and storm-relative horizontal vectors for a) the dual-Doppler analysis, b) the mean wind reference frame, c) the storm propagation reference frame and d) the fixed reference frame. Reflectivity is contoured every 10 dBZ. The Cimarron radar is located at x = -5, y = 10 and grid distances are in km.

c)

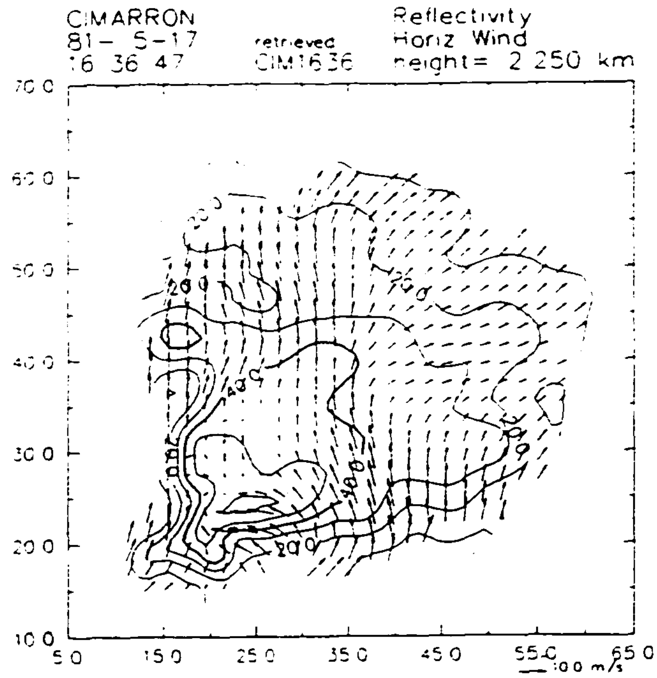

d)

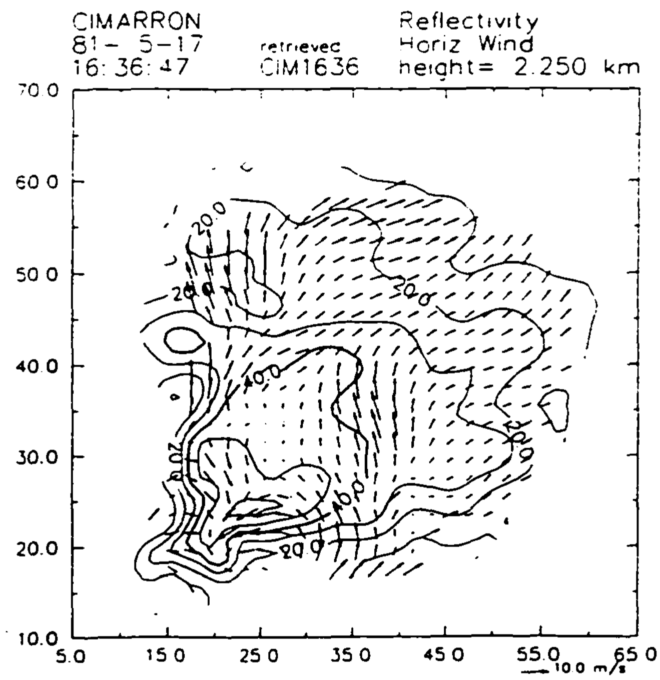

Figure 4.4 (Continued)

a)

b)

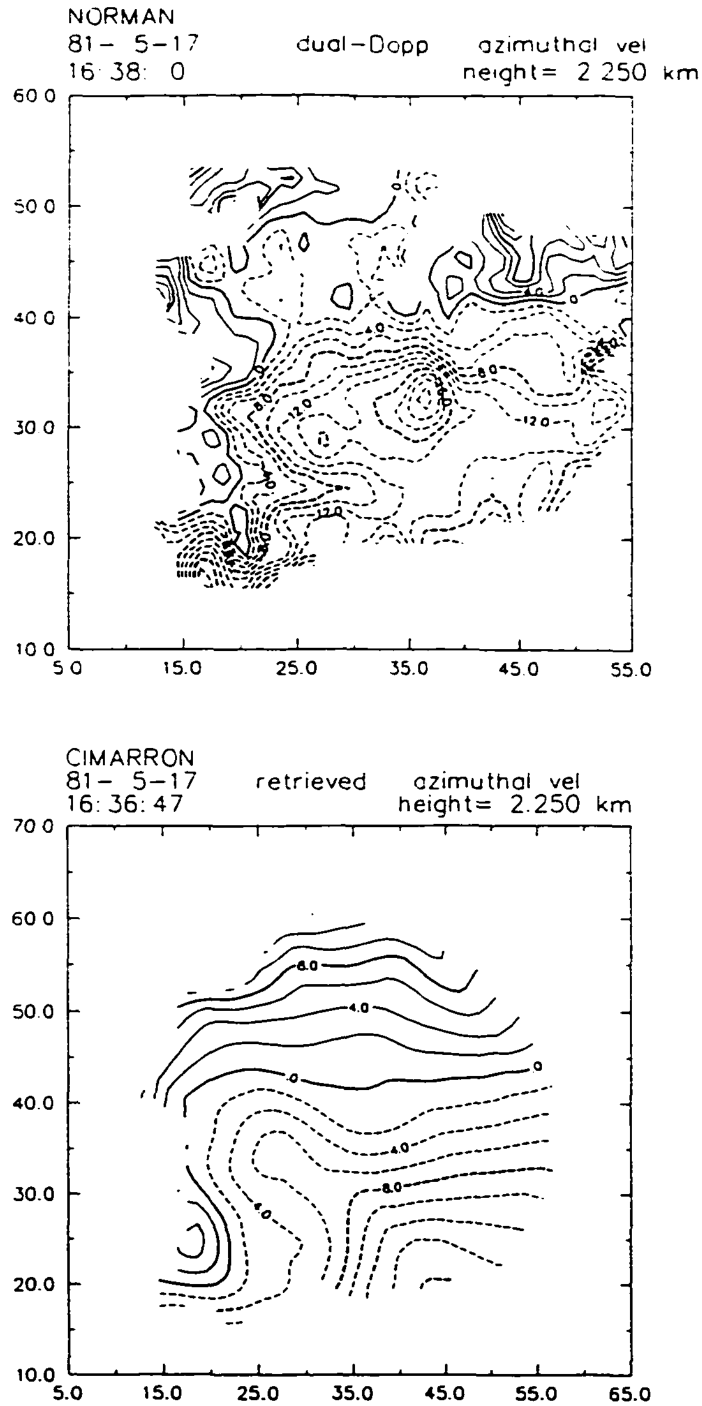

Figure 4.5 2239 UTC low-level (z = 2.25 km) azimuthal velocity (measured from the Cimarron radar) for a) the dual-Doppler analysis, b) the mean wind reference frame, c) the storm propagation reference frame and d) the fixed reference frame. Azimuthal velocity is contoured every 2 m s^{-1}. The radar location and grid distances are as in Fig. 4.4.

c)

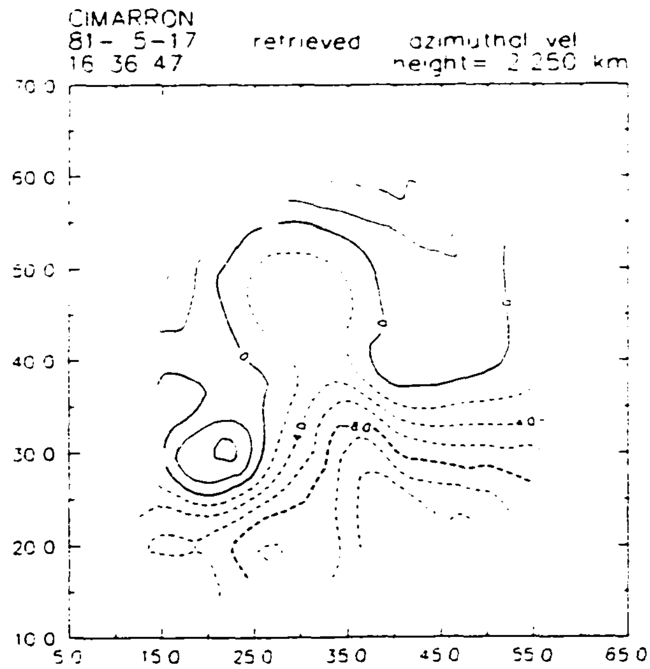

d)

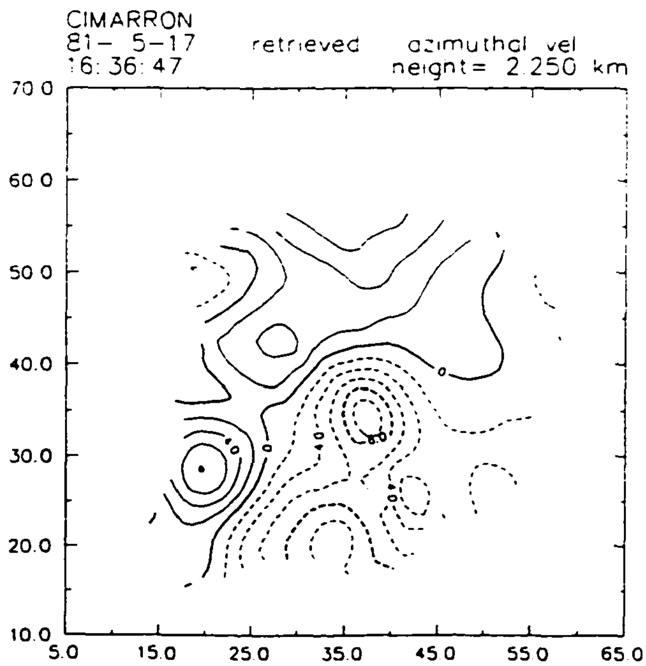

Figure 4.5 (Continued)

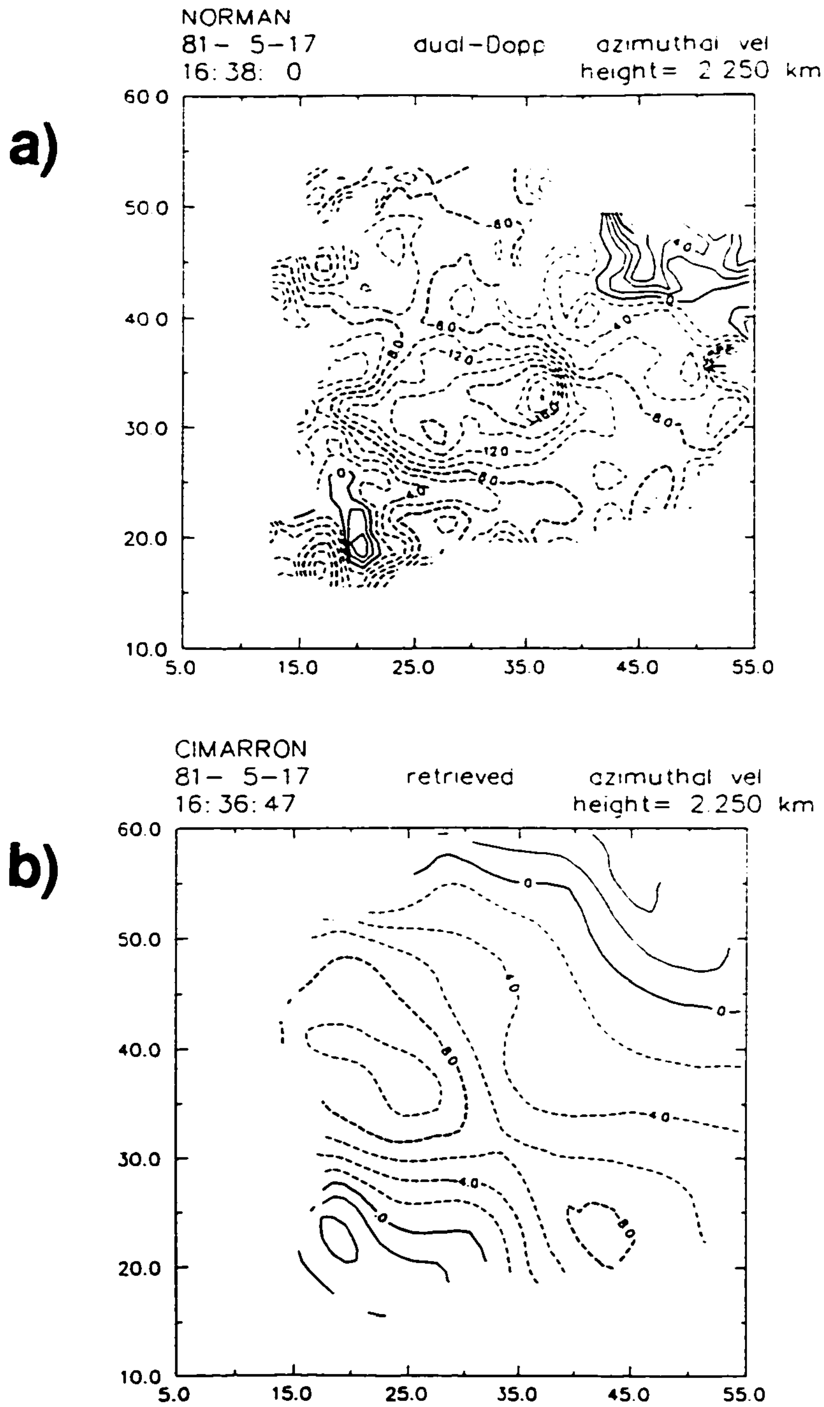

Figure 4.6 2239 UTC low-level (z = 2.25 km) perturbation azimuthal velocity (measured from the Cimarron radar) for a) the dual-Doppler analysis and b) the mean wind reference frame. Contour interval, radar location, and grid distances are as in Fig. 4.5.

$\frac{\partial(r\, v_\phi)}{\partial r}$, and suggests that at this level, rotational velocities are more successfully retrieved than divergent velocities. The implications of this will be examined in Section 4.3.

Fig 4.7 shows the retrieved and verifying horizontal wind fields from the upper portion of the storm (z = 10.25 km). Although the retrieved wind field is clearly dominated by the constant mean wind, a weak storm top divergence signature is retrieved in all three experiments. The total retrieved azimuthal velocity fields (Fig. 4.8b-d) clearly show the associated storm top velocity couplet. The corresponding dual-Doppler field (Fig. 4.8a) also shows this feature, but with a significantly reduced scale. Comparison of the different retrieval experiments again shows the clear superiority of the mean wind moving reference frame, as reflected in the skill scores for this level.

Subtracting off the projection of the mean wind yields the perturbation fields shown in Fig. 4.9. They further illustrate the difference in scale between dual-Doppler derived and single-Doppler retrieved divergent velocity couplet. It is important to note, however, that in contrast to the low-levels, the SDVR does yield a qualitatively correct divergence signature at upper levels.

Lastly, the retrieved and dual-Doppler derived mid-level (z = 6.25 km) Cartesian vertical velocity fields are shown in Fig. 4.10. As before, the retrieved fields are significantly smoother than the dual-Doppler field, but capture the principal features of interest quite well. In particular, the horseshoe shaped updraft maximum surrounding a local velocity minimum is faithfully reproduced. Comparison of the maximum values, however, indicates that all three experiments significantly under-retrieve the updraft strength. Furthermore, none of the experiments shows a clear superiority over the others.

a)

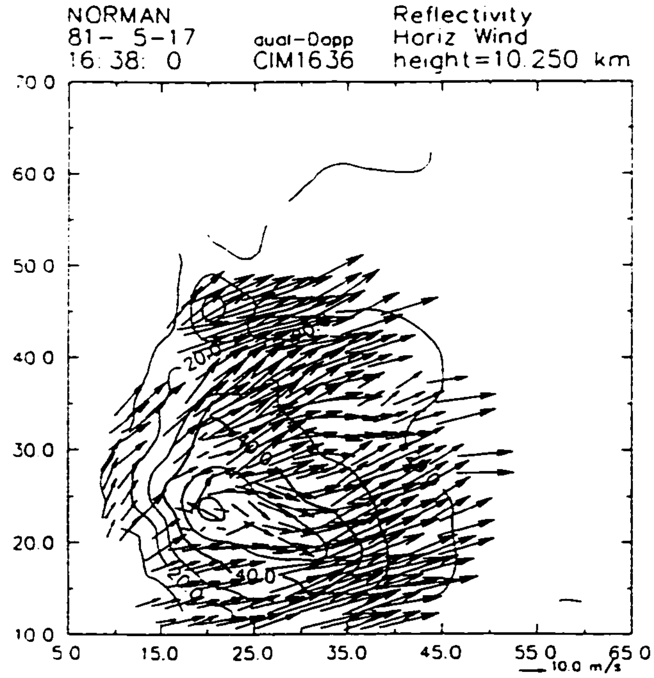

b)

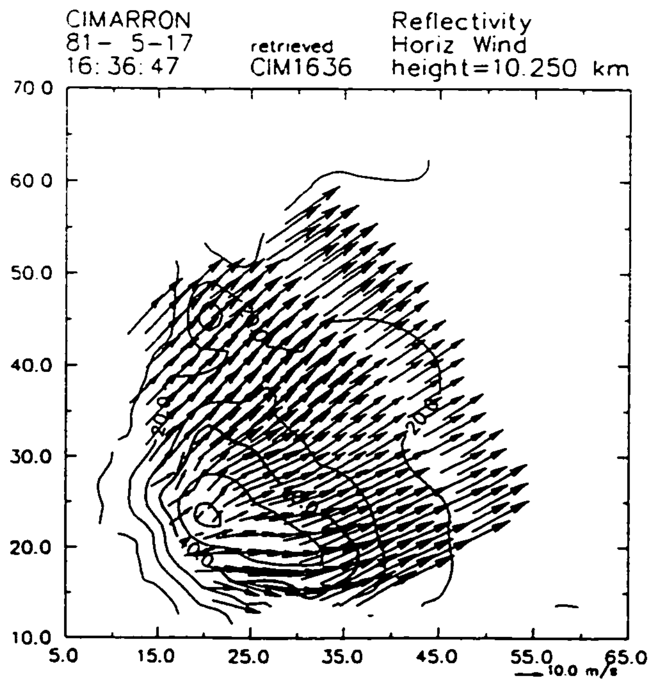

Figure 4.7 2239 UTC upper-level (z = 10.25 km) reflectivity and storm-relative horizontal vectors for a) the dual-Doppler analysis, b) the mean wind reference frame, c) the storm propagation reference frame and d) the fixed reference frame. Contour interval, radar location, and grid distances are as in Fig. 4.4.

c)

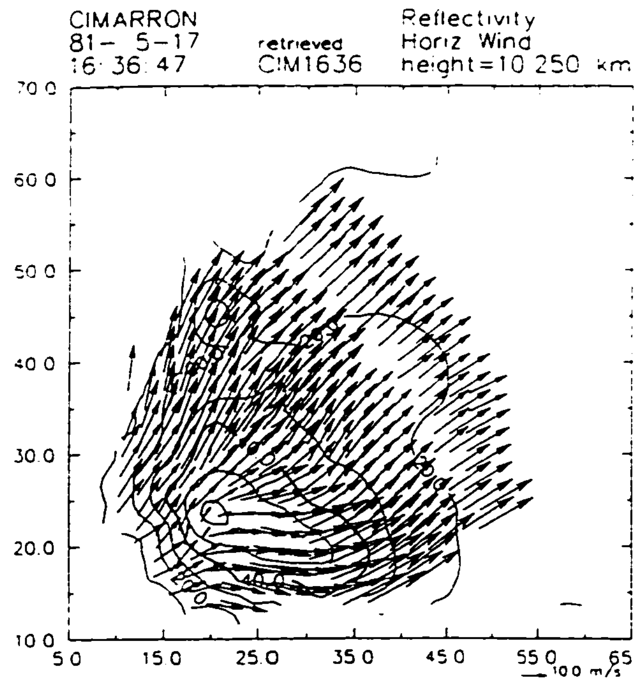

d)

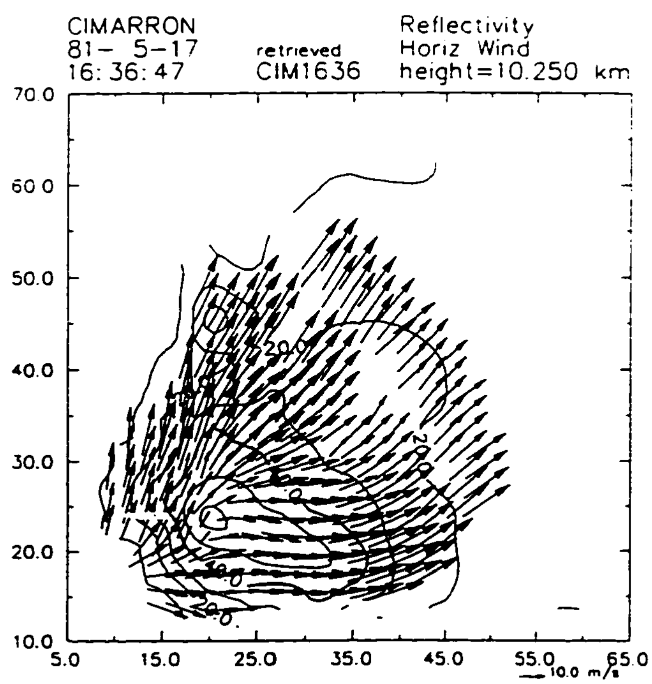

Figure 4.7 (Continued)

a)

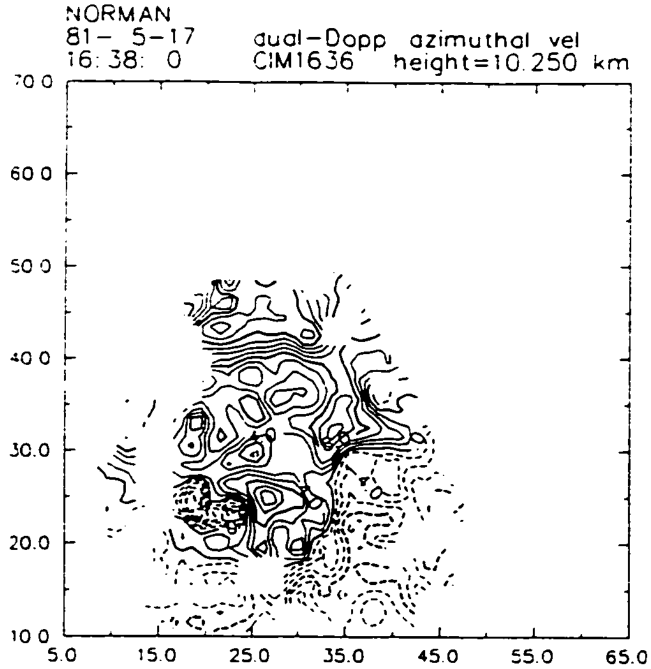

b)

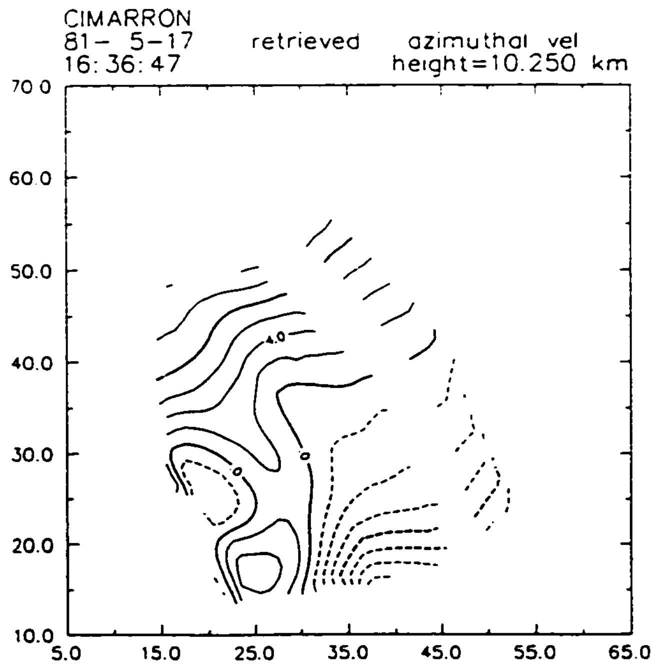

Figure 4.8 2239 UTC upper-level (z = 10.25 km) azimuthal velocity (measured from the Cimarron radar) for a) the dual-Doppler analysis, b) the mean wind reference frame, c) the storm propagation reference frame and d) the fixed reference frame. Contour interval, radar location, and grid distances are as in Fig. 4.5.

c)

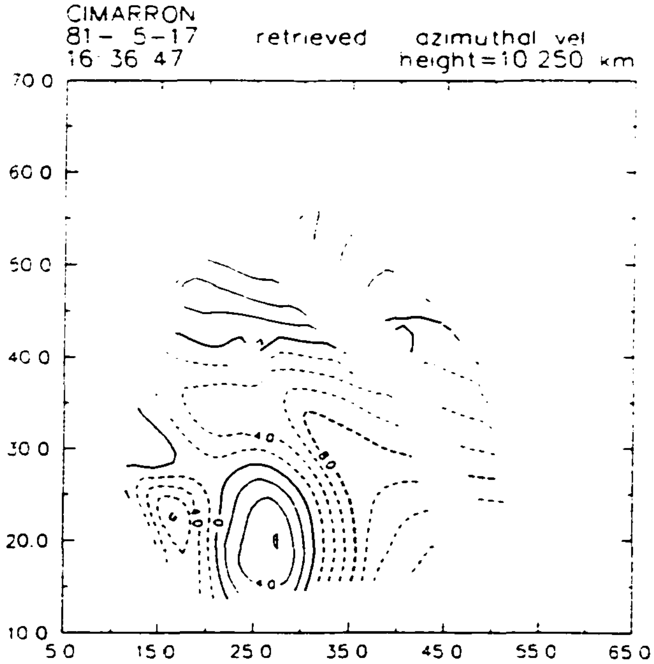

d)

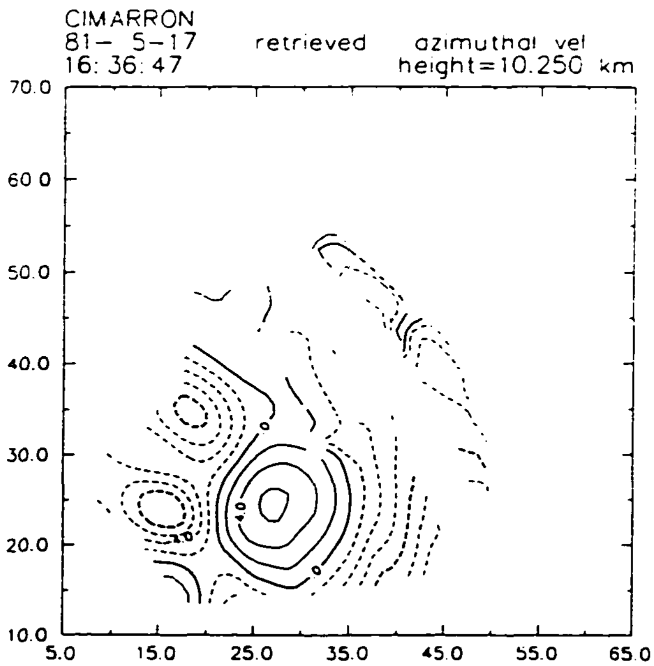

Figure 4.8 (Continued)

a)

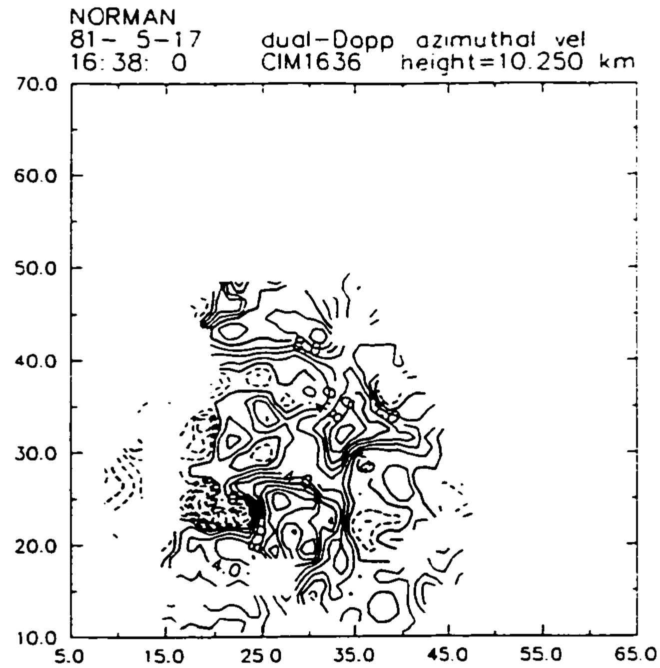

b)

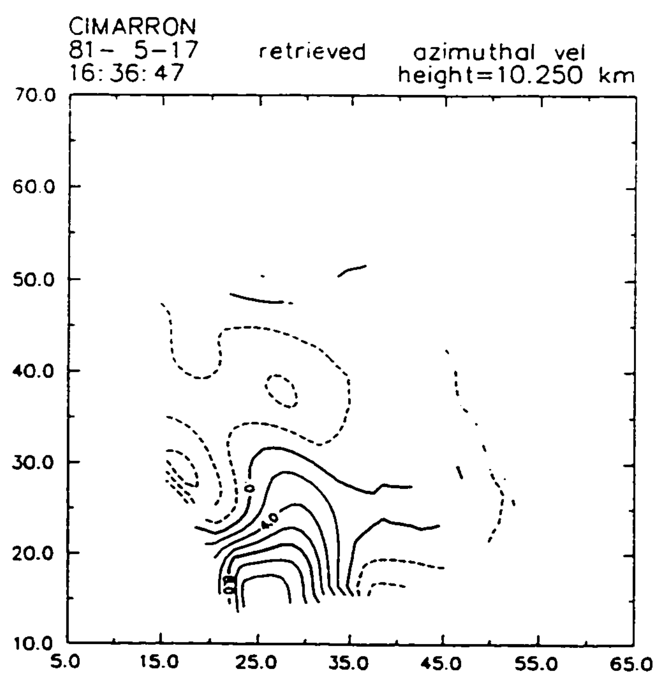

Figure 4.9 2239 UTC upper-level (z = 10.25 km) perturbation azimuthal velocity (measured from the Cimarron radar) for a) the dual-Doppler analysis and b) the mean wind reference frame. Contour interval, radar location, and grid distances are as in Fig. 4.5.

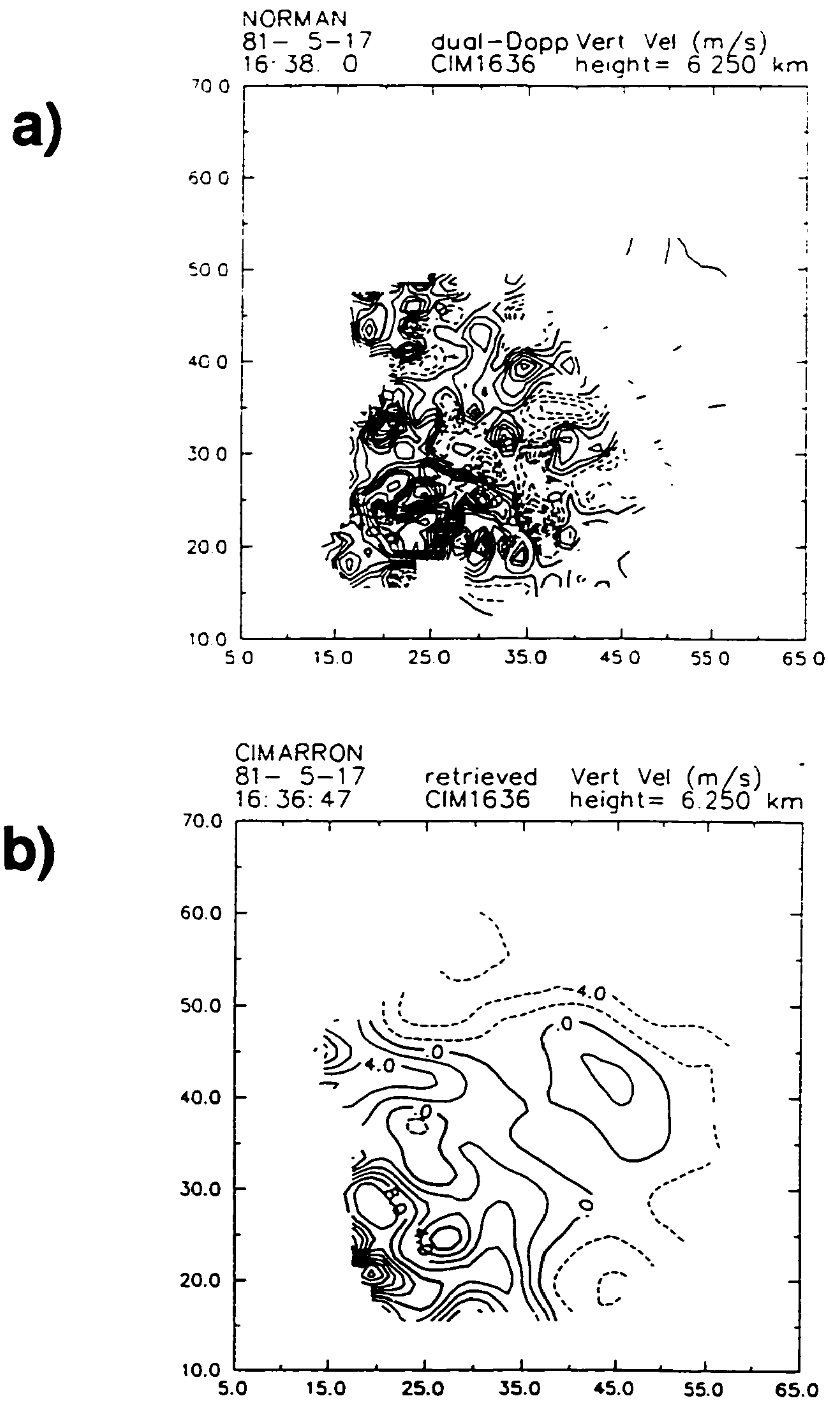

Figure 4.10 2239 UTC mid-level (z = 6.25 km) vertical velocity for a) the dual-Doppler analysis, b) the mean wind reference frame, c) the storm propagation reference frame and d) the fixed reference frame. Vertical velocity is contoured every 2 m s^{-1}. Radar location and grid distances are as in Fig. 4.4.

c)

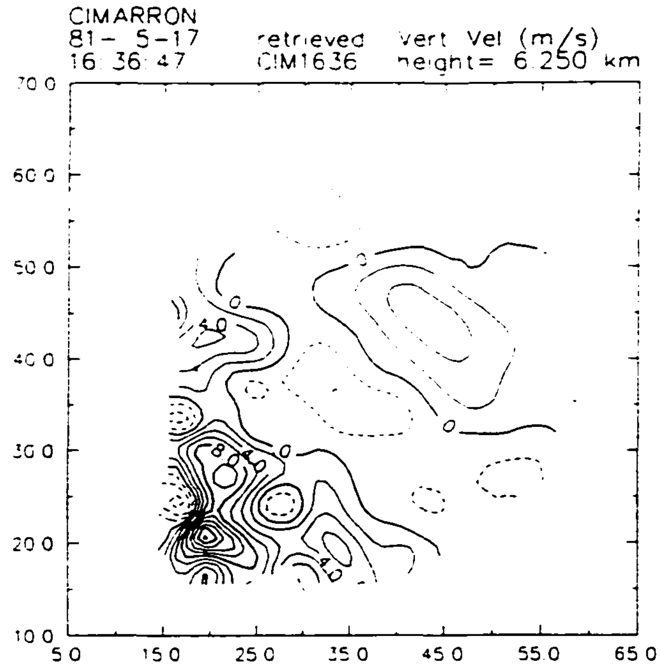

d)

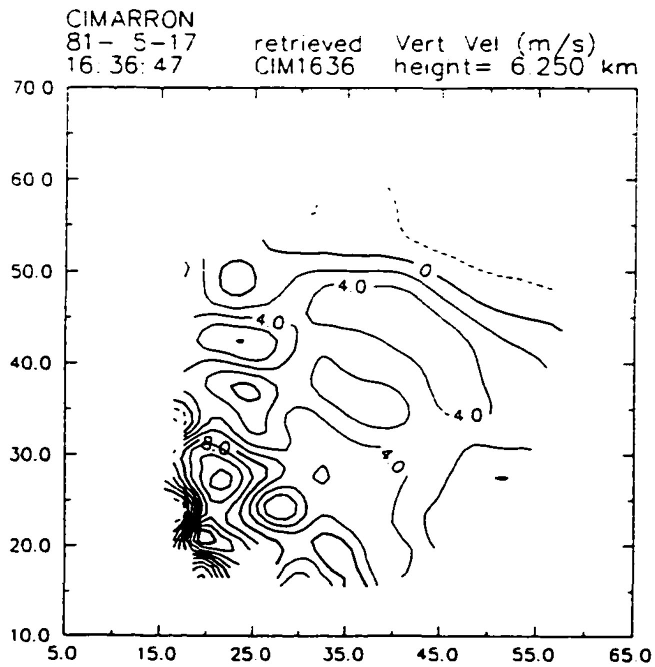

Figure 4.10 (Continued)

4.3 Analysis of the retrieved wind fields

In addition to confirming the superiority of the mean wind reference frame for this case, the fields presented in the previous section exhibit a number of intriguing features. First, although the spatial patterns of the retrieved vertical velocity fields match those of the corresponding dual-Doppler analysis quite well, the retrieved maximum values are significantly smaller in magnitude. Second, the skill scores for the SDVR are very good at low-levels of the storm (z = 2.25 km); however, qualitative examination of the retrieved perturbation azimuthal velocity suggests a preponderance of polar vorticity, $\frac{1}{r}\frac{\partial(r\,v_\phi)}{\partial r}$, compared to azimuthal divergence, $\frac{1}{r\cos\theta}\frac{\partial v_\phi}{\partial\phi}$. In contrast, the dual-Doppler analysis shows a significant convergent azimuthal velocity couplet associated with the low-level inflow into the storm updraft. Third, near the storm-top (z = 10.25 km) the SDVR skill scores are worse than at low-levels; however, a portion of the observed divergent azimuthal velocity couplet was successfully retrieved.

Noting that the vertical profile of horizontal divergence and vertical velocity are kinematically linked via mass conservation, a vertical velocity decomposition is performed in section 4.3.2 to help explain the results noted above. As a prelude to this exercise, the appropriate vorticity and divergence components are computed to confirm the qualitative assessments of the last section.

4.3.1 Vorticity and divergence calculations

The three-dimensional vorticity vector can be expressed in radar coordinates as:

$$\vec{\omega} = \hat{e}_r \frac{1}{r\cos\theta}\left[\frac{\partial(\cos\theta\, v_\phi)}{\partial\theta} - \frac{\partial v_\theta}{\partial\phi}\right]$$

$$+ \ \hat{e}_\phi \frac{1}{r}\left[\frac{\partial(r\,v_\theta)}{\partial r} - \frac{\partial v_r}{\partial \theta} \right]$$

$$+ \ \hat{e}_\theta \frac{1}{r}\left[\frac{1}{\cos\theta}\frac{\partial v_r}{\partial \phi} - \frac{\partial(r\,v_\phi)}{\partial r} \right] \quad . \tag{4.30}$$

At low levels, the polar ($\hat{e}_\theta$) component is approximately equal to the vertical vorticity component in the Cartesian expression ($\frac{\partial v}{\partial x} - \frac{\partial u}{\partial y}$). Within the polar component, the first term ($\frac{1}{r\cos\theta}\frac{\partial v_r}{\partial \phi}$) involves only the radial velocity field (which is *observed* by the radar), while the second term ($\frac{1}{r}\frac{\partial(r\,v_\phi)}{\partial r}$) involves only the azimuthal velocity field (which is *retrieved* by the SDVR).

The three-dimensional divergence in radar coordinates is given by:

$$\nabla \cdot \vec{v} = \frac{1}{r^2}\frac{\partial(r^2 v_r)}{\partial r} + \frac{1}{r\cos\theta}\frac{\partial v_\phi}{\partial \phi} + \frac{1}{r\cos\theta}\frac{\partial(\cos\theta\, v_\theta)}{\partial \theta} \quad . \tag{4.31}$$

At low levels, the first two terms are approximately equal to the Cartesian expression for horizontal divergence ($\frac{\partial u}{\partial x} + \frac{\partial v}{\partial y}$). The first term, $\frac{1}{r^2}\frac{\partial(r^2 v_r)}{\partial r}$, involves only the radial velocity field (which is *observed* by the radar), while the second term, $\frac{1}{r\cos\theta}\frac{\partial v_\phi}{\partial \phi}$, involves only the azimuthal velocity field (which is *retrieved* by the SDVR).

In contrast to the Cartesian formulation, however, for a constant horizontal wind the individual terms in the radar coordinate system are not all identically zero. Rather, cancellation between the terms (including the polar divergence) results in a net three-dimensional divergence of zero for a constant horizontal wind. Note that a similar cancellation occurs between the constant horizontal wind contributions to the radial and azimuthal portions of the polar vorticity.

This mean wind issue has important implications for the calculation of radial divergence from single-Doppler radar data. These implications are discussed in Appendix B, where it is shown that the radial and azimuthal divergence calculations, as well as the calculations for the radial contribution to the polar vorticity, should be performed using perturbation velocity fields, i.e., by subtracting the projection of the mean horizontal wind from the spherical components. The relationship between the total, mean and perturbation spherical velocities is given as:

$$v_r = \bar{v}_r + v_r' = \cos\theta \sin\phi\, U + \cos\theta \cos\phi\, V + v_r' \tag{4.32}$$

$$v_\phi = \bar{v}_\phi + v_\phi' = \cos\phi\, U - \sin\phi\, V + v_\phi' \tag{4.33}$$

$$v_\theta = \bar{v}_\theta + v_\theta' = -\sin\theta \sin\phi\, U - \sin\theta \cos\phi\, V + v_\theta' \tag{4.34}$$

Using (4.32) and (4.33), the qualitative assessment made in section 4.2, i.e., that the retrieved low-level perturbation azimuthal velocity is associated with polar vorticity rather then azimuthal convergence, can now be quantitatively verified. This is accomplished by calculating the perturbation azimuthal divergence,

$$\frac{1}{r\cos\theta}\frac{\partial v_\phi'}{\partial \phi} , \tag{4.35}$$

and the azimuthal contribution to the perturbation polar vorticity,

$$\frac{1}{r}\frac{\partial\left(r\,v_{\phi}^{'}\right)}{\partial r} \quad , \tag{4.36}$$

for both the retrieved and dual-Doppler fields. Because the dual-Doppler derived divergence and vorticity fields are extremely noisy, a 5-point smoother has been applied to them.

A comparison of the retrieved and dual-Doppler-derived perturbation azimuthal divergence (shown in Fig. 4.11) confirms that the SDVR obtains very little of the observed low-level azimuthal convergence. In fact, the retrieved field shows weak divergence in the southwest portion of the storm, whereas the dual-Doppler verification shows strong convergence associated with the low-level inflow into the main updraft. As will be shown, this is consistent with the substantially weaker retrieved updraft maximum compared with the dual-Doppler analysis.

In contrast, the retrieved azimuthal contribution to the polar vorticity field (Fig. 4.12b) matches its dual-Doppler counterpart reasonably well (Fig. 4.12a). In particular, the zero lines and positive maximum near x = 20, y = 30 match quite well. Taken in conjunction with Fig. 4.2, which shows this level to have nearly the best RMS scores, it is concluded that, at low-levels, the SDVR does well by accurately retrieving the azimuthal contribution to the polar vorticity, but retrieves little of the observed azimuthal convergence. Fig. 4.13 (the azimuthal divergence at z = 10.25 km) shows that, in contrast to low levels, the retrieval does capture a portion of the observed storm-top divergence. Examination of the azimuthal vorticity fields at 10.25 km (not shown) indicates that the SDVR obtains sufficient amplitude; however, the skill is fairly low.

a)

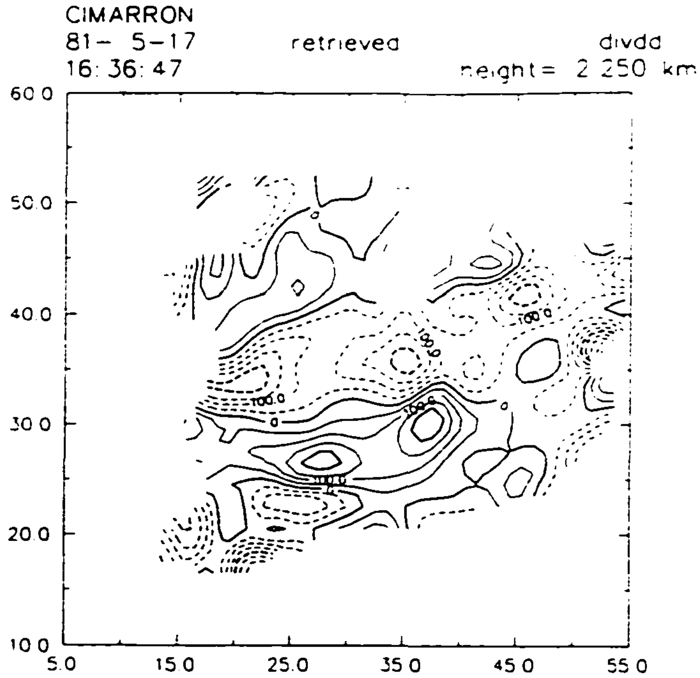

b)

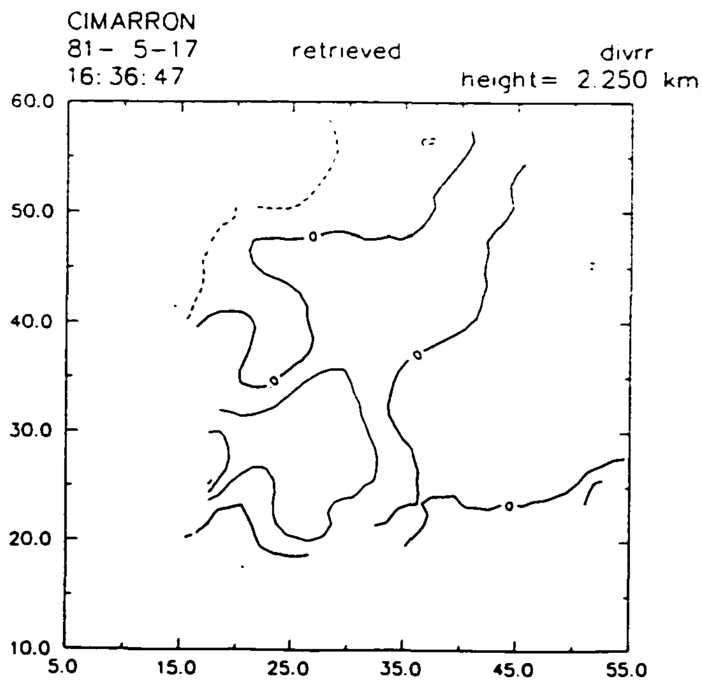

Figure 4.11 2239 UTC low-level (z = 2.25 km) perturbation azimuthal divergence (10^{-3} s^{-1}) for a) the dual-Doppler analysis and b) the mean wind reference frame. Divergence is contoured every 0.5 (10^{-3} s^{-1}). Radar location and grid distances are as in Fig. 4.4.

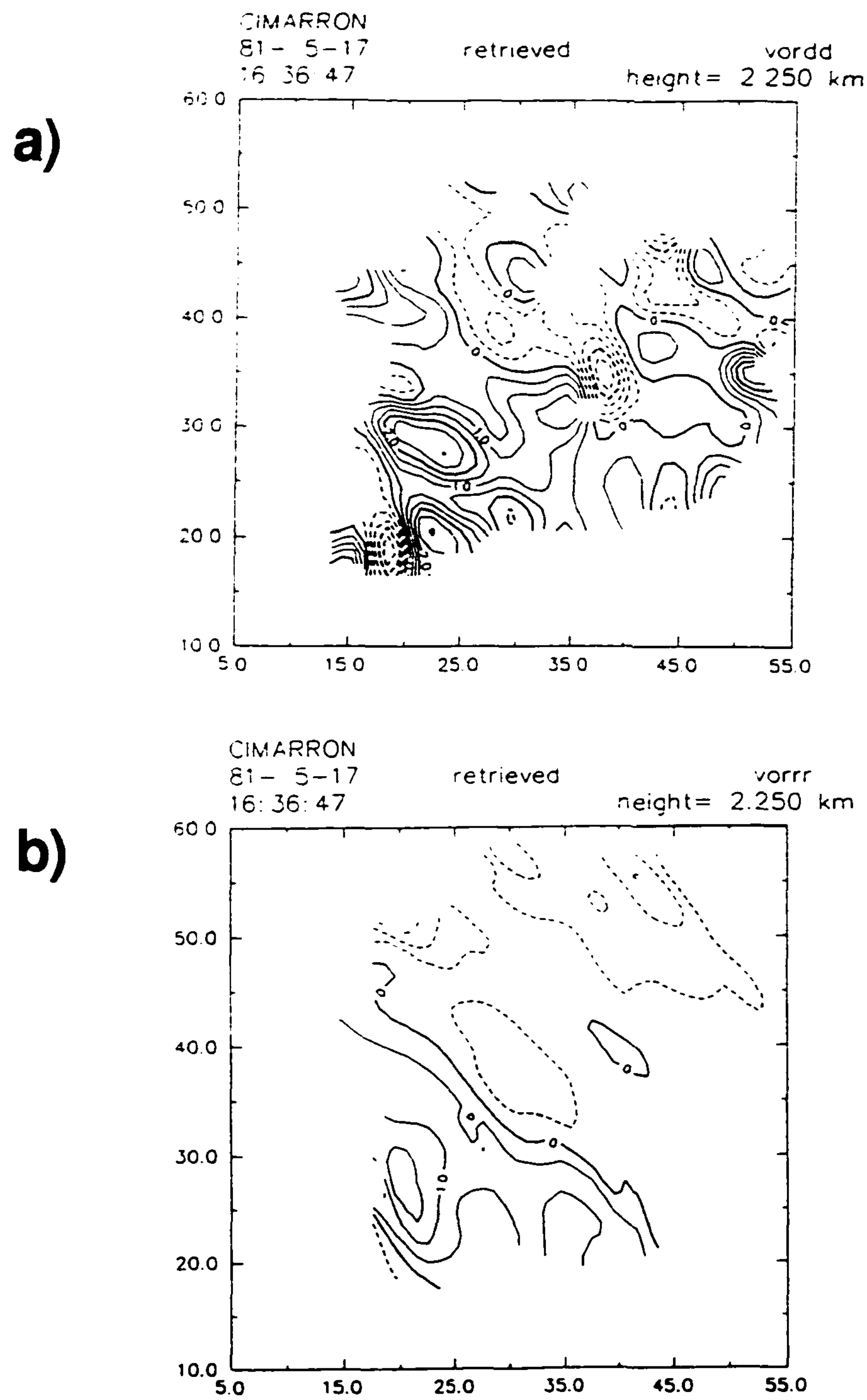

Figure 4.12 2239 UTC low-level (z = 2.25 km) perturbation azimuthal contribution to the polar vorticity (10^{-3} s^{-1}) for a) the dual-Doppler analysis and b) the mean wind reference frame. Vorticity is contoured every 0.5 (10^{-3} s^{-1}). Radar location and grid distances are as in Fig. 4.4.

a)

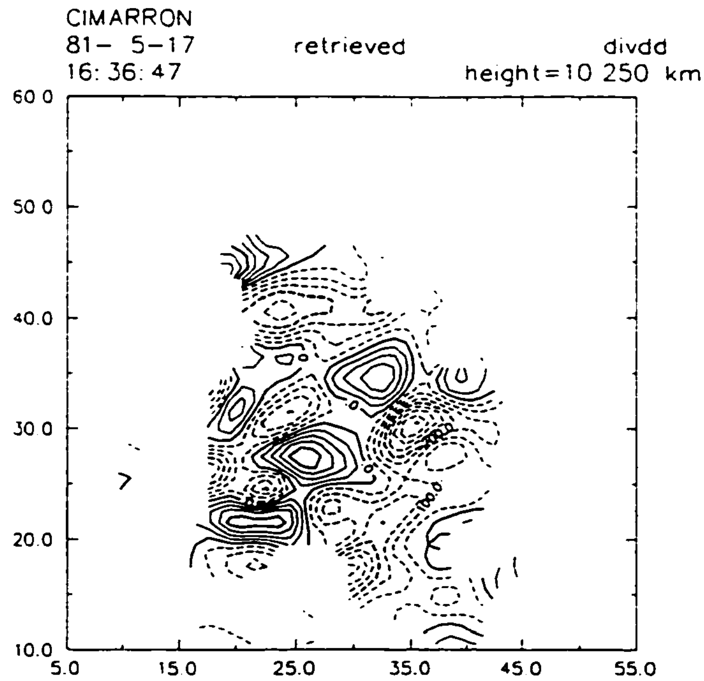

b)

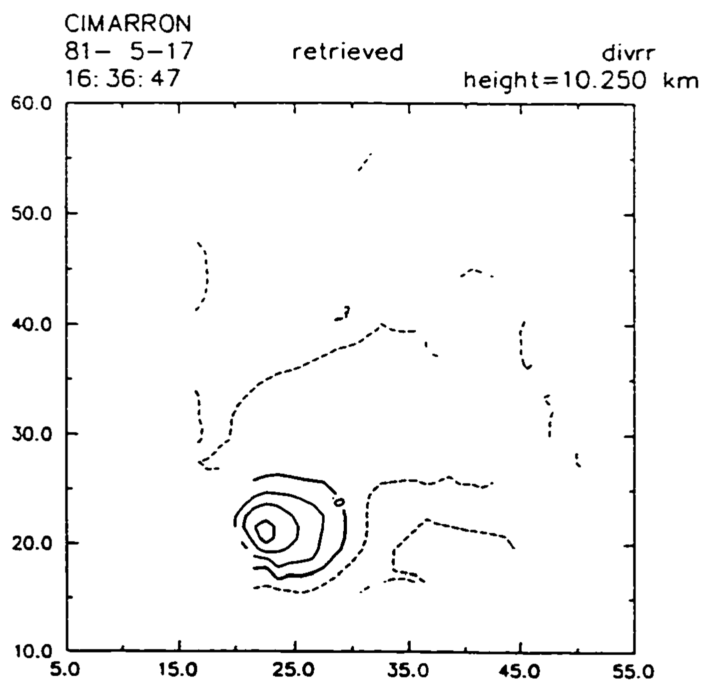

Figure 4.13 2239 UTC upper-level (z = 10.25 km) perturbation azimuthal divergence (10^{-3} s^{-1}) for a) the dual-Doppler analysis and b) the mean wind reference frame. Contour interval, radar location, and grid distances are as in Fig. 4.11.

4.3.2 Vertical velocity decomposition

Results from a vertical velocity decomposition are now presented to illustrate the impact of the retrieved azimuthal divergence on the retrieved updraft strength. Mass conservation in radar coordinates is expressed as:

$$\frac{1}{r^2}\frac{\partial\left(r^2 v_r\right)}{\partial r} + \frac{1}{r\cos\theta}\frac{\partial v_\phi}{\partial \phi} + \frac{1}{r\cos\theta}\frac{\partial\left(\cos\theta\, v_\theta\right)}{\partial\theta} = 0 \quad . \tag{4.37}$$

Integration of the r-ϕ divergence in the polar direction leads to:

$$v_\theta = \frac{\cos\theta_0}{\cos\theta} v_{\theta_0} - \frac{1}{r\cos\theta}\frac{\partial}{\partial r}\left[r^2\int_{\theta_0}^{\theta}\cos\Theta\, v_r\, d\Theta\right] - \frac{1}{\cos\theta}\frac{\partial}{\partial\phi}\left[\int_{\theta_0}^{\theta} v_\phi\, d\Theta\right] . \tag{4.38}$$

Defining a mean wind to be that used by the SDVR for the moving reference frame, the radial, azimuthal and polar velocity components (v_r, v_ϕ, v_θ) can be partitioned into mean and perturbation parts using (4.32) - (4.34). Substitution of the mean and perturbation parts into (4.38) and evaluation of the integrals involving the mean terms leads to (after some cancellation):

$$v_\theta = \frac{\cos\theta_0}{\cos\theta} v'_{\theta_0} - \frac{1}{r\cos\theta}\frac{\partial}{\partial r}\left[r^2\int_{\theta_0}^{\theta}\cos\Theta\, v'_r\, d\Theta\right] - \frac{1}{\cos\theta}\frac{\partial}{\partial\phi}\left[\int_{\theta_0}^{\theta} v'_\phi\, d\Theta\right]$$

$$- \sin\theta\left[\sin\phi\,\overline{U} + \cos\phi\,\overline{V}\right] \quad . \tag{4.39}$$

The Cartesian vertical velocity can be expressed in terms of the radial and polar velocity components as:

$$w = \sin\theta \, v_r + \cos\theta \, v_\theta \, . \tag{4.40}$$

Substitution of (4.32) and (4.39) into (4.40) leads to an expression for the Cartesian vertical velocity in terms of spherical components.

$$w(\theta) = \sin\theta \, v_r' + \cos\theta_0 \, v_{\theta_0}' - \frac{1}{r}\frac{\partial}{\partial r}\left[r^2 \int_{\theta_0}^{\theta} \cos\Theta \, v_r' \, d\Theta \right] - \frac{\partial}{\partial \phi}\left[\int_{\theta_0}^{\theta} v_\phi' \, d\Theta \right] \, . \tag{4.41}$$

Equation (4.41) is analogous to the Cartesian expression for vertical velocity in terms of the vertical integral of the horizontal divergence:

$$w(z) = w_{z_0} - \frac{\partial}{\partial x}\left[\int_{z_0}^{z} u \, dz' \right] - \frac{\partial}{\partial y}\left[\int_{z_0}^{z} v \, dz' \right] , \tag{4.42}$$

and is especially relevant to the present SDVR algorithm because it relates the Cartesian vertical velocity to terms involving the observed radial velocity and retrieved cross-beam velocity. The last two terms in (4.41) are the contribution from the radial divergence (which can be calculated from the *observed* radial velocity) and the azimuthal divergence (which can be calculated from the *retrieved* azimuthal velocity). It is important to note that these terms involve the *perturbation* radial and azimuthal velocities. As discussed earlier, perturbation velocities are used in (4.41) because the contributions from the divergence of the individual mean wind components are not all zero for the radar coordinate system. Additional details concerning this can be found in Appendix B.

The second term on the RHS of (4.41) is the lower boundary condition for the polar divergence integral and is analogous to the lower boundary condition on w in the Cartesian vertical velocity expression. One of the advantages of the two-scalar retrieval algorithm is that it implicitly obtains this term at the lowest data level. This level is usually above the ground, leading to difficulties applying the impermeability conditions for retrieval schemes that do not obtain this term. The first term on the RHS of (4.41) is the vertical projection of the perturbation radial velocity and is usually small.

The contribution of each of these terms toward the total retrieved vertical velocity is now examined. The decomposition can be computed at any level by integrating upward along an arc of constant range and azimuth. Fortunately, the main updraft in the Arcadia storm is large in horizontal extent, allowing a profile arc to be found that lies almost entirely within the storm updraft. Fig. 4.14 shows the profiles of the retrieved vertical velocity and the various terms in the decomposition. The most striking result is that retrieved vertical velocity is produced almost entirely by the observed convergence of the radial velocity. Consistent with Fig. 4.11, which showed that the retrieval obtains weak azimuthal divergence at low-levels, the contribution to the retrieved vertical velocity from the azimuthal divergence term is actually slightly negative at low-levels. The retrieved storm top divergence seen in Fig. 4.12 is apparent in the azimuthal divergence term and helps to sharpen the vertical velocity decrease with height above the level of maximum updraft. Lastly, note that the retrieval obtains a reasonable value of about 3 m s^{-1} for the lower boundary condition term.

4.3.3 A simplified wind retrieval

The results from the wind decomposition suggest that it may be enlightening to compare the fields obtained from the full-SDVR with fields obtained from a simplified single-Doppler retrieval. In this simplified retrieval, terms that can be obtained directly from the observed radial velocity are retained, while terms that require solution of the Poisson equation for Q [Eq. (2.13)] are omitted. The various terms can be more explicitly

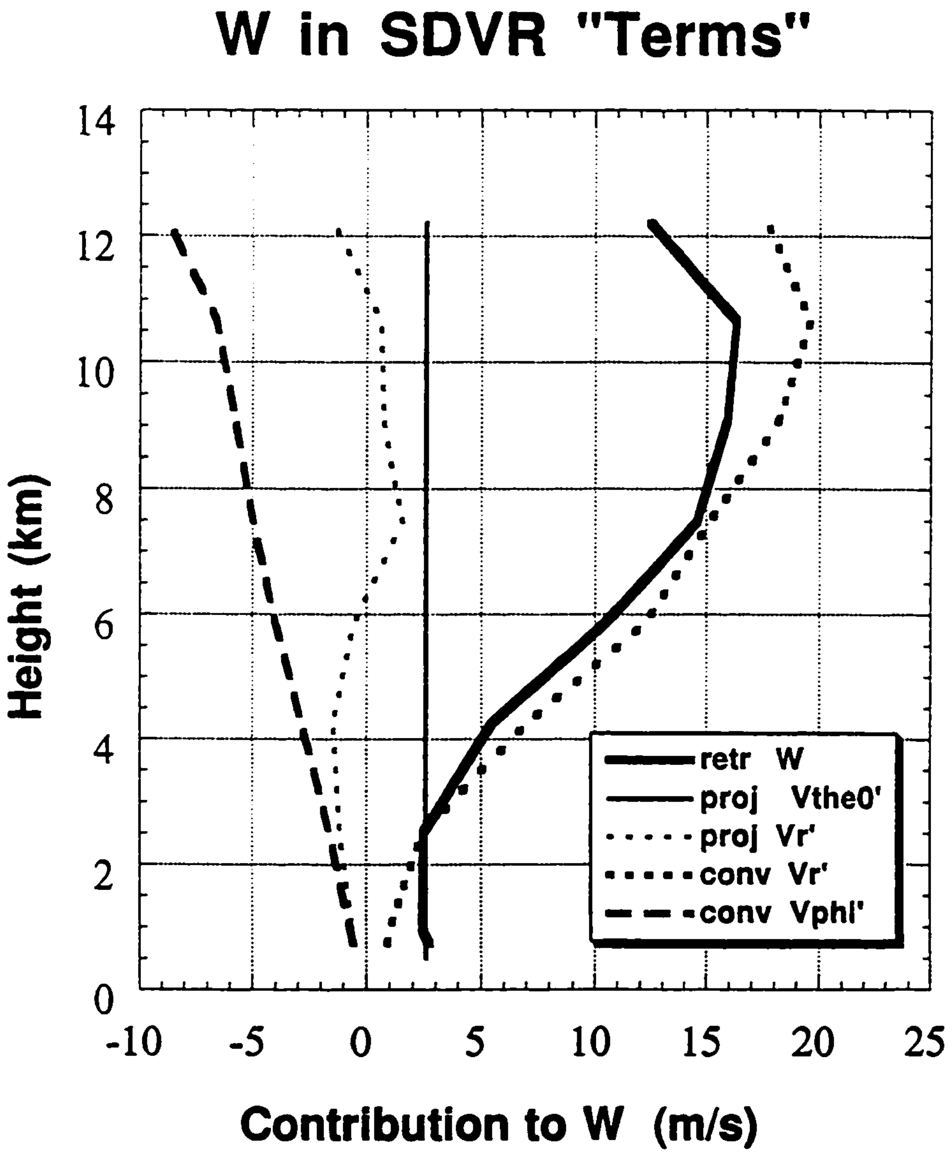

Figure 4.14 Vertical profile of the contributions to the Cartesian vertical velocity ($m\ s^{-1}$) from the various terms in the single-Doppler retrieval.

written by recognizing that application of the SDVR in a mean wind moving reference frame is equivalent to defining a perturbation pseudo-stream function. Thus, equations (2.4) and (2.5) become:

$$v_\phi' = \frac{\partial Q'}{\partial \theta} , \tag{4.43}$$

$$v_\theta' = -\frac{1}{\cos\theta}\frac{\partial Q'}{\partial \phi} - \frac{1}{r\cos\theta}\frac{\partial}{\partial r}\left(r^2 \int_{\theta_0}^{\theta} \cos\Theta \, v_r' d\Theta \right) . \tag{4.44}$$

Substitution of these expressions into (4.33), (4.34) results in a very useful decomposition of the unobserved spherical components:

$$v_\phi = \bar{v}_\phi + v_\phi' = \cos\phi \, U - \sin\phi \, V + \frac{\partial Q'}{\partial \theta} \tag{4.45}$$

$$v_\theta = \bar{v}_\theta + v_\theta' = - \sin\theta \sin\phi \, U - \sin\theta \cos\phi \, V$$

$$- \frac{1}{r\cos\theta}\frac{\partial}{\partial r}\left(r^2 \int_{\theta_0}^{\theta} \cos\Theta \, v_r' d\Theta \right) - \frac{1}{\cos\theta}\frac{\partial Q'}{\partial \phi} . \tag{4.46}$$

Thus, by using the radial velocity to obtain the horizontal mean wind components [via (2.39)] and a portion of the perturbation polar velocity (via mass conservation), the simple retrieval obtains all but the final term in each of (4.45) and (4.46). Note that the perturbation radial divergence [the integral appearing in (4.46)] could be used to obtain a portion of the azimuthal velocity instead of the polar velocity. Furthermore, it is important to recognize that while the results of the simple retrieval depend on the direction in which we chose to integrate the radial divergence, the results from the two-scalar retrieval are independent of this choice.

The resultant fields from this simplified retrieval are shown in Fig. 4.15. Comparison of the storm-relative low-level horizontal vectors (Fig. 4.15a) with the corresponding SDVR field (Fig. 4.4b) indicates that the simple retrieval fails to capture the southeasterly storm-relative winds ahead of the mesocyclone. This is confirmed in the retrieved azimuthal velocity (Fig. 4.15b), which is merely the projection of the mean horizontal wind in the azimuthal direction. Note that the non-zero azimuthal divergence can clearly be seen in this plot. The upper-level storm-relative vectors are shown in Fig. 4.15c and the mid-level vertical velocity is shown in Fig. 4.15d. As expected, the retrieved vertical velocity field is very similar to that shown for the other experiments (Fig. 4.10b-d).

4.4 Summary of wind retrieval results

The results presented in this chapter show that, at low-levels, the perturbation azimuthal velocity is retrieved with a high degree of accuracy, but is associated primarily with polar vorticity, rather than azimuthal convergence. The failure of the retrieval to obtain the latter at low-levels results in a significant under-retrieval of the observed updraft strength. While the spatial pattern of the retrieved vertical velocity field matches the dual-Doppler verification, it is due almost entirely to the convergence of observed radial velocity. A simplified retrieval that utilizes only the observed radial velocity and information that can be obtained directly from it (mean horizontal wind and radial convergence) is found to produce retrieved fields that are surprisingly similar to the those of the full-SDVR.

In Chapters 5 and 6, the thermodynamic retrieval results and model prediction results will be compared for three sets of 3-D wind fields, including those obtained from the dual-

a)

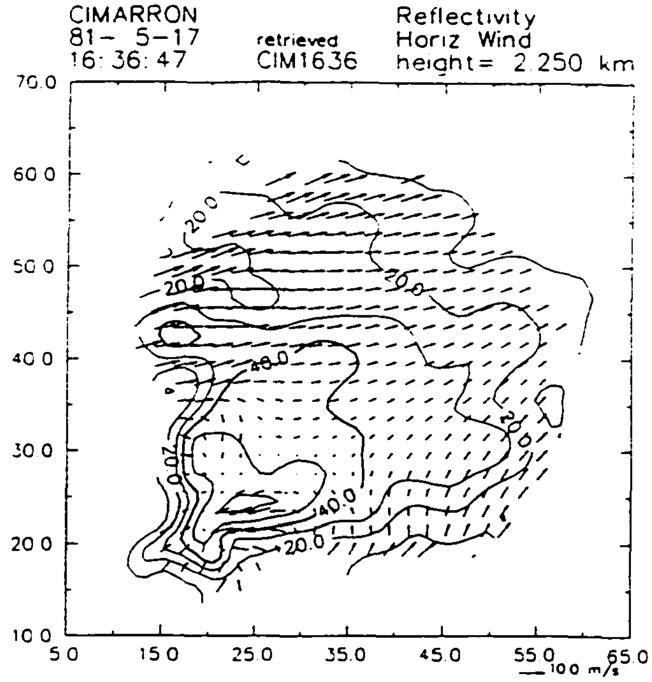

b)

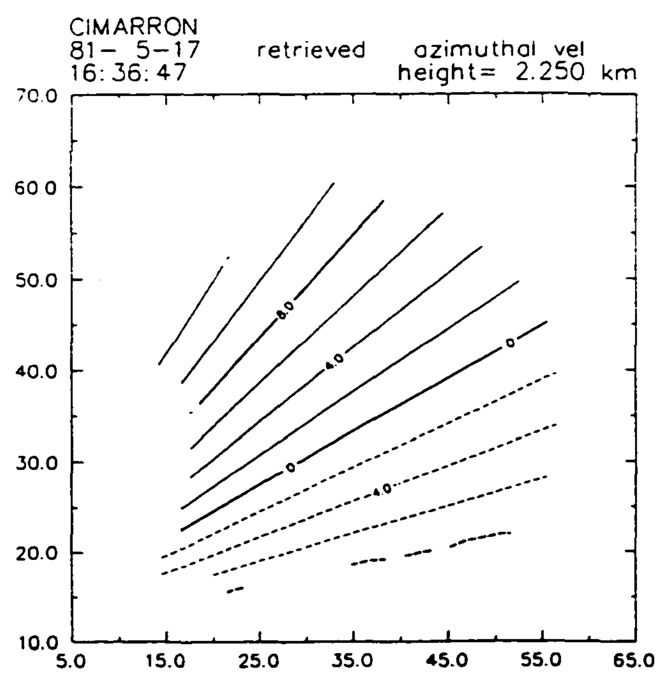

Figure 4.15 2239 UTC retrieved fields from the simple velocity retrieval (UVVR). Low-level (z = 2.25 km) a) reflectivity and storm-relative horizontal vectors and b) azimuthal velocity (measured from the Cimarron radar), c) upper-level (z = 10.25 km) reflectivity and storm-relative horizontal vectors, and d) mid-level (z = 6.25 km) vertical velocity. Reflectivity is contoured every 10 dBZ and azimuthal and vertical velocity are contoured every 2 m s^{-1}. Radar location and grid distances are as in Fig. 4.4.

c)

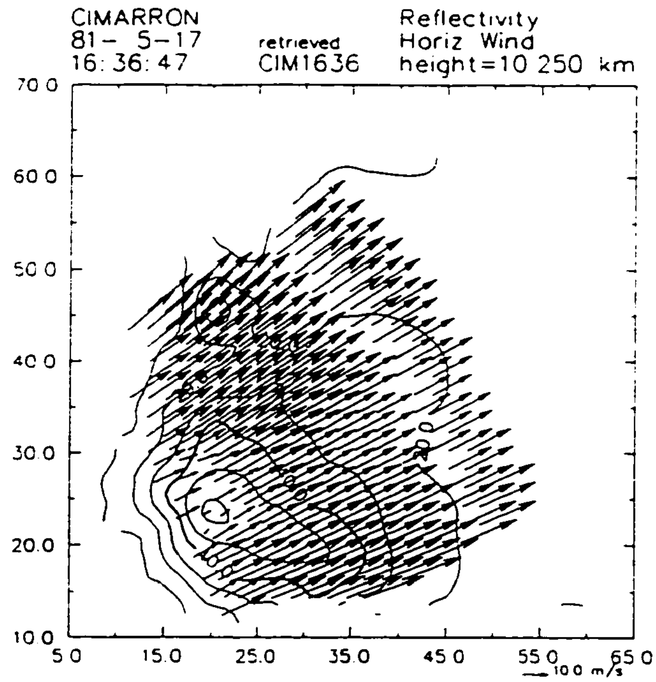

d)

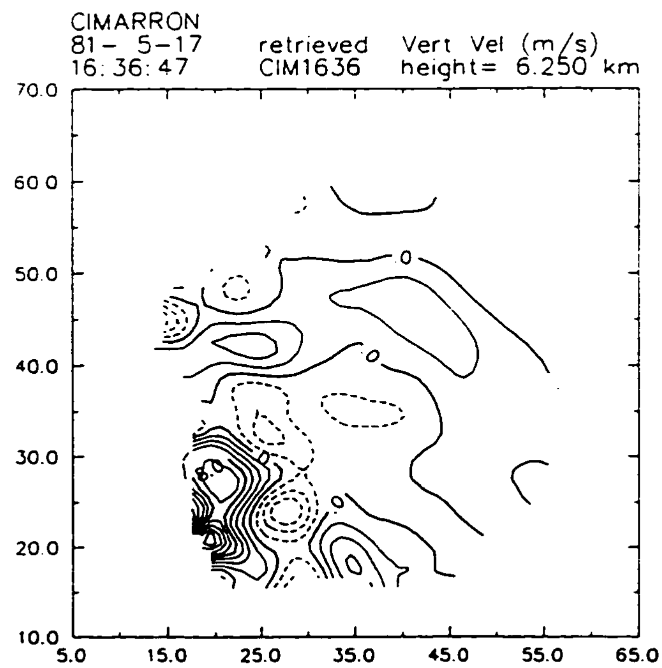

Figure 4.15 (Continued)

Doppler analysis (denoted DDOP), from the full single-Doppler velocity retrieval (denoted SDVR), and from the simplified retrieval (denoted UVVR). A principal focus will be to evaluate the impact on the thermodynamic retrieval and model prediction of the differences among these three sets of wind fields.

CHAPTER 5

THERMODYNAMIC RETRIEVAL RESULTS

In this chapter, results are presented from the application of a Gal-Chen (1978) type thermodynamic retrieval to both the dual-Doppler derived (DDOP) and single-Doppler retrieved (SDVR) vector wind fields. Also presented are results from a thermodynamic retrieval applied to the wind vectors from the simplified wind retrieval (UVVR) that omits the contribution from the pseudo-streamfunction. These experiments are summarized in Table 5.1. By comparing the retrieved thermodynamic fields from these experiments, we can evaluate the impact of the wind field differences between the DDOP, SDVR and UVVR retrievals.

Prior to performing the thermodynamic retrieval, the vector wind field within the storm is blended with an environmental profile using the procedure described in Section 2.2. Results from this velocity hole-filling and adjustment procedure are shown in Section 5.1. In Section 5.2, the retrieved pressure and temperature fields for all three cases are shown. An analysis of the contribution to the retrieved perturbation temperature from the various terms in the vertical momentum equation is presented in Section 5.3. Based on this analysis, comparisons between these retrieved fields and the predictions from simple linear theory are made. Finally, the specified water vapor field is shown in Section 5.4, and a brief summary of the thermodynamic retrieval results is presented in Section 5.5.

Table 5.1 Wind field datasets used for the thermodynamic retrieval experiments.

Name	Description
DDOP	**Dual-Doppler analyzed 3-D wind fields (DB97)**
SDVR	**Single-Doppler retrieved 3-D wind fields from CIM radar**
UVVR	**Simplified 3-D retrieved winds from CIM radial velocity** (mean horizontal winds, perturbation radial velocity, contribution to polar velocity from perturbation radial divergence)

5.1 Velocity blending and adjustment

As described in detail in Chapter 2, the steps in the wind blending and adjustment procedure are as follows:

1) On the spherical wind retrieval grid, convert the retrieved v_r, v_φ, v_θ to Cartesian components u, v, w
2) Tri-linearly interpolate the retrieved Cartesian components and the observed radial velocity to the Cartesian ARPS model grid.
3) Solve 2-D horizontal Laplace equations to blend the retrieved u and v and the observed v_r with the background sounding winds, thereby obtaining u^m, v^m, $v_r{}^o$. Assume vertical velocity is zero outside the storm volume to get w^m. Calculate $v_r{}^m$ from u^m, v^m, and w^m.
4) Iteratively solve (2.53) and (2.54) to get λ_1 and λ_2 from u^m, v^m, w^m, $v_r{}^m$ and $v_r{}^o$.
5) Solve the Euler-Lagrange equations (2.50)-(2.52) for the adjusted velocities u^a, v^a, w^a.

In hole-filling the radial velocity field, v_r is first decomposed into Cartesian "pseudo-components" $v_r^u = \cos\theta \sin\phi \, v_r$ and $v_r^v = \cos\theta \cos\phi \, v_r$. As illustrated by Lazarus (1996), directly hole-filling the radial velocity will lead to an erroneous divergence centered about a vertical axis through the radar origin. The nature of the problem can be seen by noting that the hole-filler simply provides a smoothly varying *scalar* field without regard to the radar origin. This is problematic for the radial component, because the radial unit vector, $\hat{e}_r$, changes direction by 180° across the radar origin. In contrast, the Cartesian unit vectors have a constant direction throughout the entire domain.

Figs. 5.1a - 5.3a show the z = 2.25 km hole-filled perturbation (departure from mean sounding wind) vector wind fields for the DDOP, SDVR and UVVR wind fields. Consistent with the Dirichlet mean wind lateral boundary conditions, all the vector wind fields approach zero at the domain edge. Along the storm-edge boundary, the wind vectors transition smoothly from the radar-derived values within the storm to the hole-filled values outside the storm. Within the hole-filled region, the winds show a gradual trend toward the boundary values. The most significant difference among the three experiments is the region of strong west-northwesterly winds near the small northern storm in the SDVR and UVVR cases. This difference is due to the fact that the DDOP dataset (analyzed independently by DB97) retained no wind information from this storm. The SDVR case in particular illustrates that the 2-D hole-filler can spread the influence of an isolated area of large amplitude perturbation velocities a great distance. Examination of the perturbation u-component (shown in Figs. 5.1b - 5.3b) confirms the smooth transition from the storm edge values to zero along the domain edge. With the exception of decreased velocity amplitudes in both the main and northern storm, the simplified retrieval (UVVR) looks quite similar to the full SDVR.

A vertical cross-section through the updraft/mesocyclone of the storm (x = 19.5 km, as indicated by the N-S line in Figs. 5.1a-5.3a) is shown in Fig. 5.4 and indicates an even greater similarity between the SDVR and UVVR methods. This is not surprising, however, because, as shown in Chapter 4, almost all of the SDVR vertical velocity comes from the integral of the radial convergence term, which is retained in the UVVR experiment.

Comparison of the vertical cross-sections from the two single-Doppler experiments with the DDOP cross-section indicates two significant differences. First, despite the good qualitative agreement among the retrievals, the DDOP updraft is significantly stronger than its single-Doppler counterparts. Second, both single-Doppler cases show a very sharp,

a)

b)

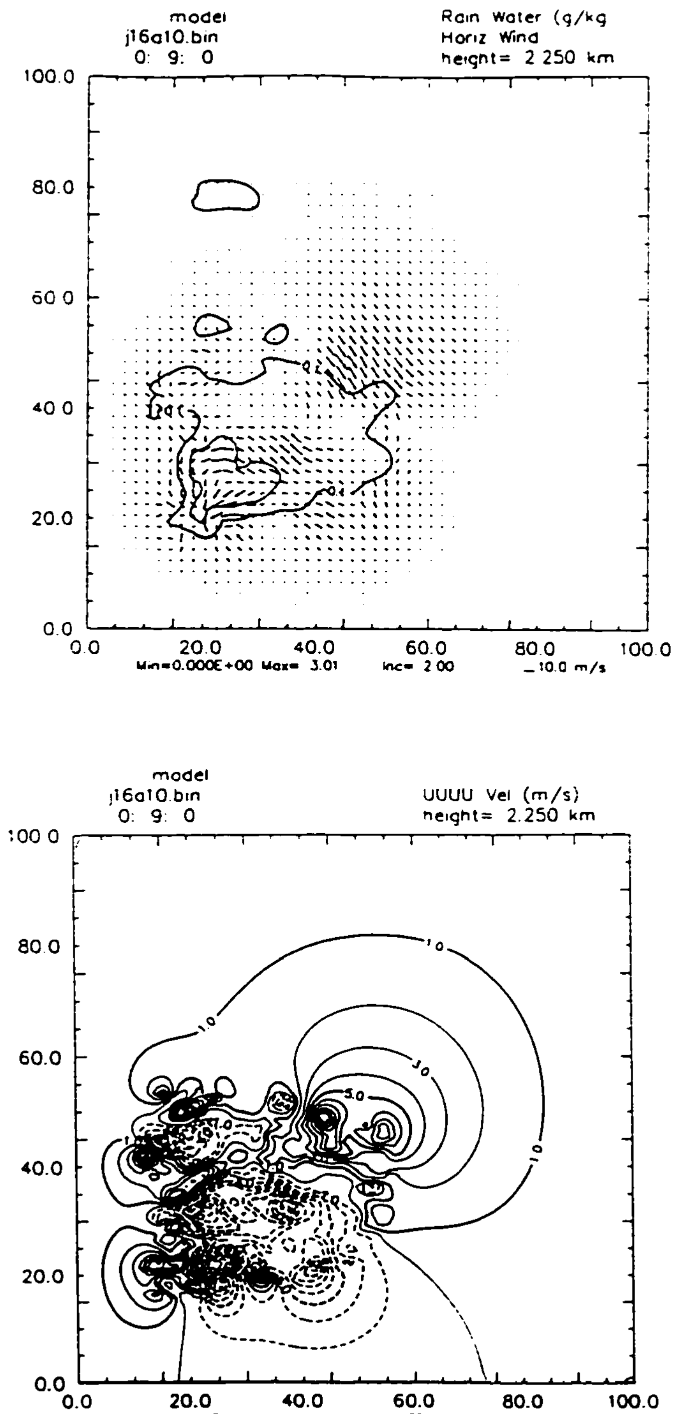

Figure 5.1 2239 UTC low-level (z = 2.25 km) perturbation (from the base-state sounding) winds for the DDOP case. a) Rainwater and horizontal vectors and b) u-component of the wind. Rainwater is contoured every 2 g kg^{-1} and the u-component is contoured every 1 m s^{-1}. Radar location and grid distances are as in Fig. 4.4.

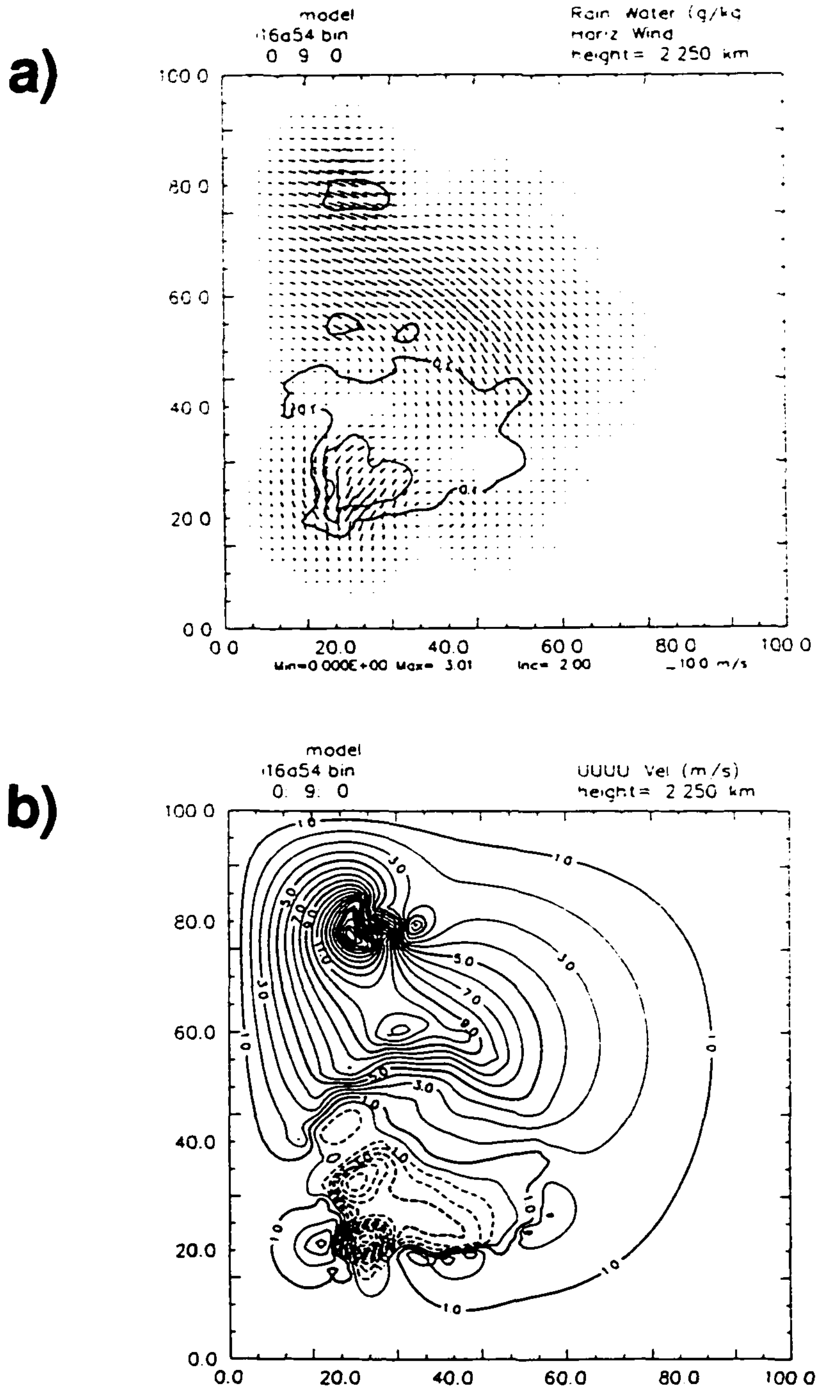

Figure 5.2 2239 UTC low-level (z = 2.25 km) perturbation (from the base-state sounding) winds for the SDVR case. a) Rainwater and horizontal vectors and b) u-component of the wind. Contour intervals, radar location, and grid distances are as in Fig. 5.1.

a)

b)

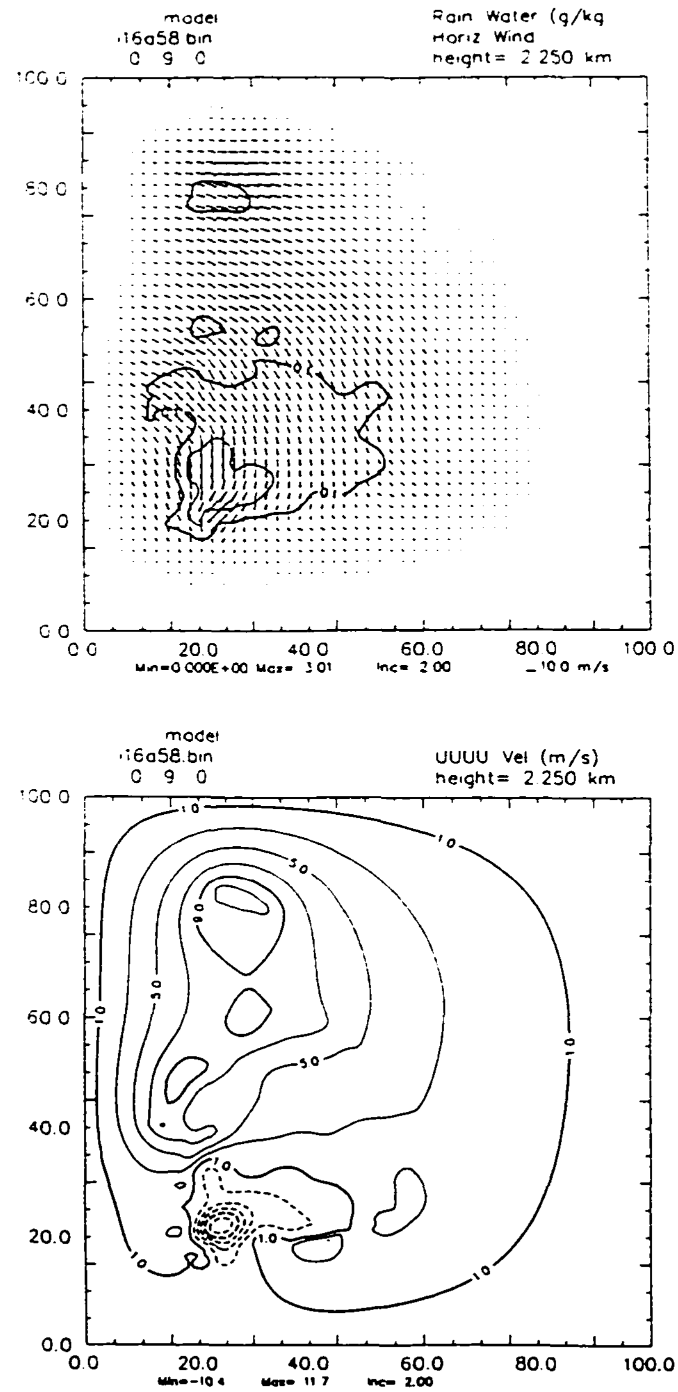

Figure 5.3 2239 UTC low-level (z = 2.25 km) perturbation (from the base-state sounding) winds for the UVVR case. a) Rainwater and horizontal vectors and b) u-component of the wind. Contour intervals, radar location, and grid distances are as in Fig. 5.1.

a)

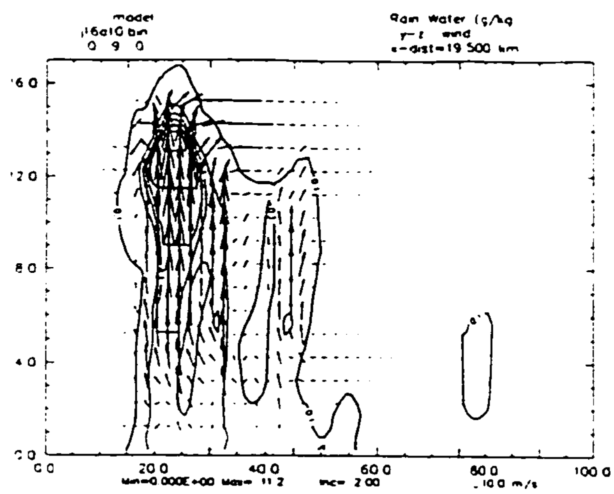

b)

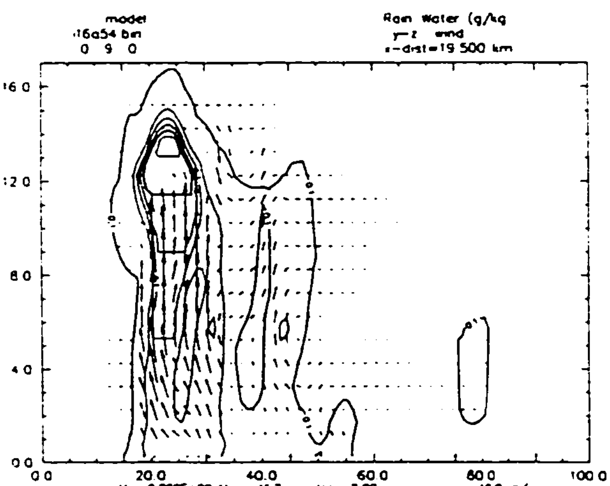

c)

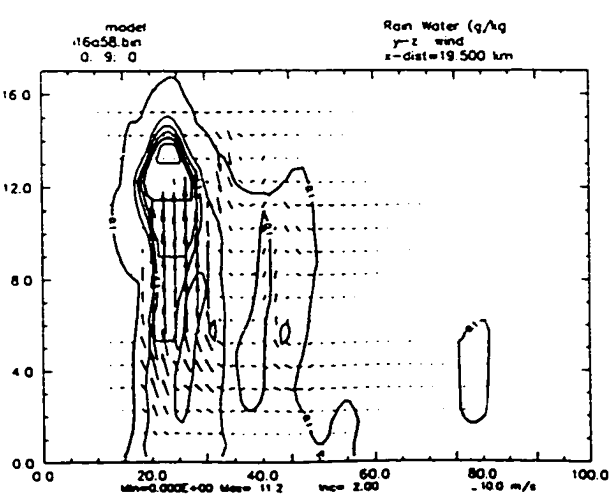

Figure 5.4 2239 UTC N-S cross-section (x = 19.5) of the perturbation (from the base-state sounding) winds and rainwater for the a) DDOP, b) SDVR and c) UVVR cases. Rainwater is contoured every 2 g kg^{-1}. Radar location and grid distances are as in Fig. 5.1.

sloping top edge to the storm updraft. This is due to a loss of data caused by the use of the mean wind moving reference frame. While the storm propagation moving reference frame retrieval (shown in Chapter 4) resulted in a nearly perfect overlap of the three successive volume scans of reflectivity, the mean wind moving reference frame (which exceeds the storm propagation speed) "over shifts" the three time-levels of data. Despite the resultant loss of data coverage, this experiment yielded the best results, as shown in Chapter 4. It is important to keep Fig. 5.4 in mind as the impact of the variational velocity adjustment on this storm-top vertical velocity pattern will be examined later in this section.

Once the 2-D Laplace solver has been applied at each level to obtain horizontal wind fields throughout the domain and the vertical velocity has been set to zero outside the storm volume, the wind fields are ready for the variational velocity adjustment. As described in Chapter 2, this procedure iteratively solves a system of equations to obtain a wind field that satisfies mass conservation, projects accurately onto the observed radial velocity field, and minimizes departures from the retrieved wind components. Because there are two equally valid radial velocity fields for the DDOP dataset, application of this procedure to the DDOP wind fields is problematic. I chose to use the radial velocity from the Cimarron radar. A more suitable approach would be to use the adjustment procedure described by Ray et al. (1981) and used by Lin et al. (1993). As noted in Chapter 2, a new variational velocity adjustment that can be used for both the single- and dual-Doppler problem is derived in Appendix A.

Solution convergence for the iterated Laplace solver is determined via a gridlength dependent iteration threshold for λ_2:

$$\text{tol} = \text{veltol} * \bar{\rho} * \sqrt{\Delta x^2 + \Delta y^2 + \Delta z^2} \quad , \tag{5.1}$$

where veltol is a user specified maximum error velocity. For these experiments ($\Delta x = \Delta y = 1000$ m, $\Delta z = 500$ m), the radical is equal to 1500 m, and veltol is set equal to 0.03 m s^{-1}, yielding a λ_2 tolerance of 45 kg m^{-1} s^{-1}. Equations (2.53) and (2.54) are then iteratively solved using underrelaxation techniques (relaxation coefficient = 0.25) until the domain maximum λ_2 residual is less than tol.

The convergence rate for the SDVR and DDOP experiments (for the central time) are shown in Fig. 5.5. Results for the first and third times (not shown) were slightly faster, while the UVVR experiment converged in around 200 iterations for all three times (also not shown). For both the DDOP and SDVR experiments, λ_2 residuals decrease very rapidly for the first 50-75 iterations, then decrease only very slowly after that. Both reached the convergence criterion in just under 450 iterations, and, as shown in Figs. 5.6 and 5.7, resulted in about a decadal decrease in the 3-D anelastic divergence.

This similarity in performance for the DDOP and SDVR datasets is somewhat surprising, considering the marked differences in the nature of the initial divergence fields. As shown in Fig. 5.8, anelastic mass conservation is clearly violated by the DDOP winds at z = 2.25 km. This is apparently due to the O'Brien correction in the dual-Doppler analysis performed by DB97. In contrast, the two-scalar SDVR imposes 3-D non-divergence as a weak constraint, leading to much smaller anelastic divergences [maximum of $5(10)^{-2}$] within the storm volume. For the SDVR fields, the only region of significant departure from anelastic mass conservation is at the interface between the retrieved and hole-filled velocities. It should be noted that this area of imbalance also exists within the DDOP fields, but is less obvious due to the presence of significant imbalances throughout the storm volume.

Fig. 5.9 shows that, consistent with Figs. 5.6 and 5.7, the z = 2.25 km maximum divergence magnitudes are reduced by nearly an order of magnitude. Interestingly, for the DDOP case, the extrema are aligned along arcs of constant range from the Cimarron radar.

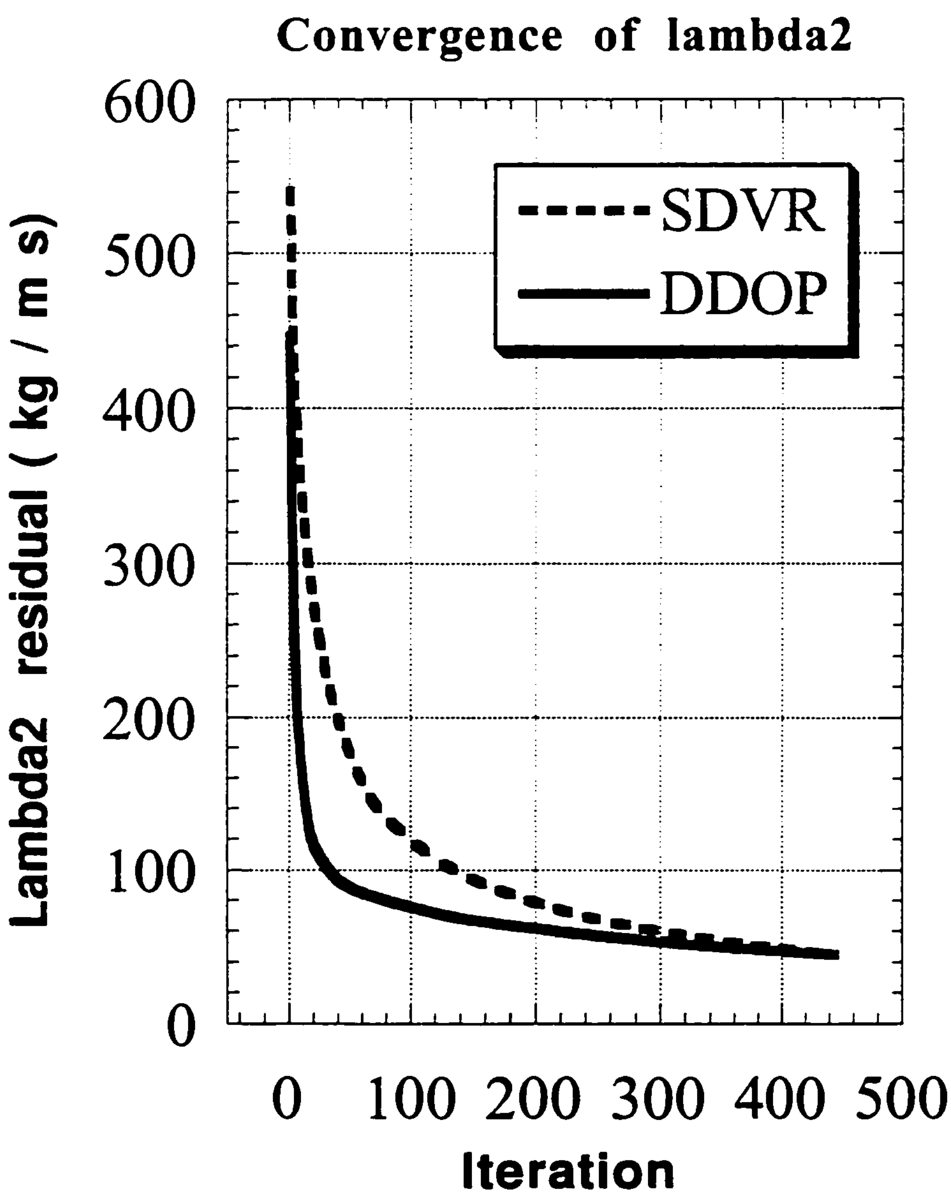

Figure 5.5 Convergence rate of λ_2 in the variational velocity adjustment for a) the DDOP case and b) the SDVR case. Plotted is the domain maximum residual for each iteration.

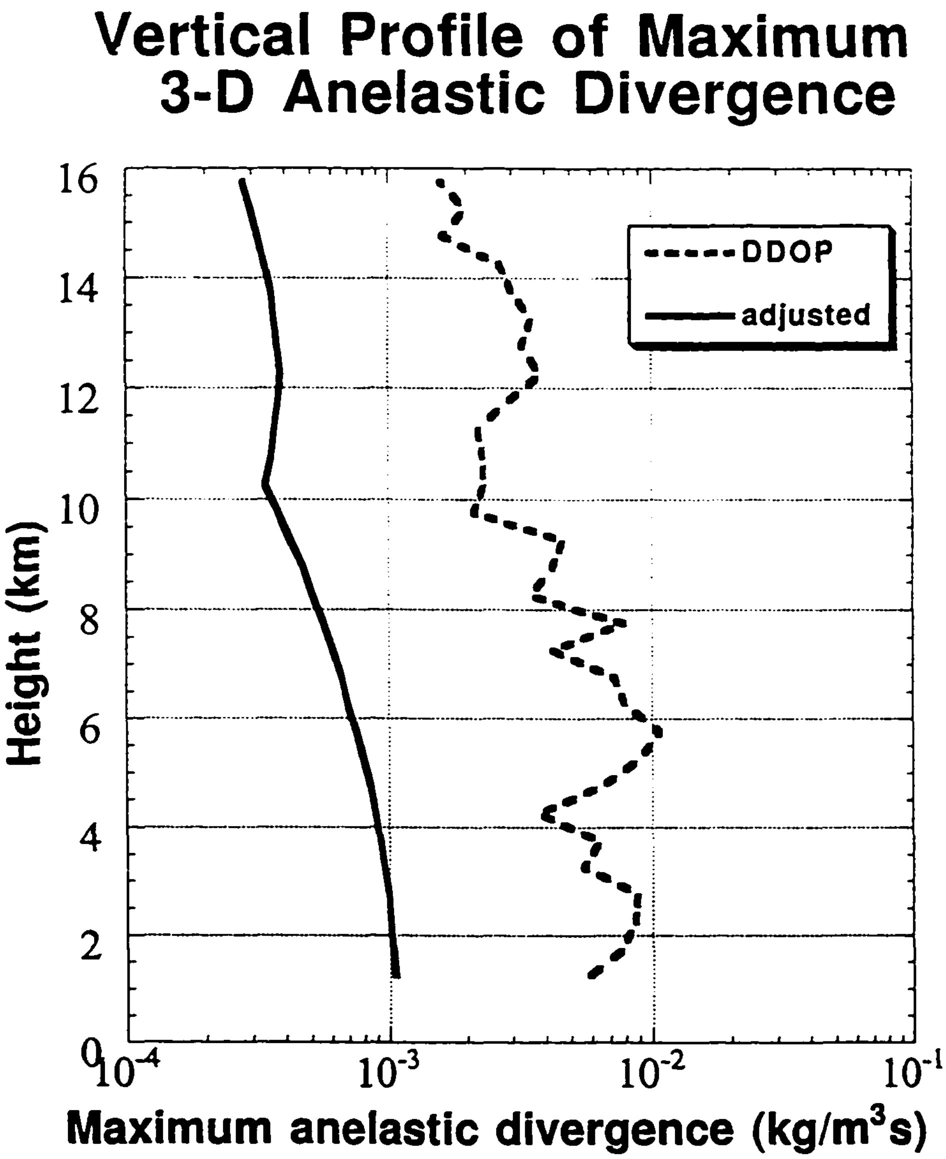

Figure 5.6 Vertical profile of maximum 3-D anelastic divergence ($kg\ m^{-3}\ s^{-1}$) for the 2239 UTC DDOP retrieved and adjusted wind fields.

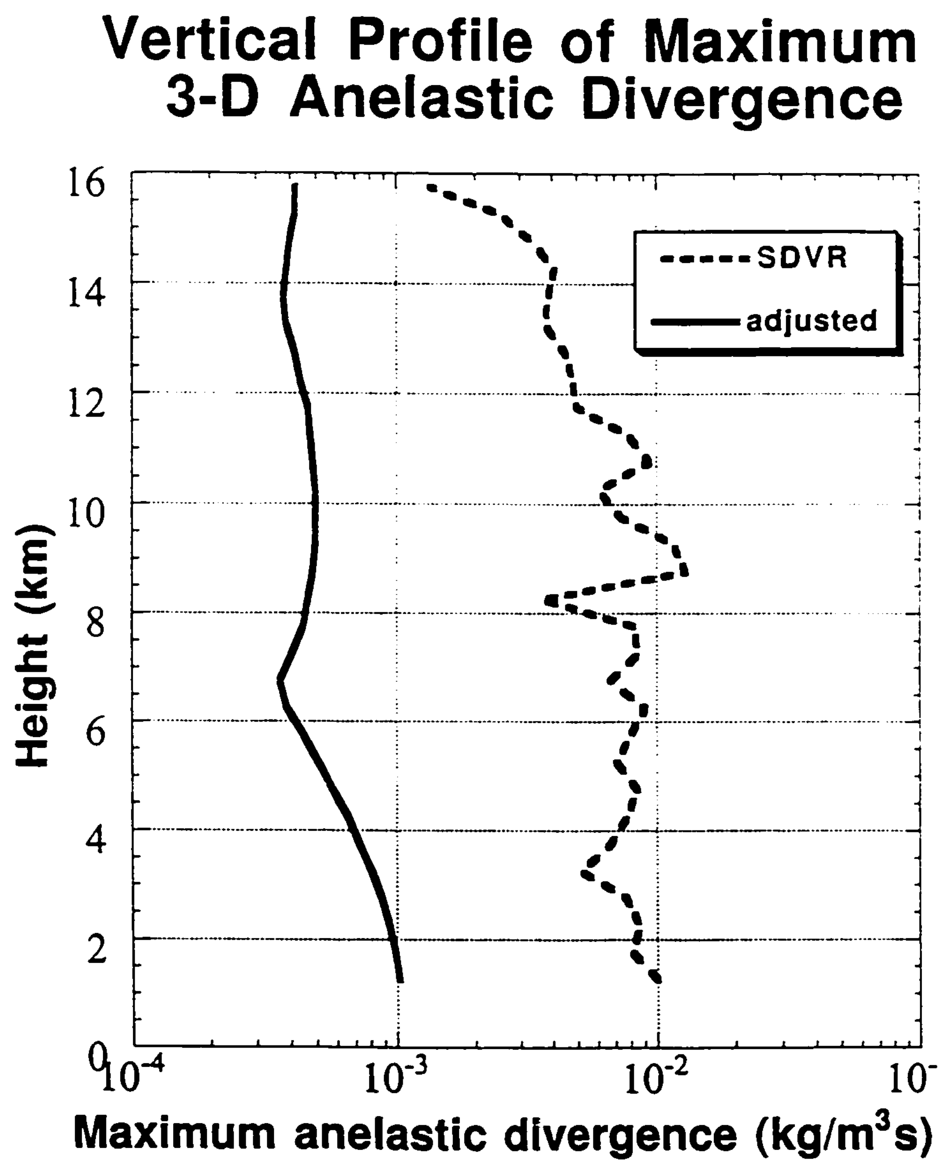

Figure 5.7 Vertical profile of maximum 3-D anelastic divergence (kg m^{-3} s^{-1}) for the 2239 UTC SDVR retrieved and adjusted wind fields.

a)

b)

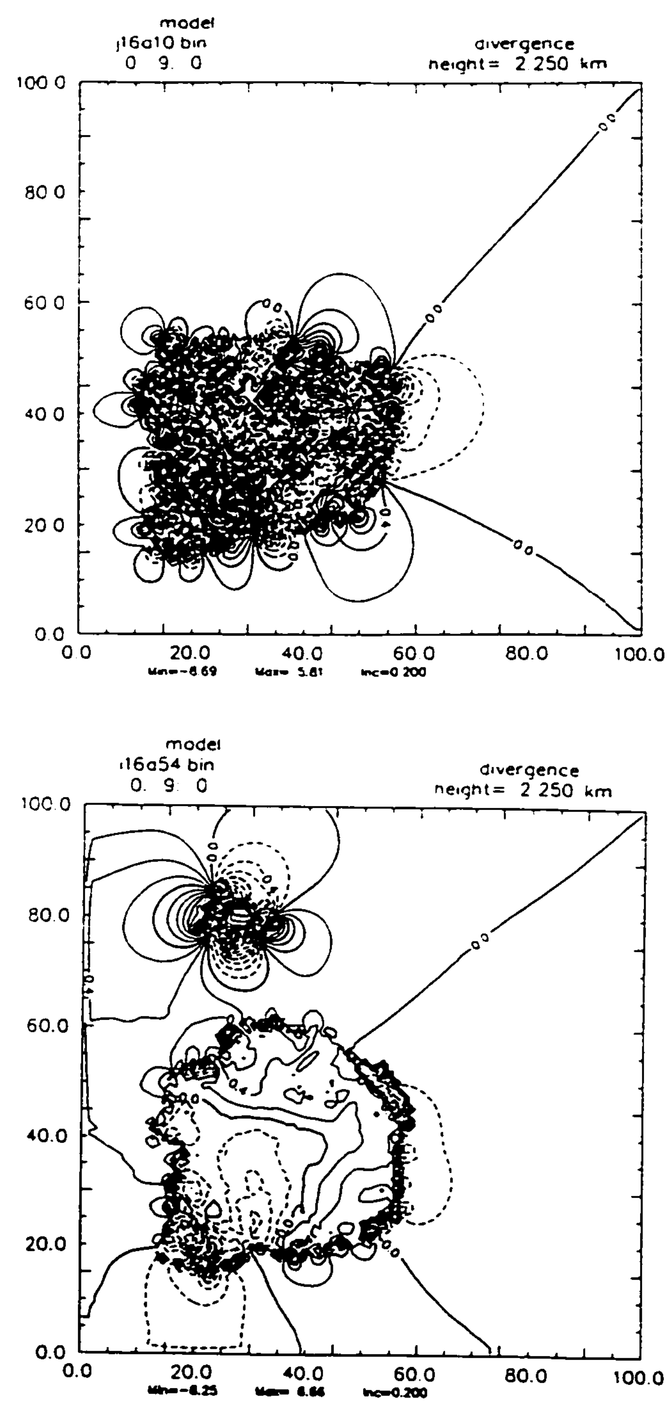

Figure 5.8 2239 UTC low-level (z = 2.25 km) 3-D anelastic divergence (10^{-3} kg m^{-3} s^{-1}) for a) the DDOP and b) the SDVR retrieved wind field. Anelastic divergence is contoured every 0.2 (10^{-3} kg m^{-3} s^{-1}). Radar location and grid distances are as in Fig. 5.1.

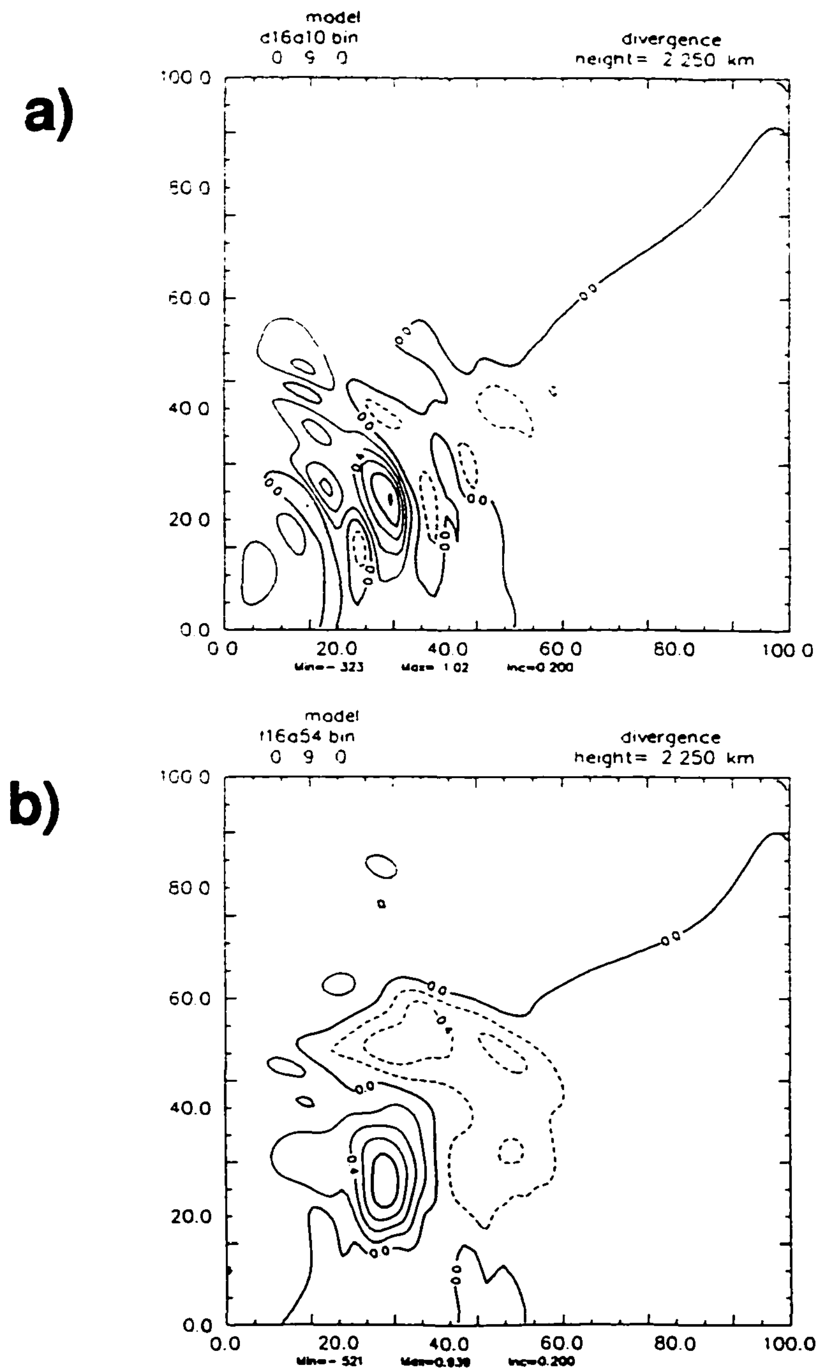

Figure 5.9 2239 UTC low-level (z = 2.25 km) 3-D anelastic divergence (10^{-3} kg m^{-3} s^{-1}) for a) the DDOP and b) the SDVR adjusted wind field. Contour interval, radar location, and grid distances are as in Fig. 5.8.

This is perhaps not surprising, considering that the 3-D Poisson equation for λ_2 (2.54) can be expressed using (2.53) as a 2-D spherical Poisson equation on constant range (ϕ–θ) surfaces (2.55). Interestingly, this banding pattern is less pronounced in the adjusted SDVR fields.

N-S (x = 19.5 km) vertical cross-sections of the 3-D anelastic divergence before and after the wind adjustment are shown in Figs. 5.10 and 5.11 for the DDOP and SDVR cases, respectively. The divergence reductions are similar to those shown in Figs. 5.8 and 5.9. For the DDOP case, the pre-adjustment divergences are significant over the entire storm-volume, while for the SDVR case, the pre-adjustment divergences are most significant along the upper and lower data edges. The adjusted fields (Figs. 5.10b and 5.11b) again illustrate the near decadal reduction in the maximum divergence magnitude and the elimination of the large values along the original data edges.

Figs. 5.12 - 14 show the storm-relative adjusted wind fields for the DDOP, SDVR, and UVVR experiments, respectively. For the z = 2.25 km horizontal fields, all three experiments show a smooth, gradual transition to the constant mean wind vector along the lateral boundaries. The principal differences among the three cases are in the storm-relative southeasterlies in the central portion of the main storm and the wind flow surrounding the small northern cell. Both features are minimally changed from the unadjusted fields and are due to previously explained differences in the radar-derived winds.

Examination of the x = 19.5 km vertical cross-sections (5.12b - 14b) reveals an interesting difference between the DDOP case and the SDVR and UVVR cases. For the DDOP case, the adjusted updraft looks very similar to its unadjusted counterpart (Fig. 5.4a). For the SDVR and UVVR cases, however, the sharp, sloping top edge of the unadjusted updraft (Figs. 5.4b,c) has been replaced by a smooth transition to the upper boundary. This difference is even more apparent in Fig. 5.15, a comparison of the

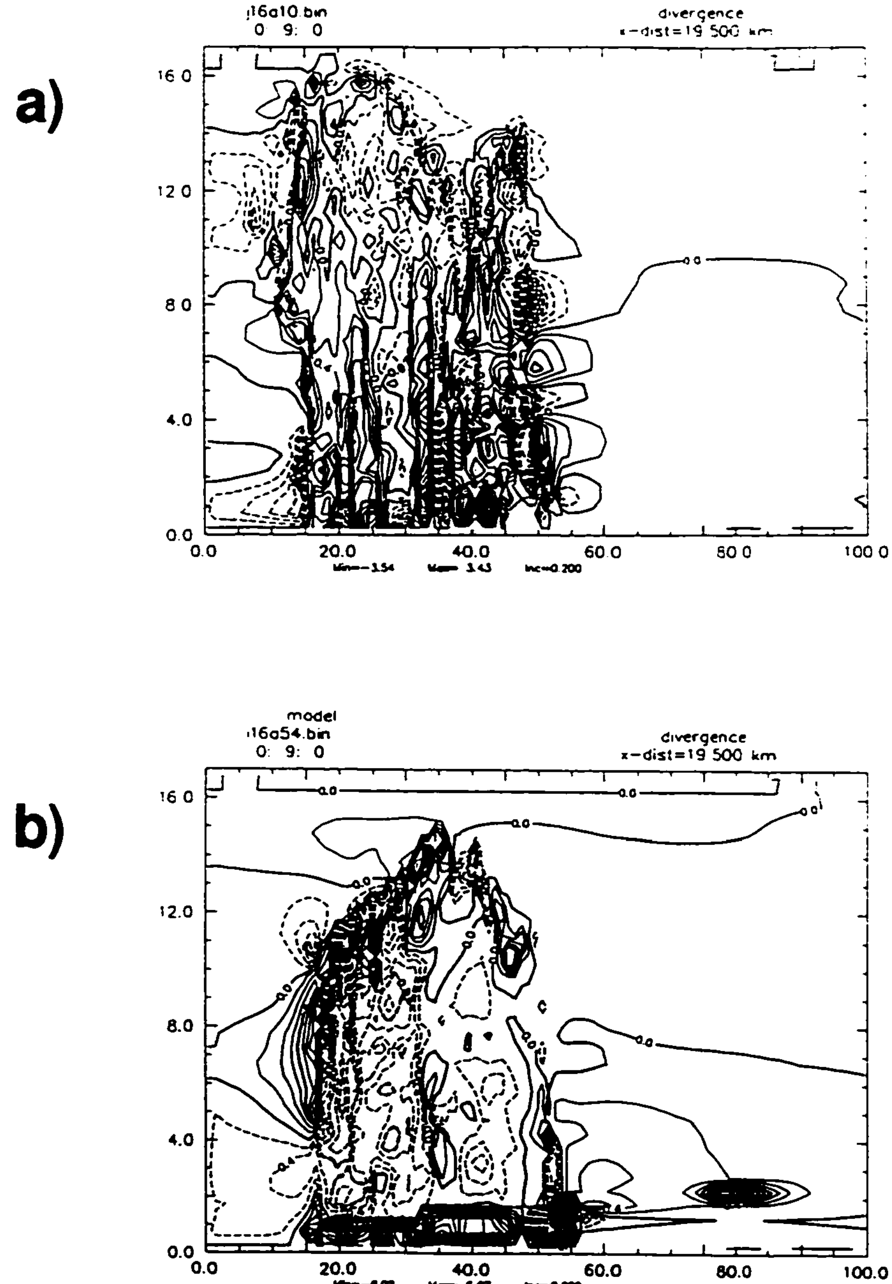

Figure 5.10 2239 UTC N-S cross-section (x = 19.5) of the 3-D anelastic divergence (10^{-3} kg m^{-3} s^{-1}) for a) the DDOP and b) the SDVR retrieved wind field. Contour interval, radar location, and grid distances are as in Fig. 5.8.

a)

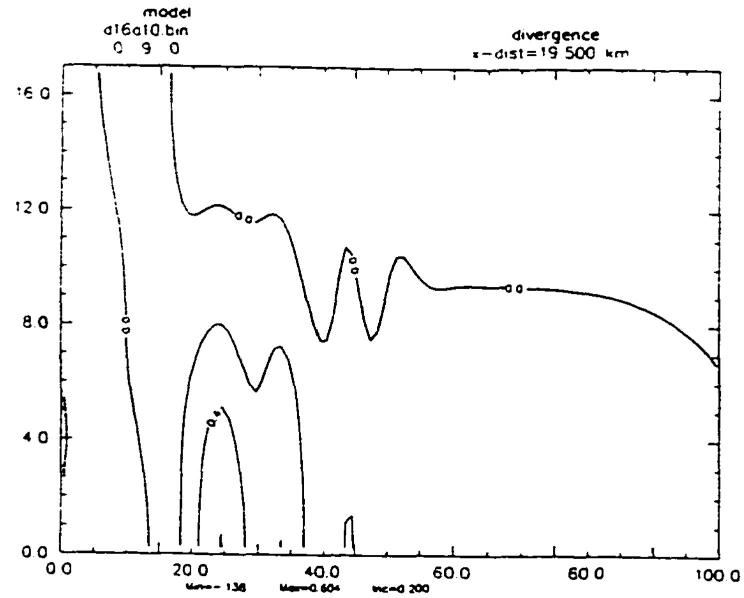

b)

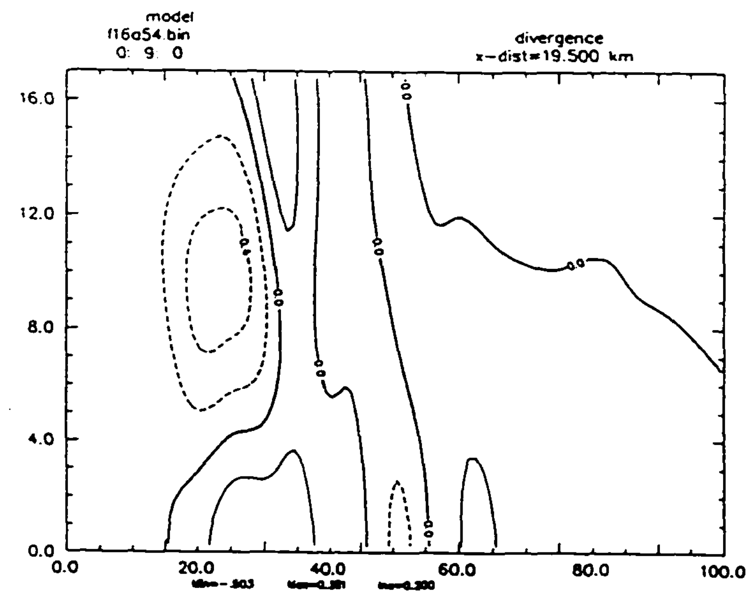

Figure 5.11 2239 UTC N-S cross-section (x = 19.5) of the 3-D anelastic divergence (10^{-3} kg m^{-3} s^{-1}) for a) the DDOP and b) the SDVR adjusted wind field. Contour interval, radar location, and grid distances are as in Fig. 5.8.

a)

b)

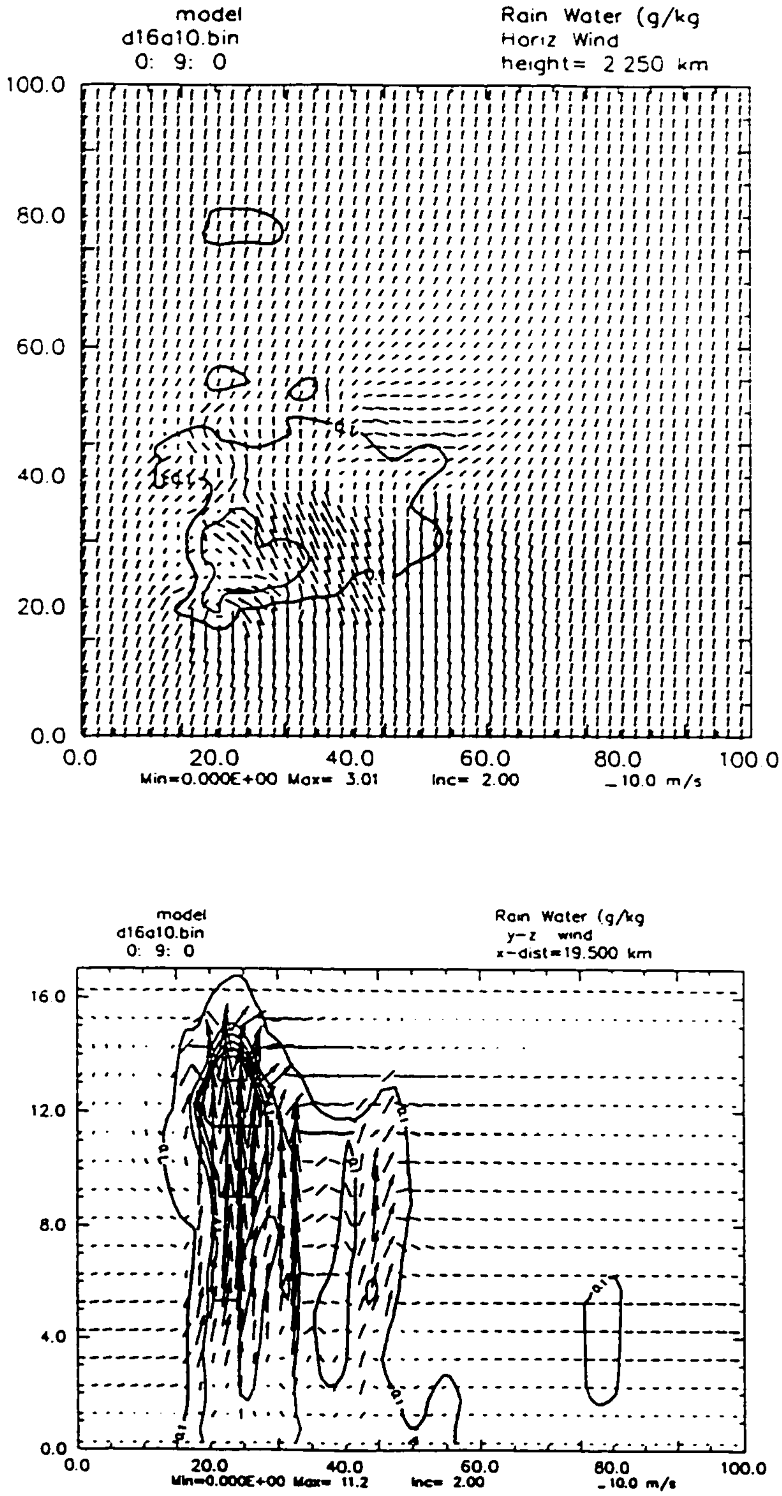

Figure 5.12 2239 UTC adjusted wind fields for the DDOP case. a) Low-level ($z = 2.25$ km) and b) N-S cross-section ($x = 19.5$) of rainwater and storm-relative wind vectors. Contour interval, radar location, and grid distances are as in Fig. 5.4.

a)

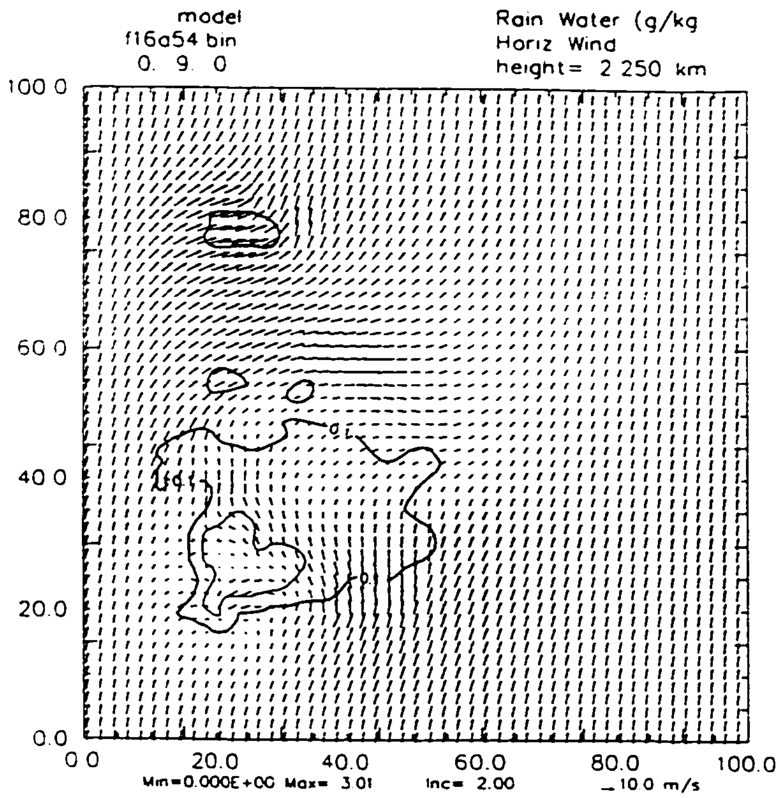

b)

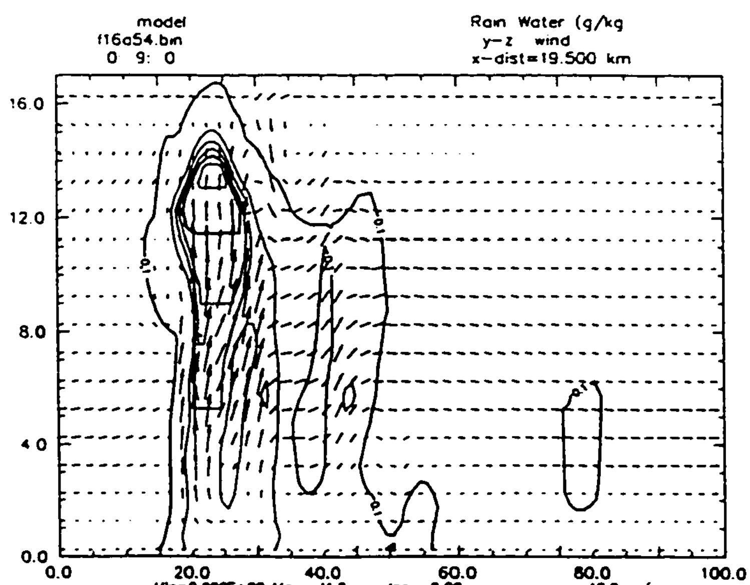

Figure 5.13 2239 UTC adjusted wind fields for the SDVR case. a) Low-level ($z = 2.25$ km) and b) N-S cross-section ($x = 19.5$) of rainwater and storm-relative wind vectors. Contour interval, radar location, and grid distances are as in Fig. 5.4.

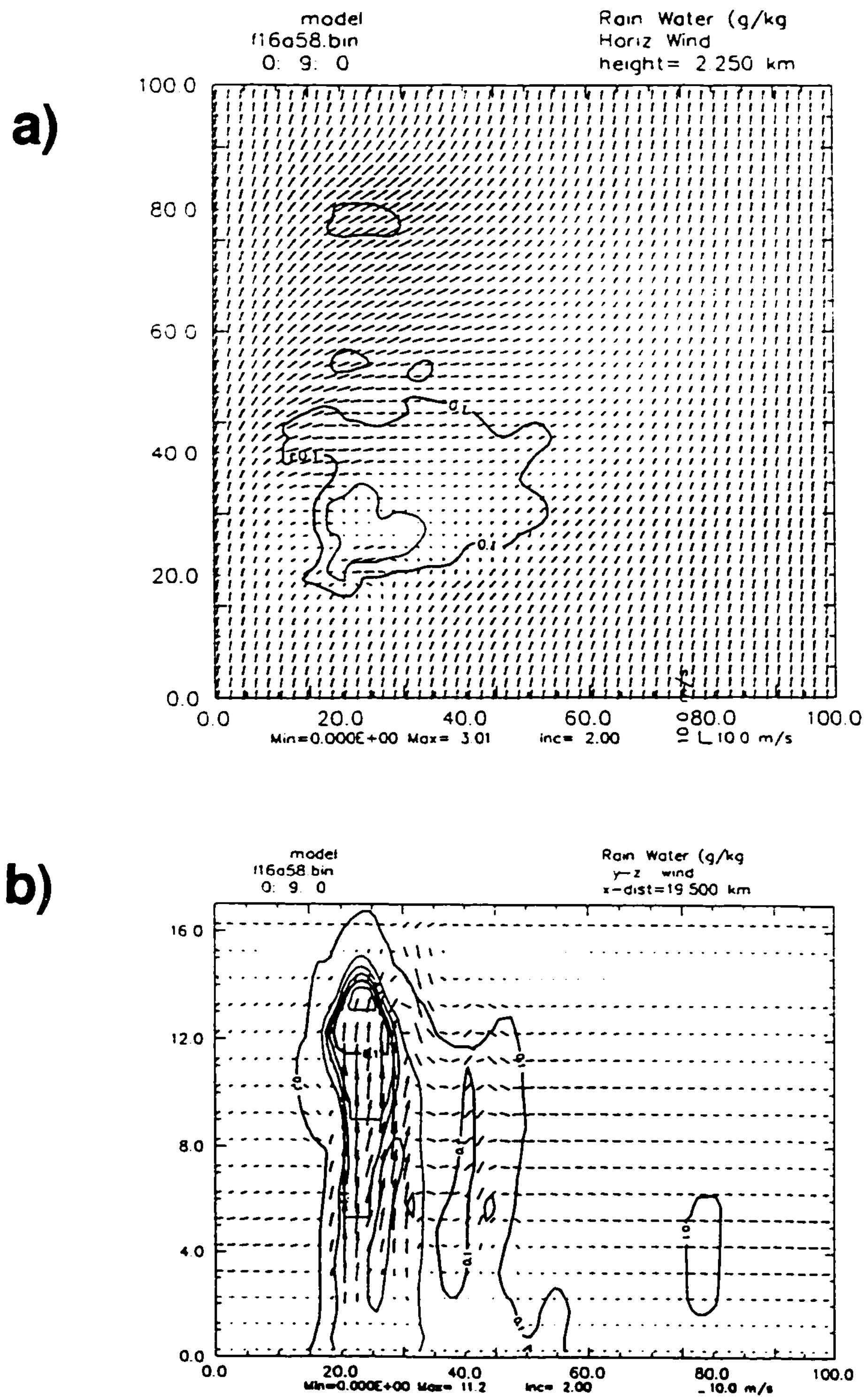

Figure 5.14 2239 UTC adjusted wind fields for the UVVR case. a) Low-level (z = 2.25 km) and b) N-S cross-section (x = 19.5) of rainwater and storm-relative wind vectors. Contour interval, radar location, and grid distances are as in Fig. 5.4.

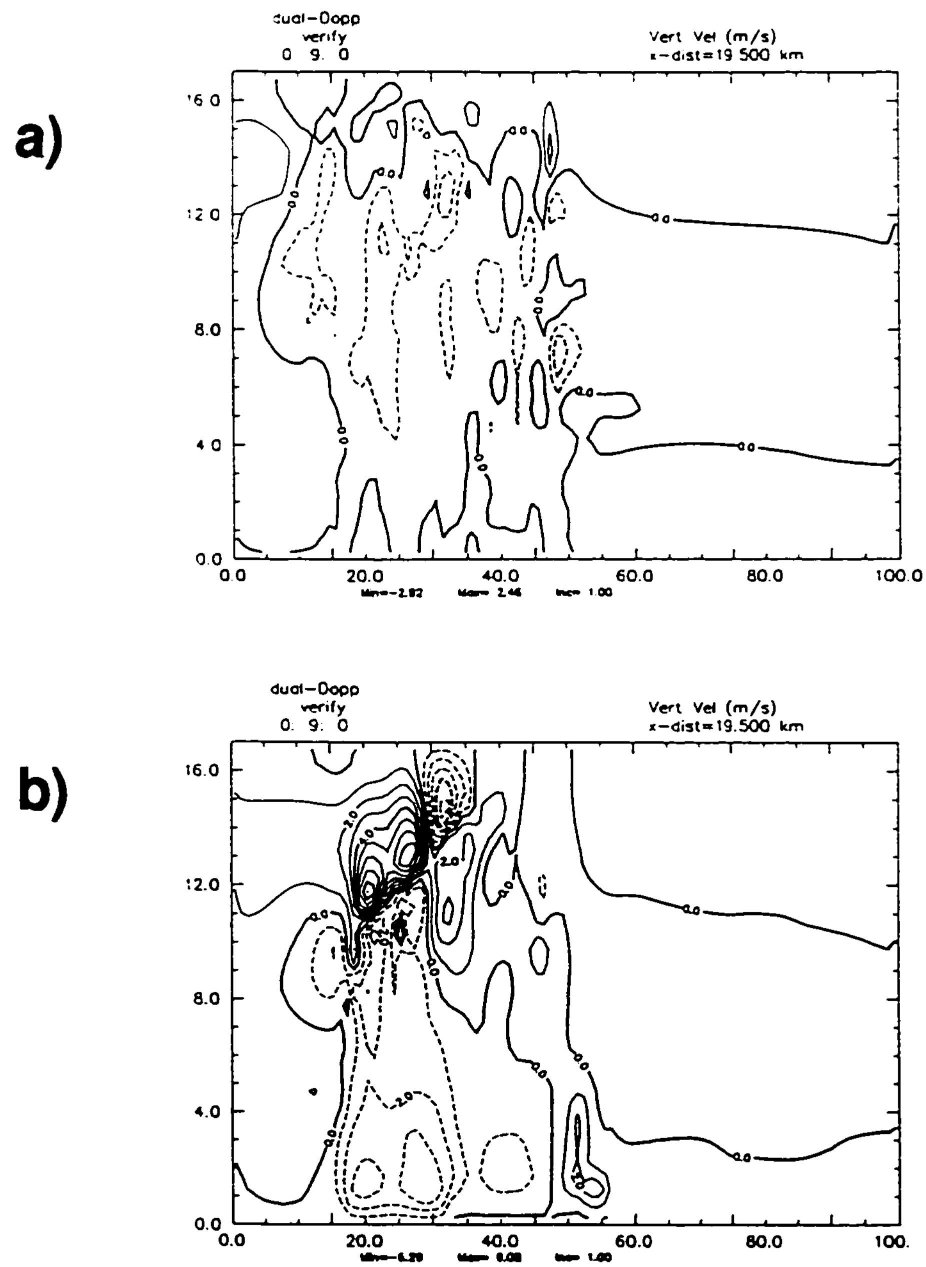

Figure 5.15 2239 UTC N-S cross-section (x = 19.5) of the vertical velocity change (adjusted - retrieved) due to the variational adjustment for a) the DDOP and b) the SDVR cases. Vertical velocity is contoured every 1 m s^{-1}. Radar location and grid distances are as in Fig. 5.4.

vertical velocity change due to the wind adjustment for the DDOP and SDVR cases. In contrast to the DDOP case, where only a modest change occurs, the SDVR case exhibits a strong velocity change couplet along the top data edge.

Apparently, the variational adjustment is modifying the vertical velocity field in a manner similar to that produced by an O'Brien (1970) correction. This is not surprising since a zero vertical velocity boundary condition is imposed at both the top and bottom of the domain. Profiles of the original and adjusted maximum vertical velocity profiles for the DDOP and SDVR cases (shown in Figs. 5.16 and 5.17) further illustrate the nature of the adjustment and the differences between the two cases. Because an O'Brien correction has already been applied to the dual-Doppler data, the DDOP maximum vertical velocity profile is only slightly modified. In contrast, the uppermost and lowermost values of the unadjusted SDVR maximum vertical velocity profile are significantly greater than zero. Because of this, the variational adjustment imposes more substantial changes on the SDVR vertical velocity field to enforce the impermeability condition at both the domain bottom and top, resulting in the more classic "bowstring" shape of the adjusted SDVR profile.

As discussed in Lazarus (1996), the spherical radar geometry leads to two difficulties in solving the variational adjustment problem. First, a singularity is present in the $1/r^2$ term in (2.53). This can be overcome by simply requiring that the radar origin not be co-located with an analysis gridpoint (a distance of a few meters is sufficient). The second singularity is more serious and is found in the $z/(x^2+y^2)$ term in the vertical boundary condition (2.56). This can be expressed as $\tan\theta/r \cos\theta$, exposing the $\infty/0$ nature of the singularity for $\theta = 90°$. In general, the problem can be mitigated by applying a $\lambda_2 = 0$ Dirichlet condition in a circular "patch" around the projection of the radar origin on the domain top (typically defined with a radius of 5 km). Unfortunately, this results in an area of non-zero vertical velocities in a region near the patch.

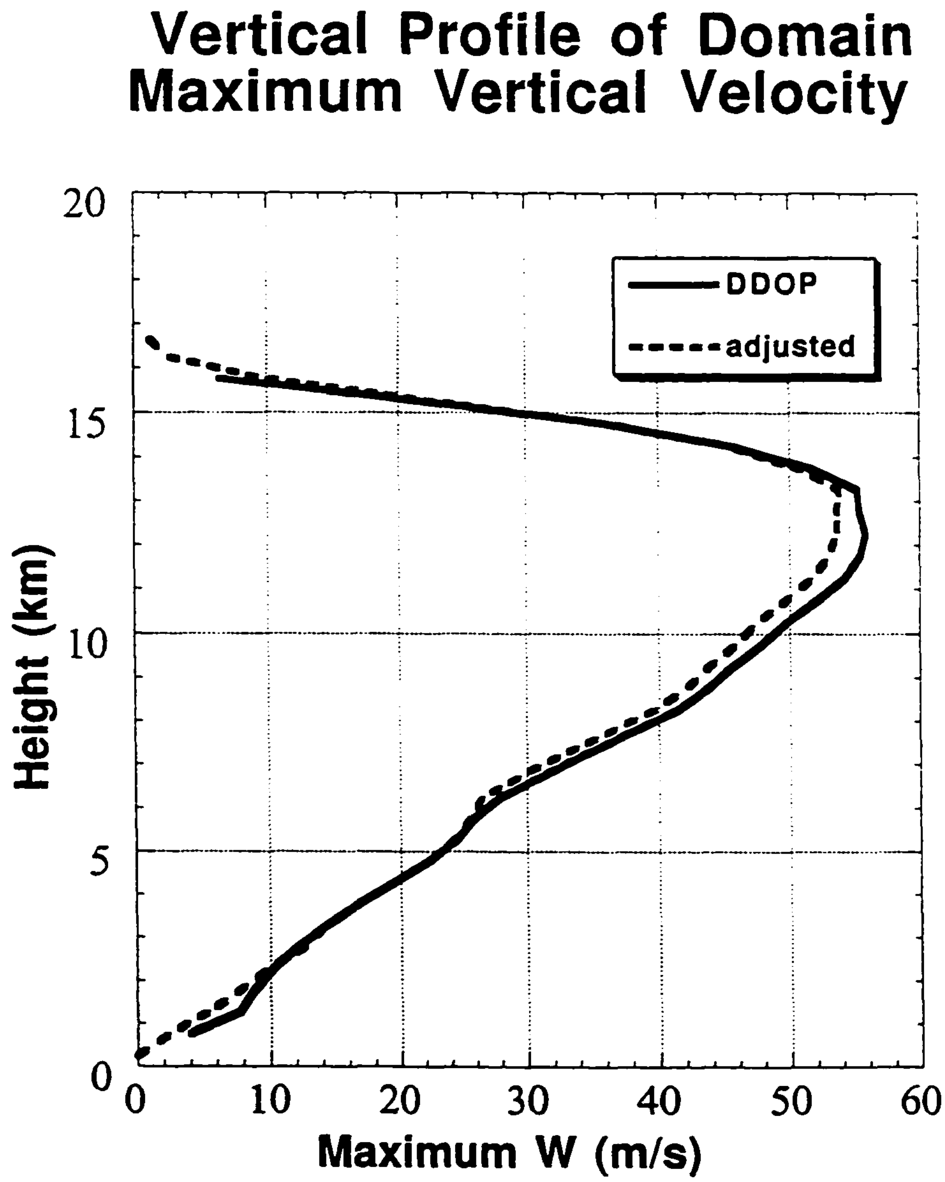

Figure 5.16 Vertical profile of the 2239 UTC retrieved and adjusted maximum vertical velocity (m s^{-1}) for the DDOP case.

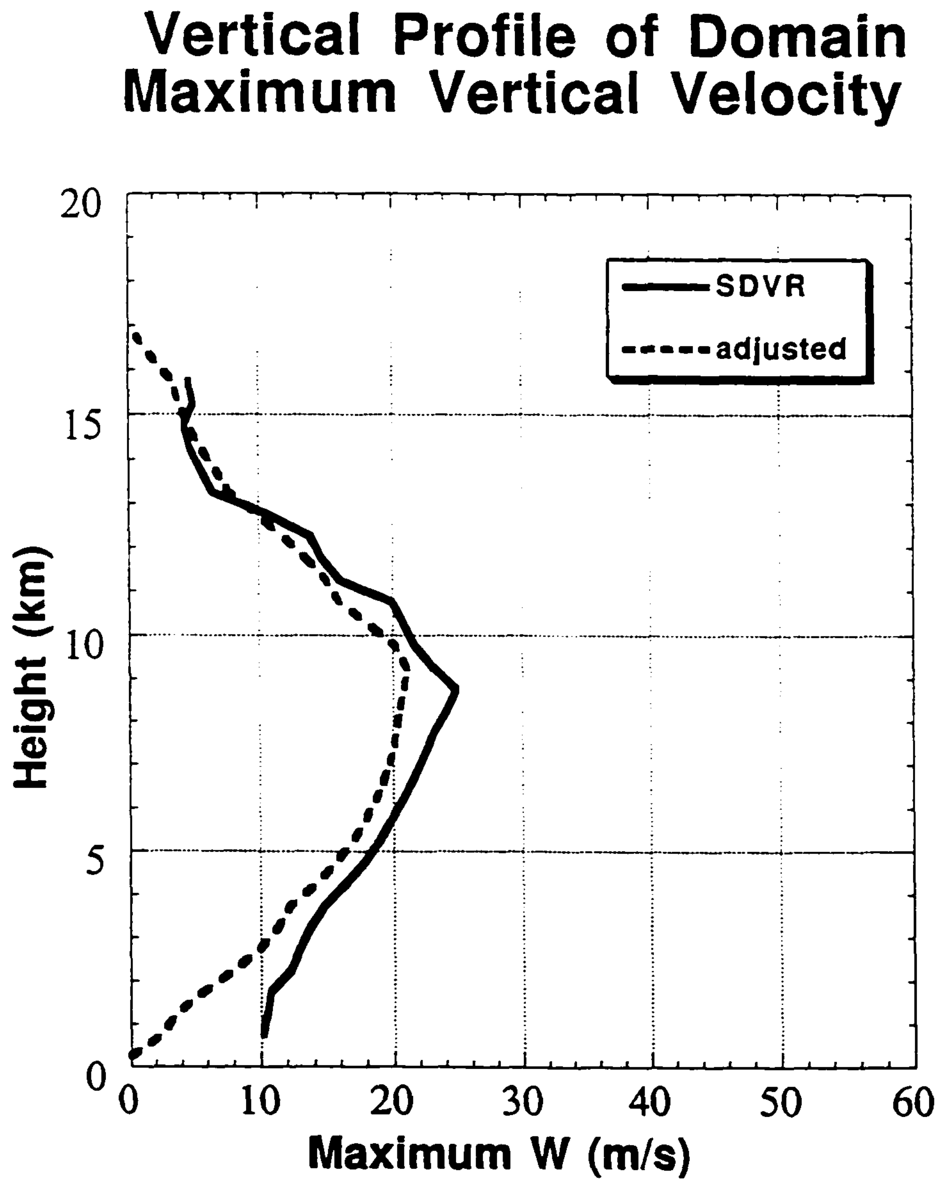

Figure 5.17 Vertical profile of the 2239 UTC retrieved and adjusted maximum vertical velocity (m s^{-1}) for the SDVR case.

In this study, the radar was located 5 km outside of the western domain edge to minimize the influence of the problem. Nevertheless, a weak vertical velocity signature can be seen in the wind field along the western face of the domain. Fig. 5.18 shows the vertical velocity and vector wind field for an x = 0.5 km vertical cross-section. A vertical velocity maximum of slightly greater than 5 m s^{-1} and an associated weak circulation are evident. Fortunately, this spurious upward motion does not appear to cause any contamination in the forecast. As mentioned previously, an improved variational adjustment that should avoid this problem is derived in Appendix A.

5.2 Retrieved pressure and temperature fields

For each experiment, three time levels of hole-filled, variationally adjusted winds are used as input to the thermodynamic retrieval. As described in Section 2.3, the thermodynamic retrieval is performed on the model grid using the model subroutines to calculate the various forcing terms. As a first step, the three unevenly-spaced, adjusted wind fields are interpolated to three successive time steps (centered around the central time of the middle wind field) using a three-point Lagrangian interpolating polynomial (Carnahan et al. 1969). A Poisson equation for pressure (2.61) is then solved on a series of horizontal surfaces using a successive overrelaxation and alternating direct implicit technique (Roache 1982). As discussed in Section 2.3, the non-uniqueness problem associated with the use of Neumann boundary conditions is overcome by using a Dirichlet condition of $p' = 0$. The suitability of this boundary condition is enhanced by solving the problem over a large domain (100 x 100 km) with the storm well displaced from the domain edges. Outside the storm volume, the values for A and B in the forcing function of (2.61) are set equal to zero.

a)

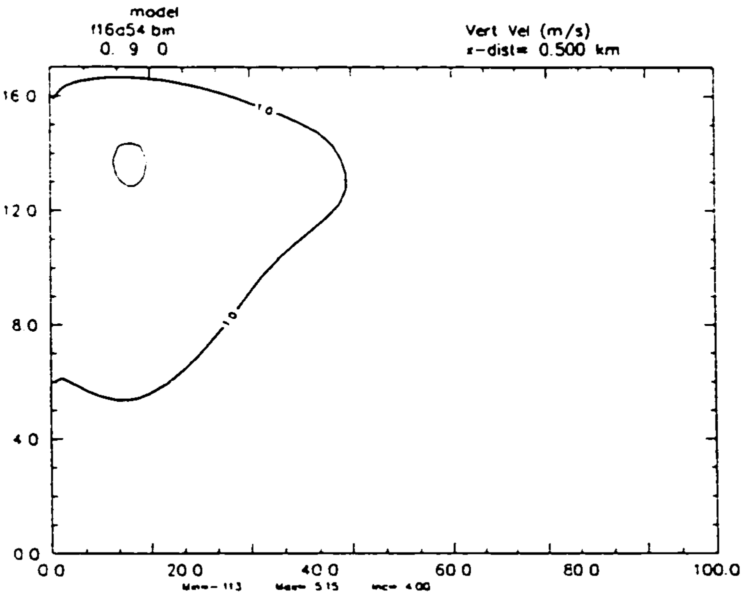

b)

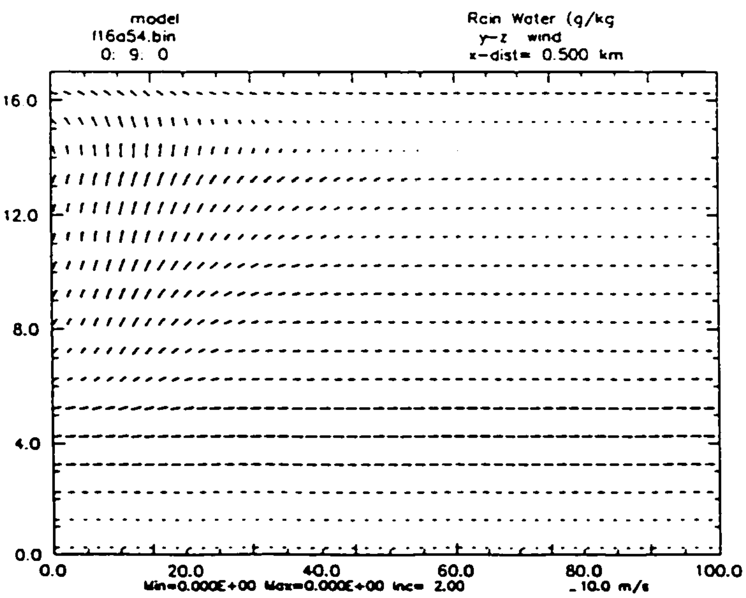

Figure 5.18 2239 UTC N-S cross-section (x = 0.5) of a) the vertical velocity and b) the storm-relative wind vectors for the SDVR case. Vertical velocity is contoured every 1 m s^{-1}. Radar location and grid distances are as in Fig. 5.4.

Once a unique perturbation pressure field is found at all levels, the perturbation temperature is found as a residual from the vertical momentum equation (2.62). Rainwater is computed from the semi-empirical formula (2.63) and water vapor and cloudwater are neglected. In order to reduce the impact of the discontinuities along the original data edges, the retrieved pressure and temperature along the outer edge points of the storm volume are discarded (in both the horizontal and vertical directions).

Figs. 5.19a shows the retrieved perturbation pressure field at $z = 5.25$ for the SDVR case (over a portion of the model domain). In addition, storm-relative vectors are overlain, regions of vertical velocity greater than 5 m s^{-1} shaded and the $qr = 0.1$ g kg^{-1} contour is included. Lastly, the mean shear vector calculated from the retrieved in-storm velocities over a 1-km deep layer centered at $z = 5.25$ km is indicated by the heavy arrows centered on each of the three updraft maximum. The accompanying panel (Fig. 5.19b) shows the $z = 5.25$ vertical vorticity field with the same features overlaid.

As can be seen in Fig. 5.19a, associated with the three vertical velocity maxima are perturbation pressure couplets, each aligned with the shear vector through the updraft maximum in a manner that is consistent with the linear theory proposed by Rotunno and Klemp (1982). This theory predicts low (high) perturbation pressure down- (up-) shear from the updraft due to the interaction of the updraft with the environmental shear. Interestingly, the northern two vertical velocity maxima, which are presumably associated with older, decaying updrafts, are located further toward the high pressure side of the perturbation pressure gradient. Note that only for the southernmost updraft maximum does the pressure couplet also align with the storm-relative wind vectors. This closer alignment of the pressure couplets with the shear vector rather than with the storm-relative flow vectors favors the linear arguments of Rotunno and Klemp (1982) over the obstacle flow explanations that have been offered (Newton and Newton 1959, Fujita and Grandoso 1968, Alberty 1969 and Brown 1992).

a)

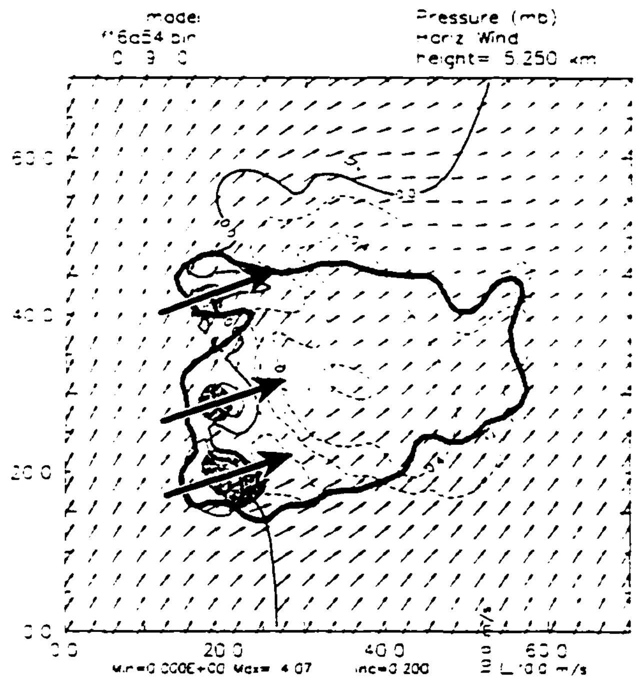

SDVR

b)

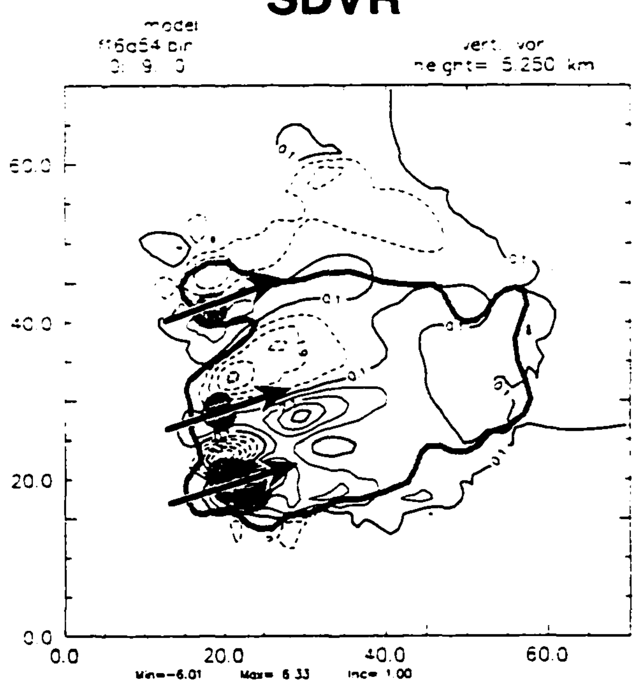

Figure 5.19 2239 UTC mid-level (z = 5.25 km) a) perturbation pressure and b) vertical vorticity (10^{-3} s^{-1}) for the SDVR case. Pressure is contoured every 0.2 mb and vorticity is contoured every $1(10^{-3}\ s^{-1})$. Updrafts greater than 5 m s^{-1} are shaded, the qr = 0.1 g kg^{-1} contour is shown, and the shear vector indicated.

Examination of Fig. 5.19b indicates that each updraft is also associated with a couplet of positive and negative vertical vorticity. The general alignment of these features perpendicular to the shear vector is also consistent with the linear theory of Rotunno and Klemp (1982) and Davies-Jones (1984), who postulated that the generation of vertical vorticity in thunderstorms is due to the tilting of environmental shear by the updraft. As might be expected, the positive vorticity maximum is most closely aligned with the updraft maximum in the southern, most intense updraft.

A similar set of pressure and vorticity fields for the DDOP experiment is shown in Fig. 5.20. Here the fields are noisier, and the match to the linear theory is not as clear. It is possible that non-linear terms neglected by the linear theory may be better resolved in the dual-Doppler data. In particular, vorticity (which would favor low-pressure wherever the magnitude of the vorticity is large) may be playing a more significant role. Nevertheless, the vorticity couplets and horizontal pressure gradient tend to be aligned perpendicular to and parallel to the shear vector, respectively. Comparison with similar dual-Doppler derived fields shown by Brandes et al. (1988) indicates a reasonable qualitative agreement.

It is important to note that several different 2-D and 3-D pressure decompositions exist that could be used to more precisely quantify the various pressure forcing terms. A number of different researchers have applied these decompositions to both simulated and dual-Doppler derived thunderstorms fields (Rotunno and Klemp 1982, 1985, Klemp and Rotunno 1983, Brandes 1984, Brandes et al. 1988). A detailed application of them to this dataset would likely yield useful results, but is beyond the scope of this study.

Comparison of the SDVR and DDOP vorticity fields indicates an excellent agreement. In both cases, three distinct vorticity couplets can be seen along the west side of the storm. Furthermore, the SDVR also captures the large vorticity maximum near x=30, y = 30, and reproduces the sideways "H" shape of the associated positive vorticity field.

a)

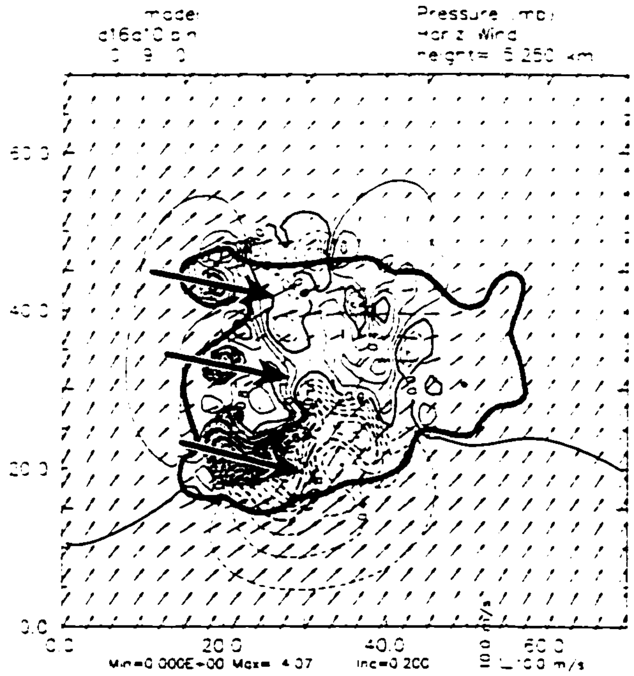

DDOP

b)

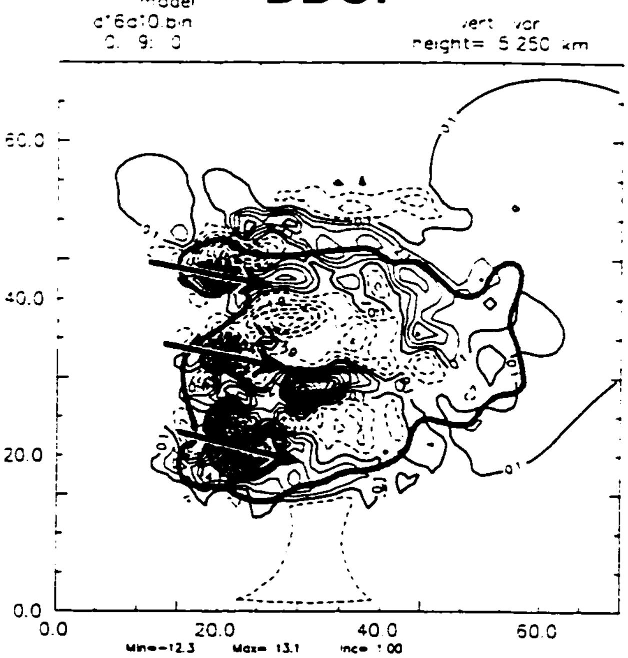

Figure 5.20 2239 UTC mid-level (z = 5.25 km) a) perturbation pressure and b) vertical vorticity (10^{-3} s^{-1}) for the DDOP case. Pressure is contoured every 0.2 mb and vorticity is contoured every 1(10^{-3} s^{-1}). Updrafts greater than 5 m s^{-1} are shaded, the qr = 0.1 g kg^{-1} contour is shown, and the shear vector indicated.

Vertical cross-sections of the retrieved pressure and temperature fields for all three experiments are shown in Figs. 5.21-23, respectively. The perturbation pressures are fairly similar, with the amplitude of the features decreasing from the DDOP case to the SDVR case to the UVVR case. All three experiments show a N-S couplet of positive and negative perturbation pressures at upper levels, with the positive region extending down into the central portion of the storm. A secondary region of negative pressure on the north side of the storm at mid-levels is also common to all three experiments. The close similarity between the SDVR and UVVR experiments indicates that the retrieved cross-beam wind field does not play a significant role in the pressure retrieval.

Gal-Chen and Hane (1981) describe a technique for quantifying the accuracy of the retrieved pressure field. Known as "momentum checking", the techniques involves calculating a quantity defined as:

$$E_r = \frac{\iint \left[\left(\frac{\partial p'}{\partial x} - A \right)^2 + \left(\frac{\partial p'}{\partial y} - B \right)^2 \right] dx\, dy}{\iint \left[A^2 + B^2 \right] dx\, dy} , \qquad (5.2)$$

where A and B are defined by (2.57) and (2.58). Calculated for each horizontal level, this quantity represents a normalized goodness of fit between the retrieved pressure gradients and the forcing functions. There is some disagreement about what values of E_r are considered acceptable, with Gal-Chen and Kropfli (1984) presenting a rationale for using 0.5 as an upper bound. Furthermore, as illustrated by Sun and Crook (1996), momentum checking can produce inaccurate assessments of the retrieval accuracy for cases where the error in the forcing function is purely divergent or purely rotational.

For the present experiments, (5.2) has been summed over the entire 3-D volume to obtain a single value for E_r. For both the DDOP and SDVR experiments, $E_r = 0.52$,

a)

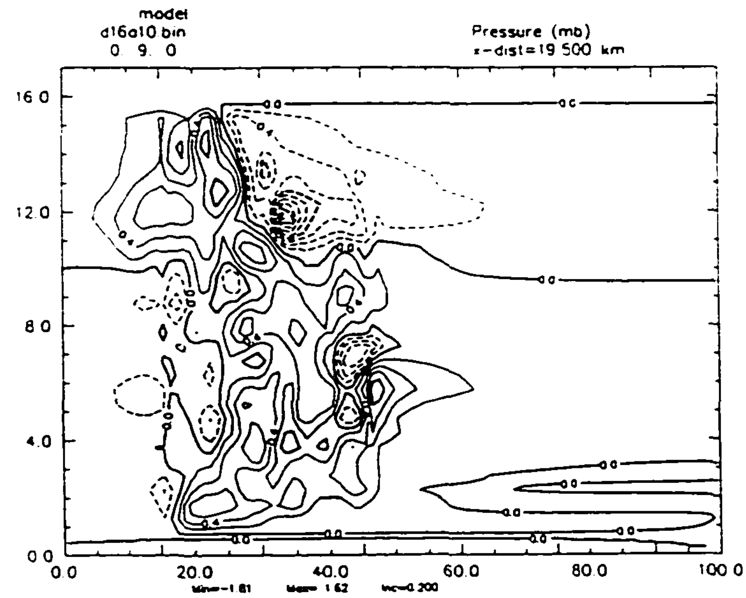

b)

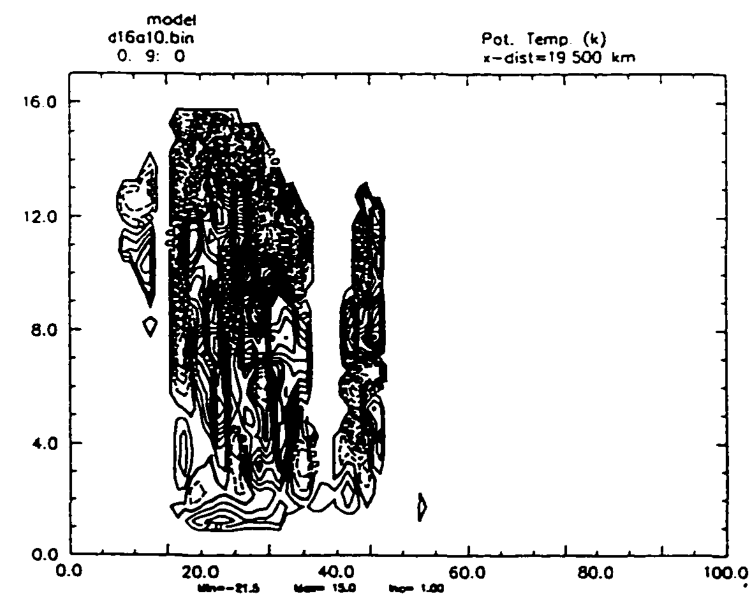

Figure 5.21 2239 UTC N-S cross-section (x = 19.5) of the retrieved a) perturbation pressure and b) perturbation potential temperature for the DDOP case. Pressure is contoured every 0.2 mb and potential temperature is contoured every 1 K.

a)

b)

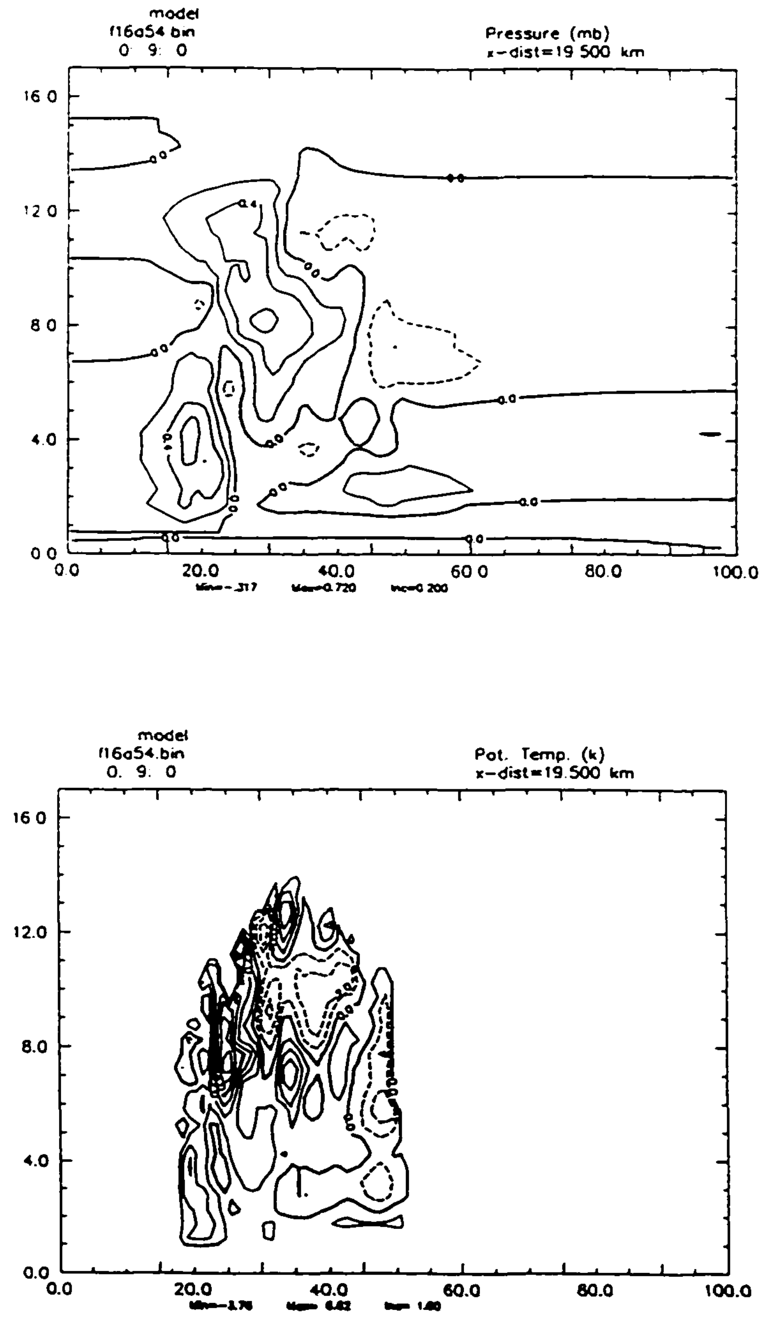

Figure 5.22 2239 UTC N-S cross-section (x = 19.5) of the retrieved a) perturbation pressure and b) perturbation potential temperature for the SDVR case. Pressure and potential temperature are contoured as in Fig. 5.21.

a)

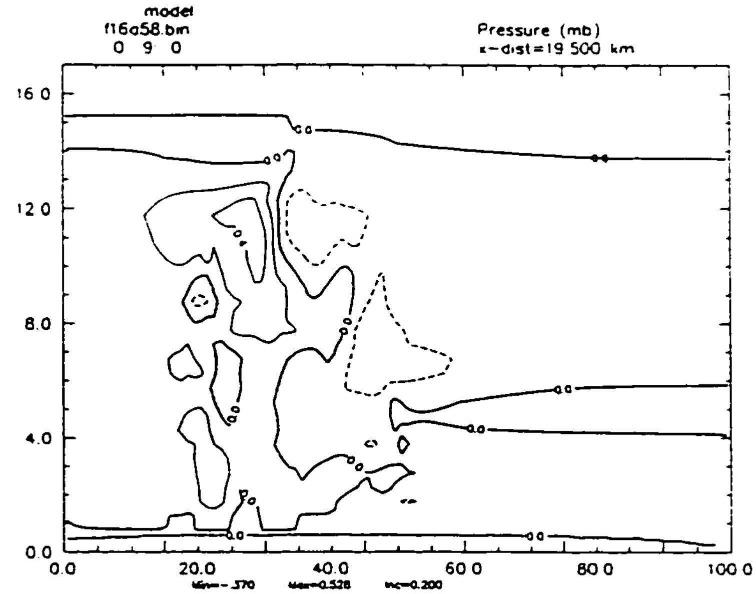

b)

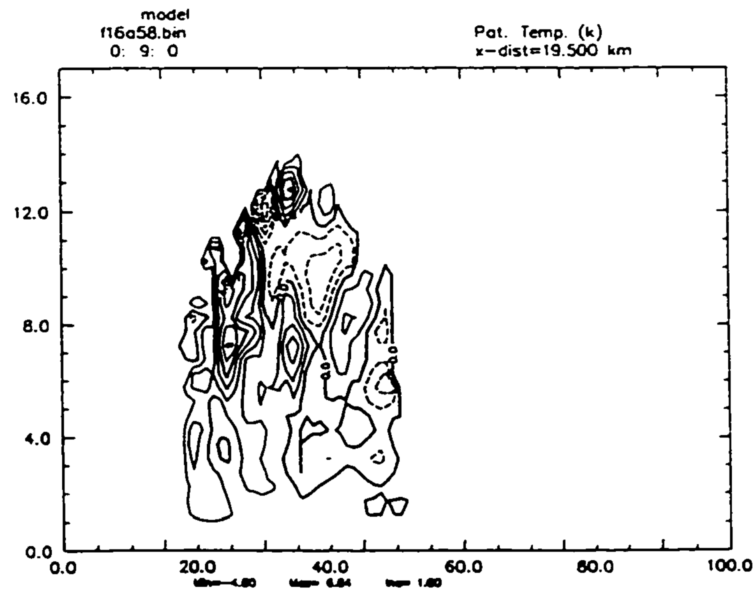

Figure 5.23 2239 UTC N-S cross-section (x = 19.5) of the retrieved a) perturbation pressure and b) perturbation potential temperature for the UVVR case. Pressure and potential temperature are contoured as in Fig. 5.21.

while for the UVVR case it was 0.43. Although these values are quite large, other performance measures, such as physical plausibility recommended by Sun and Crook (1996) and the reasonable agreement with linear theory predictions, suggest that the retrievals do provide useful information.

Comparison of the retrieved perturbation potential temperature cross-sections (Figs. 5.21b - 5.23b) indicates a similarity of features. All three experiments show a narrow column of positive perturbations that coincides quite well with the main storm updraft (see Figs. 5.12 - 14). On the right side (north) of the main updraft, all three experiments also show negative perturbations associated with the downdraft depicted in Figs. 5.12-14.

Especially striking in the retrieved potential temperature fields is the near perfect match between the SDVR and UVVR experiments. Both have a nearly +7 K maximum near z = 8 km. Parcel theory calculations based on the environmental sounding (Fig. 3.3a) indicate a maximum perturbation potential temperature of about +9 K over a large depth of the atmosphere. This is a reasonable agreement, given the pronounced dry layer in the sounding and the associated likelihood of significant entrainment of dry air into the storm updraft.

The retrieved temperature field for the DDOP case is significantly noisier than either of the single-Doppler cases, but exhibits many of the same features with a local maximum of + 9 K near z = 8 km. Clearly apparent in the DDOP field is an area of strongly negative perturbation temperatures at the storm-top. Comparison with the equilibrium level in the background sounding (Fig. 3.3a) indicates a reasonably good agreement, especially if an allowance is made for entrainment.

At lower levels along the southern edge of the storm, all three experiments appear to capture the warm inflow into the updraft. Conspicuously absent from the cross-sections, however, is any hint of a low-level cold pool. Attempts were made to retrieve the cold pool; however, low-level retrieved temperatures exhibited an extreme sensitivity to the lower boundary condition when radar data was extrapolated to the ground. Because of this, no downward extrapolation of the radar data was allowed, and all attempts at retrieving the low-level cold pool were abandoned. In Chapter 6, the time required for the generation of cold pools during the numerical integration will be examined.

5.3 Analysis of terms in the vertical momentum equation

5.3.1 Calculations from the radar-derived fields

In order to gain further insight into the nature of the perturbation temperature retrieval, an analysis of the forcing terms in the vertical momentum equation is performed. To facilitate this analysis, the vertical momentum equation (2.62) is expressed as follows:

$$\theta' = \underset{\substack{\text{Vertical}\\ \text{PGF}}}{\frac{\bar{\theta}}{\bar{\rho}g}\frac{\partial p'}{\partial z}} + \underset{\substack{\text{Vertical}\\ \text{Accel.}}}{\frac{\bar{\theta}}{\bar{\rho}g}\frac{d(\bar{\rho}w)}{dt}} + \underset{\substack{\text{Pressure}\\ \text{Buoy.}}}{\frac{\bar{\theta}p'}{\gamma\bar{p}}} - \underset{\substack{\text{Water-}\\ \text{vapor}}}{.608\,\bar{\theta}\,q_v} + \underset{\substack{\text{Cloud-}\\ \text{water}}}{\bar{\theta}\,q_c} + \underset{\substack{\text{Rain-}\\ \text{water}}}{\bar{\theta}q_r} + \underset{\text{Friction}}{\frac{\bar{\theta}}{\bar{\rho}g}F_z}\ , \qquad (5.3)$$

where the annotations indicate the names of the various terms. From (5.3) it is easy to see that each g kg^{-1} of cloudwater or rainwater will result in a potential temperature perturbation of approximately $+0.3$ K. Similarly, each g kg^{-1} of perturbation water vapor will result in a potential temperature perturbation of approximately -0.2 K. As discussed in Section 2.3, radar-observed reflectivity is converted to rainwater using a semi-empirical formula, and cloud water and perturbation water vapor effects are neglected.

As expected, the dominant forcing terms in (5.2) are the vertical pressure gradient force, vertical acceleration, and the rainwater loading terms. Fig. 5.24 shows the retrieved SDVR perturbation potential temperature and the three dominant forcing terms

a)

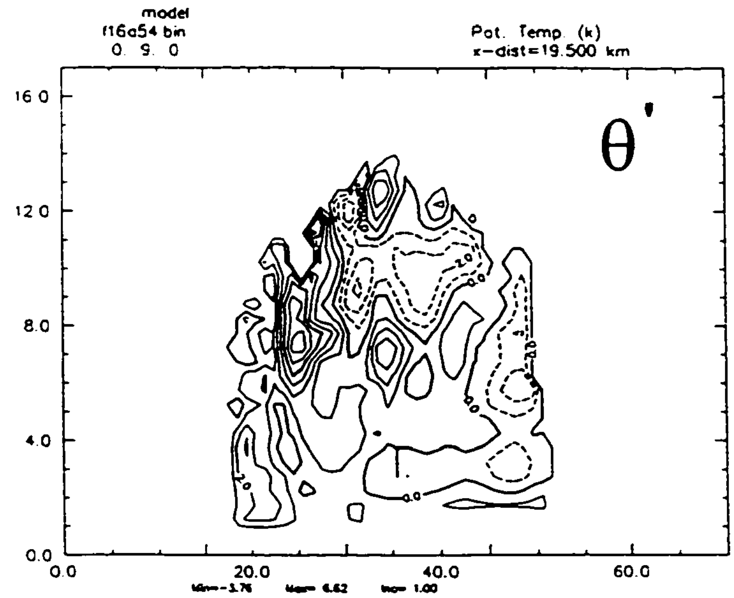

SDVR

b)

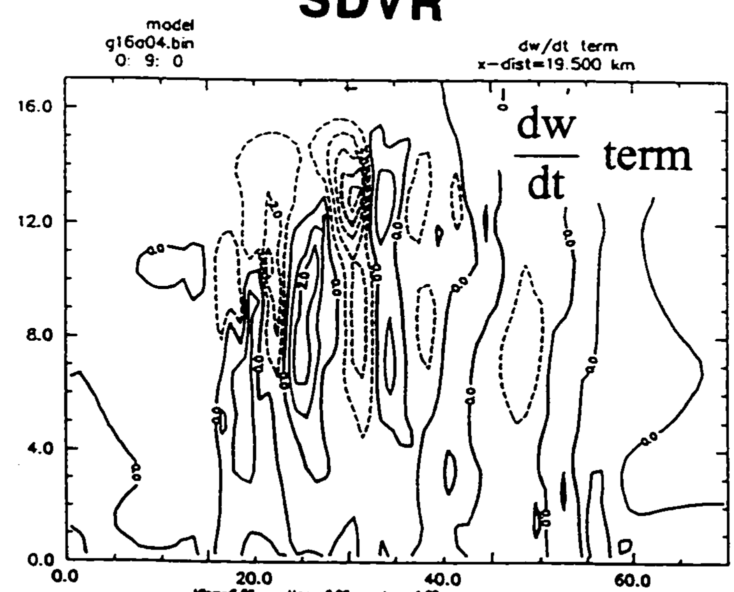

Figure 5.24 2239 UTC N-S cross-section (x = 19.5) of a) the retrieved perturbation potential temperature and the main contributing terms for the SDVR case, including b) the vertical acceleration term, c) the rainwater term and d) the vertical pressure gradient term. Potential temperature and all terms are contoured every 1 K.

c)

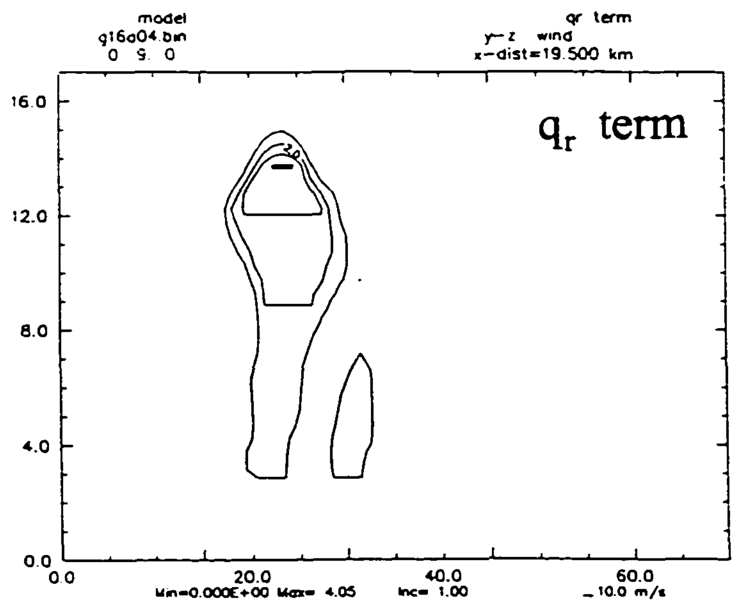

d)

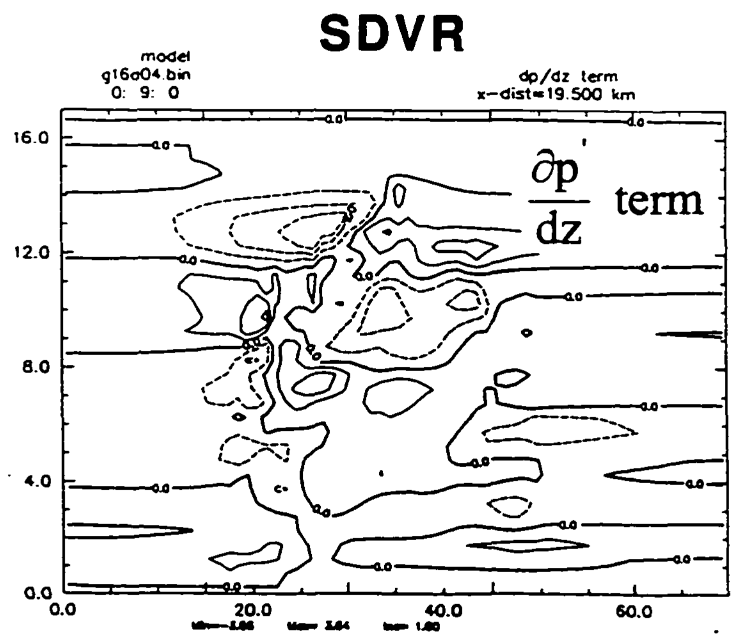

Figure 5.24 (Continued)

for a portion of the x = 19.5 vertical cross-section. [Although the retrieved potential temperature field is only retained in the radar data coverage region (as indicated in Fig. 5.24a), the contributing terms are shown over the entire portion of the domain. Note that, consistent with (5.3), all terms are expressed with units of temperature (K).]

Examination of the vertical pressure gradient term (Fig. 5.24d) indicates that the field smoothly transitions from values along the storm edge to near zero outside the storm, where A and B in the forcing function of (2.61) are set equal to zero. Coincident with the positive potential temperature perturbation shown in Fig. 5.24a (and the updraft) is a column of positive contribution from the vertical acceleration term (Fig. 5.24b), with a vertically elongated maximum of nearly + 3 K. Comparison with the other terms indicates that the narrow columnar shape of this term is the most significant factor in the similar shape of the retrieved temperature field. Further decomposition of this term (not shown) indicates that most of the maximum in the updraft region is due to the $\vec{V}_h \cdot \nabla_h w$ term. Fig. 5.24c indicates a positive contribution from the rainwater term throughout much of the updraft region, with a value of nearly + 2 K near the retrieved temperature maximum. Comparison with 5.24a reveals, however, that the region of maximum contribution is above the data coverage region, and is therefore not utilized in the SDVR case.

In contrast to the columnar appearance of the vertical acceleration term, the vertical pressure gradient term is more horizontally stratified. It also shows a significant contribution (more than + 2 K) in a region nearly co-located with the maximum perturbation temperature. Also significant is the negative contribution associated with the high altitude downdraft north of the main updraft (see Fig. 5.13b).

Fig. 5.25 shows a similar comparison of the perturbation potential temperature contributions for the DDOP experiment. With the exception of the rainwater contribution

a)

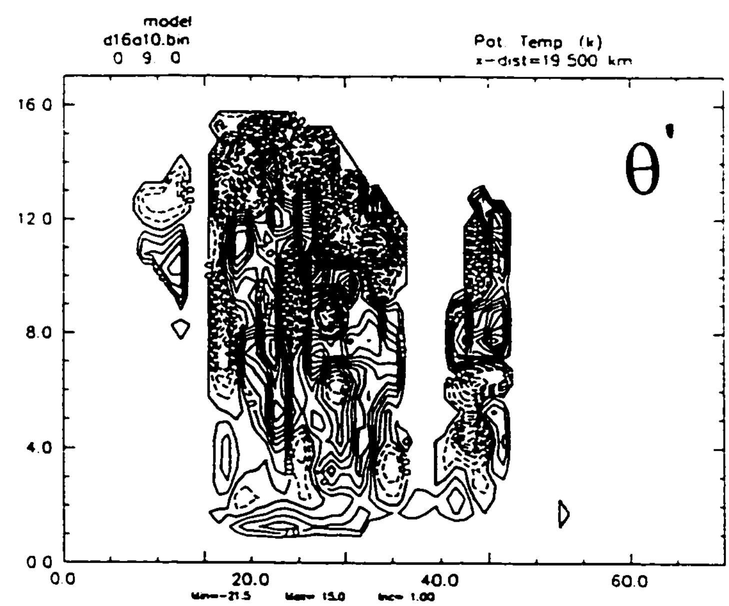

DDOP

b)

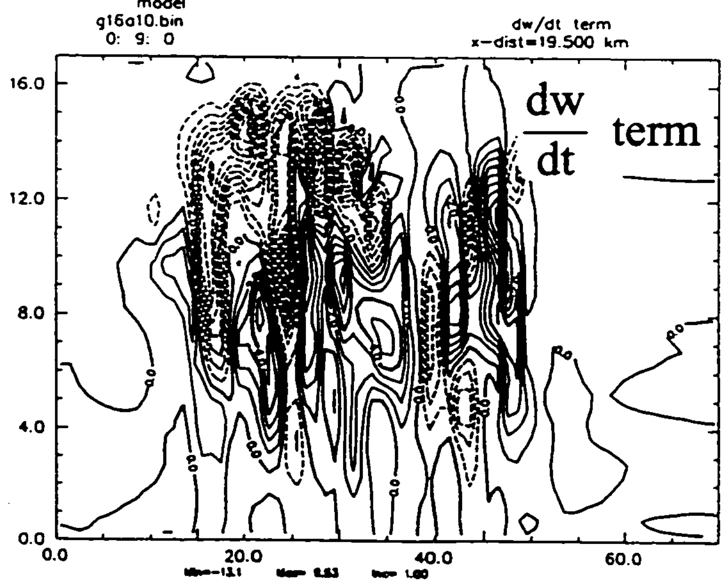

Figure 5.25 2239 UTC N-S cross-section (x = 19.5) of a) the retrieved perturbation potential temperature and the main contributing terms for the DDOP case, including b) the vertical acceleration term, c) the rainwater term and d) the vertical pressure gradient term. Potential temperature and all terms are contoured every 1 K.

c)

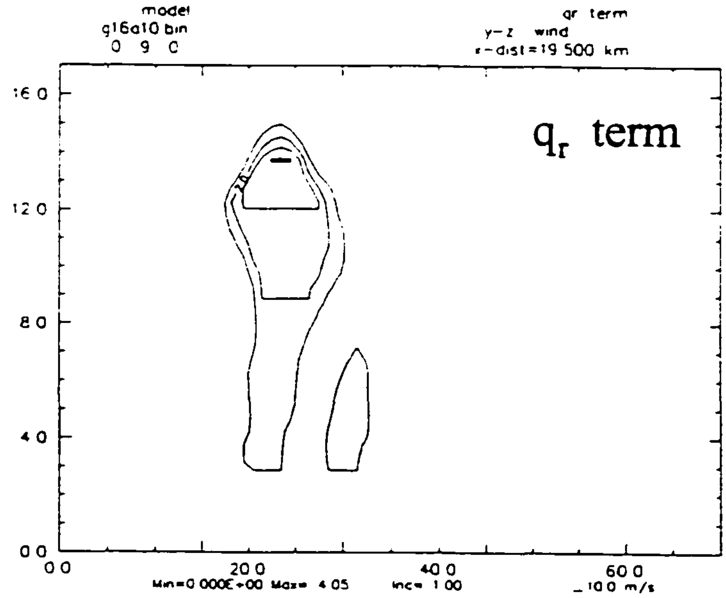

DDOP

d)

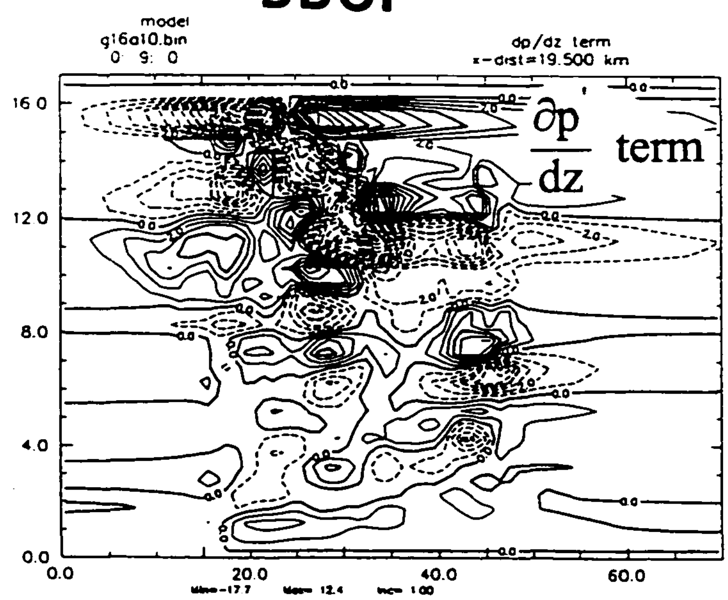

Figure 5.25 (Continued)

(which is identical to that for the SDVR case), all fields are significantly noisier than their SDVR counterparts, but show a similar pattern of contributions to the retrieved perturbation temperature. The vertical acceleration term (shown in Fig. 5.25b) is again the dominant factor in the narrowness of the positive perturbation temperature field within the storm updraft. It contributes more than + 5 K in a vertically elongated maximum coincident with the temperature maximum. The vertical pressure gradient term has a large number of local extrema, but also exhibits a fair amount of similarity to its SDVR counterpart.

As noted above, the rainwater contribution is identical to that from the SDVR case. Note that because of the increased data coverage at upper levels for the DDOP case, the region of maximum positive potential temperature contribution from the rainwater term is retained. That maximum of just over + 4 K, in conjunction with a small area of + 4 K in the vertical pressure gradient force term (located at x = 21, z = 14), accounts for the small extension of positive potential temperatures above z = 13 km in Fig. 5.25a. That feature and the general shape of storm-top positive and negative temperature anomalies are consistent with the storm-top wind field shown in Fig. 5.13a. As the strong updraft overshoots its equilibrium level and begins to spread laterally, the region of positive perturbation potential temperature narrows to a small extended feature suggestive of an overshooting top. Surrounding this small feature is a large region of negative temperature perturbation as one would expect above the equilibrium level.

5.3.2 Comparisons with linear theory

Linear theory for a Boussinesq fluid at rest provides a predicted relationship between the various terms in the vertical momentum equation. The ratio of the magnitudes of the various terms can also be used to assess the validity of the hydrostatic approximation.

While the assumptions made in the linear derivation are clearly violated by this dataset, it is nevertheless useful to compare the actual ratios with predictions from linear theory.

Consider the instantaneous vertical acceleration produced by buoyancy in a two-dimensional Boussinesq fluid initially at rest. The governing equations for the system are:

$$\frac{\partial w}{\partial t} + \frac{\partial P}{\partial z} = B \ , \tag{5.4}$$

$$\frac{\partial u}{\partial t} + \frac{\partial P}{\partial x} = 0 \ , \tag{5.5}$$

$$\frac{\partial u}{\partial x} + \frac{\partial w}{\partial z} = 0 \ , \tag{5.6}$$

where, $P = p'/\rho$, $B = - g\, \rho'/\rho_0$, and all other symbols have their usual meaning. (5.4) and (5.5) can be combined to obtain a Poisson equation for P:

$$\frac{\partial^2 P}{\partial x^2} + \frac{\partial^2 P}{\partial y^2} = \frac{\partial B}{\partial z} \ . \tag{5.7}$$

If a cellular initial buoyancy field is specified:

$$B = b \sin\left(\frac{\pi}{L} x\right) \sin\left(\frac{\pi}{H} z\right) \ , \tag{5.8}$$

then

$$\frac{\partial B}{\partial z} = \frac{\pi}{H} b \sin\left(\frac{\pi}{L} x\right) \cos\left(\frac{\pi}{H} z\right) \ , \tag{5.9}$$

and (5.7) can be solved for P:

$$P = -\frac{H\,L^2}{\pi\left(H^2 + L^2\right)}\, b \sin\left(\frac{\pi}{L}x\right)\cos\left(\frac{\pi}{H}z\right) \quad . \tag{5.10}$$

The vertical derivative of P can then be calculated from (5.10):

$$\frac{\partial P}{\partial z} = \frac{L^2}{\left(H^2 + L^2\right)}\, b \sin\left(\frac{\pi}{L}x\right)\sin\left(\frac{\pi}{H}z\right) \quad , \tag{5.11}$$

and (5.8) and (5.11) can be substituted into (5.4), to obtain the following relationship between the initial vertical acceleration and the magnitude of the initial buoyancy field:

$$\frac{\partial w}{\partial t} = \left(\frac{H^2}{H^2 + L^2}\right) b \quad . \tag{5.12}$$

This simple formula expresses the ratio of the vertical acceleration to the buoyancy as a function of the aspect ratio (H/L = height / width) of the initial buoyancy field. Following discussions by Fiedler (1995), Houze (1993) and others, (5.12) also expresses the degree of departure from hydrostatic balance, and has the following physical interpretation. The initial buoyancy perturbation induces an opposing vertical pressure gradient force [termed the buoyancy pressure gradient force by Houze (1993)] that partially offsets the vertical acceleration induced by the initial buoyancy field. The degree to which the buoyancy pressure gradient force counteracts the original buoyancy force provides a measure of how hydrostatic the flow is.

Equation (5.12) is plotted in Fig. 5.26, illustrating the derived relationship between vertical acceleration / buoyancy ratio and the aspect ratio (H/L) of the buoyancy field. As can be seen, the left and right ends of the curve approach two extreme cases. The left side

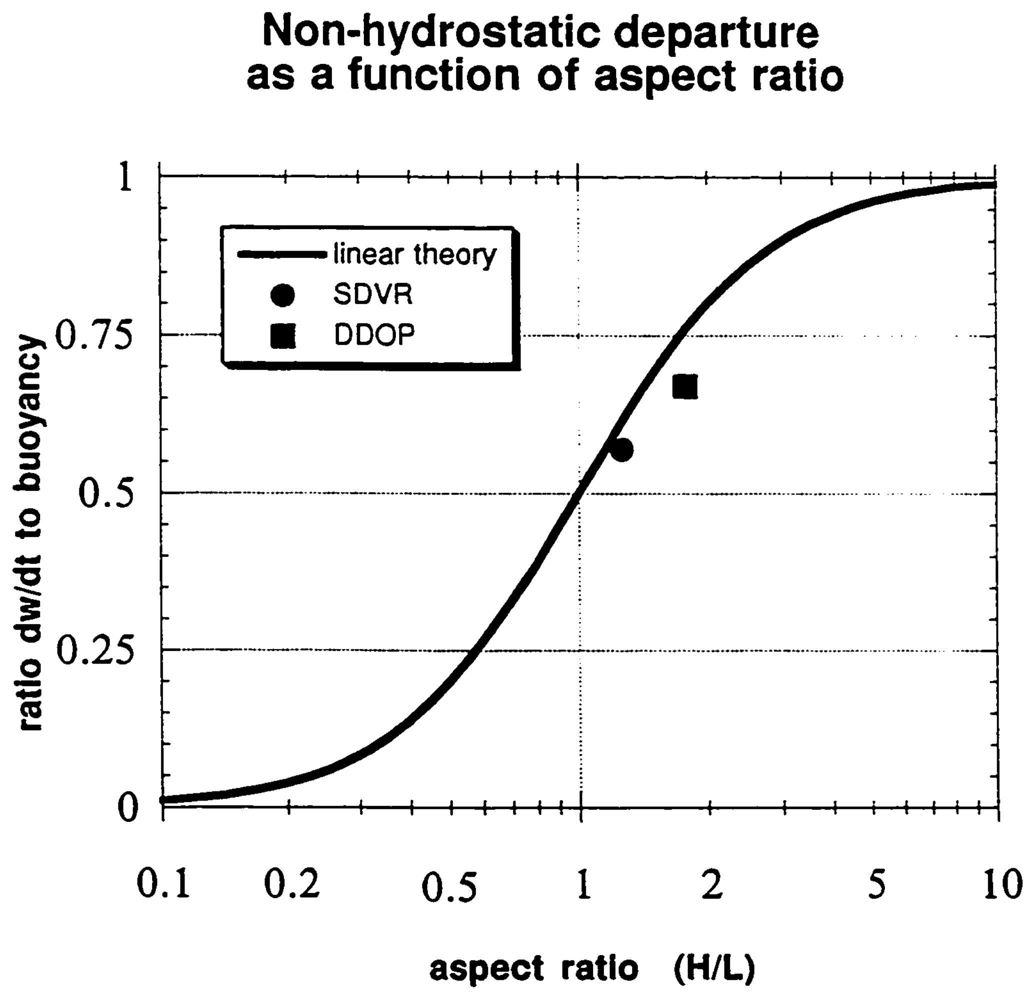

Figure 5.26 Linear theory predicted relationship between the vertical acceleration / buoyancy ratio and the aspect ratio (height / width) of the buoyancy field.

corresponds to an infinitely wide buoyancy field, in which the vertical pressure gradient force exactly cancels the buoyancy force, and the resultant vertical acceleration is zero. The right side corresponds to an infinitely narrow buoyancy field, in which the vertical pressure gradient force is zero, and the vertical acceleration is equal to the buoyancy. The first case is completely hydrostatic, while the second case is completely non-hydrostatic. These differences can be understood physically by noting that as the width of the buoyant region increases, more work must be done to displace the environmental air in the path of the vertically accelerated buoyant region.

The ratio of the vertical acceleration to the buoyancy can be easily calculated for the Doppler-derived fields shown in Figs. 5.24 and 5.25. Because water vapor and cloudwater effects have been neglected in the thermodynamic retrieval, the buoyancy is found by subtracting the rainwater term from the retrieved potential temperature term. Choosing a location near the approximately co-located vertical acceleration and temperature maxima, subjective estimates of 0.57 and 0.67 have been obtained for the SDVR and DDOP ratios. Determining the aspect ratio (H/L) of the buoyancy field is a bit more difficult; however, reasonable subjective estimates of 1.3 and 1.8 have been obtained for the SDVR and DDOP cases, respectively. These pairs of values have been used to define points on Fig. 5.26 for both the SDVR and DDOP cases, thereby allowing a comparison of the retrieval results with the predictions from linear theory.

As shown in Fig. 5.26, both the SDVR case and the DDOP case are in reasonably good agreement with the predictions from linear theory. It is perhaps not surprising that compared to the SDVR case, the DDOP case has both a narrower updraft (responsible for the larger aspect ratio) and a larger vertical acceleration (relative to the magnitude of the buoyancy field). Said another way, the DDOP fields are less hydrostatic. Calculations of this type have not been made for the UVVR case, but the results would almost certainly be very similar to the SDVR results. The fact that the degree of hydrostatic departure for both DDOP and SDVR cases fits theoretical predictions reasonably well provides a further degree of confidence in the suitability of the retrieved fields for initializing a numerical prediction model.

5.4 Specification of moisture fields

The final step in preparing the initial forecast fields is the specification of the water vapor within the storm volume. As discussed earlier, the rainwater field is computed from the observed reflectivity during the hole-filling step for use in the thermodynamic retrieval, and no attempt is made to initialize the cloudwater field. The present method of specifying the water vapor based on simple saturation assumptions within the storm updraft regions is perhaps the most ad-hoc step in the entire retrieval procedure. As such it must be viewed as a temporary solution, to be replaced in the future by a more sophisticated procedure. One possible replacement is the reverse Kessler technique described by Zhang and Carr (1998).

The goal of the present procedure is simply to use the available information (principally the rainwater and vertical velocity information) to prescribe the water vapor field in regions where there is a high degree of confidence about what the likely value should be; thus, the rationale behind saturating the updrafts within the reflectivity region. Originally, a threshold of $w > 0$ within the reflectivity region was used. This, however, lead to the generation of a large amount of spurious convection along the lateral edge of the original storm, especially for the DDOP case. Examination of the fields indicated that weak vertical velocity maxima (1-2 m s^{-1}) at low-levels were being saturated, triggering the spurious convection.

In light of this, and after examining the water vapor patterns in a number of idealized supercell simulations, a more stringent threshold of $w > 3$ m s^{-1} and $qr > 0.1$ g kg^{-1} was adopted. This restricted the saturation to regions of coherent updraft away from the extreme edges of the storm-volume. The result was a dramatic reduction in the amount of spurious convection with little impact on the initial development of the main storm. Recognizing the somewhat arbitrary nature of the chosen thresholds, a sensitivity experiment is performed in Chapter 6 in which the model is initialized without any perturbation water vapor field.

Fig. 5.27 illustrates the total and perturbation water vapor fields produced by the saturation procedure for the $x = 19.5$ vertical cross-section. Note the pronounced dry layer in the sounding ($q_v < 1.1$ g kg^{-1}) centered at $z = 4$ km (see Fig. 3.3a). As can be seen in Fig. 5.27a, the saturation assumption results in the high values of water vapor near the ground being extended upward in the storm updraft. Fig. 5.27b more clearly delineates the region of water vapor enhancement and indicates a maximum increase of more than 7.5 g kg^{-1} near the bottom of the dry layer.

5.5 Summary of thermodynamic retrieval results

The results shown in this chapter indicate that realistic thermodynamic fields are retrieved from the sequence of three single-Doppler retrieved 3-D wind fields. Despite the fairly large value for the momentum checking statistic, the SDVR retrieved fields were qualitatively similar to those from the dual-Doppler analysis. Furthermore, simple comparisons with predictions from linear theory show good agreement for both the orientation of the pressure couplets relative to the updraft maxima and the degree of departure from hydrostatic balance.

While not impacting the thermodynamic retrieval (because A and B were set equal to zero outside the storm volume), the simple procedure for blending the storm wind field with the background base-state sounding produced a smooth velocity transition within the

a)

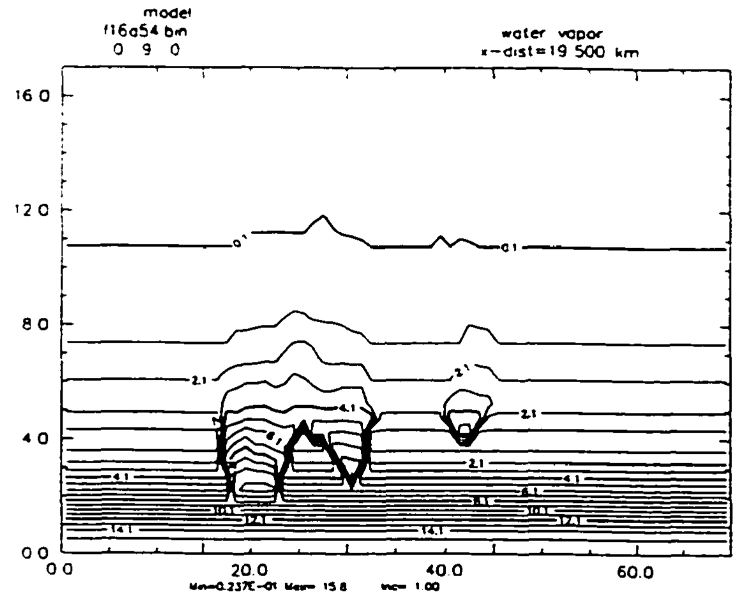

b)

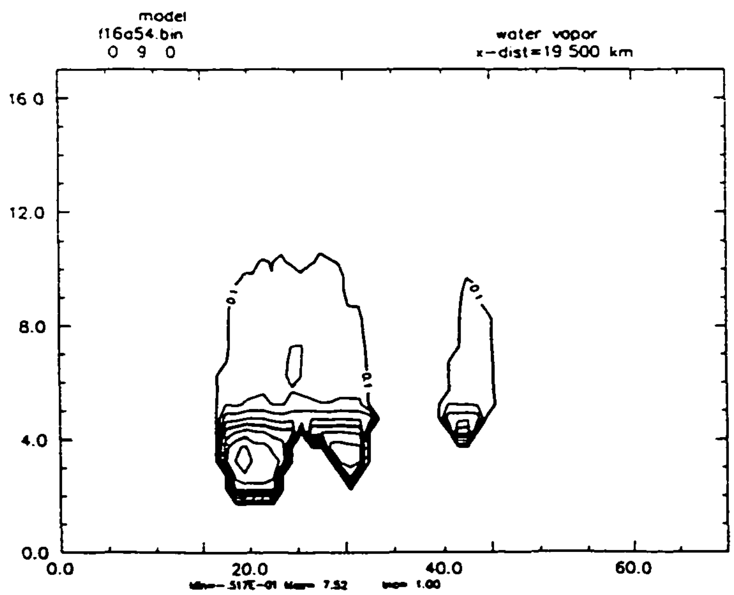

Figure 5.27 2239 UTC N-S cross-section (x = 19.5) of the specified a) total water vapor and b) perturbation (from the base state sounding) water vapor. Both fields are contoured every 1 g kg^{-1}.

data void region. For the SDVR case, significant departures from 3-D anelastic mass conservation were observed only along the storm boundary and were significantly reduced by the variational wind adjustment procedure.

Perhaps the most surprising result in this chapter is that the retrieved temperature fields for the SDVR and UVVR cases are nearly identical. This poses an important question to be answered by the numerical prediction experiments in Chapter 6. As described in Chapter 4, the principal difference between the SDVR and UVVR wind fields was the addition of perturbation azimuthal velocity to the SDVR winds. At low-levels, this additional component is composed almost entirely of polar vorticity; however, at upper-levels it does contain some azimuthal divergence. If this additional component (obtained from the pseudo-streamfunction in the two-scalar retrieval) has virtually no impact on the retrieved temperature field (compared with the UVVR experiment), will it have any impact on the numerical prediction? With that question in mind, as well as the fundamental question of forecast accuracy for all three sets of initial fields (DDOP, SDVR, and UVVR), I now move to the prediction portion of this study.

CHAPTER 6

NUMERICAL PREDICTION RESULTS

As a final test of the single-Doppler retrieval procedure, the retrieved fields have been used to initialize a numerical prediction model. While numerical prediction experiments represent a very useful and practical way to test the quality of the initial fields, it must be emphasized that a poor prediction does not necessarily indicate that a poor retrieval of the initial fields has occurred. This is because a number of other factors, most notably inadequacies in the numerical model, could lead to a poor forecast regardless of the quality of the initial conditions. If, however, the numerical model accurately predicts the observed storm evolution, then there is increased confidence in the quality of the retrieved initial fields.

For each of the three sets of retrieved fields in Chapter 5, a numerical prediction has been initiated and the model-predicted fields evaluated against a time series of dual-Doppler verification analyses. The three sets of retrieved fields include the dual-Doppler derived fields (experiment DDOP), the single-Doppler retrieved fields (experiment SDVR), and the fields from the simplified single-Doppler case in which only the mean horizontal wind components (calculated from the single-Doppler radial velocity) and the perturbation radial velocity and its contribution to the perturbation polar velocity are retained (experiment UVVR). From these experiments, the accuracy of the SDVR prediction can be evaluated not only with respect to the observed storm evolution, but also with respect to the differences in the input wind fields between the SDVR case and the DDOP and UVVR cases. The predicted storm evolution is also verified against projections based on the 0-6 km mean wind and a continuation of the initial storm motion. Finally, an idealized "bubble" simulation is conducted, using the base-state sounding and hodograph (Fig. 3.3). It is described in Appendix C, and serves as another benchmark by which the skill of the SDVR prediction can be judged.

Table 6.1 summarizes the set of single- and dual-Doppler experiments, the results of which are presented in Section 6.2, as well as two sets of sensitivity experiments that are described in Section 6.3. The first set of sensitivity experiments examines the impact on the predicted storm evolution of variations in the initial moisture specification. The second set of sensitivity experiments examines the impact of initial mass (retrieved pressure and temperature) versus velocity fields on the predicted storm evolution. The presentation of the prediction results is preceded by a brief description of the numerical model in Section 6.1 and followed by a brief summary in Section 6.4

6.1 Description of the numerical model

The numerical model used for this study is the Advanced Regional Prediction System (ARPS) (Xue et al. 1995), a three-dimensional non-hydrostatic fully-compressible model developed at the Center for Analysis and Prediction of Storms (CAPS). Using an Arakawa C grid (Arakawa and Lamb 1977), prognostic equations for the three Cartesian velocity components, potential temperature, pressure, turbulent kinetic energy, and mixing ratios for several microphysical variables are solved within the ARPS model. The severe time-step constraint associated with fully-compressible models is circumvented by using a mode-splitting technique, whereby advective terms are calculated using a big time step and acoustic terms are calculated using a small time step. For the time-differencing, a second-order leap-frog scheme with an Asselin (1972) time-filter is used for the big time step,

Table 6.1 Summary of the numerical prediction experiments.

Name	Wind field source	Fields retained	Field removed
Single- and dual-Doppler experiments			
DDOP	DDOP	$u, v, w, p', \theta', q_v', q_r$	none
SDVR	SDVR	$u, v, w, p', \theta', q_v', q_r$	none
UVVR	UVVR	$u, v, w, p', \theta', q_v', q_r$	none
Moisture sensitivity			
SDVR	SDVR	$u, v, w, p', \theta', q_v', q_r$	none
NOQV	SDVR	$u, v, w, p', \theta', q_r$	q_v'
NOQR	SDVR	$u, v, w, p', \theta', q_v'$	q_r
NOQQ	SDVR	u, v, w, p', θ'	q_v', q_r
Thermodynamic versus velocity fields			
SDVR	SDVR	$u, v, w, p', \theta', q_v', q_r$	none
NOPT	SDVR	u, v, w, q_v', q_r	p', θ'
NOVL	SDVR	p', θ', q_v', q_r	u, v, w

while a first-order forward-backward scheme is used for the small time-step. The space-differencing is accomplished using a second order quadratically conserving scheme.

For this application, a Kessler (1969) explicit warm-rain microphysics scheme is used, whereby conservation equations for water vapor, cloud water and rainwater mixing ratios are solved. A Smagorinsky (1963) / Lilly (1962) diagnostic first-order turbulence closure is used, in which the mixing coefficients are diagnosed from the deformation and stability of the grid-resolved flow. For the lateral boundary conditions, the Klemp and Lilly (1978) / Durran and Klemp and (1983) wave-radiation open boundary condition is used. In this modification to the Orlanski (1976) scheme, the wave phase speed is vertically averaged before being applied to a one-dimensional wave equation to determine the time-tendencies of the normal velocities at the lateral boundaries. Rigid boundaries are used for the model top and bottom.

Table 6.2 provides a summary of some of the important model parameter settings used in this study. Additional information concerning the ARPS model can be found in the ARPS User's Guide (Xue et al. 1995).

6.2 Single- and dual-Doppler prediction results

In this section, results are presented from the DDOP, SDVR and UVVR numerical prediction experiments summarized in Table 6.1. The predictions are initiated at 2239 UTC, and the integrations carried forward until 2322 UTC (the time of the last dual-Doppler verification analysis), resulting in a 43 minute forecast period.

Because the focus of this study is on retrieving initial forecast fields rather than performing a comprehensive investigation of the predicted storm evolution, the analysis of the prediction results is limited to the following four criteria. First, model-predicted and verification low-level (z = 2.25) rainwater and horizontal wind vector fields are shown to

Table 6.2 Summary of the ARPS model parameters used in the prediction experiments.

Parameter	**Symbol**	**Value**
Horizontal domain size	L_x x L_y	100 x 100 km
Vertical domain size	L_z	17 km
Horizontal grid spacing	Δx , Δy	1000 m
Vertical grid spacing	Δz	500 m
Large time step	Δt	6 s
Small time step	$\Delta \tau$	1 s
Turbulent Prandtl Number	K_m / K_h	1.0
Mixing coefficient limit	kmlimit	1.0
2nd order vertical mixing coefficient	cfcm2h	$1(10)^{-3}$ s^{-1}
4th order vertical mixing coefficient	cfcm4h	$1(10)^{-3}$ s^{-1}
Divergence damping coefficient	divdmpnd	0.05
Rayleigh damping coefficient	cfrdmp	0.003 s^{-1}
Rayleigh sponge bottom	zbrdmp	12 km
Asselin time filter	flteps	0.1

illustrate the similarities and differences among the various storm evolutions. The model prediction plots are augmented by the inclusion of the two-dimensional rainwater correlation coefficient with respect to the dual-Doppler verification. Also, individual precipitation cores are identified on each plot and tracked throughout the prediction. A summary plot of the tracks of the associated cyclonic circulation centers is then presented and the observed and model predicted storm motions are compared with simple projected storm motions.

Second, a more comprehensive evaluation of the correlation between the model predicted and dual-Doppler-derived verification rainwater fields is presented. Time series of three-dimensional correlation coefficients are shown as well as vertical profiles of two-dimensional profiles for selected times. Third, time-series of the domain maximum vertical velocity (sampled at one minute intervals) are shown to provide an overview of the updraft evolution in the predicted storms. Comparisons are also made with the corresponding values from the dual-Doppler verification analyses (available at approximately four minute intervals). Finally, the time-evolution of the predicted and verifying maximum vertical vorticity profiles is shown.

6.2.1 Evolution of the low-level fields

Fig. 6.1 shows the z = 2.25 rainwater and horizontal vector fields for the 2251 UTC dual-Doppler verification and the three corresponding 12-minute predictions. Indicated on each of the plots is the main precipitation core (denoted by an "M") and a weaker eastern precipitation core (denoted by an "E"). Consistent with their high rainwater correlations, the rainwater fields for both the DDOP and SDVR predictions look quite similar to the dual-Doppler verification. Despite a similarly high correlation coefficient, the UVVR rainwater field has decreased in magnitude. Also, the UVVR low-level wind field seems

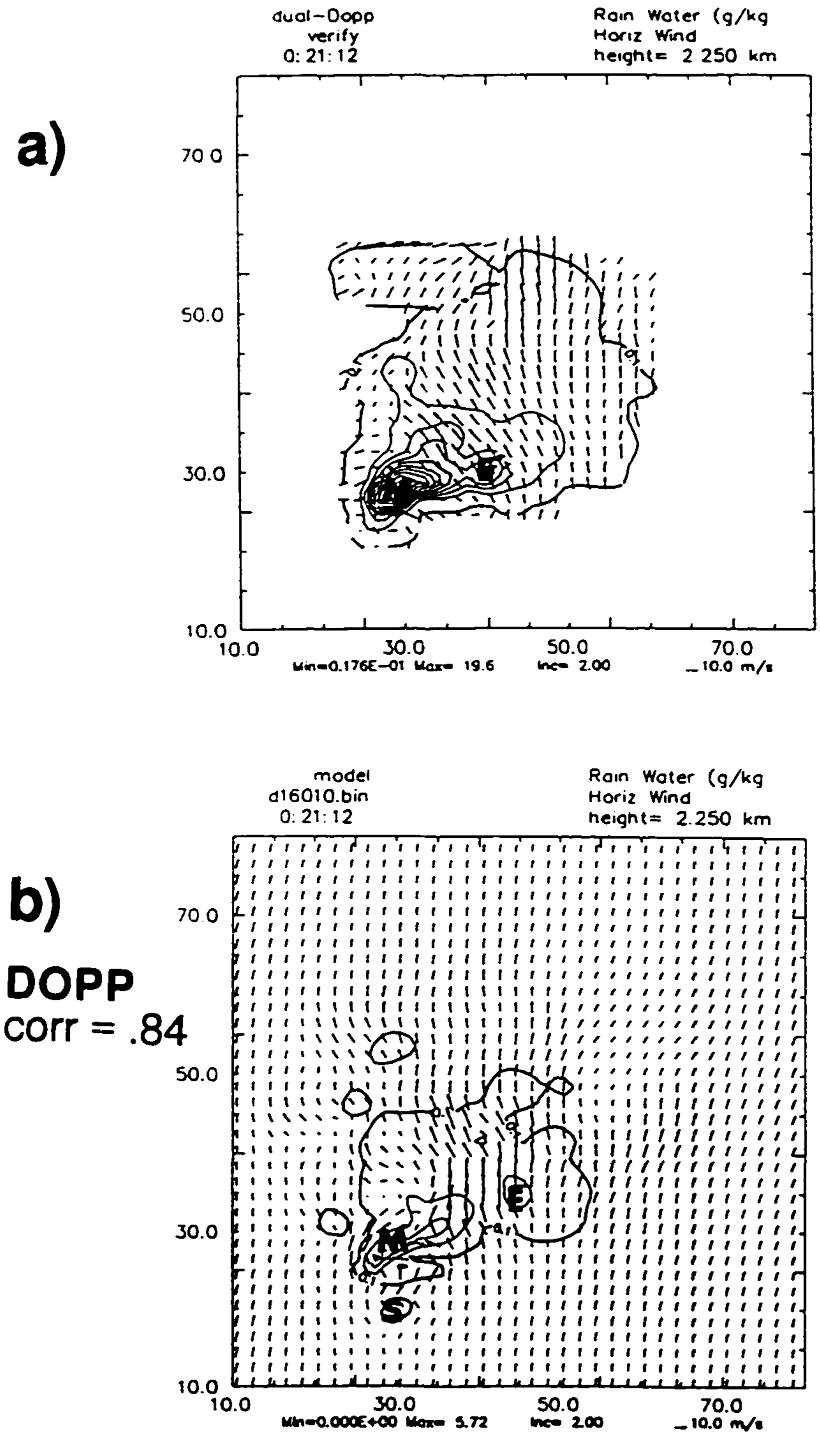

Figure 6.1 2251 UTC low-level (z = 2.25 km) rainwater and storm-relative wind vectors for a) the dual-Doppler analysis, and the 12-minute predictions from b) the DDOP case, c) the SDVR case and d) the UVVR case. Rainwater is contoured every 2 g kg^{-1}.

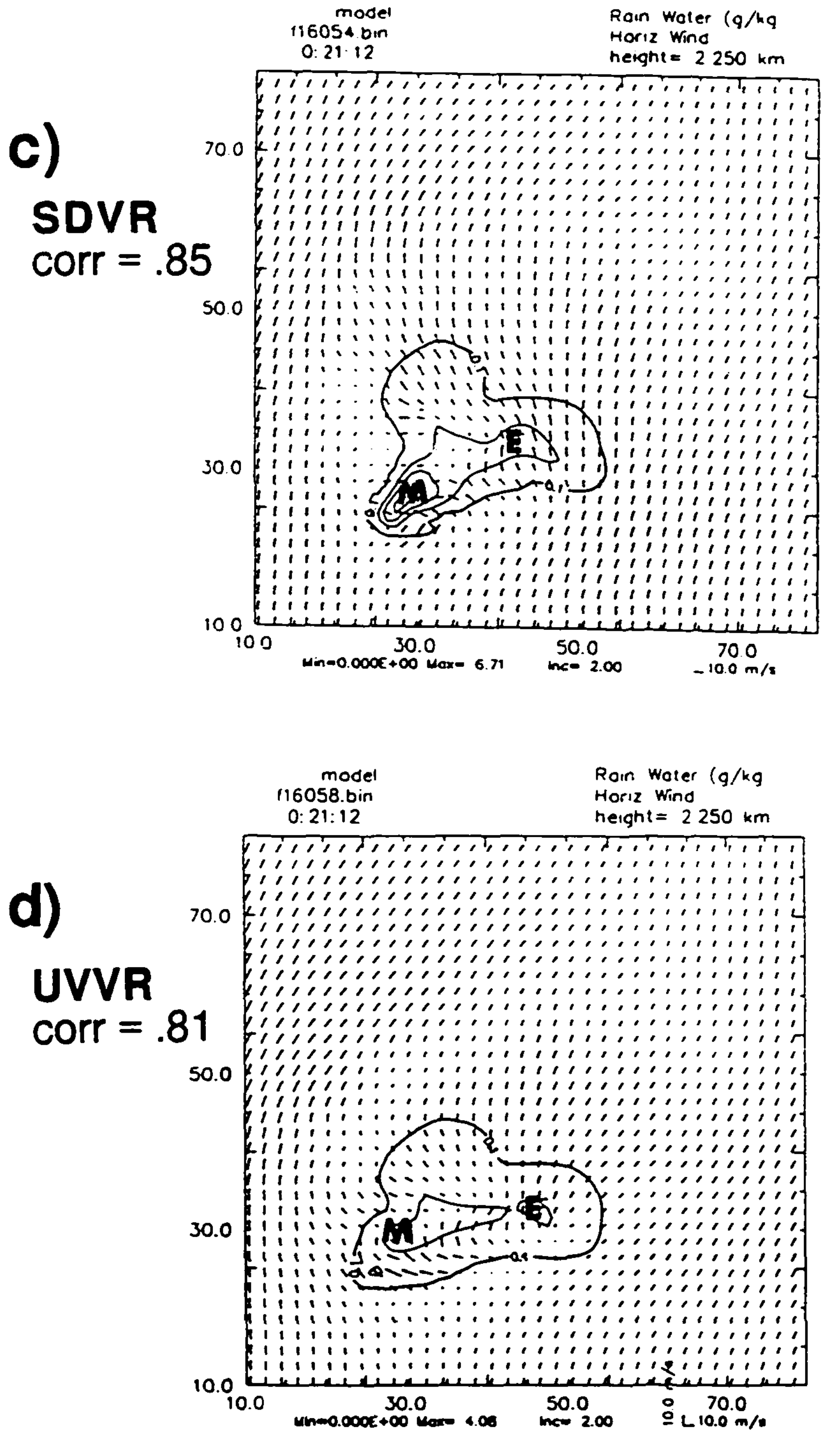

Figure 6.1 (Continued)

to be lacking the convergence and cyclonic vorticity found in the southwestern portion of the storm for the other experiments.

It is important to note that the extremely large rainwater values in the southwest portion of the verification storm are due to the poor behavior of the semi-empirical Z-qr relationship [Eq. (2.63)] for reflectivity values in excess of 60 dBZ, where hail is likely an important factor. At 2251 UTC, the Arcadia storm was producing golf-ball sized hail (Taylor 1982) and had a reflectivity maximum of about 65 dBZ.

Despite the obvious similarities between the verification and the DDOP and SDVR predictions, some differences are apparent. First, the wind field north of the main precipitation core is not well predicted. The verification (Fig. 6.1a) shows a pronounced zone of horizontal convergence extending north, then northeast from the precipitation core. Both prediction experiments show a region of very weak winds north of the precipitation core. Second, in the DDOP forecast a number of weak precipitation cores have developed around the periphery of the main storm. Of these, the core to the south ($x = 30$, $y = 19$) is the most significant, as will be seen at the next verification time. Hereafter, it (and a corresponding feature that develops in the SDVR prediction) will be referred to as the southern precipitation core and denoted by an "S".

Fig 6.2 shows the verification fields for 2305 UTC as well as the corresponding 26-minute predictions. The observed storm was producing an F2 tornado at this time and Fig. 6.2a shows the well-defined low-level vortex signature centered near $x = 35$, $y = 28$. In the DDOP prediction, the position of the main precipitation core (near $x = 39$, $y = 39$) is slightly north of the verification; however, the southwestern portion of the storm (where the tornadic circulation is occurring in Fig. 6.2a) has weakened too rapidly. Nearly in its place is the southern precipitation core, which has intensified and begun to merge with the original storm. The SDVR prediction shows a very similar evolution, with the original updraft and precipitation core weakening too quickly, but being replaced by a new

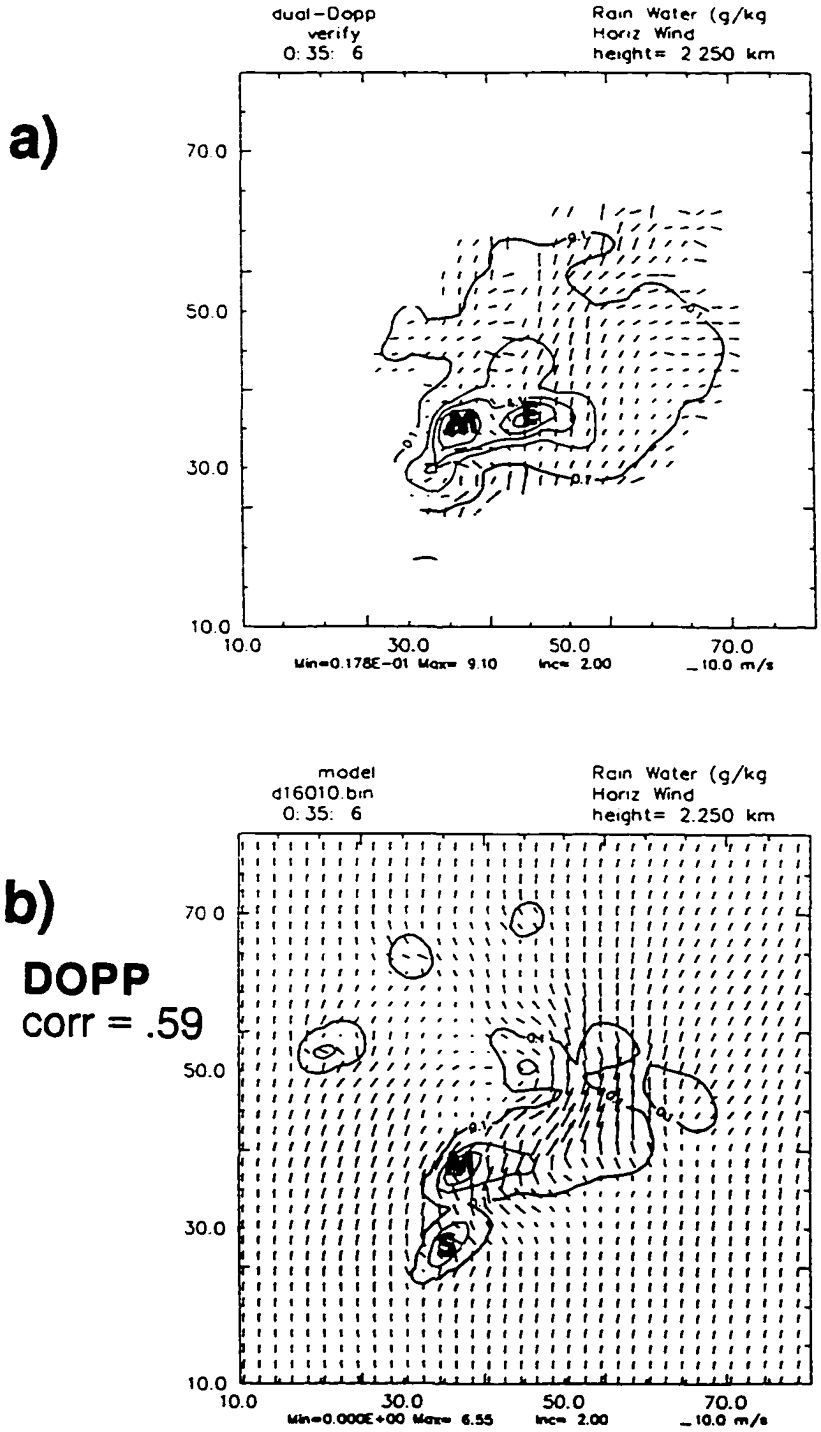

Figure 6.2 2305 UTC low-level (z = 2.25 km) rainwater and storm-relative wind vectors for a) the dual-Doppler analysis, and the 26-minute predictions from b) the DDOP case, c) the SDVR case and d) the UVVR case. Rainwater is contoured every 2 g kg^{-1}.

c)

SDVR
corr = .76

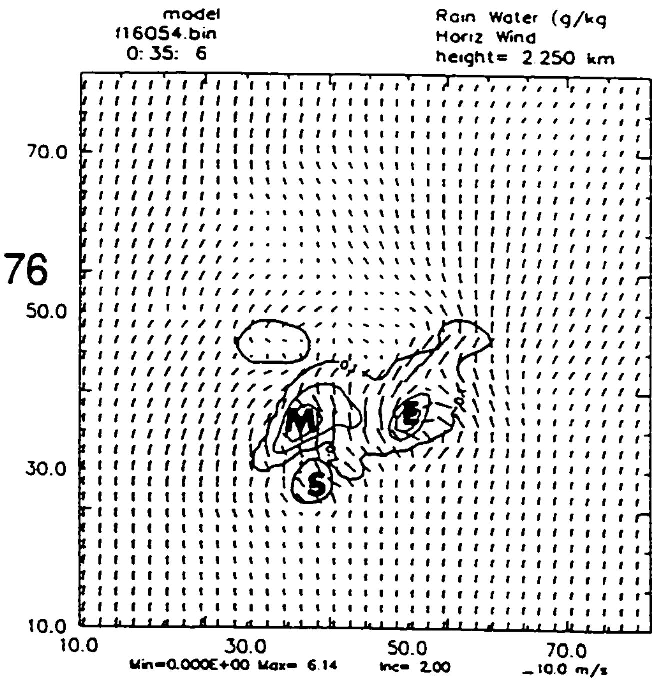

d)

UVVR
corr = .59

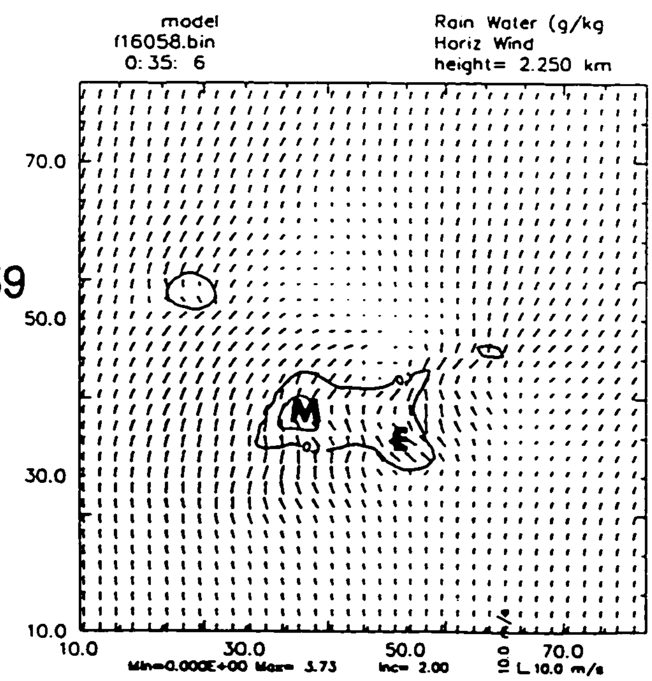

Figure 6.2 (Continued)

precipitation core forming just to its south. An additional development in the SDVR prediction is the intensification of the eastern precipitation core (near x = 50, y = 34). A weak reflection of the eastern precipitation core is also seen in the UVVR prediction. Overall, however, the UVVR rainwater continues to be too weak and the storm appears to be dissipating. Consistent with this trend is a northward displacement of the storm in a direction more aligned with the mean wind. Of the three predictions, the SDVR case has the highest correlation coefficient.

It is not clear why in both the DDOP and SDVR predictions, the original precipitation core weakens too quickly and a new precipitation core forms to its south. Detailed examination of the low-level fields for both cases (not shown) suggests that the gust front may have surged too far to the southeast, causing the main updraft to become cut off from the warm moist boundary layer inflow. This may be linked to an excessive amount of rainwater descending to the ground, producing too strong of a cold pool. Unfortunately, observations to verify the strength of the predicted cold pool are not readily available.

The predicted evolution of the rainwater, cold pool and gust front is somewhat problematic. On the one hand, the model is initialized without a low-level cold pool at a point in the storm evolution when one surely existed. On the other hand, the model is also initialized with large amounts of suspended rainwater and a simplistic microphysics scheme that allows too much precipitation to fall to the ground (as opposed to being vented out of the storm-top as ice-crystals in the anvil). The ultimate combined impact on the storm evolution from these two known deficiencies is unclear. Sensitivity experiments will be presented in Section 6.3.1, however, that illustrate the pronounced influence of the initial rainwater field on the formation of the low-level cold pool.

The rainwater and horizontal wind fields at 2313 UTC, three minutes after the tornado's demise and 34 minutes into the numerical prediction, are shown in Fig. 6.3. They indicate an increasing disagreement between the verification and model-predicted

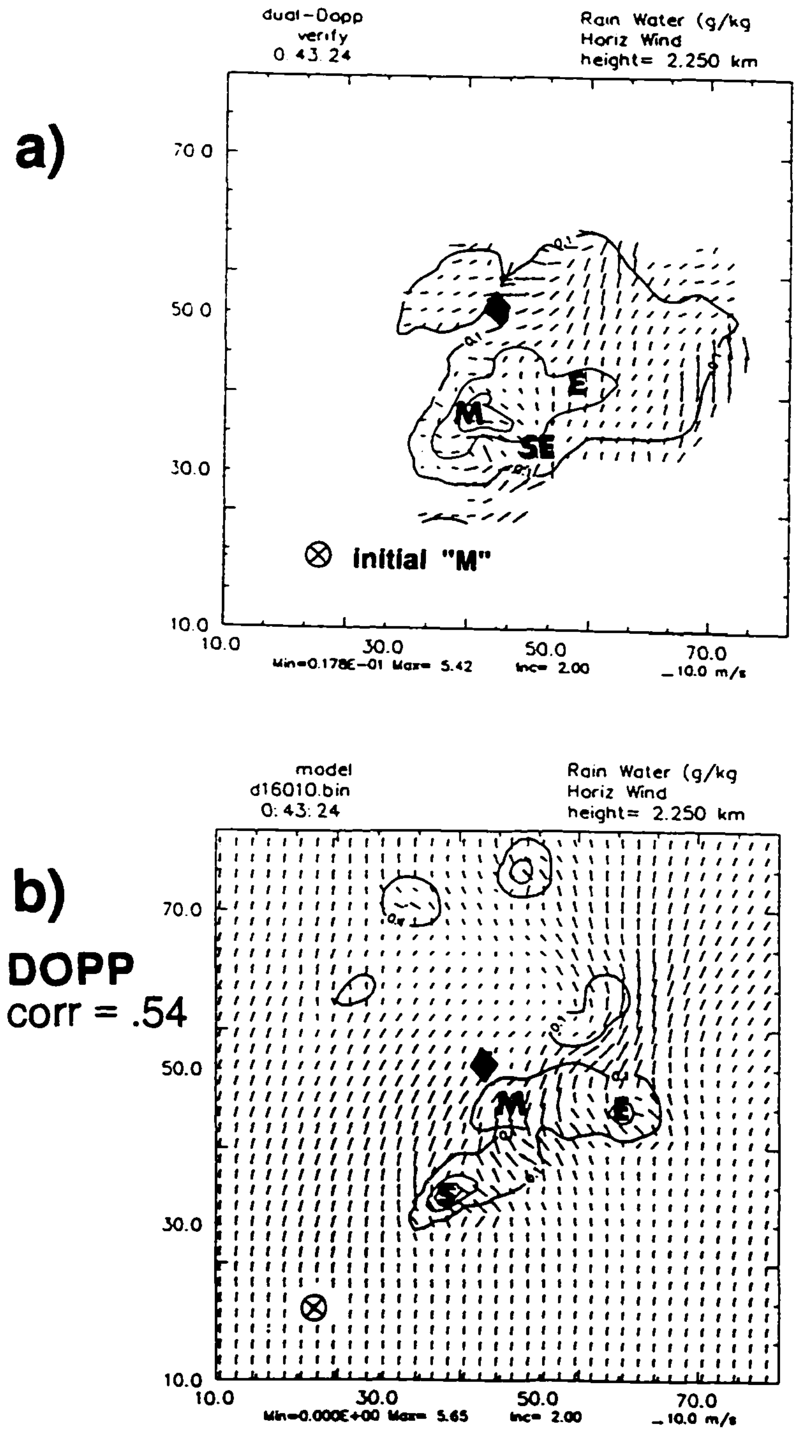

Figure 6.3 2313 UTC low-level (z = 2.25 km) rainwater and storm-relative wind vectors for a) the dual-Doppler analysis, and the 34-minute predictions from b) the DDOP case, c) the SDVR case and d) the UVVR case. Rainwater is contoured every 2 g kg^{-1}.

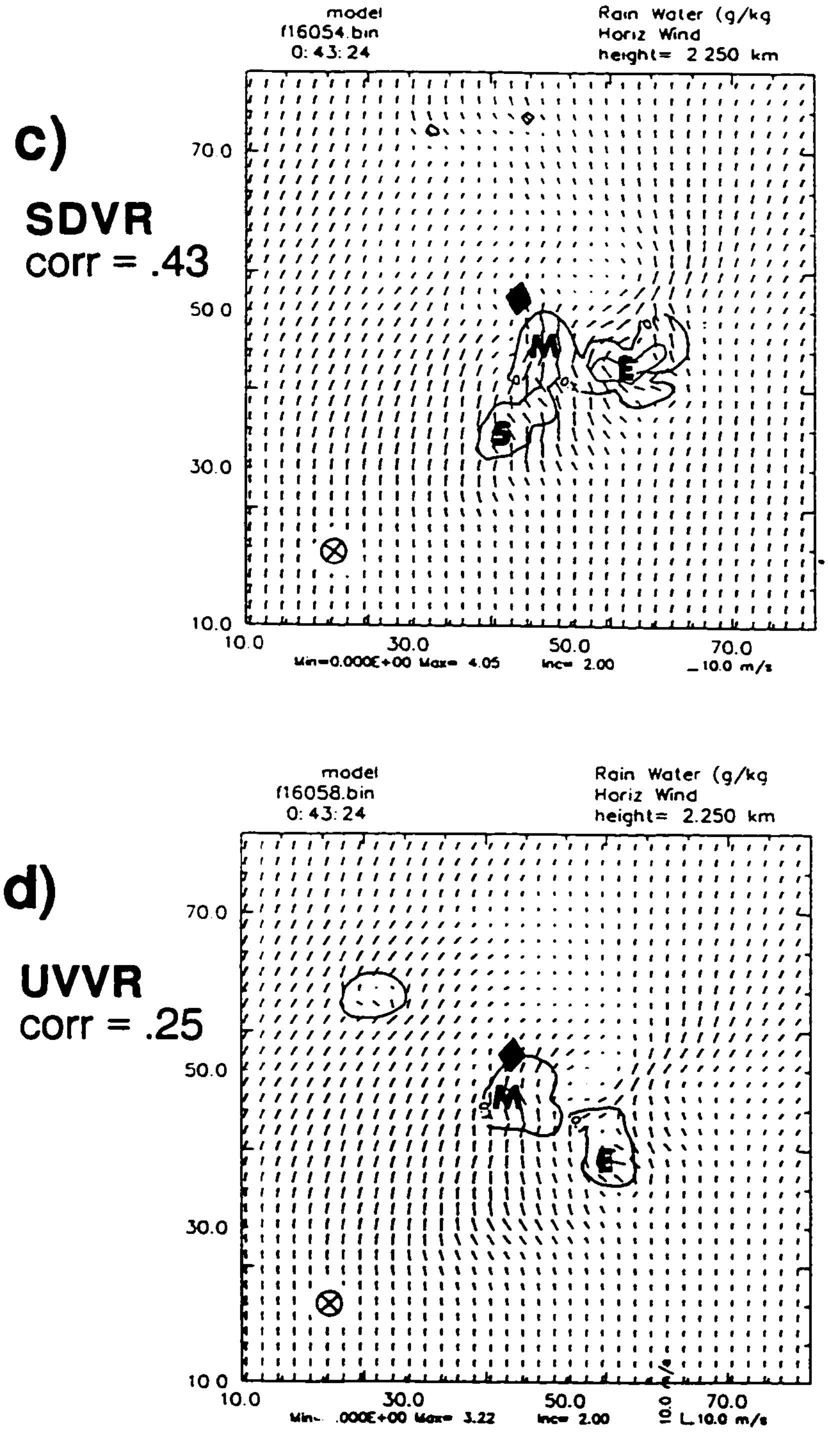

Figure 6.3 (Continued)

fields as indicated by the reduced correlation coefficients. Curiously, in both the DDOP and SDVR predictions, the southern precipitation core now corresponds quite favorably with the main core in the verification. For the UVVR forecast, there is no such southern development and the main and eastern precipitation cores continue to weaken, resulting in a very poor correlation coefficient.

Careful examination of the verification rainwater field (confirmed by examination of plots at other levels) indicates the development of a new precipitation core southeast of the observed main storm. This feature (referred to as the southeastern precipitation core and denoted by "SE"), can be seen in the reflectivity bulge near x = 49, y = 33 in Fig. 6.3a and will become the dominant cell by the final verification time.

Consideration of the development of the southern cells in DDOP and SDVR prediction experiments versus the actual development of a southeastern cell allows for at least two possible interpretations. The first is that the DDOP and SDVR southern precipitation cores essentially replace the main cell that has weakened too quickly, and the observed southeastern development has no predicted counterpart. The second interpretation is that the model-predicted southern development (for both the DDOP and SDVR forecasts) does in fact correspond to the observed southeastern development, albeit with a significant spatial error. Regardless of the interpretation, *the 34-minute DDOP and SDVR predictions manage to place their most intense precipitation cores within 5-km of the most intense observed precipitation core.*

Comparison of the location of the observed main precipitation core with a persistence forecast calculated from a 0-6 km density weighted base-state mean wind (indicated by the ♦ in Fig. 6.3a) illustrates the observed rightward propagation of the main storm relative to the mean wind. Similar comparisons for the predicted storms show a less substantial rightward propagation for the weakening main cell.

A problem common to all three prediction experiments is the absence of a large, weak rainwater region surrounding the main precipitation core. This is likely due to the use of a warm-rain microphysical scheme that does not include ice-species. Because of this, the predicted storms do not develop realistic anvils and are considerably shallower than the verification storms. Besides possibly impacting the strength of the cold pool as discussed previously, the lack of ice-microphysics also likely precludes the formation of a large, weak precipitation region around the storm.

The storm fields from the final verification time (2322 UTC, 43 minute forecast) are shown in Fig. 6.4. In the verification analysis (Fig. 6.4a), the new precipitation core to the southeast of the main core is now clearly apparent near $x = 51$, $y = 39$. The southeastern core is associated with a cyclonically rotating updraft, but never attains the strength observed previously in the main core, which is now weakening near $x = 42$, $y = 46$ (DB97). Also apparent in the verification is the northern fringe of a large separate storm which is entering the analysis domain from the south.

Examination of the SDVR fields in Fig. 6.4c (and at other levels which are not shown) indicates that the southern precipitation core has dissipated and three new weak cells have formed along its outflow boundary. While the DDOP prediction has a correlation coefficient only slightly higher than that of the SDVR prediction, its predicted southern precipitation core still matches the observed main precipitation core reasonably well. Conspicuously absent from all of the prediction experiments is a feature corresponding to the observed southeastern precipitation core. No coordinated dual-Doppler sampling of the Arcadia storm occurred after 2322 UTC. Subsequent single-Doppler scans indicated a weakening multicellular storm (DB97).

The accuracy of the SDVR and DDOP predicted storm motion is evaluated by comparing the predicted and observed locations of the $z = 3.25$ km cyclonic circulation center at various times. Use of this particular feature proved to be a very precise method

a)

b)

DOPP
corr = .25

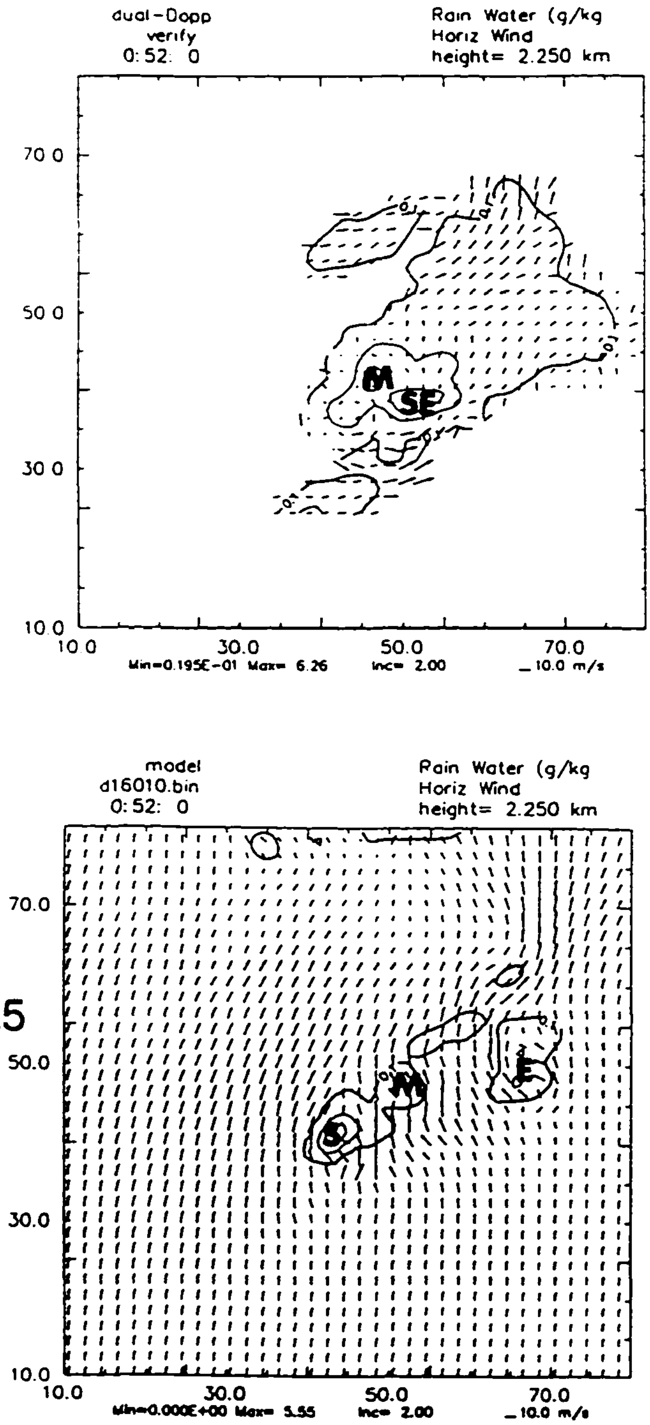

Figure 6.4 2322 UTC low-level (z = 2.25 km) rainwater and storm-relative wind vectors for a) the dual-Doppler analysis, and the 43-minute predictions from b) the DDOP case, c) the SDVR case and d) the UVVR case. Rainwater is contoured every 2 g kg^{-1}.

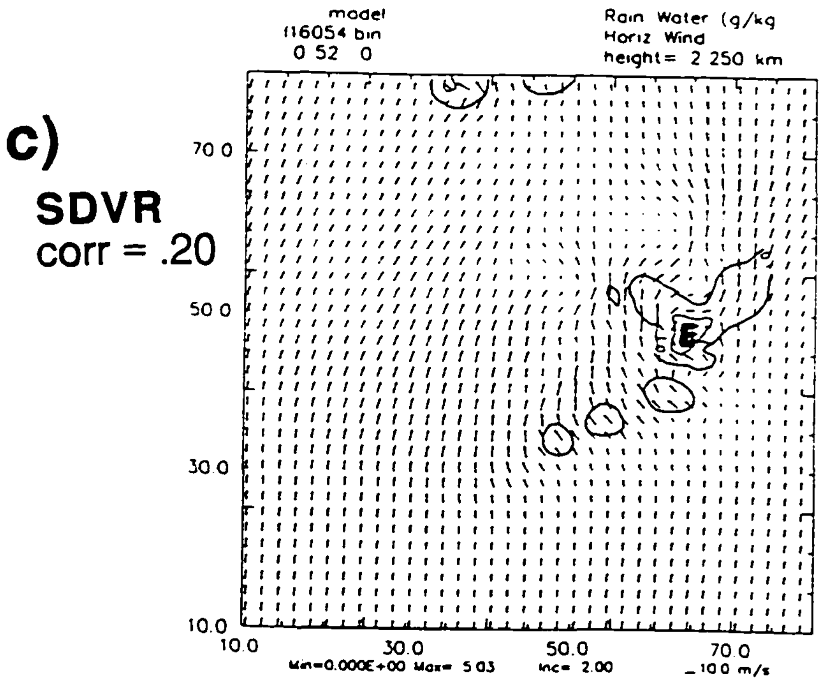

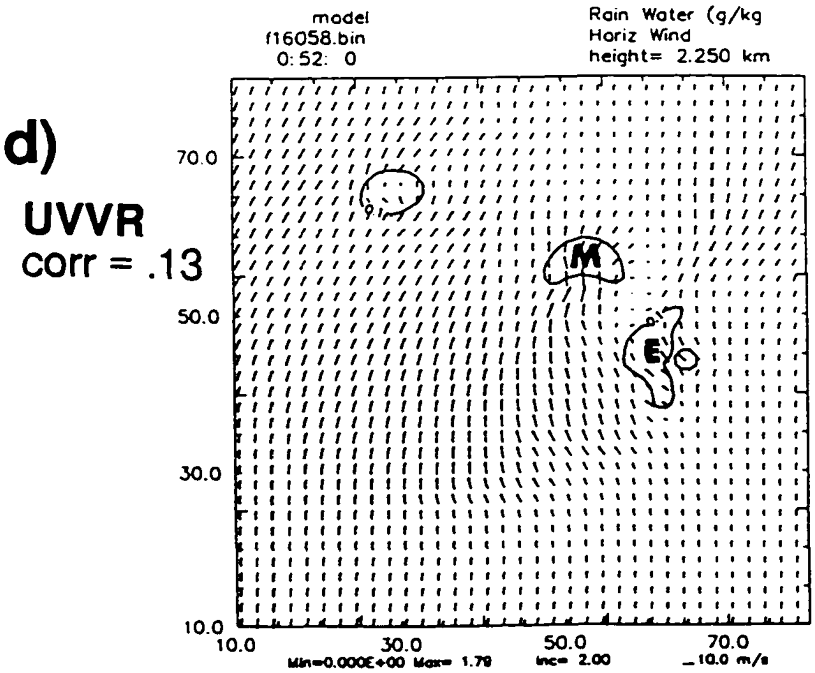

Figure 6.4 (Continued)

for tracking the storm motion as a coherent center was found that corresponded to each of the labeled precipitation cores in Figs. 6.1-4. Fig. 6.5 shows the location of these centers at the model initial time (2239 UTC) and the four subsequent times shown in Figs. 6.1-4. The DDOP, SDVR and UVVR predicted main ("M") circulation centers are shown in Fig. 6.5a, and the DDOP and SDVR predicted southern ("S") circulation centers are shown in Fig. 5.6b (UVVR never developed a southern precipitation core or circulation center). The location of the observed main circulation center is shown in both plots, as are extrapolated circulation center locations based on the 0-6 km mean wind and the initial circulation center motion.

As can be seen in Fig. 6.5a, the predicted location of the main circulation center is quite accurate at 2251 UTC (12 min. into the prediction), but by 2305 the predicted circulation centers have begun to move more with the mean wind (as they began to prematurely weaken). Fig. 6.5b shows that the DDOP southern circulation center, which developed at 2251 UTC, begins to deviate to the right of the mean flow after 2305 UTC. The SDVR southern circulation center does not develop until 2305 UTC and only deviates slightly from the mean wind. Nevertheless, at 2313 UTC (34 min. into the prediction) both the DDOP and SDVR southern circulation centers provide a much more accurate forecast of the observed main circulation center's location than either of the two extrapolation techniques.

6.2.2 Rainwater correlation time series and profiles

To better quantify the accuracy of the model-predicted storms, a time-series of three-dimensional rainwater correlation coefficients is shown in Fig. 6.6. The initial (t = 0) correlation deviates from unity for two reasons. First, reflectivity from the Norman radar was used to compute rainwater for the independently computed dual-Doppler verification

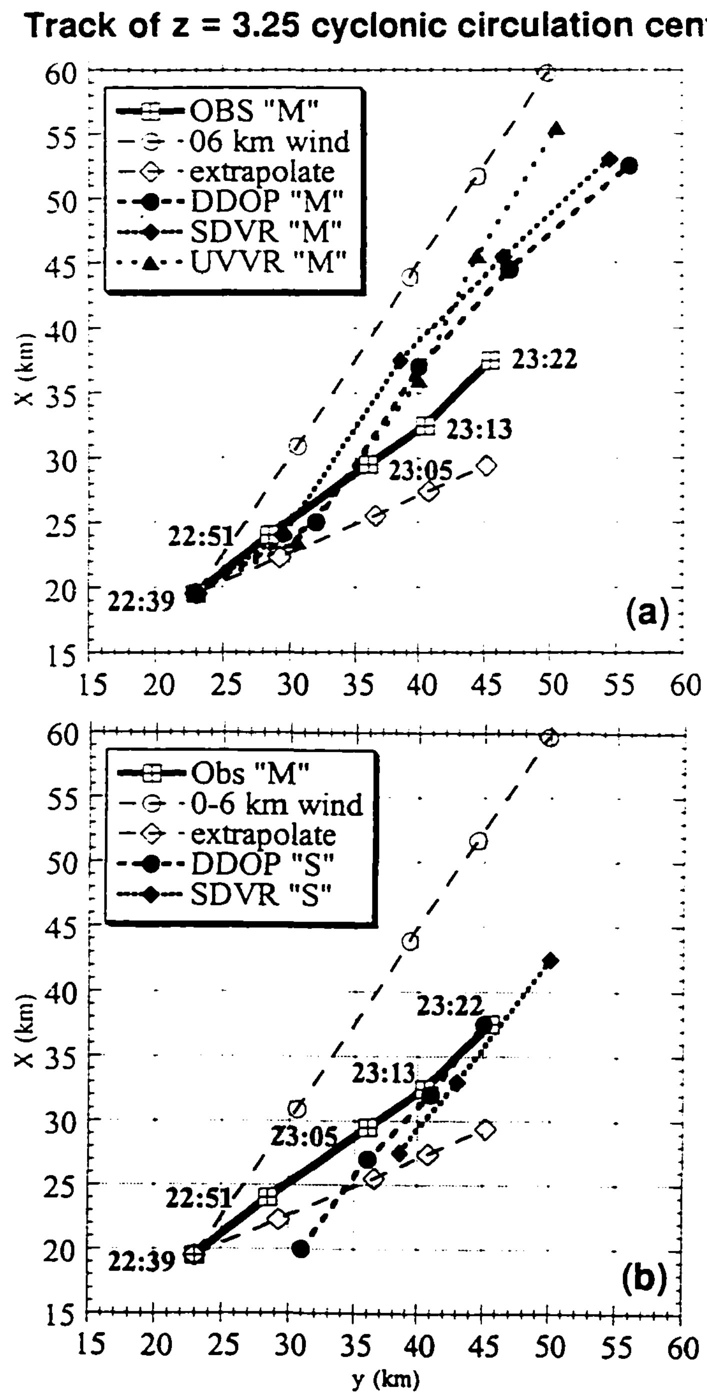

Figure 6.5 Predicted and observed locations of the z = 3.25 km cyclonic circulation centers at various times. Tracks for a) the predicted main ("M") circulation center and b) the predicted southern ("S") circulation center are indicated. The observed main circulation center track is indicated on both panels, along with projected tracks based on the 0-6 km mean wind and the initial circulation center motion. Times indicated are UTC.

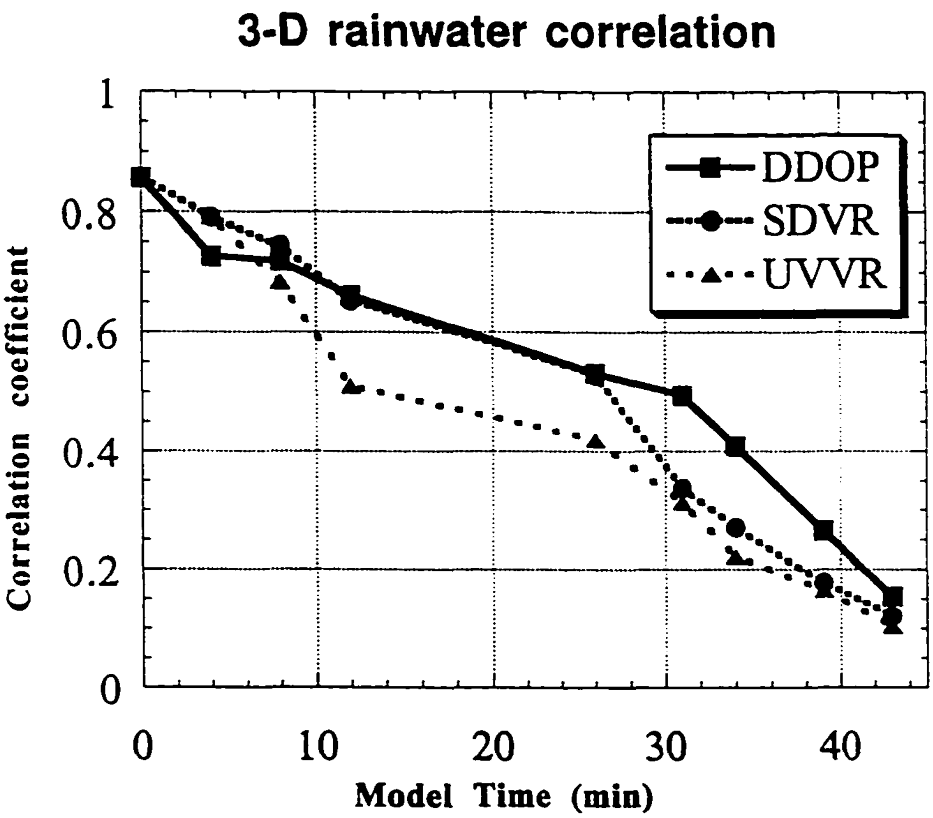

Figure 6.6 Time series of 3-D rainwater correlation coefficients between the verification analyses and the various prediction experiments.

analyses (DB97), whereas reflectivity from the Cimarron radar was used for the SDVR and DDOP input fields. Second, as discussed in Chapter 2, limitations associated with the warm rain microphysics and Z-qr relationships necessitated truncating reflectivity at 50 dBZ for the model input fields. The absence of this truncation for the dual-Doppler verification fields combined with the observed maximum reflectivity values of 68 dBZ leads to significant differences between the model input and verification rainwater field.

For all three predictions, the rainwater correlation coefficient decreases at a fairly steady rate throughout the 43 minute prediction period. After a brief period of rapid decrease for the DDOP prediction, the DDOP and SDVR predictions have almost identical correlation scores through 26 minutes. This is consistent with the similarities shown in the rainwater plots and represents a very encouraging result. *The fact that a model prediction initialized with single-Doppler derived fields maintains equal performance to one initialized with dual-Doppler-derived fields indicates that the single-Doppler velocity retrieval captures those flow features in the dual-Doppler analysis that are important to the storm evolution.* In contrast, the UVVR correlation is significantly lower than the others by 12 minutes and remains lower than the others throughout the remainder of the prediction. This significant result confirms that the perturbation components obtained from the pseudo-streamfunction in the SDVR improve the prediction accuracy.

By 31 minutes, the three-dimensional SDVR correlation is worse than the DDOP correlation and remains that way throughout the rest of the prediction. This degradation of the SDVR performance is associated with a differing depiction of the southern and eastern precipitation cores. As can be seen in the t = 34 min. rainwater plots (Fig. 6.3), the southern core is too weak and the eastern core is too strong for the SDVR forecast relative to the DDOP forecast.

It is important to note that the three-dimensional correlations are generally much lower than the z = 2.25 two-dimensional correlations presented in Fig. 6.1-4. To further illustrate the vertical structure of the rainwater correlation coefficients, vertical profiles of the two-dimensional correlations are presented for two model prediction times. Fig. 6.7 shows the values for the three experiments at t = 12 min. (2251 UTC). At this time 3-D correlations were approximately 0.65 for the DDOP and SDVR predictions. Throughout the lowest eight kilometers both experiments maintain values close to 0.80. Above eight kilometers, values rapidly decrease to 0.40 or less.

Examination of vertical rainwater cross-sections for the model predictions (not shown), indicates that the depth of the model predicted updraft decreases just after the initialization. The associated collapse of the high altitude rainwater is likely the cause of the poor correlations at upper-levels. While a detailed analysis to ascertain the cause of this storm-top collapse has not been performed, a possible candidate is the lack of a provision for ice-phase microphysics in the initialization and the prediction.

Based on the vertical profile of correlation scores, it can be concluded that for this time the overall 3-D correlation gives a pessimistic estimate of the accuracy of the rainwater field at low- and mid-levels. Even for the UVVR forecast, which had a 3-D correlation of about .50, 2-D correlations are above .80 for the lowest two kilometers and .60 or greater through the lowest eight kilometers.

A similar comparison of the 2-D correlation profiles at t = 34 min. (2313 UTC) is shown in Fig. 6.8. For the DDOP prediction, low- and mid-level values are again significantly higher than upper-level values. The SDVR profile shows a somewhat similar pattern; however, there is a layer of very low correlations centered at about five kilometers. This is caused by the over-intensification of the eastern precipitation core described earlier, and the associated large mid-level values of rainwater. This error is

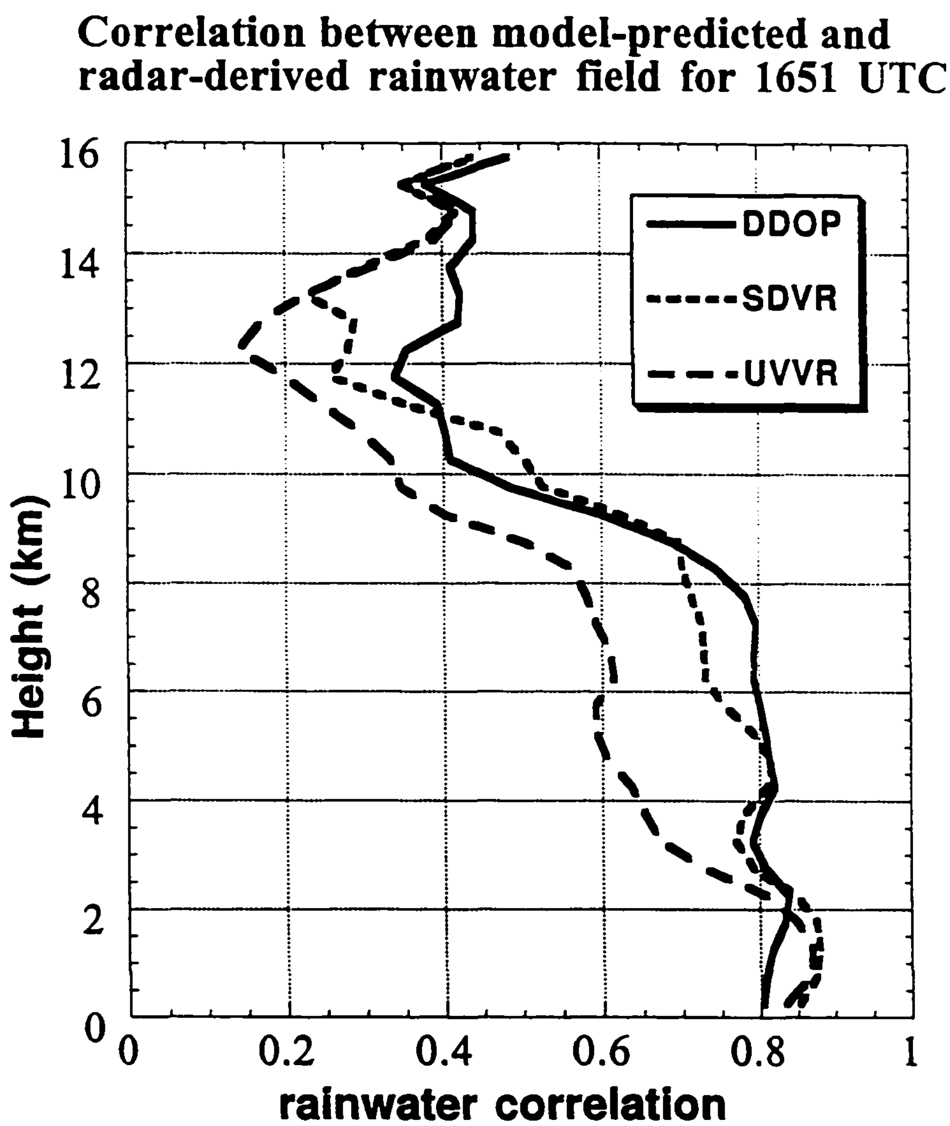

Figure 6.7 Vertical profile of 2-D horizontal rainwater correlation coefficients between the verification analysis and the 12 minute predictions (valid at 2251 UTC) for the various prediction experiments.

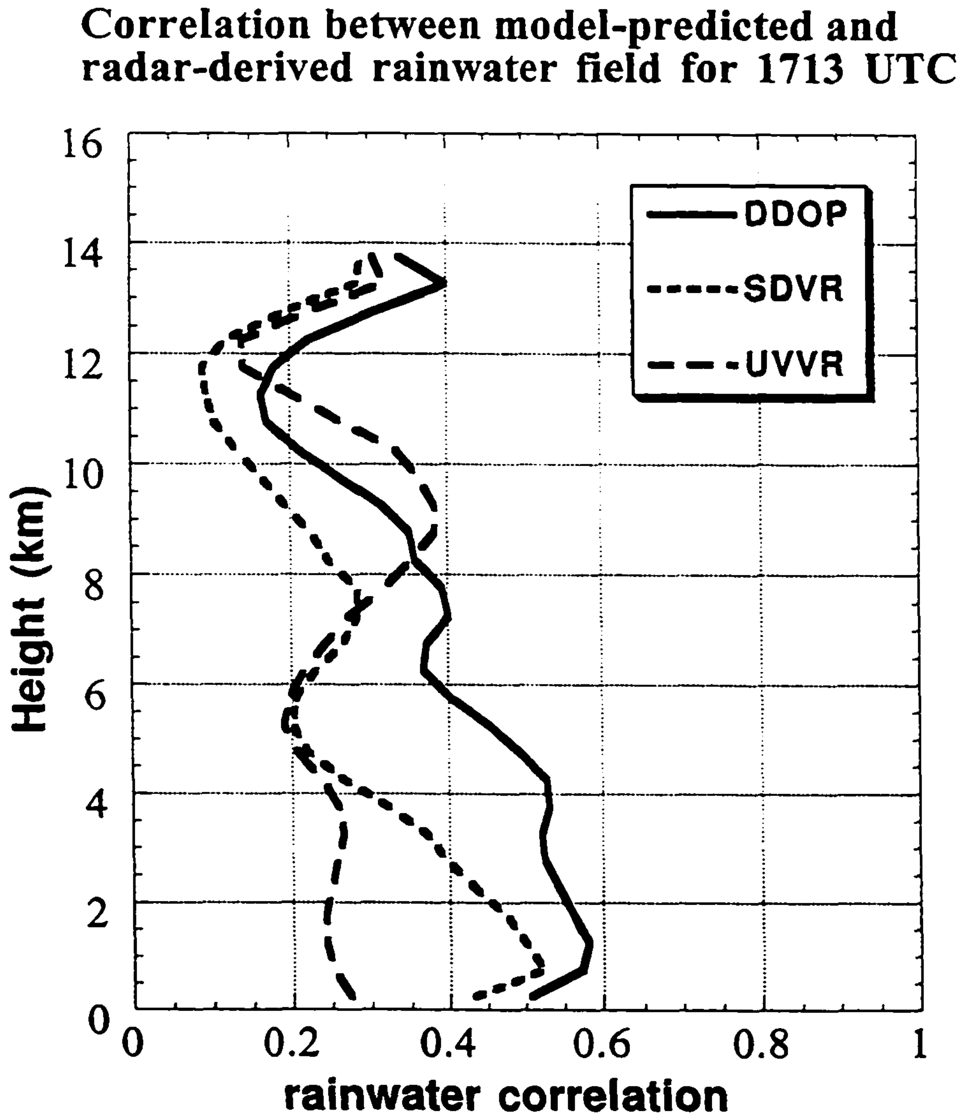

Figure 6.8 Vertical profile of 2-D horizontal rainwater correlation coefficients between the verification analysis and the 34 minute predictions (valid at 2313 UTC) for the various prediction experiments.

shared by the UVVR prediction, which shows quite low correlations throughout the lowest eight kilometers.

6.2.3 *Maximum vertical velocity time series*

Further understanding of the differences between the actual and model-predicted storm evolution can be gained by examining the domain maximum vertical velocity time-series shown in Fig. 6.9. The dual-Doppler verification values (obtained from the independent analyses of DB97) are in excess of 50 m s^{-1} before the 14 minute data gap, then near 30 m s^{-1} after the data gap. Because the dual-Doppler fields have been subjected to an O'Brien correction and do not satisfy 3-D mass conservation, they should not be viewed as precise statements of the updraft strength. For this reason, and because the evolution during the 14 minute data gap is unclear, successive maximum values have not been connected with line segments.

Examination of the DDOP time-series indicates that after an initial surge in the updraft strength, the vertical velocity maximum is not sustained by the storm. Consistent with this, the DDOP maximum vertical velocity value decreases from nearly 60 m s^{-1} to less than 25 m s^{-1} between two and eight minutes into the model prediction. Conversely, after an initial slight decrease, The SDVR maximum vertical velocity increases from less than 20 m s^{-1} at two minutes to greater than 30 m s^{-1} at eight minutes. This rapid increase for the SDVR case is not surprising, given the under-retrieval of the maximum vertical velocity by the SDVR.

In contrast to the SDVR forecast, the maximum vertical velocity for the UVVR forecast does not rapidly increase. This result further emphasizes that the differences between the SDVR and UVVR wind field (the perturbation wind components obtained from the pseudo-streamfunction) do have a significant impact on the numerical prediction

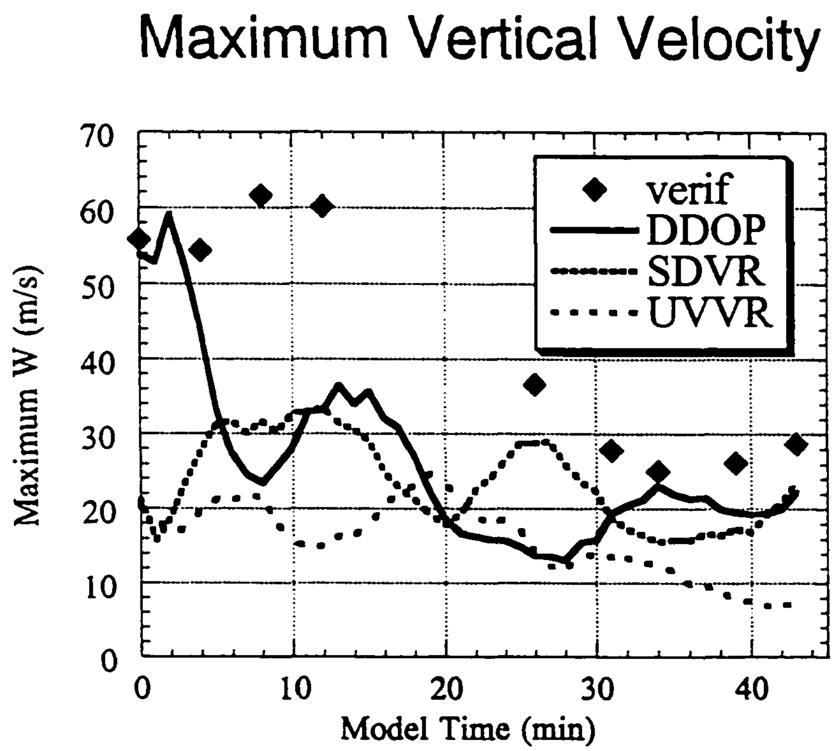

Figure 6.9 Time series of domain maximum vertical velocity (m s^{-1}) from the dual-Doppler verification analyses and the various prediction experiments.

(despite having virtually no impact on the temperature retrieval). Although the exact reason for this behavior has not been determined, the variational wind adjustment appears to play a role. In the SDVR case the wind adjustment creates azimuthal convergence in the near-surface layer below the data coverage region. Despite the presence of a very similar updraft in the UVVR case, the wind adjustment does not create low-level azimuthal convergence. Additional analysis work is needed to further elucidate the reasons for these differences.

During the prediction period from t = 12 to t = 26 minutes, the DDOP and SDVR time series show a very similar weakening of the initial updraft. The increase in the SDVR maximum vertical velocity between 20 and 26 minutes is due to the intensification of the eastern updraft, not the newly developing southern updraft (see Fig. 6.2c). No such amplification is seen in the DDOP case and the southern precipitation core (see Fig. 6.2b) never develops a strong updraft maximum in either prediction. The evolution of the predicted vertical velocity maximum after 30 min. is rather non-descript for all cases, but bears some resemblance to the verification for the DDOP and SDVR cases.

6.2.4 Maximum vorticity profiles

As a final test of the forecast quality, vertical profiles of the domain maximum vertical vorticity are shown for four prediction times. Comparisons are made between the DDOP and SDVR predicted and dual-Doppler verifying profiles. It is important to keep in mind that while capturing the vorticity evolution in a tornadic thunderstorm is obviously of enormous importance, it is also a much more difficult task than faithfully reproducing gross features like the rainwater field. As such, this comparison represents a rather extreme test of <u>both</u> the retrieval procedure and the numerical prediction model. The added challenge of verifying point values (as opposed to the circulation defined over some area) is somewhat mitigated by the relatively coarse model grid resolution, and the smoothing inherent in the various interpolations used in preparing the dual-Doppler verification data.

Fig. 6.10, which is similar to Fig. 8 in DB97, shows the verification profiles for 2239, 2251, 2305 and 2322 UTC. These correspond to the model prediction times of 0, 12, 26 and 43 minutes. At the model initial time ($t = 0$), the dual-Doppler verification analysis revealed a strong mid-level mesocyclone with vorticity in excess of $1\ (10)^{-2}\ s^{-1}$ above 4.25 km. At 1.25 km, however, the maximum vorticity is less than $6\ (10)^{-3}\ s^{-1}$. By 12 minutes, vorticity has increased at all levels below 6 km, while the level of maximum vorticity has remained unchanged at about 5.5 km. At 26 minutes, midway through the 10 min. life of the tornado, mid-level vorticity has decreased, while vorticity near the surface has increased with a maximum of $1.3\ (10)^{-2}\ s^{-1}$ at 2.25 km. This pattern is common in tornadic supercells (Brandes 1984), and is suggestive (but not conclusive) of the dynamic pipe tornado mechanism described by Trapp and Davies-Jones (1996). Finally, by the post-tornadic time of 43 minutes, vorticity has decreased at all levels.

The corresponding DDOP predicted profiles, displayed in Fig. 6.11, show both discouraging and encouraging features. The prediction captures virtually none of the maximum vorticity evolution below 3 km, as the profiles change very little from their initial value. Above 3 km, however, there is a reasonable similarity between the predicted and verification profiles. Starting from slightly different values (due to variational wind adjustment and various interpolations) at $t = 0$, the DDOP profile also increases significantly by 12 minutes. While the DDOP profile actually increases too much above 3 km, it also shows a maximum at about 5.5 km. At 26 minutes, the DDOP vorticity above 3 km is quite similar to the verification. Unfortunately, the low-level local maximum value of just over $1\ (10)^{-2}\ s^{-1}$ is located at 3.25 km instead of $z = 2.25$ km. The DDOP

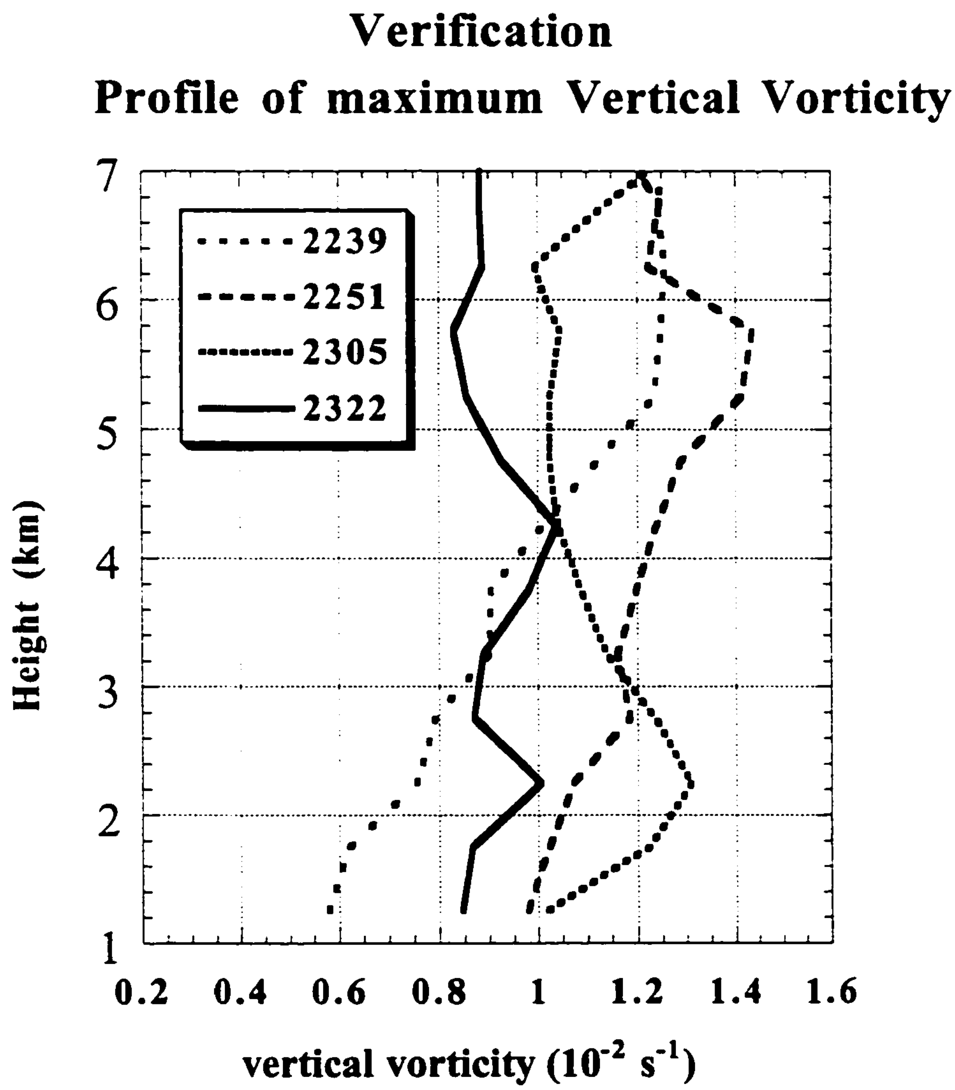

Figure 6.10 Vertical profile of maximum vertical vorticity (10^{-2} s^{-1}) at each level for various times from the dual-Doppler verification analyses. Times indicated in the legend are UTC.

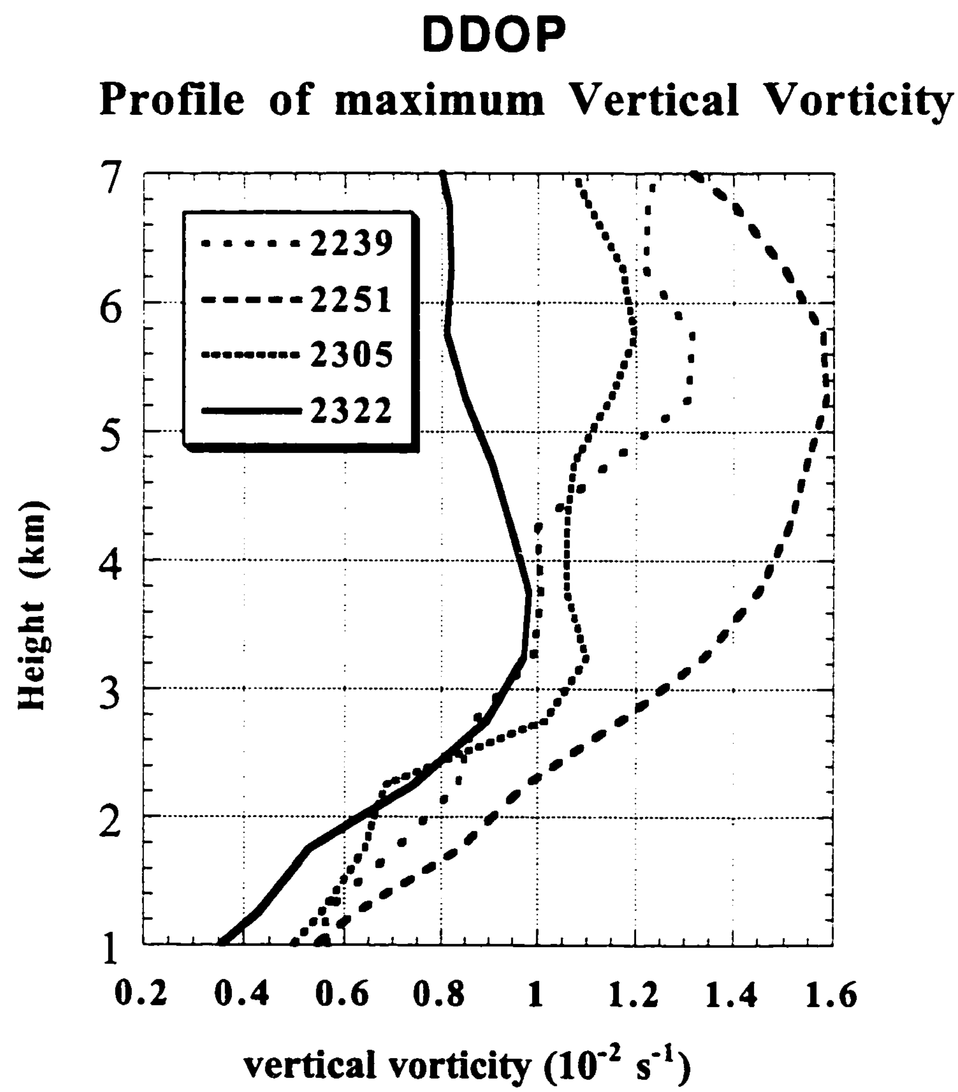

Figure 6.11 Vertical profile of maximum vertical vorticity (10^{-2} s^{-1}) at each level for various times from the DDOP predictions. Times indicated in the legend are UTC.

vorticity decrease from 26 to 43 minutes and the final profile is strikingly realistic above 3 km. Thus, the DDOP forecast appears to accurately predict the intensification of the mid-level mesocyclone, but fails to capture the low-level mesocyclone.

Fig. 6.12, the corresponding profiles for the SDVR prediction, shows a reasonable similarity to the DDOP case, including the substantially weaker vorticity below 3 km at all times (compared to the verification). One obvious difference is the significantly reduced maximum initial vorticity, which is due to inadequacies in the single-Doppler wind retrieval. By 12 minutes, however, this deficit has been overcome and the SDVR profile matches the DDOP profile almost exactly. Between 12 and 26 minutes, a local vorticity maximum similar to that in the DDOP forecast develops near 3 km. The mid-level vorticity decrease, however, is less than that of the DDOP forecast. During the final 17 minutes of the SDVR prediction, the mid-level vorticity maximum decreases substantially, while the profile in the lowest 3 km remains nearly constant.

Whereas the realism of the DDOP and SDVR vertical vorticity evolutions above 3 km is encouraging, the inability of either prediction to generate vorticity in excess of 7 $(10)^{-3}$ s^{-1} at 1 km is a troubling result. A wide variety of model- or initialization-related factors could be responsible for this. A detailed search for the source of the problem has not been conducted; however, analysis of the predicted low-level fields does indicate that the incipient low-level vortex is undercut by the cold outflow. This again leads to speculation concerning the use of warm-rain microphysics and the simplistic initialization of moisture fields.

6.3 Single-Doppler sensitivity experiments

As a supplement to the prediction experiments shown in the previous section, two sets of sensitivity experiments have been conducted. The purpose of these experiments is to

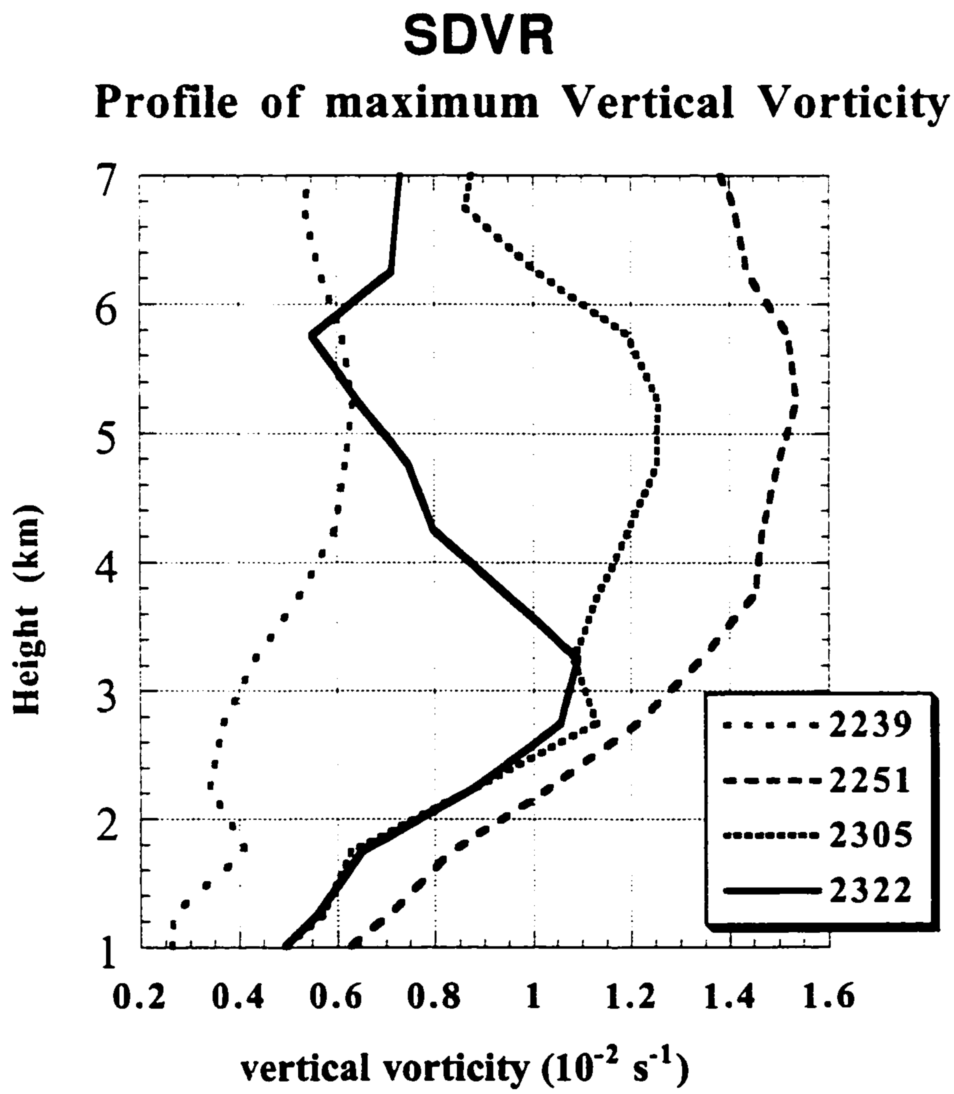

Figure 6.12 Vertical profile of maximum vertical vorticity (10^{-2} s^{-1}) at each level for various times from the SDVR predictions. Times indicated in the legend are UTC.

gain some insight into the impact of specific initial fields on the predicted storm evolution. It is worth emphasizing that the most important sensitivity experiment, in which it was shown that the SDVR initialization performs nearly as well as the DDOP initialization and significantly better than the UVVR initialization, has already been presented.

The experiments in this section, which are summarized in Table 6.1, focus on two aspects of the initialization: 1) the relative importance of the different moisture fields, and 2) the relative importance of the thermodynamic and velocity fields. Because the focus of this study is single-Doppler retrieval, the SDVR prediction has been chosen for the control experiment. Sensitivity testing has been restricted to these two areas because it is felt that the SDVR prediction is not sufficiently accurate to warrant the detailed analysis of a large number of sensitivity experiments. Rather, a few simple tests have been conducted to gain some general insights into the sensitivity of the SDVR results.

Analysis of the experiments is accomplished using three of the four criteria described in Section 6.2. First, time series of the domain maximum vertical velocities will be shown. This will provide a quick oversight of the similarities and differences between the SDVR case and the sensitivity experiments. Second, selected fields will be shown from the predictions to further illustrate the results. Third, time series of the 3-D rainwater correlation coefficients will be presented. This will allow for a quantitative comparison of the accuracy of each sensitivity experiment relative to the SDVR control.

6.3.1 Impact of initial moisture fields

To document the impact of the initial moisture fields on the subsequent storm evolution, three sensitivity experiments have been conducted as summarized in Table 6.1. The first experiment (NOQV) consists of omitting the final initialization step, in which updrafts stronger than 3 m s^{-1} in the rainwater region are saturated. In the second experiment (NOQR), the conversion of radar-observed reflectivity into rainwater is omitted. Consistent with this, the retrieved temperature is missing the rainwater contribution (shown in Fig. 5.24c). In the last experiment (NOQQ), both the rainwater specification step (and the contribution to the temperature retrieval) and the water vapor saturation step are omitted.

Fig. 6.13 shows the time series of domain maximum vertical velocities for the three experiments as well as for the SDVR control. An almost immediate impact is seen in the two experiments in which the perturbation water vapor is withheld (NOQV and NOQQ). This is consistent with the OSSE experiments of Weygandt et al. (1990), and can be easily understood by noting that the region of updraft maximum is unsaturated. For the conditionally unstable atmosphere depicted in the base-state sounding (Fig. 3.3a), unsaturated upward motion creates negative buoyancy, leading to a downward vertical acceleration.

Once the upward motion induced cooling has triggered saturation, the NOQV maximum updraft recovers quite quickly and closely matches the SDVR evolution after 15 minutes. In contrast, the NOQQ experiment does not recover from the initial weakening of the updraft until much later and maintains the weakest updraft throughout most of the prediction. Examination of the low-level NOQQ fields at 8 minutes (not shown), indicates that without the rain generated cold-pool to focus low-level convergence the unsaturated updraft weakens to the point where it never really recovers. This result emphasizes the importance of the presence of rainwater in shaping the cold-pool evolution and associated low-level convergence, which in turn plays a prominent role in the updraft evolution.

Like the NOQQ experiment, the NOQR experiment also lacks the initial rainwater; however, its initial updraft is saturated (in addition to being unburdened by rainwater loading). Because of this, it strengthens quite rapidly, briefly even exceeding the SDVR

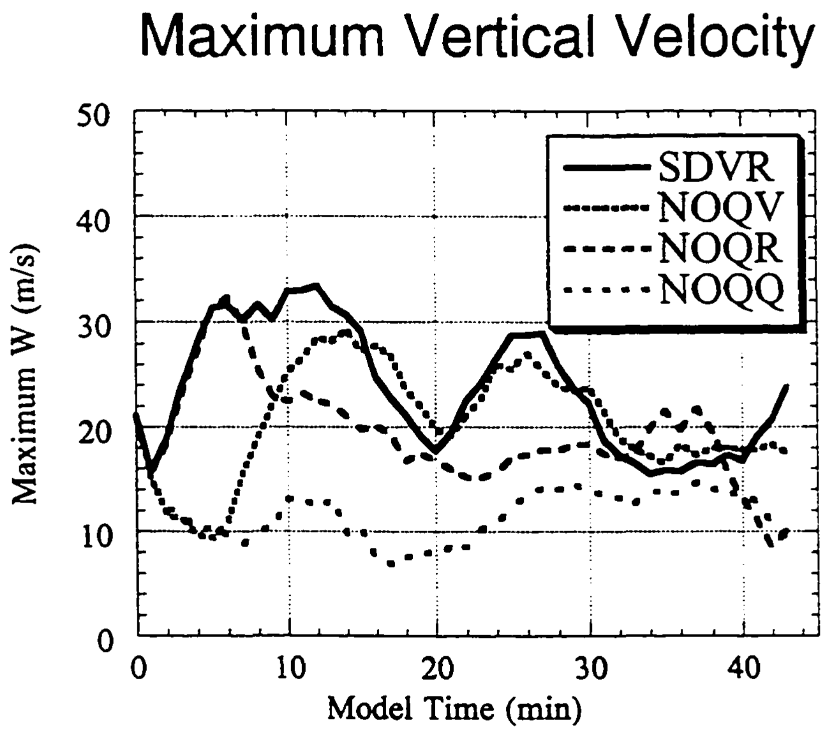

Figure 6.13 Time series of domain maximum vertical velocity (m s^{-1}) for the moisture sensitivity experiments.

updraft and rapidly begins producing rainwater. The resulting cold-pool, however, is slower to develop and smaller in size than the NOQV and SDVR cold-pools.

These cold-pool differences and the related storm differences at t = 26 minutes are illustrated in Figs. 6.14-17 for the SDVR, NOQV, NOQR and NOQQ experiments, respectively. Shown are the z = 0.25 perturbation potential temperature field and the z = 2.25 rainwater field. As expected, the SDVR control has the strongest cold-pool (Fig. 6.14a), but the NOQV cold-pool is very similar in appearance and only slightly weaker (Fig. 6.15a). Consistent with this, the SDVR and NOQV storms are quite similar in appearance. Although the rainwater maximum is slightly larger in the NOQV case, its overall rainwater field appears slightly less substantial than that of the SDVR case. This is not surprising, because the lack of saturation in the initial fields leads to slightly less production of rainwater compared to the SDVR case. Interestingly, the newly developed southern precipitation core that is present in the SDVR case, is absent in the NOQV case. This may be related to the slight differences in the southern edge of the cold pool (and its associated gust front), and ultimately to that lack of saturation in the initial NOQV fields.

The impact of the delayed cold-pool evolution for the NOQR case can be seen in Fig. 6.16a. Here the cold pool is smaller in size and somewhat weaker in strength. This is due to the fact that all the rainwater has to form from water vapor during the 26 min. prediction. Nevertheless, the resultant rainwater field (Fig. 6.16b) shows some similarities to the SDVR experiment. A small, but important feature in Fig. 6.16b is the kidney-shaped rainwater region south of the main storm (located at x = 43, y = 30). This feature continues to develop during the remainder of the prediction period (not shown) and ultimately corresponds very favorably with the southeastern core in the verification. As such, it represents the only reproduction of this observed feature in any of the prediction experiments. As will be seen shortly, it also results in the NOQR experiment having the best correlation score of any prediction at the final verification time.

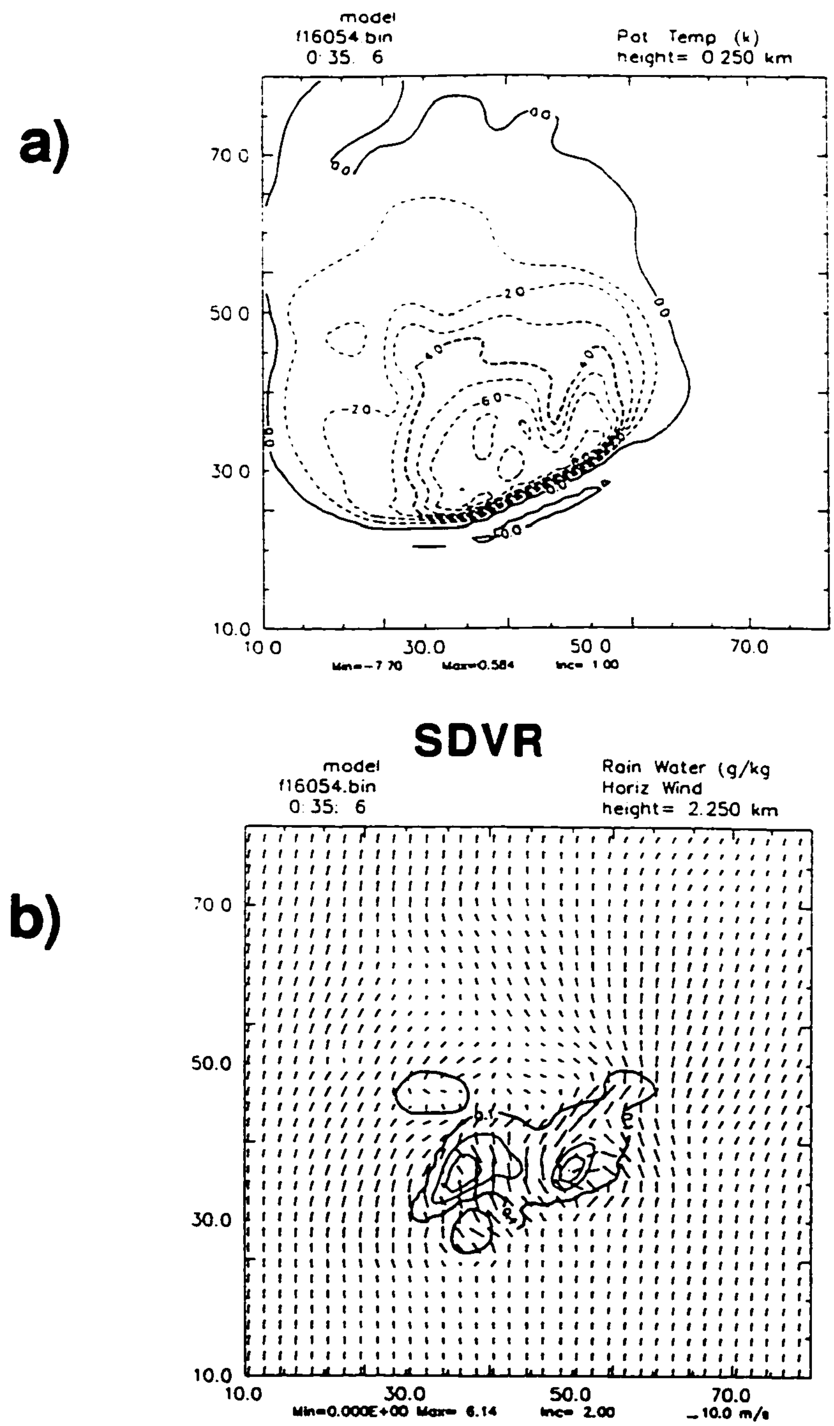

Figure 6.14 2305 UTC (26 minute prediction) a) near-surface (z = 0.25 km) perturbation potential temperature and b) low-level (z = 2.25 km) rainwater and storm-relative wind vectors for the SDVR control experiment. Potential temperature and rainwater are contoured every 1 K and 2 g kg^{-1}, respectively.

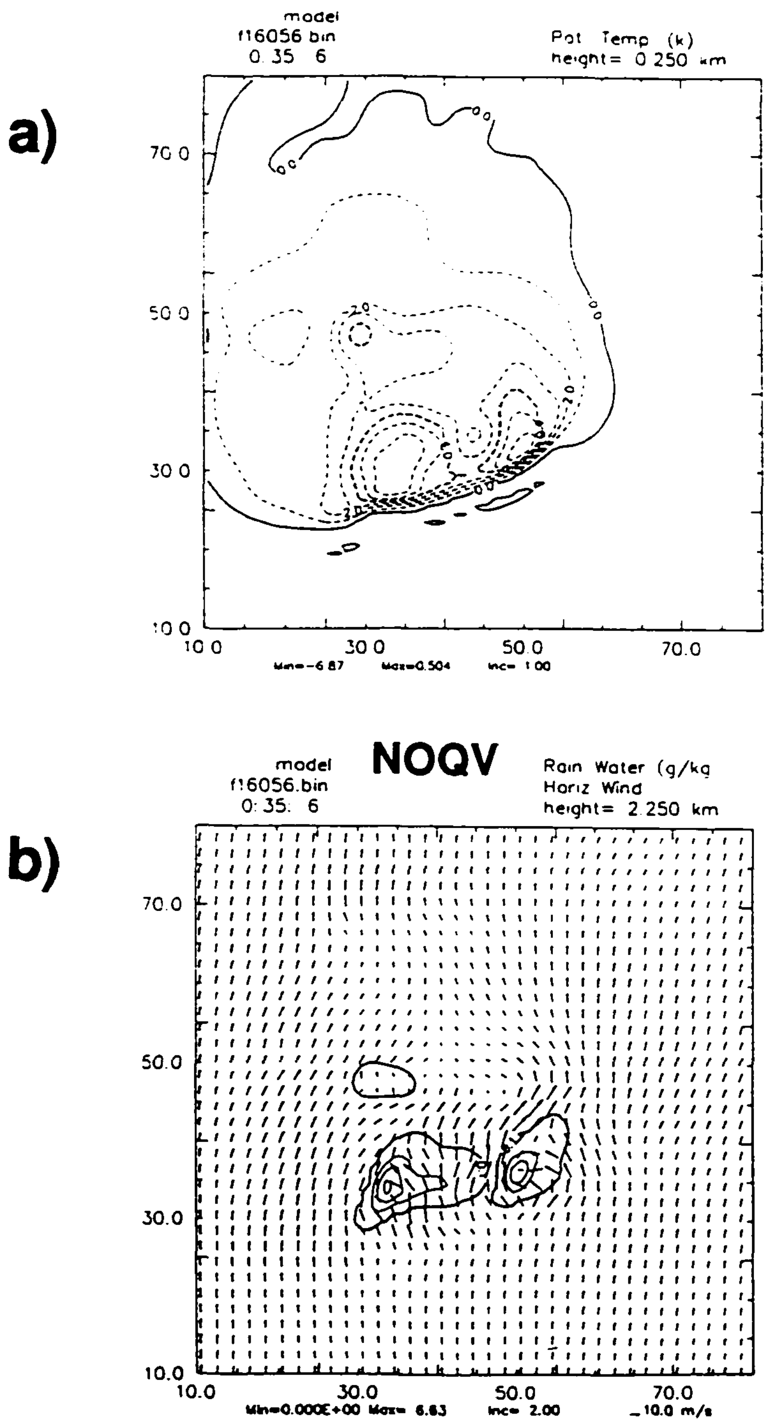

Figure 6.15 2305 UTC (26 minute prediction) a) near-surface (z = 0.25 km) perturbation potential temperature and b) low-level (z = 2.25 km) rainwater and storm-relative wind vectors for the NOQV experiment. Potential temperature and rainwater are contoured every 1 K and 2 g kg^{-1}, respectively.

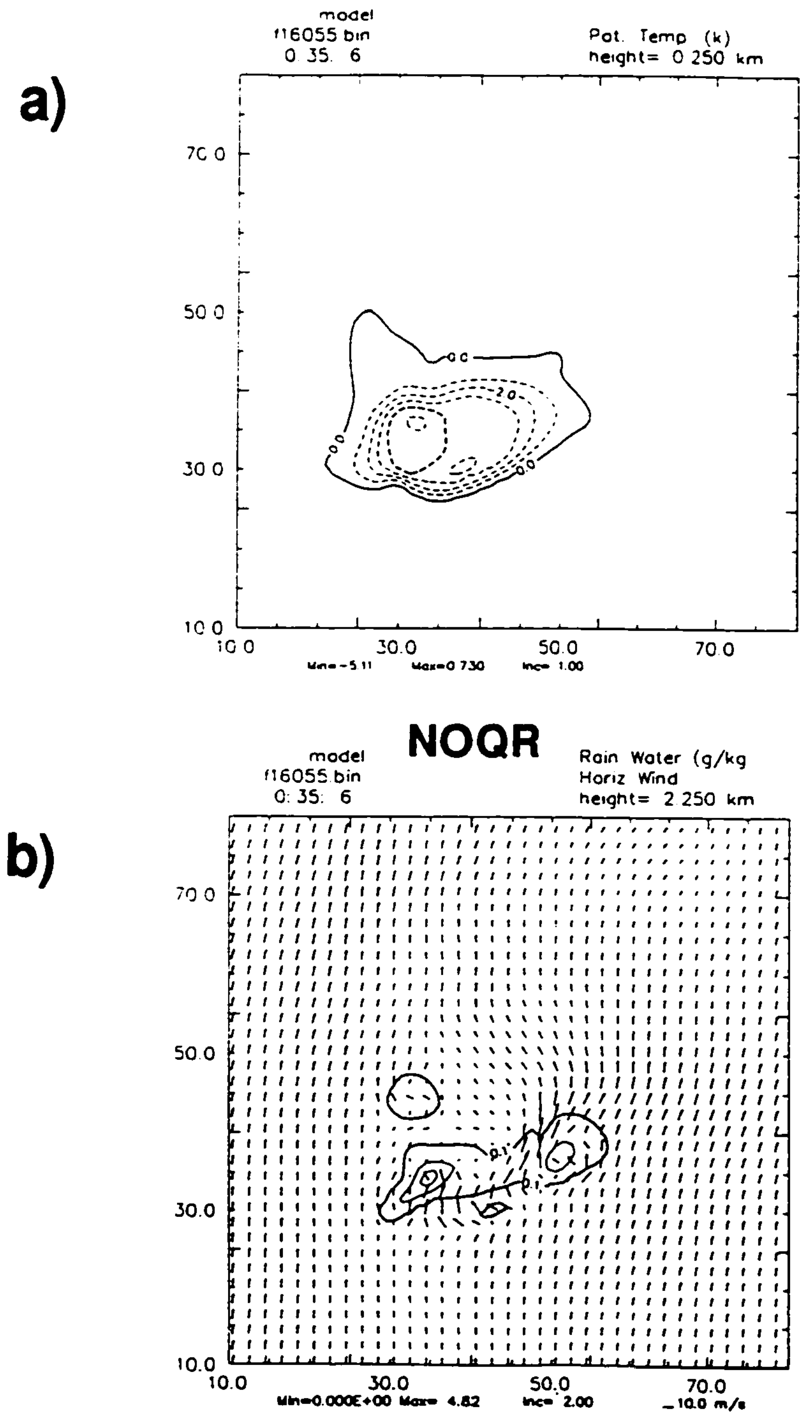

Figure 6.16 2305 UTC (26 minute prediction) a) near-surface (z = 0.25 km) perturbation potential temperature and b) low-level (z = 2.25 km) rainwater and storm-relative wind vectors for the NOQR experiment. Potential temperature and rainwater are contoured every 1 K and 2 g kg^{-1}, respectively.

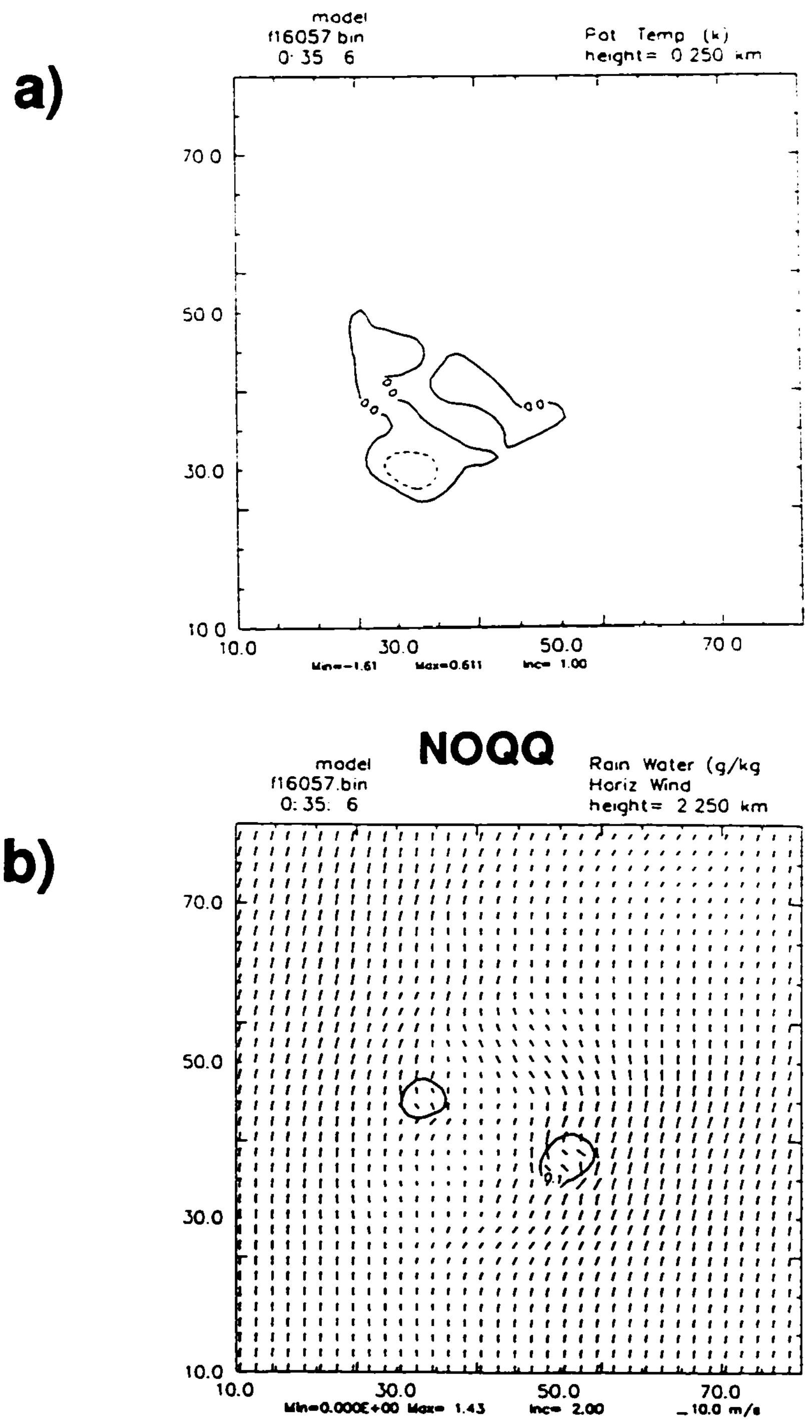

Figure 6.17 2305 UTC (26 minute prediction) a) near-surface (z = 0.25 km) perturbation potential temperature and b) low-level (z = 2.25 km) rainwater and storm-relative wind vectors for the NOQQ experiment. Potential temperature and rainwater are contoured every 1 K and 2 g kg^{-1}, respectively.

The impact of removing both the initial rainwater and perturbation water vapor is shown quite clearly in Fig. 6.17. Without initial saturation to drive the updraft, or initial rainwater to focus the low-level convergence, the updraft weakens and never generates substantial rainwater or a cold-pool.

Fig. 6.18 shows times series of the 3-D rainwater correlations for the four experiments. Comparison of the NOQV and SDVR time series illustrates the temporary nature of the impact due to omitting the saturation assumption. The lack of saturation in the initialized updraft leads to a decrease in the rainwater production, resulting in a correlation that departs from that of the SDVR. The updraft rapidly becomes saturated, however, and from 26 minutes on the NOQV correlation closely mirrors that of the SDVR.

Because there is no initial rainwater field for the NOQR and NOQQ experiments, correlations cannot be defined at t = 0. By 4 minutes, however, significant differences in the rainwater correlation are evident. The saturation of the initial updraft in the NOQR experiment leads to a large production of rainwater, and rapid increase in rainwater correlation. In contrast, the unsaturated updraft in the NOQQ experiment never produces much rainwater, resulting in very poor correlations throughout the prediction.

Between 12 and 26 minutes, the NOQR correlation evolution is similar to that of the SDVR control, and it actually exceeds the SDVR correlation after 26 minutes. As discussed above, this is due to the development of a new precipitation core southeast of the storm in close agreement with the observed evolution. Because this is the only experiment to successfully capture this feature, NOQR has the highest correlation coefficients at the end of the prediction (even exceeding the DDOP experiment). This result again illustrates the delicate balance between moisture initialization, cold-pool generation, gust-front strength, and new cell development.

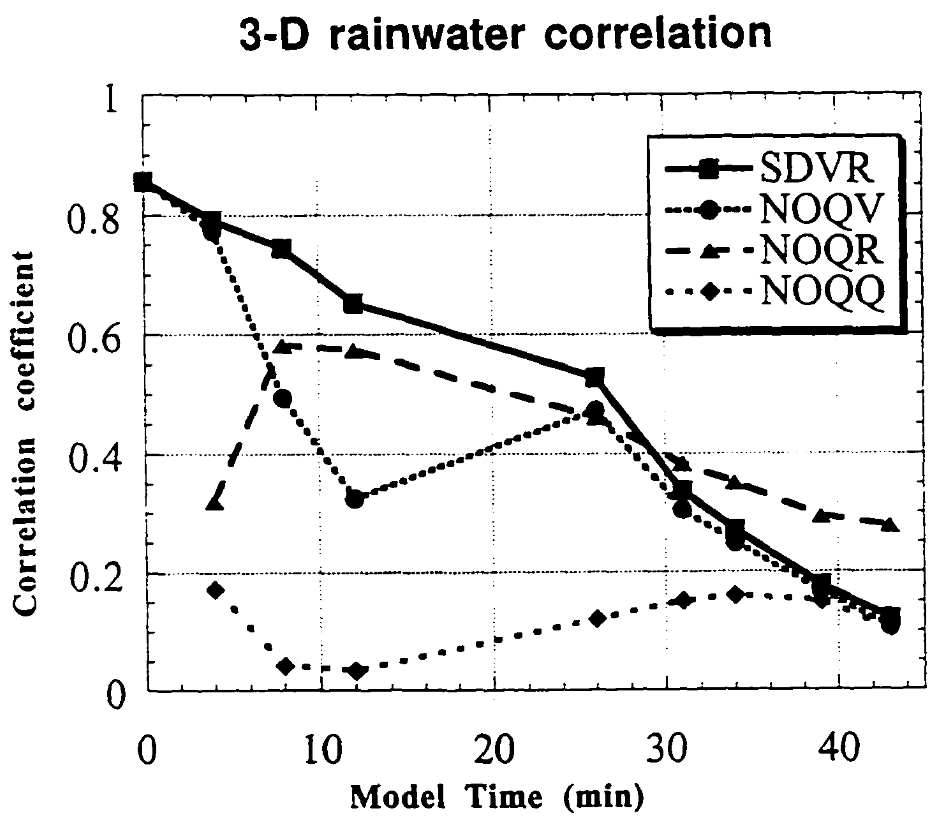

Figure 6.18 Time series of 3-D rainwater correlation coefficients between the verification analyses and the various moisture sensitivity experiments.

6.3.2 Impact of initial thermodynamic versus velocity fields

In this second set of sensitivity experiments, the relative importance of mass versus velocity fields is examined. As summarized in Table 6.1, this is accomplished by replacing the SDVR-retrieved pressure and temperature fields with the base-state sounding values in the NOPT experiment and by replacing the SDVR-retrieved wind field with the base-state sounding values in the NOVL experiment. Note that for the NOVL experiment, no saturation assumption is made because there are no updrafts. For the NOPT experiment, updrafts within the rainwater region are saturated using the base state temperature. It is also important to note that the NOPT experiment yielded results that were nearly identical to an experiment in which only the perturbation temperature was removed from the initial conditions. This is because during the numerical integration, the perturbation pressure field evolves extremely rapidly in response to the three-dimensional divergence field.

Fig 6.19 shows the maximum vertical velocity time series for the SDVR, NOPT and NOVL experiments. Following a brief, early departure from the SDVR experiment, the NOPT follows the SDVR fairly closely. Examination of the predicted fields shortly after the initialization (not shown) indicates that the saturated updraft quickly regenerated a realistic perturbation temperature field (compared to the SDVR experiment). The subsequent rainwater fields (shown at t = 12 and 26 minutes in Fig. 6.20) are quite similar to their SDVR counterparts (shown in Figs. 6.1c and 6.2c). The NOVL time series in Fig. 6.19 also shows some similarity to that of the SDVR case (after increasing from an initial value of zero). The rainwater fields at t = 12 and 26 minutes (Fig. 6.21), however, show increasing differences. Detailed examination of the predicted fields (not shown) indicates that for the NOVL case, rainwater production is rather limited during the first few minutes of the model prediction. The base state windfield appears to be simply

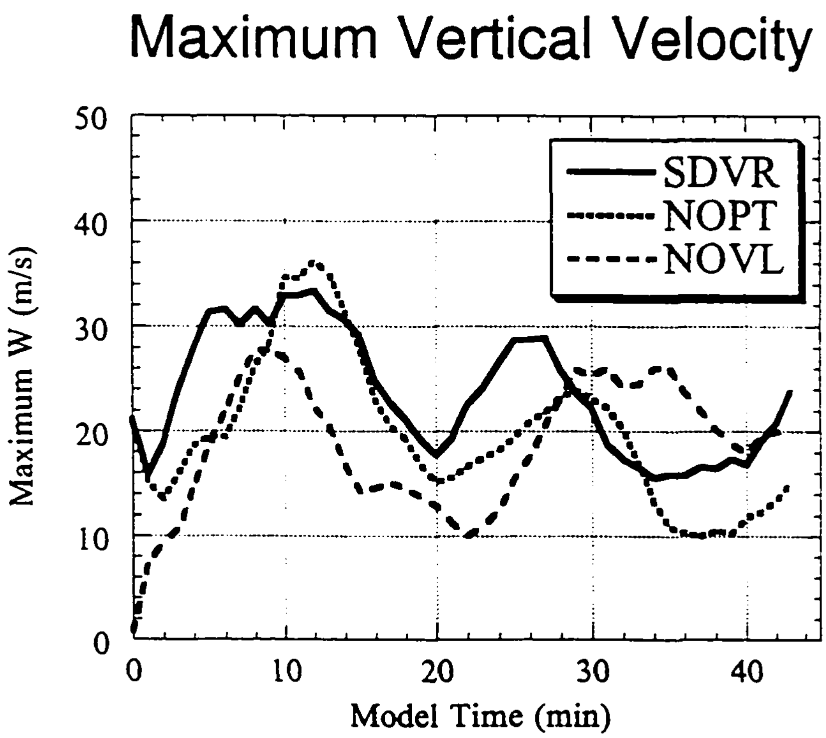

Figure 6.19 Time series of domain maximum vertical velocity (m s^{-1}) for the thermodynamic versus velocity sensitivity experiments.

a)

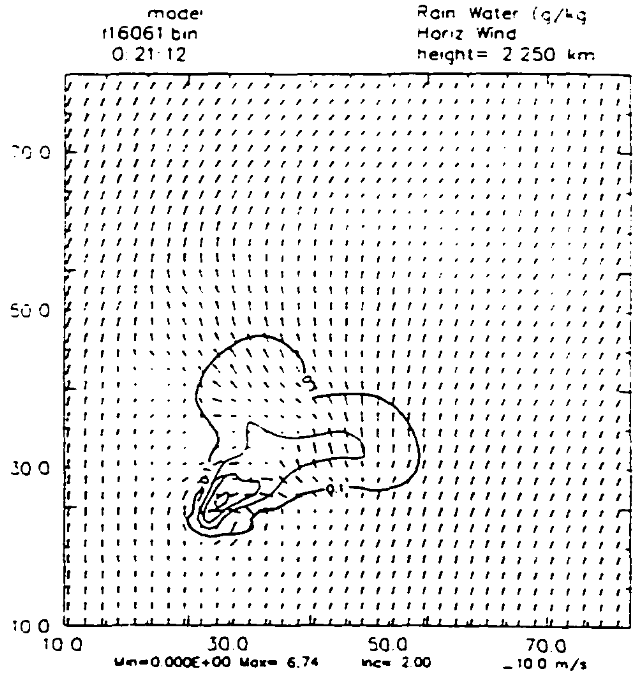

b)

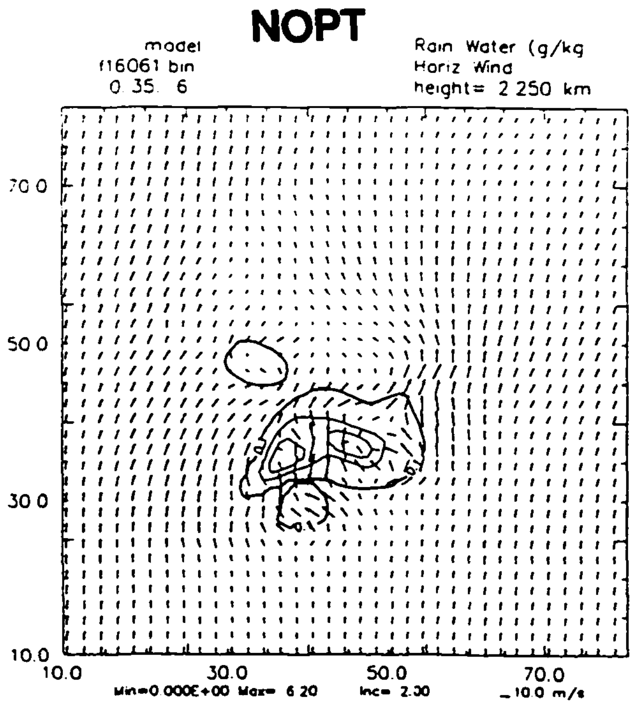

Figure 6.20 Low-level (z = 2.25 km) rainwater and storm-relative vector wind field at a) 2251 UTC (12 minute prediction) and b) 2305 UTC (26 minute prediction) for the NOPT experiment. Rainwater is contoured every 2 g kg^{-1}.

a)

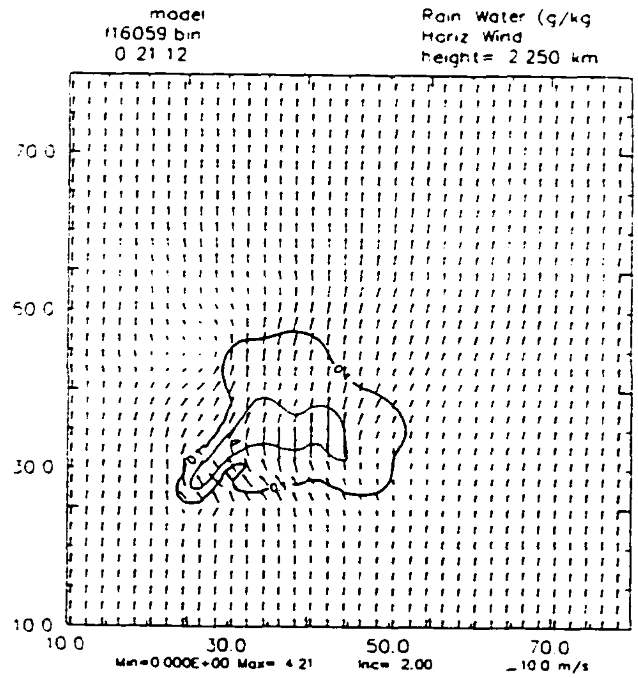

NOVL

b)

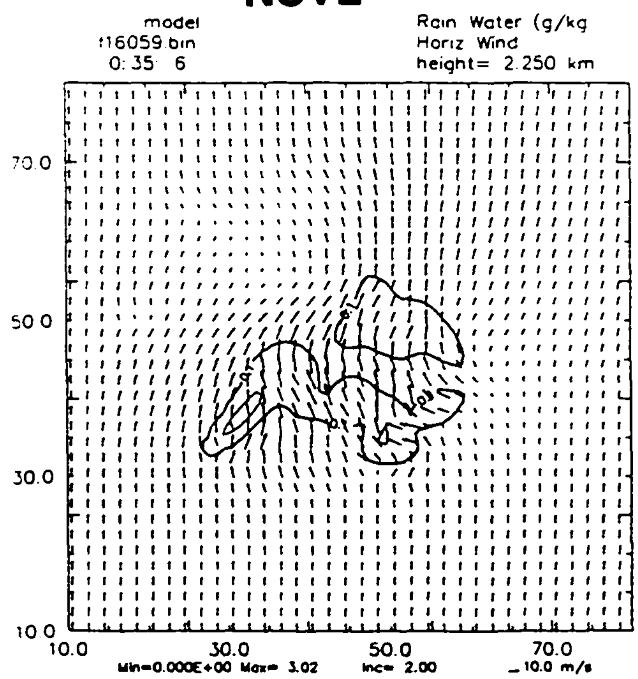

Figure 6.21 Low-level (z = 2.25 km) rainwater and storm-relative vector wind field at a) 2251 UTC (12 minute prediction) and b) 2305 UTC (26 minute prediction) for the NOVL experiment. Rainwater is contoured every 2 g kg^{-1}.

advecting the falling rainwater, during this time when the initial buoyancy field (aided by rainwater induced near-surface convergence) is generating an updraft. The resultant updraft (not shown) is quite narrow and resembles that produces by an idealized "bubble" initialization. By 26 minutes the downwind displacement of the NOVL rainwater field (relative to NOPT) can be seen.

The impact of these differences on the NOVL rainwater correlations is clearly evident in Fig. 6.22. While the NOPT correlation is quite similar to that of the SDVR experiment, the NOVL correlation decreases rapidly during the early part of the prediction. These results suggest that for this case, the inclusion of the 3-D wind field is more important than the inclusion of the perturbation temperature (and pressure) fields. It seems likely, however, that at least some of the differences in the NOVL development are due to the lack of any perturbation water vapor in its initial fields. This lack of initial saturation for the NOVL experiment is an unintended consequence of the simplistic water vapor specification procedure, and may be somewhat obscuring the temperature versus velocity comparison.

6.4 Summary of numerical prediction results

A subjective assessment of the results shown in this chapter indicates that, for this storm case and this numerical model configuration, the sequential single-Doppler retrieval procedure leads to about 35 minutes of useful prediction accuracy. In this context, "useful prediction accuracy" is loosely defined as the time period over which the predicted storm evolution sufficiently resembles the observed evolution to be of value to a forecaster. For the SDVR forecast, the loss of this resemblance appears to occur between the 34 and 43 minute model prediction times, when the southern cell dissipates. In contrast, the DDOP case still appears to retain at least some degree of predictability at 43 minutes. Its failure to

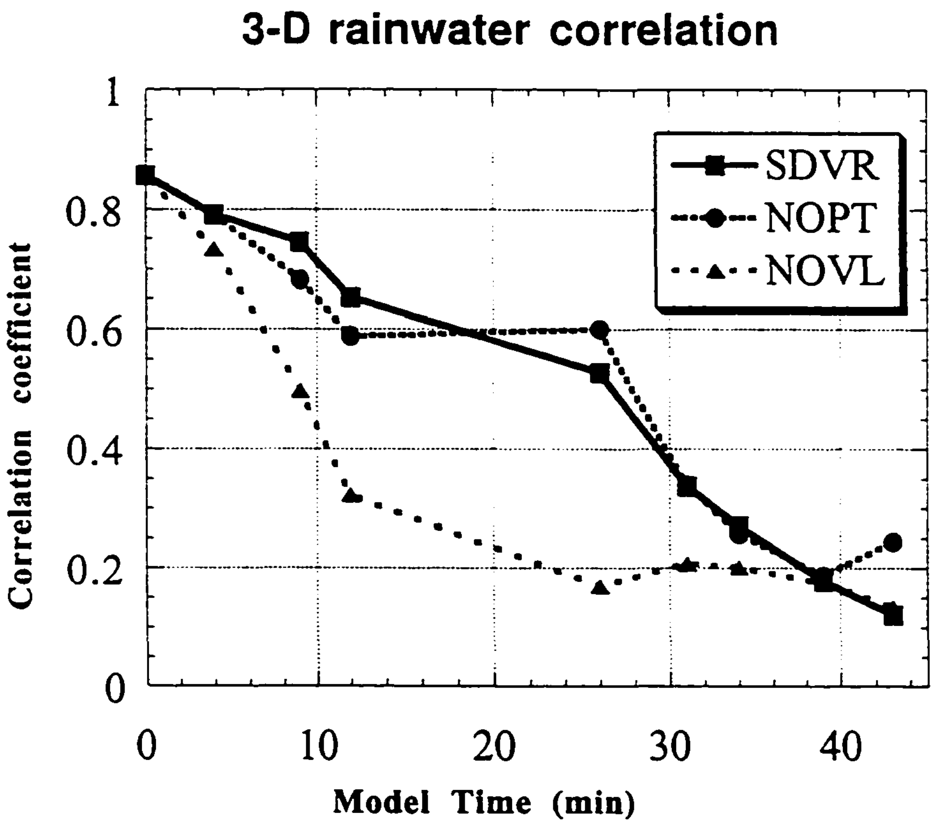

Figure 6.22 Time series of 3-D rainwater correlation coefficients between the verification analyses and the thermodynamic versus velocity sensitivity experiments.

resolve the newer, more dominant southeastern cell, however, suggests that the DDOP predictability does not extend much beyond 45 minutes. For the UVVR experiment, the 12 minute fields are the only ones that bear much resemblance to the verification. This predictability deficit, compared to the SDVR case, clearly indicates that the pseudo-streamfunction in the single-Doppler wind retrieval adds useful information. Furthermore, the small deficit between the SDVR and DDOP predictability limits indicates that for this case the single-Doppler wind retrieval largely compensates for the lack of dual-Doppler data coverage.

One of the strengths of the DDOP and SDVR predictions is their ability to reproduce the deviant storm propagation. Even when the correspondence between the individual precipitation cores begins to break down, the overall predicted storm location is quite good. Evaluating the prediction of individual precipitation cores is somewhat problematic. Obviously, the initial cells weaken too quickly in the model predictions. What is less clear, however, is whether the new cell development south of the main storm in the DDOP and SDVR cases should be considered as a replacement to the original cell, or as a mis-placed and mis-timed counterpart to the observed development southeast of the main storm. Only in the no rainwater experiment was that southeastern cell development faithfully reproduced.

The importance of differences in the strength of the rainwater induced cold-pool was seen repeatedly in the prediction experiments. These sensitivities point strongly to the need for including more realistic microphysics in the numerical predictions, and for improving techniques for initializing moisture variables. Besides the obvious inadequacies in the treatment of microphysics, other known deficiencies include the lack of an assimilation cycle and the use of greatly oversimplified background fields. In spite of these shortcomings, the forecast results represent a greater degree of success for single-

Doppler based storm prediction than has been shown before, and clearly demonstrate the usefulness of the sequential retrieval technique developed in this study.

CHAPTER 7

DISCUSSION

In this study, I have tested the hypothesis that sufficient information can be extracted from a time-series of single-Doppler observations to obtain a dynamically consistent analysis of a thunderstorm suitable for initializing a numerical forecast model. This has been accomplished by developing a sequential single-Doppler retrieval procedure that retains many of the attributes of the most sophisticated techniques (use of dynamic constraints and time-tendency information), while generally avoiding the pitfalls associated with them (computational expense, solution non-uniqueness).

The sequential retrieval procedure has been successfully applied to a real data case of an Oklahoma supercell, and the results have been evaluated by comparing the retrieved fields with dual-Doppler analyses and predictions from linear theory. The retrieved fields have also been used to initialize a short-range numerical prediction, the results of which compare favorably with corresponding dual-Doppler analyses.

The sequential retrieval procedure includes three components. First, a single-Doppler velocity retrieval is applied in a moving reference frame to obtain an estimate of the three-dimensional wind-field within a thunderstorm from three time levels of single-Doppler data. A simple procedure to blend the retrieved wind field with the environmental windfield is then applied, followed by a thermodynamic retrieval to obtain perturbation temperature and pressure within the thunderstorm volume from three time levels of retrieved wind data.

I will summarize the results of the study in Section 7.1 and describe the limitations of the study in Section 7.2. Conclusions from the study will be discussed in Section 7.3, followed by some recommendations for future work in Section 7.4

7.1 Summary of results

7.1.1 Wind retrieval results

Shapiro's (1995a) two-scalar wind retrieval was adapted for use on a deep-convective storm and successfully applied to the Arcadia, OK, tornadic supercell. The principal modification has been to apply the wind retrieval in a moving reference frame. Two different moving reference frames were tested, one that translates with the storm reflectivity volume, and one that translates with the mean wind. For both moving reference frames, simple variational procedures were employed that accurately estimated the horizontal translation components.

Both the storm propagation and mean wind moving reference frames were found to significantly improve the retrieval results compared to the fixed reference frame retrieval. The best results, however, were obtained for the mean wind moving reference frame, which effectively reduced the problem to one of retrieving the unobserved perturbation velocity, and yielded a correlation of .73 for the unobserved azimuthal velocity (averaged over the entire 3-D storm volume and over application of the retrieval at 3 different times). ***These results, reported by Weygandt et al. (1995), represent the first successful application of a single-Doppler wind retrieval to a deep-convective storm, and indicate that difficulties associated with the violation of reflectivity conservation and the relatively low radar scan frequency may not be as severe as previously*** *thought.* Similar results using this and other wind retrieval algorithms have since been reported by Lazarus (1996) and Shapiro et al. (1997).

Decomposition of the retrieved azimuthal velocity indicated that the projection of the mean wind moving reference components accounted for a substantial portion of the total retrieved azimuthal velocity. This helps to explain the superiority of the mean wind reference frame over the others. Comparison of the retrieved and verifying perturbation azimuthal velocity fields indicated a reasonable agreement and some intriguing patterns. At low-levels, the retrieved azimuthal perturbation velocity was associated mostly with polar vorticity, and exhibited weak azimuthal divergence. In contrast, the dual-Doppler verification contained strong azimuthal convergence at low-levels. Consistent with this, the retrieved updraft maximum of 25 m s^{-1} was slightly less than half of the dual-Doppler observed updraft maximum.

Consideration of the above facts lead to the derivation of an original wind-decomposition that illustrates the contributions to the retrieved Cartesian vertical velocity from the terms in Shapiro's two-scalar technique. Application of this decomposition to the retrieved wind field confirmed suspicions that the bulk of the retrieved updraft was due to the convergence of perturbation radial velocity. The retrieval did, however, obtain significant storm-top perturbation azimuthal divergence and upward motion at the lowest elevation angle.

It is not clear why the wind retrieval failed to capture the observed low-level azimuthal convergence. Based on the fact that this low-level convergence is associated with strong upward motion and condensation, I speculate that this is a region of significant deviation from reflectivity conservation. Consistent with this explanation, the successful retrieval of storm-top divergence, in a region where sublimation is occurring, may be understood by noting that sublimation occurs at a slower rate than condensation, implying a smaller departure from reflectivity conservation than at low-levels.

Recognizing that both the mean wind and the majority of the retrieved updraft were obtained directly from the observed radial velocity, comparisons were made between the fields from the full SDVR and fields obtained from a simplified retrieval. This simplified retrieval consisted of the mean horizontal wind components, the perturbation radial velocity, and the contribution of the perturbation radial divergence to the polar velocity (obtained via a polar integral). The primary difference between the fields from the simplified retrieval (which omitted the contribution from the pseudo-streamfunction) and those from the full retrieval was the presence of low-level non-divergent southeasterly to easterly velocities and storm-top azimuthal divergence in the full retrieval.

7.1.2 Thermodynamic retrieval results

Vector wind fields from the dual-Doppler analysis, and the full and simplified single-Doppler retrievals were used as input to the wind adjustment and thermodynamic retrieval. Because available background data for the Arcadia supercell case was limited to a proximity sounding, a simplified procedure was used to blend the retrieved wind field within the storm volume with the base-state sounding winds. This procedure, which involved solving two-dimensional Laplace equations for the horizontal wind components outside the storm, successfully produced a smooth transition between the radar-derived horizontal vectors along the storm edge and the base-state horizontal vectors along the edge of the model domain. The subsequent variational wind adjustment successfully reduced the maximum anelastic mass divergence by about an order of magnitude, while simultaneously retaining the observed radial velocity and minimizing the departure from the retrieved wind components. The dual-Doppler retrieved pressure field was substantially noisier than the single-Doppler retrieved pressure field, but otherwise matched it quite well. Comparisons of the single-Doppler and dual-Doppler retrieved perturbation pressure and vertical vorticity fields with the linear theory predictions of Rotunno and Klemp (1982) indicated a reasonable agreement.

In all three cases, the temperature retrieval resulted in a narrow column of positive perturbation potential temperature in the main storm updraft region. While the dual-Doppler case had a maximum temperature excess of nearly + 9 K (in reasonable agreement with parcel theory calculations from the base-state sounding), the two single-Doppler cases had nearly identical fields with maximum temperature excesses of nearly + 7 K. This similarity of results between the full single-Doppler retrieval and the simplified retrieval indicates that the portion of the unobserved wind that is obtained from the pseudo-streamfunction in the SDVR is not important to the thermodynamic retrieval.

An evaluation of the terms in the vertical momentum equation indicated, as expected, that the main contributions to the retrieved temperature were from the vertical pressure gradient force, rainwater loading and vertical acceleration. Noting that the ratio of the vertical acceleration to the buoyancy expresses the degree of departure from hydrostatic equilibrium, simple linear theory was used to derive an expression that relates this non-hydrostatic departure to the aspect ratio of the buoyancy field. Subjective calculation of these quantities for the single-Doppler and dual-Doppler retrieved fields indicated a reasonable agreement with the linear theory. As might be expected, the buoyant updraft in the dual-Doppler was taller, narrower, and slightly more non-hydrostatic than its single-Doppler counterpart.

7.1.3 Numerical prediction results

Using the ARPS numerical model, reasonably successful short-range predictions of the Arcadia, OK, thunderstorm evolution were obtained for both the single-Doppler retrieved and dual-Doppler derived fields. Subjective evaluation of the forecast fields suggested useful predictability time limits of about 35 and 45 minutes for the single-Doppler and dual-Doppler cases, respectively. In contrast, the prediction initialized with the wind and thermodynamic fields from the simplified wind retrieval (that omitted the wind contribution from the pseudo-streamfunction) was much worse, with useful predictability lost by 15 minutes.

These results are very significant in two ways. The very similar performance of the first two cases indicates that the full single-Doppler velocity retrieval captures those flow-features in the dual-Doppler analysis that are important to the storm evolution. Conversely, the poor performance of the simplified retrieval indicates that the portion of the wind field obtained from the pseudo-streamfunction in the wind retrieval is an important factor in accurately predicting the storm evolution (even though it has little impact on the thermodynamic retrieval).

For both the full single-Doppler retrieval and the dual-Doppler case, the storm evolution is quite accurate at 12 minutes; however, by 26 minutes (the time of the tornado) the original precipitation cores have weakened too quickly in the predictions. This weakening appears to be related to an excessive gust-front surge, which in turn is related to the cold-pool development. This is a known area of weakness in this study, and the model results may in fact depend on the degree to which two shortcomings cancel each other. This is because the model prediction is initiated without an existing low-level cold pool, but with a large amount of suspended rainwater that rapidly falls to the ground.

For both predictions, new precipitation cores formed to the south of the weakening original storm, and these cores compared very favorably with the observed storm at later times. Useful predictability is lost, however, when the original observed storm begins to weaken and a new cell develops to its southeast, which has no predicted counterpart. It is possible that the predicted southern development may have been an attempt to reproduce the observed southeastern development, albeit with a significant position error.

Comparison of the model-predicted and verifying maximum vorticity profiles indicated that the predictions reproduce much of the observed evolution above 3 km. Below 3 km, however, the model predictions have virtually no vorticity evolution and maximum values are significantly less than observed during the tornadic phase of the storm. The reason for this prediction deficiency has not been identified, but again may be related to the excessive gust-front surge.

Two sets of sensitivity experiments were conducted. The first examined the impact of the initial rainwater and water vapor fields. Withholding the initial vapor field was found to produce only a modest temporary departure from the single-Doppler control run, while withholding both the vapor and rainwater fields lead to a weakening of the initial updraft from which the storm never recovered. When the rainwater alone was withheld, the saturated updraft rapidly began regenerating condensate; however, the low-level cold pool was slower to develop, leading to a different storm evolution.

In the last set of experiments, the impact of initial thermodynamic versus velocity fields was examined by first withholding the retrieved temperature and pressure fields then withholding the complete wind field (other than the base-state sounding). In the first experiment the predicted storm closely matched the control. In the second experiment, the falling rainwater was simply advected by the base-state wind, until the buoyancy eventually produced an extremely narrow updraft.

7.2 Conclusions

Based on the results of this investigation three main conclusions can be made. First, for this particular supercell case, the time-series of single-Doppler observations do contain sufficient information to obtain a realistic analysis of the thunderstorm. By successfully retrieving a significant portion of the unobserved windfield, and then retrieving realistic thermodynamic fields, this study has demonstrated that a significant amount of information can indeed be extracted from single-Doppler observations, thereby confirming the original hypothesis.

Perhaps more important from a practical standpoint, this study has also demonstrated that the retrieved initial fields are of sufficient quality to be used to successfully initialize a short-range numerical prediction model. While the predictability time limit of approximately 30 minutes would only be marginally useful in a real operational setting, it is longer than has been demonstrated in other studies (Lin et al. 1993; Lazarus 1996). Furthermore, there is reason to believe that even greater predictability can be obtained by improving upon some of the very crude assumptions that were made in this study. Some of these include the use of a single proximity sounding in lieu of three-dimensional environmental fields, the use of a warm-rain microphysical parameterization in the model, and the simplistic procedure used to initialize the moisture fields in the model.

The second important conclusion from this study is that the sequential retrieval procedure developed and tested herein is a viable technique for this problem. While the sequential procedure lacks some of the theoretical underpinnings found in more sophisticated techniques, these results suggest that it is quite well suited to the single-Doppler retrieval problem. By sub-dividing the task of simultaneously retrieving all unobserved variables into a series of simpler, more tractable retrievals, some of the difficulties associated with techniques such as the full-model adjoint are avoided. Key to this simplification are certain assumptions (such as reflectivity conservation and velocity stationarity), and a decreased capacity to adjust certain fields.

There are, of course, tradeoffs associated with these assumptions and simplifications, including the fact that the objectively analyzed radar data is accepted without regard to possible errors and that the simplifying assumptions may not always be valid. Furthermore, by using simplified constraints instead of the complete model equations, the coupling between variables is expressed in an incomplete manner. This study, however, suggests that the sorts of compromises made in the sequential retrieval may be appropriate for a problem as ill-posed as the single-Doppler retrieval task.

The last major conclusion from this study is that there appears to be at least a degree of short-term predictability for individual thunderstorms. While no attempt has been made herein to address the predictability problem from a theoretical standpoint, this study offers at least empirical evidence of short-term predictability for this case. The fact that the overall storm location and intensity were reasonably well predicted for at least 30 minutes offers practical evidence that real thunderstorms can be predicted from dual- or single-Doppler observations.

7.3 Limitations of this study

The results and conclusions just described must be interpreted subject to the known limitations of the study. Foremost among these is the fact that only one radar data case was tested and that the chosen storm-type (supercell) may represent the easiest test-case (Lilly 1984). While this is appropriate for a proof-of-concept study such as this, one should not generalize our conclusions to all storm types or even all supercell cases. As an example, the location of the Cimarron radar relative to the storm was such that its look angle was aligned very closely with the mean wind vector. The degree to which the retrieval success depends on this orientation has not yet been investigated.

Second, the overly simplistic treatment of moisture in both the retrieval procedure and the numerical prediction represents another serious limitation of the study. Evidence of the strong impact of the moisture fields on the prediction was seen repeatedly in the predictions, and points to the need for more realistic treatments of all microphysical species (including ice) in both the retrieval procedure and the numerical prediction model.

Third, the use of only a proximity sounding to supply background fields as opposed to fully three-dimensional fields derived from standard observations is another shortcoming of the study. While necessitated by the lack of readily available data sources, it dictated the use of unrealistic assumptions in the wind blending procedure and undoubtedly influenced the prediction outcome. One would likely suspect that this limitation has a negative impact on the prediction accuracy, suggesting even greater predictability may be possible.

Fourth, the lack of a data assimilation cycle is a serious limitation of this study. Because the model prediction was initiated from a "cold start", the was no chance to "spin-up" features that were not directly derived from the radar data. By including an assimilation period, features such as the low-level cold pool might be generated during a pre-forecast cycle.

It is important to note that improvements that address the last two deficiencies have already been added to the ARPS model and the associated ARPS Data Analysis System (ADAS, Brewster 1996). In particular, a more sophisticated procedure has been tested for obtaining three-dimensional storm-scale analyses by blending radar-retrieved fields with data from a variety of meso- and synoptic-scale sources (surface reports, wind profilers, radiosondes, and satellite data) (Shapiro et al. 1996). A data assimilation cycle has also been added to ADAS. Tests that use the single-Doppler sequential retrieval procedure in conjunction with a data assimilation cycle have not yet been conducted; however, tests with simple radar-derived fields have yielded encouraging results (Xue et al. 1998).

7.4 Recommendations for future work

As indicated by the above listed limitations, this study represents only a starting point for a substantial amount of additional single-Doppler data assimilation work. Using the present sequential retrieval formulation, a number of additional tests could be done. Perhaps easiest among these would be to use the single-Doppler data from the other radar (Norman) as input to the retrieval procedure. As noted previously, this would test the sensitivity of the retrieval procedure to the radar look angle. Moreover, a series of carefully constructed OSSE experiments would be very useful in identifying other retrieval sensitivities. While much of the current focus on single-Doppler assimilation has rightfully shifted toward the use of real data, thoughtfully designed experiments using simulated data still represent a good way to isolate and quantify sensitivities.

Second, a number of possible enhancements could be made to the single-Doppler wind retrieval. One such enhancement would address the inadequacies of using a single moving reference frame over the entire storm volume. By sub-dividing the retrieval (which requires a minimum of five tilts of radar data) into a series of retrievals over smaller volumes, better results might be obtained.

Two other areas that would benefit significantly from additional work are the treatment of moisture fields in both the retrieval and the model predictions, and the incorporation of the retrieval into a full data assimilation cycle. While adding ice-species to the numerical predictions is a simple modification, accurately specifying their initial distribution from the radar reflectivity represents a major challenge. With regard to the full assimilation cycle, research should focus on how to best blend data from successive single-Doppler retrievals with background fields that may or may not contain any useful information on the storm-scale.

Lastly, the sequential procedure described herein needs to be compared against other competing single-Doppler retrieval procedures for a variety of different storm cases. This comparison should include full-model adjoint techniques and recent storm-scale 3DVAR and fast 4DVAR approaches (Gao et al., 1997; Wang et al. 1997; Pu et al. 1997).

This study represents one of the first attempts to retrieve initial forecast fields from single-Doppler observations of a deep-convective storm. The generally positive results argue for continued research and development of this and other single-Doppler retrieval techniques. Hopefully this continued research effort will lead to the creation of a successful real-time single-Doppler assimilation procedure, and help transform the prospect of deterministic storm-scale prediction into a reality.

APPENDIX A

A NEW SINGLE-DOPPLER VARIATIONAL WIND ADJUSTMENT PROCEDURE

The single-Doppler variational wind adjustment procedure used for this study (Shapiro et al. 1995b) minimizes deviations from a 3-D Cartesian wind field, while simultaneously enforcing anelastic mass conservation and adherence to a specified radial velocity as strong constraints. As discussed in Sections 2.2 and 5.1, this procedure suffers from three shortcomings. The first and perhaps most serious problem is the use of radial velocity as a strong constraint everywhere in the model domain. Enforcement of this constraint only makes sense in regions of single-Doppler observations. Because the radar data typically only covers a portion of the model domain, it is desirable to only enforce the radial velocity constraint within that portion of the domain. Unfortunately, this cannot be accomplished with the present procedure, and outside the storm volume the radial projection of velocity fields obtained from a variety of data sources is used as a strong constraint. Furthermore, even within the storm volume it may be desirable to only enforce radial velocity as a weak constraint.

The second problem is the existence of a singular region in a cone extending upwards from the radar. As discussed in Section 5.1, this problem is most acute at the top of the domain, requiring the use of an alternate upper boundary condition in a small circular area overlying the radar. The third problem is the relatively slow convergence of the procedure, which typically requires several hundred iterations to reduce the anelastic divergence by an order of magnitude.

In this Appendix, I derive a new single-Doppler variational wind adjustment procedure that should overcome most of these difficulties. The new formulation is identical to the original formulation, except radial velocity is enforced as a weak constraint instead of a strong constraint. Thus, the cost function to be minimized is given as:

$$J = \iiint \left(\bar{\rho}u^a - \bar{\rho}u^m\right)^2 + \left(\bar{\rho}v^a - \bar{\rho}v^m\right)^2 + \left(\bar{\rho}w^a - \bar{\rho}w^m\right)^2$$

$$+ \alpha\left(x\bar{\rho}u^a + y\bar{\rho}v^a + z\bar{\rho}w^a - r\bar{\rho}v_r^o\right)^2 + \lambda\left(\frac{\partial\bar{\rho}u^a}{\partial x} + \frac{\partial\bar{\rho}v^a}{\partial y} + \frac{\partial\bar{\rho}w^a}{\partial z}\right)d\sigma \quad , \qquad \text{(A.1)}$$

where σ represents the 3-D spatial domain. The superscripts 'a' and 'o' indicate the adjusted and observed velocities. The superscript 'm' refers to "model" or background velocities, which for this application are the single-Doppler retrieved velocities.

Taking the variation of (A.1) with respect to u^a and setting it equal to zero yields:

$$\iiint \left[2\left(U^a - U^m\right)\delta U^a + 2\,\alpha\, x\, r\,\bar{\rho}\left(v_r^a - v_r^o\right)\delta U^a + \lambda\frac{\partial \delta U^a}{\partial x}\right]d\sigma = 0 \quad , \qquad \text{(A.2)}$$

where $U = \bar{\rho}\,u$. Integrating the last term by parts, (A.2) can be expressed as:

$$\iiint \left[2\left(U^a - U^m\right) + 2\,\alpha\, x\, r\,\bar{\rho}\left(v_r^a - v_r^o\right) - \frac{\partial\lambda}{\partial x}\right]\delta U^a\, d\sigma$$

$$+ \iint \left(\lambda\,\delta U^a\right)dy\,dz\Big|_{x_W}^{x_E} = 0 \quad , \qquad \text{(A.3)}$$

where x_W and x_E indicate the west and east faces of the model domain. Since δU^a is arbitrary, the integrand in the first term must vanish everywhere, yielding the Euler-Lagrange equation:

$$2\left(U^a - U^m\right) + 2\,\alpha\,x\,r\,\bar{\rho}\left(v_r^a - v_r^o\right) - \frac{\partial \lambda}{\partial x} = 0 \quad . \tag{A.4}$$

The second term in (A.3) determines the boundary condition on the east and west faces. The two possible choices that make the term vanish are $\delta U^a = 0$ or $\lambda_2 = 0$. I choose the Dirichlet condition $\lambda = 0$.

Taking the variation of (A.1) with respect to V^a and W^a, similar Euler-Lagrange equations for V^a and W^a can de derived:

$$2\left(V^a - V^m\right) + 2\,\alpha\,y\,r\,\bar{\rho}\left(v_r^a - v_r^o\right) - \frac{\partial \lambda}{\partial y} = 0 \tag{A.5}$$

$$2\left(W^a - W^m\right) + 2\,\alpha\,z\,r\,\bar{\rho}\left(v_r^a - v_r^o\right) - \frac{\partial \lambda}{\partial z} = 0 \quad . \tag{A.6}$$

For the V^a equation (A.5) the Dirichlet condition $\lambda = 0$ is applied on the north and south faces of the model domain. For the W^a equation (A.6), however, the Neumann condition $\delta W^a = 0$ is chosen, so the model's impermeability condition at the bottom and top of the domain will not be violated. A more specific form of this boundary condition will be derived shortly.

Note that taking the variation of (A.1) with respect to λ yields the anelastic mass conservation equation that is used as a strong constraint:

$$\frac{\partial U^a}{\partial x} + \frac{\partial V^a}{\partial y} + \frac{\partial W^a}{\partial z} = 0 \quad . \tag{A.7}$$

This gives us a coupled system of four equations (A.4) - (A.7) for four unknowns (U^a, V^a, W^a, and λ). An expression for $\bar{\rho}\, v_r^a$ can be obtained by taking $x \cdot$ (A.4) + $y \cdot$ (A.5) + $z \cdot$ (A.6) :

$$\bar{\rho} v_r^a = \frac{1}{1+\alpha r^2}\left[r\,\bar{\rho}\, v_r^m + \alpha r^2\, \bar{\rho}\, v_r^o + \frac{1}{2}\frac{\partial \lambda}{\partial r} \right] \quad . \tag{A.8}$$

Taking $\partial/_{\partial x}$ (A.4) + $\partial/_{\partial y}$ (A.5) + $\partial/_{\partial z}$ (A.6) and using (A.7) yields:

$$\nabla^2 \lambda = -\,2\,\nabla \cdot \bar{\rho}\vec{v}^{\,m} + \frac{2}{r^2}\frac{\partial \alpha}{\partial r}\left[\alpha r^4\, \bar{\rho} \left(v_r^a - v_r^o \right) \right] \quad . \tag{A.9}$$

Using (A.8) to eliminate $\bar{\rho}\, v_r^a$ in (A.9) produces an elliptic equation for λ in terms of known quantities:

$$\nabla^2 \lambda - \frac{1}{r^2}\frac{\partial}{\partial r}\left[\frac{\alpha r^4}{\left(1+\alpha r^2\right)} \frac{\partial \lambda}{\partial r} \right] = -\,2\,\nabla \cdot \bar{\rho}\vec{v}^{\,m} - \frac{2}{r^2}\frac{\partial}{\partial r}\left[\frac{\alpha r^4\, \bar{\rho}}{\left(1+\alpha r^2\right)} \left(v_r^o - v_r^m \right) \right] \quad . \tag{A.10}$$

The top and bottom impermeable boundary condition ($\delta W^a = 0$) can now be expressed more explicitly by setting $W^a = W^m$ in (A.6) and using (A.8) to obtain:

$$\frac{\partial \lambda}{\partial z} = 2\,\alpha\, r\, z\, \bar{\rho}\left(v_r^a - v_r^o \right) = \frac{\alpha z}{1+\alpha x^2+\alpha y^2}\left[2r\bar{\rho}\left(v_r^m - v_r^o \right) + x\frac{\partial \lambda}{\partial x} + y\frac{\partial \lambda}{\partial y} \right] \quad . \tag{A.11}$$

The capability to specify the weight factor for the radial velocity constraint makes this procedure very flexible. Outside the storm volume, where there is no special significance to the radial velocity, one would likely set $\alpha = 0$. Inserting this into (A.10) yields the following equations for λ and the adjusted velocities:

$$\nabla^2\lambda = -2\,\nabla\cdot\bar{\rho}\vec{v}^{\,m}$$

$$U^{a} = U^{m} + \frac{1}{2}\frac{\partial\lambda}{\partial x} \quad , \quad V^{a} = V^{m} + \frac{1}{2}\frac{\partial\lambda}{\partial y} \,, \quad W^{a} = W^{m} + \frac{1}{2}\frac{\partial\lambda}{\partial z} \quad . \qquad \text{(A.12)}$$

Thus, for $\alpha = 0$, the procedure gives the favorable result of simplifying to the Ray et al. (1981) procedure.

Within the storm volume, dimensional arguments would suggest setting $\alpha = 1/r^2$. Inserting this into (A.10) yields the following system of equations:

$$\nabla^2\lambda - \frac{1}{r^2}\frac{\partial}{\partial r}\left[\frac{r^2}{2}\frac{\partial\lambda}{\partial r}\right] = -2\,\nabla\cdot\bar{\rho}\vec{v}^{\,m} - \frac{2}{r^2}\frac{\partial}{\partial r}\left[\frac{r^2\bar{\rho}}{2}\left(v_r^{o} - v_r^{m}\right)\right]$$

$$\bar{\rho}\, v_r^{a} = \frac{1}{2}\left[\bar{\rho}\left(v_r^{m} + v_r^{o}\right) + \frac{1}{2}\frac{\partial\lambda}{\partial r}\right]$$

$$U^{a} = U^{m} - \alpha\, x\, r\, \bar{\rho}\left(v_r^{a} - v_r^{o}\right) - \frac{1}{2}\frac{\partial\lambda}{\partial x}$$

$$V^{a} = V^{m} - \alpha\, y\, r\, \bar{\rho}\left(v_r^{a} - v_r^{o}\right) - \frac{1}{2}\frac{\partial\lambda}{\partial y}$$

$$W^{a} = W^{m} - \alpha\, z\, r\, \bar{\rho}\left(v_r^{a} - v_r^{o}\right) - \frac{1}{2}\frac{\partial\lambda}{\partial z} \quad . \qquad \text{(A.13)}$$

The singularity problem could be avoided with this formulation by setting $\alpha = 0$ in the singular region. This would likely be done anyway, because the singular region coincides with the "cone of silence" above the radar. Lastly, sensitivity tests indicate that the slowness of convergence in the original wind adjustment is related to the singularity problem. By overcoming the singularity problem, the number of iterations required for convergence would likely be decreased.

APPENDIX B

MEAN WIND EFFECTS ON DIVERGENCE AND VORTICITY CALCULATIONS USING SINGLE-DOPPLER RADAR DATA

Two quantities of interest to storm-scale researchers and forecasters are divergence and vorticity. These quantities are usually desired in Cartesian coordinates, where the vertical vorticity is especially important and the horizontal convergence can be vertically integrated to obtain the vertical velocity. Unfortunately, Doppler radars provide only the radial velocity, from which only the radial convergence and radial contribution to polar and azimuthal vorticity can be computed. Nevertheless, meteorologists have taken advantage of the fact that for small elevation angles the polar and vertical axes are nearly parallel to compute useful divergent and vorticity quantities from radial velocity data (Burgess and Lemon, 1990).

The purpose of this appendix is to illustrate the impact on the various spherical divergence and vorticity terms due to the radar sampling of the mean horizontal wind. Obviously, a mean horizontal wind contains no horizontal divergence or vertical vorticity. Furthermore, in a Cartesian coordinate system, the individual terms in the horizontal divergence and vertical vorticity are zero for a mean horizontal wind. If, however, radial and azimuthal components are used as proxies for the horizontal components in calculations of divergence and vorticity, non-zero contributions arise from the projection of the mean horizontal wind into the spherical components. These contributions, which can lead to biases when the radial velocity alone is used to estimate divergence and vorticity, can easily be removed by subtracting the projection of the mean horizontal wind from the radial velocity, leading to a perturbation radial velocity.

Because in this study I am interested in the relative contribution of the radial and azimuthal divergence to the Cartesian vertical velocity, I focus on the mean wind contributions to these terms. More specifically, I document that the contribution to the Cartesian vertical velocity from the radial divergence is skewed by a contribution from the part of the radial velocity associated with the mean horizontal wind. I also show that the mean horizontal wind contribution in the radial divergence term is offset by opposing mean horizontal wind contributions in the azimuthal divergence and radial velocity projection terms, leading to a correct estimate of vertical velocity from the total spherical fields.

I also illustrate that the common (but mathematically incorrect) practice of approximating radial divergence ($\frac{1}{r^2}\frac{\partial\left(r^2 v_r\right)}{\partial r}$) as $\frac{\partial v_r}{\partial r}$ fortuitously removes the mean wind contribution, but also neglects a portion of the perturbation radial divergence. Next, the magnitudes of the mean wind contributions are estimated, and it is shown that their sign depends on whether the scanned region is upwind or downwind from the radar. Finally, I show that a similar mean wind effect exists for the calculation of polar vorticity.

Based on these results a simple correction is recommended in which the mean wind projection is subtracted from the spherical components prior to calculating vorticity or divergence. A simple technique is suggested as a method for estimating the mean horizontal wind components from the radial velocity data.

I begin with mass conservation expressed in radar coordinates:

$$\frac{1}{r^2}\frac{\partial\left(r^2 v_r\right)}{\partial r} + \frac{1}{r\cos\theta}\frac{\partial v_\phi}{\partial \phi} + \frac{1}{r\cos\theta}\frac{\partial\left(\cos\theta\, v_\theta\right)}{\partial \theta} = 0 \quad . \tag{B.1}$$

To illustrate the impact of the ${\partial v_r}/{\partial r}$ approximation, I expand the radial divergence term appearing in (B.1):

$$\frac{\partial v_r}{\partial r} + \frac{2\,v_r}{r} + \frac{1}{r\cos\theta}\frac{\partial v_\phi}{\partial \phi} + \frac{1}{r\cos\theta}\frac{\partial\left(\cos\theta\; v_\theta\right)}{\partial\theta} = 0 \quad . \tag{B.2}$$

Integration of the r-ϕ divergence in the polar direction with $\theta_0 = 0$ and $V_{\theta_0} = 0$ leads to:

$$v_\theta = -\underbrace{\frac{r}{\cos\theta}\frac{\partial}{\partial r}\left[\int_0^\theta \cos\Theta\; v_r d\Theta\right]}_{\int {\partial v_r}/{\partial r}\ \mathit{term}} - \underbrace{\frac{2}{\cos\theta}\int_0^\theta \cos\Theta\; v_r d\Theta}_{\int {2\,v_r}/{r}\ \mathit{term}} - \underbrace{\frac{1}{\cos\theta}\frac{\partial}{\partial\phi}\left[\int_0^\theta v_\phi d\Theta\right]}_{\int {\partial v_\phi}/{\partial\phi}\ \mathit{term}} \quad , \tag{B.3}$$

where the terms are identified below the equation and Θ is a dummy integration variable. Note that the first two terms on the RHS of (B.3) come from the radial divergence and the last term comes from the azimuthal divergence. The first term on the RHS of (B.3) represents the simple (${\partial v_r}/{\partial r}$) approximation to the radial divergence.

The contributions from the mean horizontal wind are examined by partitioning the three spherical velocity components into mean and perturbation parts:

$$v_r = \bar{v}_r + v_r' = \cos\theta\,\sin\phi\; U + \cos\theta\,\cos\phi\; V + v_r' \tag{B.4}$$

$$v_\phi = \bar{v}_\phi + v_\phi' = \cos\phi\; U - \sin\phi\; V + v_\phi' \tag{B.5}$$

$$v_\theta = \bar{v}_\theta + v_\theta' = -\sin\theta\,\sin\phi\; U - \sin\theta\,\cos\phi\; V + v_\theta' \quad , \tag{B.6}$$

where U and V are the mean horizontal wind components in the x and y directions, respectively. Substituting (B.4) and (B.5) into (B.3) leads to:

$$
\begin{aligned}
v_\theta = & -\underbrace{\frac{r}{\cos\theta}\frac{\partial}{\partial r}\left[\left(\sin\phi\, U + \cos\phi\, V\right)\int_0^\theta \cos^2\Theta\, d\Theta\right]}_{\int \partial\bar{v}_r/\partial r \ \textit{term}} - \underbrace{\frac{r}{\cos\theta}\frac{\partial}{\partial r}\left[\int_0^\theta \cos\Theta\, v_r'\, d\Theta\right]}_{\int \partial v_r'/\partial r \ \textit{term}} \\
& -\underbrace{\frac{2}{\cos\theta}\left(\sin\phi\, U + \cos\phi\, V\right)\int_0^\theta \cos^2\Theta\, d\Theta}_{\int 2\bar{v}_r/r \ \textit{term}} - \underbrace{\frac{2}{\cos\theta}\int_0^\theta \cos\Theta\, v_r'\, d\Theta}_{\int 2v_r'/r \ \textit{term}} \\
& -\underbrace{\frac{1}{\cos\theta}\frac{\partial}{\partial\phi}\left[\int_0^\theta \left(\cos\phi\, U - \sin\phi\, V\right) d\Theta\right]}_{\int \partial\bar{v}_\phi/\partial\phi \ \textit{term}} - \underbrace{\frac{1}{\cos\theta}\frac{\partial}{\partial\phi}\left[\int_0^\theta v_\phi'\, d\Theta\right]}_{\int \partial v_\phi'/\partial\phi \ \textit{term}} , \qquad \text{(B.7)}
\end{aligned}
$$

where the various mean and perturbation terms have been identified below the equation. Note that the RHS terms in the first two lines represent the contribution from the radial divergence and the terms in the third line represent the contribution from the azimuthal divergence.

Evaluation of the integrals for the mean wind terms leads to:

$$
\begin{aligned}
v_\theta = & -\underbrace{\frac{r}{2\cos\theta}\frac{\partial}{\partial r}\left[\left(\sin\phi\, U + \cos\phi\, V\right)\left(\sin\theta\cos\theta + \theta\right)\right]}_{\int \partial\bar{v}_r/\partial r \ \textit{term}} - \underbrace{\frac{r}{\cos\theta}\frac{\partial}{\partial r}\left[\int_0^\theta \cos\Theta\, v_r'\, d\Theta\right]}_{\int \partial v_r'/\partial r \ \textit{term}} \\
& -\underbrace{\frac{1}{\cos\theta}\left(\sin\phi\, U + \cos\phi\, V\right)\left(\sin\theta\cos\theta + \theta\right)}_{\int 2\bar{v}_r/r \ \textit{term}} - \underbrace{\frac{2}{\cos\theta}\int_0^\theta \cos\Theta\, v_r'\, d\Theta}_{\int 2v_r'/r \ \textit{term}}
\end{aligned}
$$

$$- \underbrace{\frac{1}{\cos\theta}\frac{\partial}{\partial\phi}\left[\left(\cos\phi\, U - \sin\phi\, V\right)\theta\right]}_{\int \partial\bar{v}_\phi/\partial\phi \ \textit{term}} - \underbrace{\frac{1}{\cos\theta}\frac{\partial}{\partial\phi}\left[\int_0^\theta v'_\phi\, d\Theta\right]}_{\int \partial v'_\phi/\partial\phi \ \textit{term}} \quad , \qquad \text{(B.8)}$$

where, again, the various terms are indicated below the equation. Of particular interest in (B.8) are the mean wind contributions. While non-zero mean wind contributions will arise from the $\int 2\bar{v}_r/r$ *term* and the $\int \partial\bar{v}_\phi/\partial\phi$ *term* , the $\int \partial\bar{v}_r/\partial r$ *term* equals zero and will contribute nothing to the polar velocity. *Thus, we can see that the mean wind contribution in the radial divergence arises entirely within the* $\int 2\bar{v}_r/r$ *term, and that the simple* $\partial v_r/\partial r$ *approximation does not contain a mean wind contribution. Unfortunately, the* $\partial v_r/\partial r$ *approximation fails to account for the contribution from the* $\int 2v'_r/r$ *term, leading to an inaccurate estimate of the perturbation radial divergence.*

Evaluation of the derivatives for the mean quantities (noting that the contribution from the $\int \partial\bar{v}_r/\partial r$ *term* is zero), recombining the perturbation radial divergence terms and splitting $\int 2\bar{v}_r/r$ into two terms leads to:

$$v_\theta = - \underbrace{\frac{1}{r\cos\theta}\frac{\partial}{\partial r}\left[r^2\int_0^\theta \cos\Theta\, v'_r\, d\Theta\right]}_{\frac{1}{r^2}\int \frac{\partial}{\partial r}\left(r^2 v'_r\right) \ \textit{term}} - \underbrace{\frac{1}{\cos\theta}\frac{\partial}{\partial\phi}\left[\int_0^\theta v'_\phi\, d\Theta\right]}_{\int \partial v'_\phi/\partial\phi \ \textit{term}}$$

$$\underbrace{- \sin\theta\left(\sin\phi\, U + \cos\phi\, V\right) - \frac{\theta}{\cos\theta}\left(\sin\phi\, U + \cos\phi\, V\right)}_{\int 2\bar{v}_r/r \ \textit{terms}}$$

$$+ \underbrace{\frac{\theta}{\cos\theta}\left(\sin\phi\, U + \cos\phi\, V\right)}_{\int \partial\bar{v}_\phi/\partial\phi \ \textit{term}} . \qquad \text{(B.9)}$$

Note that cancellation occurs between two of the mean wind terms. Now, substitution of (B.4) and (B.9) into the Cartesian vertical velocity expression:

$$w = \sin\theta\, v_r + \cos\theta\, v_\theta \qquad \text{(B.10)}$$

yields:

$$w = -\frac{1}{r}\frac{\partial}{\partial r}\left[r^2\int_0^\theta \cos\Theta\, v_r'\, d\Theta\right] - \frac{\partial}{\partial\phi}\left[\int_0^\theta v_\phi'\, d\Theta\right] + \sin\theta\, v_r'$$

$$- \cos\theta\sin\theta\left(\sin\phi\, U + \cos\phi\, V\right) \underbrace{- \theta\left(\sin\phi\, U + \cos\phi\, V\right)}_{\int 2\bar{v}_r/r \textit{ terms}}$$

$$\underbrace{+ \theta\left(\sin\phi\, U + \cos\phi\, V\right)}_{\int \partial\bar{v}_\phi/\partial\phi \textit{ term}}$$

$$\underbrace{+ \cos\theta\sin\theta\left(\sin\phi\, U + \cos\phi\, V\right)}_{\bar{v}_r \textit{ term}} \quad , \qquad \text{(B.11)}$$

where the term names have only been retained for the mean wind contributions.

As can be seen in equation (B.11), cancellation occurs between the various mean horizontal wind terms, resulting in no net contribution to the vertical velocity. Note, however, that the value of the individual mean wind terms is not zero. This is in contrast to the Cartesian coordinate formulation, in which the individual mean wind terms, as well as their sum, is equal to zero. For the spherical formulation, the polar integral of the radial divergence results in two mean wind terms. One of these terms is offset by a mean wind term from the polar integral of the azimuthal divergence, while the other term is offset by the projection of the mean wind in the radial direction. Thus, the Cartesian vertical velocity can be accurately calculated by retaining only the perturbation terms listed on the first line of equation (B.11). *More importantly, any calculation of the radial convergence contribution to the vertical velocity should be done using only the perturbation velocity.* As will be shown shortly, inclusion of the mean radial divergence term introduces an artificial dependence on the position of the radar-sampled region relative to the location of the radar and the direction of the mean wind.

The signs and magnitudes of the mean wind terms is evaluated as follows. The $\left(\sin\phi\, U + \cos\phi\, V\right)$ factor that is common to all terms simply gives the azimuthal dependence as being a maximum when the radar beam is aligned with the mean horizontal wind, and decreasing to zero when the radar beam is perpendicular to the mean horizontal wind. Considering the maximum error case of the radar beam aligned with the mean wind, the erroneous contribution from the two radial divergence terms is:

$$W_{err}^{max} = \left|\bar{\vec{V}}_h\right|\left(\cos\theta \sin\theta + \theta\right) . \tag{B.12}$$

The error from the first term in (B.12) has a maximum magnitude of $0.5\left|\bar{\vec{V}}_h\right|$ for a radar elevation angle of 45°. For typical radar elevation angles, the error (expressed as a fraction of the mean wind magnitude) increases linearly with θ. This dependency results in error that increases by about 5% of the mean wind for each 3 degrees of elevation angle. Because the error is offset by the radial projection of the mean wind (a term that is available from single-Doppler observations), it typically is not a problem. The second term in (B.12) increases with increasing elevation angle and has a maximum magnitude of about $1.5\left|\bar{\vec{V}}_h\right|$ as the radar beam approaches vertical. For typical radar elevation angles it has the same dependency as the first term. It is more significant, however, because the offsetting term from the azimuthal divergence is not available from single-Doppler observations.

If the region sampled by the radar is upwind (downwind) from the radar, the erroneous mean wind contributions from the two radial divergence terms will be positive (negative) [i.e. upward (downward) motion]. *This artificial dependence of the estimated vertical velocity on the position relative to the radar can be avoided simply by using perturbation spherical velocities.* Note that the erroneous contributions from the azimuthal divergence and the projection of the radial velocity will be of opposite sign to the radial divergence contributions. This has important consequences for wind analysis techniques that rely solely on projection of the radial velocity into the Cartesian direction. If the total radial velocity is used, the erroneous projection of radar-sampled horizontal mean wind will lead to large areas of weak upward (downward) motion downwind (upwind) from the radar.

As a final note, I illustrate that a similar cancellation of mean horizontal wind contributions occurs for the radial and azimuthal contributions to the polar vorticity. The polar vorticity is given as:

$$\omega_\theta = \underbrace{\frac{1}{r\cos\theta}\frac{\partial v_r}{\partial \phi}}_{\partial v_r/\partial\phi \ term} - \underbrace{\frac{1}{r}\frac{\partial(r\, v_\phi)}{\partial r}}_{\partial v_\phi/\partial r \ term}\,, \tag{B.13}$$

where the names of the terms have been indicated below the equation. Using (B.4) and (B.5) to partition the radial and azimuthal velocities into mean and perturbation parts, the polar vorticity can be re-written as:

$$\omega_\theta = \underbrace{\frac{1}{r}\left(\cos\phi\, U - \sin\phi\, V\right)}_{\partial\bar{v}_r/\partial\phi \ term} + \underbrace{\frac{1}{r\cos\theta}\frac{\partial v_r'}{\partial\phi}}_{\partial v_r'/\partial\phi \ term}$$

$$- \underbrace{\frac{1}{r}\left(\cos\phi\, U - \sin\phi\, V\right)}_{\partial\bar{v}_\phi/\partial r \ term} - \underbrace{\frac{1}{r}\frac{\partial\left(r\, v_\phi'\right)}{\partial r}}_{\partial v_\phi'/\partial r \ term} \quad , \qquad \text{(B.14)}$$

where the mean and perturbation terms have been identified below the equation. As with the divergence calculation, cancellation between the mean horizontal wind contributions occurs in (B.14). If, however, only the radial velocity terms are retained, an erroneous mean wind contribution will result.

The $\left(\cos\phi\, U - \sin\phi\, V\right)$ factor that is common to both mean wind terms simply gives the azimuthal dependence as being a maximum when the radar beam is perpendicular to the mean horizontal wind, and decreasing to zero when the radar beam is aligned with the mean horizontal wind. Considering the maximum error case of the radar beam perpendicular to the mean wind, the erroneous contribution to the polar vorticity is given by:

$$\omega_{\theta_{err}}^{max} = \frac{1}{r}\left|\vec{\bar{V}}_h\right| \quad . \qquad \text{(B.15)}$$

The $1/r$ factor results in fairly significant errors at close range. For example, a 20 m s^{-1} mean wind at a range of 20 km would give a vorticity error of $1(10)^{-3}$ s^{-1}.

If the region sampled by the radar is to the left (right) of the mean wind vector, the erroneous mean radial wind contribution to the polar vorticity will be positive (negative) [i.e. cyclonic (anti-cyclonic)]. This artificial dependence of the estimated vertical velocity on the position relative to the radar can be avoided simply by using perturbation spherical velocities.

A simple least squares technique that is ideally suited to estimating the mean wind from radial velocity data is described in Chapter 2. This procedure variationally fits constant horizontal velocity components to the observed radial velocity field. Tests of this method for obtaining the mean wind moving reference frame for the two-scalar retrieval showed that it obtained very good results for the supercell case. Difficulties would be anticipated for cases where a frontal boundary dividing regions of opposing velocities lies across the radar data coverage region. In that situation, mean wind components of near zero would be obtained.

APPENDIX C

IDEALIZED SIMULATIONS USING THE BASE-STATE SOUNDING

In evaluating the results from the radar-initialized predictions presented in Chapter 6, it is useful to compare them with results from simpler prediction methods. One particularly useful comparison standard is that of an idealized simulation, in which convection is initiated via a warm thermal within a horizontally-homogeneous base-state derived from the proximity sounding. For more than 20 years, this technique has been successfully used to create simulated storms that exhibit many of the features observed in real convective storms (Schlesinger 1975; Klemp and Wilhelmson 1978; Wilhelmson and Klemp 1981; Weisman and Klemp 1984; Rotunno and Klemp 1985). More recently, attempts have been made to apply this technique in operational settings to make forecasts of storm types based on observed or model derived soundings (Brooks et al. 1993; Janish et al. 1995, Wicker et al. 1997). Thus, it is appropriate to compare the results shown in Chapter 6 with an idealized prediction using only the base-state sounding information.

To facilitate this comparison, two idealized simulations were completed. Using the base-state wind and thermodynamic profiles from the real-data predictions, convection was initiated in these "bubble" simulations by specifying an axially symmetric thermal perturbation of horizontal radius 10 km and vertical radius 1500 m. In the first experiment, a positive perturbation temperature excess of 2 K was specified at the center of the thermal, which was located at x = y = 40 km, z = 1500 m within the same 100 x 100 km domain used for the real-data predictions. Allowing for a grid translation equal to the observed storm motion ($U_{gr} = 10$ m s^{-1}, $V_{gr} = 6$ m s^{-1}), a 100 minute simulation was completed. The convective development was fairly weak and dissipated within 60 min., apparently due to the pronounced dry-layer in the sounding (see Fig. 3.3a). A second experiment was then conducted, in which a temperature excess of 4 K was specified at the center of the thermal. The initial convective evolution was similar to that of the 2 K experiment; however, weak re-development occurred after 60 min. Selected results from the 4 K idealized simulation are presented to highlight the similarities and differences between it and the radar-initialized storm predictions, and the observed storm evolution. These results include a time-series of the domain maximum vertical velocity and plots of the low-level rainwater and horizontal wind fields.

Comparison of the domain maximum vertical velocity time series (Fig. C.1) with the corresponding time-series for real data predictions (Fig. 6.9), indicates some similarities, but also highlights the difficulties inherent in verifying the idealized simulations. For example, the pronounced decrease in updraft strength beginning at 40 minutes in the idealized experiment compares favorably with the decrease seen in the radar-initialized predictions and the actual storm beginning at about 12 min. (2251 UTC). In reality, however, this decrease was occurring well over two hours into the lifetime of the storm, which developed around 2045 UTC (DB97). Clearly, the idealized experiment fails to accurately reproduce the full life-cycle of the storm. It should be noted, however, that the real-data predictions have not demonstrated an ability to reproduce the *complete* life-cycle of the storm either. Because the available Doppler radar data dictated an initialization at a time when the storm was already a mature supercell, the real-data experiments can only test the evolution through the tornadic phase and the subsequent weakening.

Based on the short life-span of the idealized storm (less than 60 min.), it cannot be classified as a supercell. This represents a failure of the idealized simulation to predict the dominant convective mode of the day. Examination of the low-level rainwater fields at

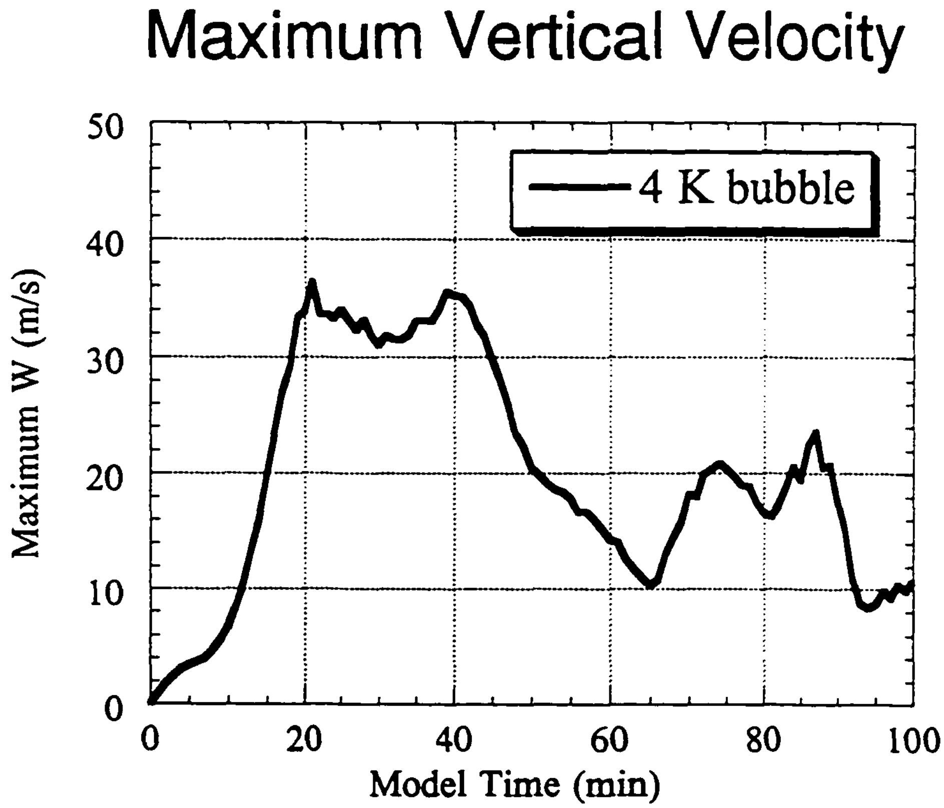

Figure C.1 Time series of domain maximum vertical velocity (m s^{-1}) for the 4 K idealized "bubble" simulation.

40, 60, 80 and 100 minutes (Fig. C.2) illustrates the trends seen in the maximum vertical velocity time-series. Clearly evident is the weakening of the storm between 40 and 60 minutes and the modest re-development around 80 min. By 100 minutes, the storm has diminished to a series of small, weak rainwater features along the edge of the low-level cold pool (not shown). A positive result from the idealized simulation is that the predicted storm motion matches the observed storm motion reasonable well.

Detailed examination of the 40 min. idealized rainwater field (Fig. C.2a) indicates that it reproduces some of the features seen during the first 20 minutes of the real-data predictions (see Fig. 6.1). These include the northeast to southwest orientation of the most intense rainwater region, the cyclonic turning of the storm-relative wind vectors, and the weak rainwater appendage in the southwestern portion of the storm. Attempts to more precisely match predicted fields from the idealized simulation with fields from either the verifying dual-Doppler analysis or the real-data predictions were not fruitful.

Overall, the idealized simulation can be characterized as showing some similarities to the observed storm, but failing to accurately predict the storm type or faithfully reproduce the storm evolution. Thus, the usefulness of the idealized simulation to an operational forecaster is likely rather marginal. It is not clear how much greater utility is gained from the single-Doppler initialized prediction. It does, however, forecast the specific storm evolution with a reasonable degree of accuracy for a period of about 30 minutes.

a)

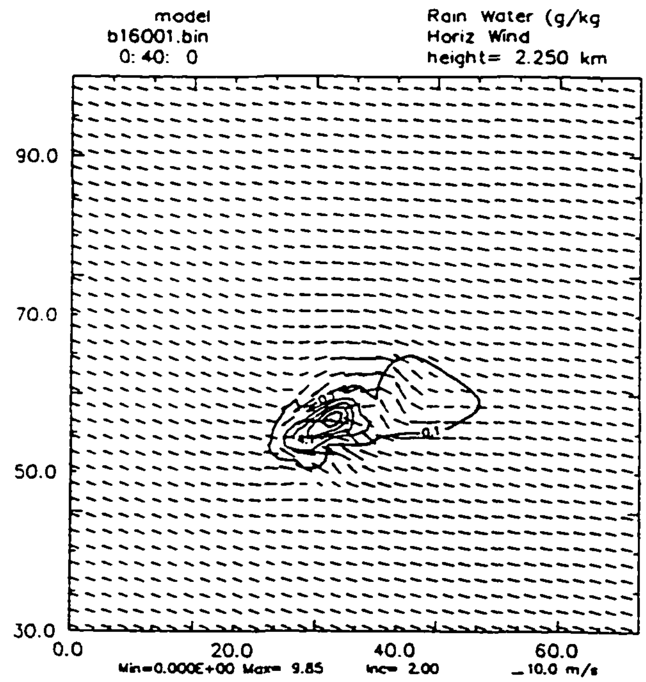

b)

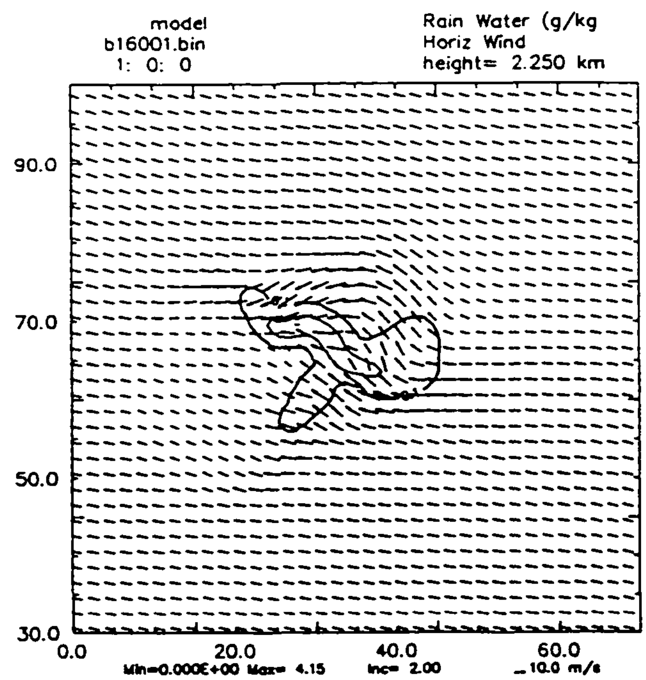

Figure C.2 Low-level (z = 2.25 km) rainwater and storm-relative wind vectors from the 4 K idealized storm simulation at a) 40 min, b) 60 min, c) 80 min, and d) 100 min. Rainwater is contoured every 2 g kg^{-1}.

c)

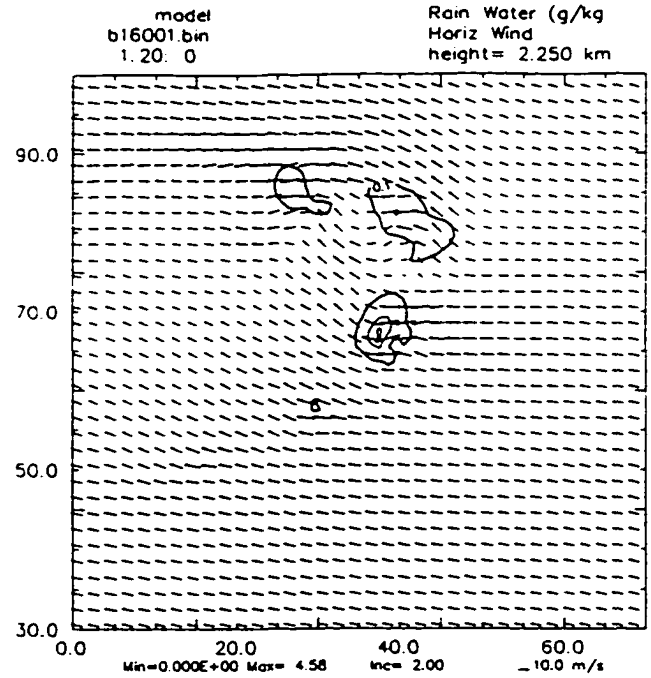

d)

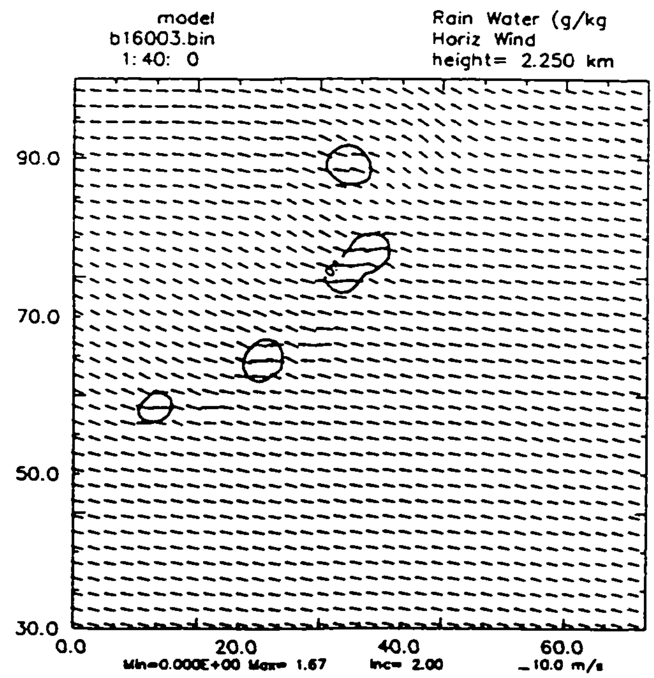

Figure C.2 (Continued)

REFERENCES

Alberty, R. L., 1969: A proposed mechanism for cumulonimbus persistence in the presence of strong vertical shear. *Mon. Wea. Rev.,* **97**, 590-597.

Arakawa, A., and V. R. Lamb, 1977: Computational design of the basic dynamical processes of the UCLA general circulation model. *Methods in Computational Physics,* **17**, 174-265, Academic Press, 337 pp.

Asselin, R., 1972: Frequency filter for time integrations. *Mon. Wea. Rev.,* **97**, 487-490.

Baer, F., 1977: Adjustments of initial conditions required to suppress gravity oscillations in non-linear flows. *Beitr. Phys. Atmosph.,* **50**, 350-366.

Bao, J. W., and Y. H. Kuo, 1995: On/off switches in the adjoint method: Step functions. *Mon. Wea. Rev.,* **123**, 1589-1594.

Bao, J. W., and T. T. Warner, 1993: Treatment of on/off switches in the adjoint method: FDDA experiments with a simple model. *Tellus,* **45A**, 525-538.

Barnes, S., 1964: A technique for maximizing details in numerical map analysis. *J. Appl. Meteor,.* **3**, 395-409.

Bergthorsson, P., and B. Doos, 1955: Numerical weather map analysis. *Tellus,* **7**, 329-340.

Bjerknes, J., and H. Solberg, 1922: Life cycle of cyclones and polar front theory of atmospheric circulation. *Geofys. Publ., Norske, Videnskaps-Akad. Oslo,* **3** (1) 1-18

Bjerknes, V., 1904: Das problem von der wettervorhersage, betrachtet vom standpunkt der mechanik und der physik. *Meteor. Z.,* **21**, 1-7.

Brandes, E. A., 1984: Relationships between radar-derived thermodynamic variables and tornadogenesis. *Mon. Wea. Rev.,* **112**, 1033-1052.

Brandes, E. A., R. Davies-Jones, and B. Johnson, 1988: Streamwise vorticity effects on supercell morphology and persistence. *J. Atmos. Sci.,* **45**, 947-963.

Brewster, K. A., 1984: Kinetic energy evolution in a developing severe thunderstorm. Master's Thesis, University of Oklahoma, Norman, OK, 171 pp.

Brewster, K., 1996: Application of a Bratseth analysis scheme including Doppler radar data. Preprints, *15th Conf. on Wea. Analysis and Forecasting,* Norfolk, VA, Amer. Meteor. Soc., 92-95.

Brooks, H. E., C. A. Doswell III, and L. J. Wicker, 1993: STORMTIPE: A forecasting experiment using a three-dimensional cloud model. *Wea. Forecasting*, **8**, 352-362.

Brown, R. A., 1992: Initiation and evolution of updraft rotation within an incipient supercell thunderstorm. *J. Atmos. Sci.*, **49**, 1997-2014.

Browning, K. A., and R. Wexler, 1968: A determination of kinematic properties of a wind field using Doppler-radar. *J. Appl. Meteor,*. **7**, 105-113.

Burgess, D. W. and L. R. Lemon, 1990: Severe thunderstorm detection by radar, *Radar in Meteorology,* edited by D. Atlas, AMS, Boston, MA, 619-647.

Carnahan, B., H. A. Luther, and J. O. Wilkes, 1969: *Applied Numerical Methods*. John Wiley and Sons, 604 pp.

Charney, J. G., 1955: The use of primitive equations of motion in numerical prediction. *Tellus*, **7**, 22-26.

Charney, J. G., R. Fjortoft, and J. von Neumann, 1950: Numerical integration of the barotropic vorticity equation. *Tellus*, **2**, 237-254.

Charney, J. G., M. Halem, and R. Jastrow, 1969: Use of incomplete historical data to infer the present state of the atmosphere. *J. Atmos. Sci.*, **26**, 1160-1163.

Cressman, G., 1959: An operational objective analysis system. *Mon. Wea. Rev.*, **122**, 1189-1203.

Crook, A., 1994: Numerical experiments initialized with radar-derived winds. Part I: Simulated data experiments. *Mon. Wea. Rev.*, **122**, 1189-1203.

Crook, A., and J. D. Tuttle, 1994: Numerical experiments initialized with radar-derived winds. Part II: Forecasts of three gust front cases. *Mon. Wea. Rev.*, **122**, 1204-1217.

Daley, R., 1991: *Atmospheric Data Analysis*. Cambridge University Press, 457 pp.

Davies, H., and R. Turner, 1977: Updating prediction models by dynamic relaxation: An examination of the technique. *Quart. J. Roy. Meteor. Soc.*, **103**, 225-245.

Davies-Jones, R., 1984: Streamwise vorticity: The origin of updraft rotation in supercell storms. *J. Atmos. Sci.*, **41**, 2991-3006.

Derber, J. C., 1989: A variational continuous assimilation technique. *Mon. Wea. Rev.*, **117**, 2437-2446.

Dey, C., and L. Morone, 1985: Evolution of the National Meteorological Center global data assimilation system: January 1982-December 1983. *Mon. Wea. Rev.*, **106**, 304-318.

Dickinson, R., and D. Williamson, 1972: Free oscillations of a discrete stratified fluid with application to numerical weather prediction. *J. Atmos. Sci.,* **29**, 623-640.

Dowell, D. C., and H. B. Bluestein, 1997: The Arcadia, Oklahoma, storm of 17 May 1981: Analysis of a supercell during tornadogenesis. *Mon. Wea. Rev.*, **125**, 2562-2582.

Droegemeier, K. K., 1990: Toward a science of storm-scale prediction. Preprints, *16th Conf. on Sev. Local Storms,* Kananaskis Park, Alberta, Canada, Amer. Meteor. Soc., 256-262.

Droegemeier, K. K., 1997: Numerical prediction of thunderstorms: Challenges, potential benefits and results from real-time operational tests. *WMO Bulletin,* **46** (4), 1-13.

Durran, D. R., and J. B. Klemp, 1983: A compressible model for the simulation of moist mountain waves. *Mon. Wea. Rev.,* **111**, 2341-2361.

Easterbrook, C. C., 1975: Estimating horizontal winds by two-dimensional curve fitting of single Doppler radar measurements. Preprints, *16th Conf. on Radar Meteor.*, Amer. Meteor. Soc., 214-219.

Eliassen, A., 1954: *Provisional report on calculation of spatial covariance and autocorrelation of the pressure field. Rep. No. 5* (Oslo: Videnskaps-Akademiet Institut for Vaer og Klimaforskning).

Ellis, S., 1997: Holefilling data voids in meteorological fields. Master's Thesis, University of Oklahoma, Norman, OK, 198 pp.

Fiedler, B., 1995: Rudiments of static stability and convective instability. Class notes, METR 3113, Univ. Okla., Norman, Oklahoma.

Fujita, T., and H. Grandoso, 1968: Split of a thunderstorm into anticyclonic and cyclonic motion as determined from numerical model experiments. *J. Atmos. Sci.,* **25**, 416-439.

Gal-Chen, T., 1978: A method for initializing the anelastic equations: Implications for matching models with observations. *Mon. Wea. Rev.,* **106**, 587-606.

Gal-Chen, T., 1982: Errors in fixed and moving frame of references: Applications for conventional and Doppler radar analysis. *J. Atmos. Sci.,* **39**, 2279-2300.

Gal-Chen, T., and C. E. Hane, 1981: Retrieving buoyancy and pressure fluctuations from Doppler radar observations: A status report. *Progress in radar meteorology, Atmos. Technol.,* No. 13, 98-104.

Gal-Chen, T., and R. A. Kropfli, 1984: Buoyancy and pressure perturbations derived from dual-Doppler radar observations of the planetary boundary layer: Applications for matching models with observations. *J. Atmos. Sci.,* **41**, 3007-3020.

Gandin, L., 1963: *Objective analysis of meteorological fields.* (Leningrad: Gridomet). English translation (Jerusalem: Israeli program for scientific translations), 1965.

Gao, J. D., M. Xue, and K. Droegemeier, 1997: A possible option for ARPS data assimilation: A 3-D variational analysis by direct minimization. Internal CAPS memo. 22 pp.

Ghil, M., S. Cohn, J. Tavantzis, K. Bube, and E, Isaacson, 1981: Applications of estimation theory to numerical weather prediction. *Dynamic meteorology: data assimilation methods,* L. Bengtsson, M. Ghil, and E. Kallen eds. Springer-Verlag, 139-224.

Gilchrist, B., and G. Cressman, 1954: An experiment in objective analysis. *Tellus,* **6**, 309-318.

Hane, C. E., and B. C. Scott, 1978: Temperature and pressure perturbations within convective clouds derived from detailed air motion information: preliminary testing. *Mon. Wea. Rev.,* **106**, 654-661.

Hane, C. E., R. B. Wilhelmson, and T. Gal-Chen 1981: Retrieval of thermodynamic variables within deep convective clouds: Experiments in three-dimensions. *Mon. Wea. Rev.,* **106**, 564-576.

Hauser, D., and P. Amayenc, 1986: Retrieval of cloud water and water vapor contents from Doppler radar data in a tropical squall line. *J. Atmos. Sci.,* **43**, 823-838.

Hinkelmann, K., 1951: Der mechanismus des meteorologischen larmes. *Tellus,* **3**, 285-296.

Hoke, J., and R. Anthes, 1976: The initialization of numerical models by a dynamic relaxation technique. *Mon. Wea. Rev.,* **104**, 1551-1556.

Houze, R. A., 1993: *Cloud Dynamics*, Academic Press, 573 pp.

Janish, P. R., K. K. Droegemeier, M. Xue, K. Brewster, and J. Levit, 1995: Evaluation of the advanced regional prediction system (ARPS) for storm-scale operational forecasting. *14th Conf. on Wea. Analysis and Forecasting,* Dallas, TX, Amer. Meteor. Soc., 224-229.

Joss, J., and A. Waldvogel, 1970: Raindrop size distributions and Doppler velocities. Preprints, *14th. Radar Meteor. Conf.,* Tucson, AZ, Amer. Meteor. Soc., 153-156.

Kalman, R., 1960: A new approach to linear filtering and prediction problems. *Trans. ASME, SER. D, J. Basic Eng.,* **83**, 95-108.

Kapitza, H., 1991: Numerical experiments with the adjoint of a non-hydrostatic mesoscale model. *Mon. Wea. Rev.,* **119**, 2993-3011.

Kessler, E., 1969: On the distribution of continuity of water substance in atmospheric circulations. Meteor. Monogr., **10**, 84 pp.

Klazura, G. E., and D. A. Imy, 1993: A description of the initial set of analysis products available from the NEXRAD WSR-88D system. *Bull. Amer. Meteor. Soc.*, **74**, 1293-1311.

Klemp, J. B., and D. K. Lilly, 1978: Numerical simulations of hydrostatic mountain waves. *J. Atmos. Sci.*, **35**, 78-107.

Klemp, J. B., and R. Rotunno, 1983: A study of the tornadic region within a thunderstorm. *J. Atmos. Sci.*, **40**, 359-377.

Klemp, J. B., and R. B. Wilhelmson, 1978: The simulation of three-dimensional convective storm dynamics. *J. Atmos. Sci.*, **35**, 1070-1096.

Koscielny, A. J., R. J. Doviak, and A. Rabin, 1981: Statistical considerations in the estimation of divergence from single-Doppler radar and application to pre-storm boundary-layer observations. *J. Appl. Meteor*,. **21**, 197-210.

Laroche, S., and I. Zawadzki, 1994: A variational analysis method for the retrieval of three-dimensional wind field from single-Doppler radar data. *J. Atmos. Sci.*, **51**, 2664-2682.

Lazarus, S. M., 1996: The assimilation and prediction of a Florida multicell storm using single-Doppler data. Ph.D. Dissertation, University of Oklahoma, Norman, OK, 340 pp.

LeDimet, F. X., 1982: A general formalism of variational analysis. *Cimms Report*, Norman, OK, 34 pp.

LeDimet, F. X., and O. Talagrand, 1986: Variational algorithms for analysis and assimilation of meteorological observations: theoretical aspects. *Tellus*, **38A**, 97-110.

Lewis, J., and J. Derber, 1985: The use of adjoint equations to solve a variational problem with advective constràints. *Tellus*, **30**, 309-327.

Lhermitte, R. M., and D. Atlas, 1961: Precipitation motion by pulse Doppler radar. *Proc. 9th Weather Radar Conf.*, Amer. Meteor. Soc., 218-223.

Li. Y., 1991: A note on the uniqueness problem of variational adjustment approach to four-dimensional data assimilation. *J. Meteor. Soc. Japan*, **69**, 581-585.

Lilly, D. K., 1962: On the numerical simulation of buoyant convection. *Tellus*, **14**, 168-172.

Lilly, D. K., 1984: Some facets of the predictability problem for atmospheric mesoscales. *Proceedings, American Institute of Physics*, 287-294.

Lilly, D. K., 1990a: Numerical prediction of thunderstorms -- has its time come? *Quart. J. Roy. Meteor. Soc.*, **116**, 779-798.

Lilly, D. K., 1990b: Convergence analysis of the Gal-Chen-Liou 4DDA insertion model. Internal CAPS memo. 7 pp.

Lin, Y., P. S. Ray, and K. W. Johnson 1993: Initialization of a modeled convective storm using Doppler radar-derived fields. *Mon. Wea. Rev.,* **121**, 2757-2775.

Lions, J. L., 1971: *Optimal control theory of systems governed by partial differential equations*. Translated by S. K. Mitter, Springer-Verlag, Berlin, 404 pp.

Liou, Y. C., 1989: Retrieval of three-dimensional wind and temperature fields from one component wind data by using the four-dimensional data assimilation technique. Master's Thesis, University of Oklahoma, Norman, OK, 112 pp.

Lorenc, A., 1981: A global three-dimensional multivariate statistical interpolation scheme. *Mon. Wea. Rev.,* **109**, 701-721.

Machenhauer, B. 1977: On the dynamics of gravity oscillations in a shallow water model with application to normal mode initialization. *Contrib. Atmos. Phys.* **50**, 352-271.

Marchuk, G., 1974: *Numerical solution of problems of the dynamics of the atmosphere and ocean.* (in Russian) (Leningrad: Gridomet).

Matsuno, T. 1966: Numerical integrations of the primitive equations by a simulated backward difference method. *J. Meteor. Soc. Japan,* **44**, 76-83.

Miyakoda, K., and R. Moyer, 1968: A method of initialization for dynamical weather forecasting. *Tellus,* **20**, 115-128.

Navon, I. M., X. L. Zou, J. Derber and J. Sela, 1992: Variational data assimilation with an adiabatic version of the NMC spectral model. *Mon. Wea. Rev.,* **122**, 1433-1446.

Newton, C. W., and H. R. Newton, 1959: Dynamical interactions between large convective clouds and environment with vertical shear. *J. Meteor.,* **16**, 483-496.

Nitta, T., and J. Hovermale, 1969: A technique of objective analysis and initialization for the primitive forecast equations. *Mon. Wea. Rev.,* **97**, 652-658.

O'Brien, J. J., 1970: Alternative solutions to the classical vertical velocity problem. *J. Appl. Meteor,.* **9**, 197-203.

Orlanski, I., 1976: A simple boundary condition for unbounded hyperbolic flows. *J. Comput. Phys.,* **21**, 251-269.

Panofsky, H., 1949: Objective weather map analysis. *J. Appl. Meteor.,* **6**, 386-392.

Park, S. K., and K. K. Droegemeier, 1997: 4DVAR with a moist adjoint applied to deep convective storms - simulated data experiments. *2nd. US-Korea Joint workshop for storm- and meso-scale weather analysis and prediction,* Seoul, Korea.

Parsons, D. B., C. G. Mohr and T. Gal-Chen, 1987: A severe frontal rainband. Part III: Derived thermodynamic structure. *J. Atmos. Sci.*, **44**, 1615-1631.

Phillips, N., 1960: On the problem of the initial data for primitive equations. *Tellus*, **12**, 121-126.

Pu, Z. X., E. Kalnay, J. Sela, and I. Szunyogh, 1997: Sensitivity of forecast errors to initial conditions with a quasi-inverse linear model. *Mon. Wea. Rev.*, **125**, 2479-2503.

Ray, P. S., B. C. Johnson, K. W. Johnson, J. S. Bradberry, J. J. Stephens, K. K. Wagner, R. B. Wilhelmson, and J. B. Klemp, 1981: The morphology of several tornadic storms on 20 May 1977. *J. Atmos. Sci.*, **38**, 1643-1663.

Rhinehart, R. E., 1979: Internal storm motions from single non-Doppler weather radar. NCAR/TN-146+STR, 262 pp.

Richardson, L. F. 1922: *Weather Prediction by Numerical Process*. Cambridge University Press, reprinted Dover, 1965, 236 pp.

Roache, P. J., 1982: *Computational Fluid Dynamics*. Hermosa Publishers, Albuquerque, N.M., 446 pp.

Rogers, R. R., 1964: An extension of the Z-R relation for Doppler radar. Preprints, *11th. Radar Meteor. Conf.*, Boulder, CO, Amer. Meteor. Soc., 158-161

Rotunno, R., and J. B. Klemp, 1982: The influence of the shear-induced pressure gradient on thunderstorm motion. *Mon. Wea. Rev.*, **110**, 136-151.

Rotunno, R., and J. B. Klemp, 1985: On rotation and propagation of simulated supercell thunderstorms. *J. Atmos. Sci.*, **42**, 271-292.

Roux, F., 1985: Retrieval of thermodynamic fields from multiple Doppler radar data using the equations of motion and thermodynamic equation. *Mon. Wea. Rev.*, **113**, 2142-2157.

Rutledge, S. A., and P. V. Hobbs, 1983: The mesoscale and microscale structure and organization of clouds and precipitation in a mid-latitude cyclone. XII: A diagnostic modeling study of precipitation development in narrow cold-frontal rainbands. *J. Atmos. Sci.*, **41**, 2949-2972.

Rutledge, S. A., and P. V. Hobbs, 1984: The mesoscale and microscale structure and organization of clouds and precipitation in a mid-latitude cyclone. VIII: A model for the "seeder-feeder" process in warm frontal rainbands. *J. Atmos. Sci.*, **40**, 1185-1206.

Sasaki, Y. 1955: A functional study of the numerical prediction based on the variational principle. *J. Meteor. Soc. Japan*, **33**, 262-275.

Sasaki, Y. 1958: An objective analysis based on the variational method. *J. Meteor. Soc. Japan*, **36**, 77-88.

Sasaki, Y. 1969: Proposed inclusion of time-variation terms, observational and theoretical in numerical variational objective analysis. *J. Meteor. Soc. Japan,* **47**, 115-124.

Sasaki, Y. 1970: Some basic formalisms in numerical variational analysis. *Mon. Wea. Rev.,* **98**, 899-910.

Schlesinger, R. E., 1975: A three-dimensional numerical model of an isolated deep convective cloud: Preliminary results. *J. Atmos. Sci.,* **32**, 934-957.

Shapiro, A., and S. Lazarus, 1993: A modified dynamic recovery technique for cloud-scale numerical models. Preprints, *17th Conf. on Sev. Local Storms,* St. Louis, MO, Amer. Meteor. Soc., 455-459.

Shapiro, A., S. Ellis, and J. Shaw, 1995a: Single-Doppler velocity retrievals with Phoenix II data: Clear air and microburst wind retrievals in the planetary boundary layer. *J. Atmos. Sci.,* **52**, 1265-1287.

Shapiro, A., K. Droegemeier, S. Lazarus, and S. Weygandt, 1995b: Forward variational four-dimensional data assimilation and prediction experiments using a storm-scale numerical model. *International Symposium on Assimilation of Observations in Meteorology and Oceanography.* Tokyo, WMO, 361-366.

Shapiro, A. et al., 1995c: Highlights from a single-Doppler velocity retrieval intercomparison project. *Sixth Conf. on Aviation Weather Systems,* Dallas, TX, Amer. Meteor. Soc., 541-546.

Shapiro, A., L. Zhao, S. Weygandt, K. Brewster, S. Lazarus, and K. Droegemeier, 1996: Initial forecast fields created from single-Doppler wind retrieval, thermodynamic retrieval and ADAS. Preprints, *11th Conf. on Num. Wea. Pred.,* Norfolk, VA, Amer. Meteor. Soc., 119-121.

Shapiro, A., L. Zhao, and S. Weygandt, 1997: Single-Doppler velocity retrieval experiments with WSR-88D data of an Oklahoma squall line. Preprints, *28th Conf. on Radar Meteor.,* Austin, TX, Amer. Meteor. Soc., 414-415.

Smagorinsky, J., 1963: General circulation experiments with primitive equations. I. The basic experiment. *Mon. Wea. Rev.,* **91**, 99-164.

Smythe, G. R., and D. S. Zrnic, 1983: Correlation analysis of Doppler radar data and retrieval of the horizontal wind. *J. Appl. Meteor,.* **22**, 297-311.

Sun, J., D. W. Flicker, and D. K. Lilly, 1991: Recovery of three-dimensional wind and temperature fields from simulated single-Doppler radar data. *J. Atmos. Sci.,* **48**, 876-890.

Sun, J., and A. Crook, 1994: Wind and thermodynamic retrieval from single-Doppler measurements of a gust front observed during Phoenix II. *Mon. Wea. Rev.,* **124**, 1075-1091.

Sun, J., and A. Crook, 1996: Comparison of thermodynamic retrieval by the adjoint method with the traditional retrieval method. *Mon. Wea. Rev.,* **124**, 308-324.

Sun, J., and A. Crook, 1997: Dynamic and microphysical retrieval from Doppler radar observations using a cloud model and its adjoint. Part I: Model development and simulated data experiments. *J. Atmos. Sci.,* **54**, 1642-1661.

Sun, J., and A. Crook, 1998: Dynamic and microphysical retrieval from Doppler radar observations using a cloud model and its adjoint. Part II: Retrieval experiments of an observed Florida convective storm. *J. Atmos. Sci.,* **55**, 835-852.

Taylor, G. I., 1938: The spectrum of turbulence. *Proc. Roy. Soc. London,* **A164**, 476-490.

Taylor, W. L., Ed. 1982: 1981 spring program summary. NOAA Tech. Memo. ERL NSSL-93, 97 pp.

Talagrand, O., and P. Courtier, 1987: Variational assimilation of meteorological observations with the adjoint vorticity equations. Part I: Theory. *Quart. J. Roy. Meteor. Soc.,* **113**, 1311-1328.

Thacker, W., and R. Long, 1988: Fitting dynamics to data. *J. Geophys. Res.,* **93**, 1227-1240.

Thepaut, J., D. Vasiljevic and P. Coutier, 1993: Variational assimilation of conventional meteorological observations with a multilevel primitive equation model. *Quart. J. Roy. Meteor. Soc.,* **119**, 153-186.

Thompson, P., 1961: A dynamic method of analyzing meteorological data. *Tellus,* **13**, 334-349.

Thompson, P., 1969: Reduction of analysis error through constraints of dynamic consistency. *J. Appl. Meteor.,* **8**, 739-742.

Trapp, R. J., R. Davies-Jones, 1997: Tornadogenesis with and without a dynamic pipe effect. *J. Atmos. Sci.,* **54**, 113-133.

Tuttle, J. D., and G. B. Foote, 1990: Determination of the boundary layer airflow from a single Doppler radar. *J. Atmos. and Oceanic Technol.,* **7**, 218-232.

Verlinde, J., and W. R. Cotton 1990: A critical look at microphysical retrieval algorithms. Preprints, *Conf. on Cloud Physics,* San Francisco, CA, Amer. Meteor. Soc. 453-457.

Verlinde, J., and W. R. Cotton 1993: Fitting microphysical observations of non-steady convective clouds to a numerical model: An application of the adjoint technique of data assimilation to a kinematic model. *Mon. Wea. Rev.,* **121**, 2776-2793.

Waldteufal, P., and H. Corbin, 1979: On the analysis of single Doppler-radar. *J. Appl. Meteor.*, **18**, 532-542.

Wang, Z., K. K. Droegemeier, L. White, and I. M. Navon, 1997: Application of a new adjoint Newton algorithm to the 3D ARPS Storm-scale model using simulated data. *Mon. Wea. Rev.*, **125**, 2460-2478.

Weisman, M. L., and J. B. Klemp, 1984: The structure and classification of numerically simulated convective storms in directionally varying wind shears . *Mon. Wea. Rev.*, **112**, 2479-2498.

Weygandt, S. S., K. K. Droegemeier, C. E. Hane, and C. L. Ziegler, 1990: Data assimilation experiments using a two-dimensional cloud model. Preprints, *16th Conf. on Severe Local Storms*, Kananaskis Park, Alta., Canada, Amer. Meteor. Soc., 493-498.

Weygandt, S. S., A. Shapiro, and K. K. Droegemeier, 1995: Adaptation of a single-Doppler velocity retrieval to a deep convective storm. Preprints, *27th Conf. on Radar Meteor.*, Vail, CO, Amer. Meteor. Soc., 264-266.

Wicker, L. J., M. P. Kay, and M. P. Foster, 1997: STORMTIPE-95: Results from a convective storm forecast. *Wea. Forecasting*, **12**, 388-398.

Wilhelmson, R. B., and J. B. Klemp, 1981: A three-dimensional numerical simulation of splitting severe storms on 3 April 1964. *J. Atmos. Sci.*, **35**, 1037-1063.

Williamson, D., and R. Dickinson 1976: Free oscillations of the NCAR global circulation model. *Mon. Wea. Rev.*, **104**, 1372-1391.

Xu, Q., 1996a: Generalized adjoint for physical properties with parameterized discontinuities. Part I: Basic and heuristic examples. *J. Atmos. Sci.*, **53**, 1123-1142.

Xu, Q., 1996b: Generalized adjoint for physical properties with parameterized discontinuities. Part II: Vector formulations and matching conditions. *J. Atmos. Sci.*, **53**, 1143-1155.

Xu, Q., C. J. Qiu, and J. X. Yu 1994a: Adjoint method retrievals of low-altitude wind fields from single-Doppler reflectivity measured during Phoenix-II. *J. Atmos. and Oceanic Technol.*, **11**, 275-288.

Xu, Q., C. J. Qiu, and J. X. Yu 1994b: Adjoint method retrievals of low-altitude wind fields from single-Doppler wind data. *J. Atmos. and Oceanic Technol.*, **11**, 579-585.

Xu, Q., C. J. Qiu, H. D. Gu, and J. X. Yu 1995: Simple adjoint retrievals of microburst winds from single-Doppler data. *Mon. Wea. Rev.*, **123**, 1822-1833.

Xue, M., K. K. Droegemeier, V. Wong, A. Shapiro, and K. Brewster, 1995: ARPS User's Guide, Version 4.0. Center for Analysis and Prediction of Storms, 380 pp.

Xue, M., D. Wang, D. Hou, K. Brewster, and K. Droegemeier, 1998: Prediction of the 7 May 1995 squall lines over the central U.S. with intermittent data assimilation. Preprints, *12th Conf. on Num. Wea. Pred.*, Phoenix, AZ, Amer. Meteor. Soc., 191-194.

Zhang, J., and T. Gal-Chen, 1996: Single-Doppler wind retrieval in the moving frame of reference. *J. Atmos. Sci.*, **53**, 2609-2623.

Zhang, J., and F. Carr, 1996: Moisture and latent heating rate retrieval from radar data. Preprints, *12th Conf. on Num. Wea. Pred.*, Phoenix, AZ, Amer. Meteor. Soc., 205-208.

Zhao, L. 1995: A 3-D Cressman smoother in the radar coordinate. Internal CAPS memo. 3 pp.

Ziegler, C. L., 1985: Retrieval of thermal and microphysical variables in observed convective storms. Part I: Model development and preliminary testing. *J. Atmos. Sci.*, **42**, 1487-1509.

Ziegler, C. L., 1988: Retrieval of thermal and microphysical variables in observed convective storms. Part II: Sensitivity of cloud processes to variation of the microphysical parameterization. *J. Atmos. Sci.*, **45**, 1072-1090.

Zou, X. L., I. M. Navon, and J. Sela, 1993: Variational data assimilation with threshold processes using the NMC multilevel primitive-equation model. *Tellus*, **45A**, 370-387.

Zou, X. L., 1995: Tangent linear and adjoint "on-off" processes and their feasibility for use in four-dimensional variational data assimilation. *Tellus*, **49A**, (1) 3-31.

IMAGE EVALUATION TEST TARGET (QA-3)

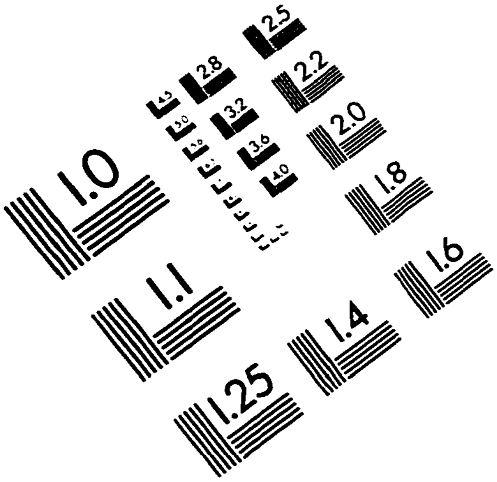

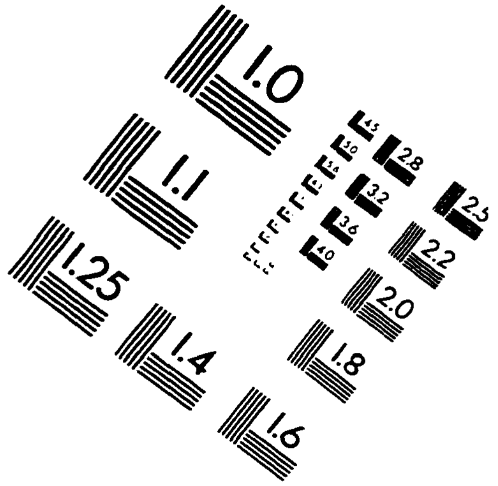

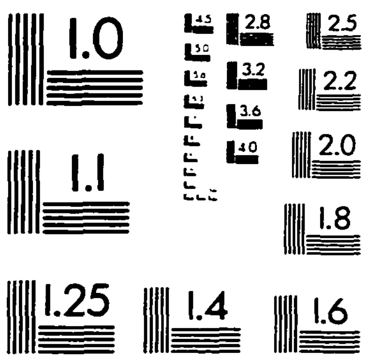

150mm

6″

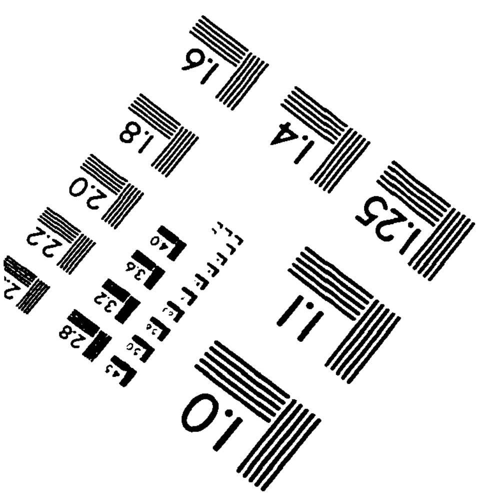

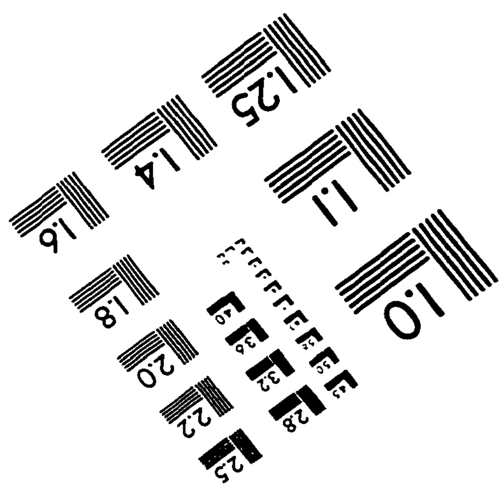

APPLIED IMAGE . Inc
1653 East Main Street
Rochester, NY 14609 USA
Phone: 716/482-0300
Fax: 716/288-5989